



UNIVERSITAT POLITÈCNICA
DE CATALUNYA
BARCELONATECH

Synthetic quantum matter using atoms and light

Javier Argüello-Luengo

ADVERTIMENT La consulta d'aquesta tesi queda condicionada a l'acceptació de les següents condicions d'ús: La difusió d'aquesta tesi per mitjà del repositori institucional UPCommons (<http://upcommons.upc.edu/tesis>) i el repositori cooperatiu TDX (<http://www.tdx.cat/>) ha estat autoritzada pels titulars dels drets de propietat intel·lectual **únicament per a usos privats** emmarcats en activitats d'investigació i docència. No s'autoritza la seva reproducció amb finalitats de lucre ni la seva difusió i posada a disposició des d'un lloc aliè al servei UPCommons o TDX. No s'autoritza la presentació del seu contingut en una finestra o marc aliè a UPCommons (*framing*). Aquesta reserva de drets afecta tant al resum de presentació de la tesi com als seus continguts. En la utilització o cita de parts de la tesi és obligat indicar el nom de la persona autora.

ADVERTENCIA La consulta de esta tesis queda condicionada a la aceptación de las siguientes condiciones de uso: La difusión de esta tesis por medio del repositorio institucional UPCommons (<http://upcommons.upc.edu/tesis>) y el repositorio cooperativo TDR (<http://www.tdx.cat/?locale-attribute=es>) ha sido autorizada por los titulares de los derechos de propiedad intelectual **únicamente para usos privados enmarcados** en actividades de investigación y docencia. No se autoriza su reproducción con finalidades de lucro ni su difusión y puesta a disposición desde un sitio ajeno al servicio UPCommons No se autoriza la presentación de su contenido en una ventana o marco ajeno a UPCommons (*framing*). Esta reserva de derechos afecta tanto al resumen de presentación de la tesis como a sus contenidos. En la utilización o cita de partes de la tesis es obligado indicar el nombre de la persona autora.

WARNING On having consulted this thesis you're accepting the following use conditions: Spreading this thesis by the institutional repository UPCommons (<http://upcommons.upc.edu/tesis>) and the cooperative repository TDX (<http://www.tdx.cat/?locale-attribute=en>) has been authorized by the titular of the intellectual property rights **only for private uses** placed in investigation and teaching activities. Reproduction with lucrative aims is not authorized neither its spreading nor availability from a site foreign to the UPCommons service. Introducing its content in a window or frame foreign to the UPCommons service is not authorized (*framing*). These rights affect to the presentation summary of the thesis as well as to its contents. In the using or citation of parts of the thesis it's obliged to indicate the name of the author.

UNIVERSITAT POLITÈCNICA DE CATALUNYA
INSTITUT DE CIÈNCIES FOTÒNIQUES (ICFO)

DOCTORAL THESIS

**Synthetic quantum matter
using atoms and light**

Author: Javier
ARGÜELLO-LUENGO

Supervised by:
Prof. Darrick E. CHANG
Dr. Alejandro
GONZÁLEZ-TUDELA

Thesis committee:
Dr. Diego Porras Torre
Prof. Maciej Lewenstein
Dr. Johannes Feist
Prof. Leticia Tarruell (reserve)
Prof. Bruno Juliá Díaz (reserve)

*A thesis submitted in fulfillment of the requirements
for the degree of PhD in Photonics*

Barcelona, 2022

Synthetic quantum matter using atoms and light
Javier Argüello-Luengo, PhD Thesis ©2022

First printing, September 2022.

*A mis abuelos:
Angelines, Dolores, José María y Rafael*

Abstract

” You write a book, and it takes you forever, and you make all kinds of mistakes, and then you finally figure out what you’re doing. And you go back, and you take out all of the worst mistakes, the ones that you can find, and you make it look like you knew what you were doing all along. That’s the final illusion.

— **Richard Russo**

(Pulitzer awardee, in an interview to WNYC, 2016)

Atomic and optical physics are two fields closely connected by a shared range of energy scales, and the interactions between them. Atoms represent the most fundamental components of matter, and interactions with electromagnetic fields are responsible for many properties used to characterize a material, like the emission and absorption of radiation by these systems. Over the last decades, this has allowed us to use light as a tool to access and manipulate the internal states of atomic systems. Such a quantum control has transformed atoms into one of the preferred platforms to explore fundamental science, including applications in quantum information, quantum metrology or, more recently, the realization of synthetic materials where light can induce interactions that would be difficult to find intrinsically in real materials.

In the first part of this Thesis, we show how single atoms coupled to a cavity field can offer unique opportunities as quantum optomechanical devices because of their small mass and strong interaction with light. In particular, we focus on the "single-photon strong coupling" regime, where motional displacements on the order of the zero-point uncertainty are sufficient to shift the cavity resonance frequency by more than its linewidth. By coupling atomic motion to the narrow cavity-dressed atomic resonance, we theoretically observe that the scattering properties of single photons can become highly entangled with the atomic wavefunction, even if the cavity linewidth is large. This leads to a per-photon motional heating that is significantly larger than the single-photon recoil energy, as well as mechanically-induced oscillations that could be observed in the correlations of state-of-the-art cavity systems.

In the second part of the Thesis, we investigate how synthetic materials built using light can be harnessed as quantum simulators, defeating the limitations that classical computers face in the exploration of quantum phenomena. We particularly focus on ultracold atomic mixtures trapped in optical lattices, where atom-mediated long-range interactions can provide an enabling tool in the simulation of relevant problems in condensed matter or quantum chemistry.

First, we show that fermionic atoms in an ultracold gas can act as a mediator,

giving rise to effective long-range RKKY interactions among other neutral atoms trapped in an optical lattice. We further propose several experimental knobs to tune these interactions, which are characterized by the density and dimensionality of the gas and are accessible in current experimental platforms. We also show that these knobs open up the exploration of new frustrated regimes where symmetry-protected topological phases and chiral spin liquids emerge.

Second, we introduce a set of experimental schemes where long-range interactions are mediated by an additional bosonic species trapped in a commensurate optical lattice, both in 2D and 3D. In particular, we show that the interplay with cavity QED can lead to effective Coulomb-like repulsion, which opens the door to the analog simulation of quantum chemistry problems using ultracold fermionic atoms as simulated electrons. Apart from explaining the emergent mechanism, we provide operational conditions for the simulator, benchmark it with simple atoms and molecules, and analyze how the continuous limit is approached for increasing optical lattice sizes. Finally, we compare our results with those of the continuum limit, where conventional quantum chemistry methods can be evaluated and tested.

In summary, our results show connections between different areas of theoretical and experimental physics where light-matter interaction can play a dominant role, and suggest how this can be harnessed to further advance our understanding of strongly-correlated quantum matter.

Resumen

La física óptica y atómica son dos campos de investigación conectados por un rango de energías común. El átomo representa el componente más fundamental de la materia, y su interacción con campos electromagnéticos es responsable de muchas de las propiedades utilizadas para caracterizar materiales, como por ejemplo la emisión y absorción de radiación por estos sistemas. Este control a nivel cuántico ha erigido los átomos como una de las plataformas preferidas para explorar ciencia fundamental, incluyendo aplicaciones en información cuántica, metrología o, más recientemente, la fabricación de materiales sintéticos en que la luz es capaz de inducir interacciones que serían difíciles de encontrar intrínsecamente en materiales convencionales.

En la primera parte de esta Tesis mostramos cómo un átomo individual acoplado a una cavidad puede manifestar propiedades optomecánicas a nivel cuántico únicas, debido a su baja masa y fuerte interacción con la luz. En particular, nos centramos en el límite de acoplamiento fuerte al nivel de un único fotón, donde un desplazamiento en el orden de la incertidumbre del punto cero es suficiente para cambiar la frecuencia de resonancia de la cavidad más allá de su ancho de línea. Al acoplar este movimiento del átomo a su estrecha resonancia, observamos teóricamente que la dispersión de fotones individuales queda fuertemente entrelazada con la función de onda del átomo, incluso cuando la resonancia de la cavidad es ancha. Como resultado, cada fotón calienta el átomo significativamente más de lo que se esperaría de su energía de retroceso, y podría manifestarse en dispositivos actuales en forma de oscilaciones dictadas por el movimiento del átomo.

En la segunda parte de la Tesis investigamos cómo algunos materiales sintéticos

fabricados con luz pueden utilizarse como simuladores cuánticos, desafiando así las limitaciones que los ordenadores clásicos enfrentan actualmente a la hora de explorar fenómenos cuánticos. En particular, nos centramos en el estudio de mezclas de átomos ultrafríos atrapados en redes ópticas, donde interacciones de largo alcance mediadas por estos átomos pueden jugar un papel fundamental en la simulación de problemas relevantes en materia condensada o química cuántica.

Primero, mostramos que átomos fermiónicos en un gas ultrafrío pueden actuar como mediadores, dando lugar a interacciones efectivas de largo alcance tipo RKKY entre átomos neutros atrapados. Asimismo, proponemos diferentes estrategias para modular estas interacciones a través de la densidad y dimensión del gas, lo que es experimentalmente accesible en plataformas actuales. Mostramos también que esta versatilidad permite la exploración de sistemas frustrados, donde aparecen fases topológicas protegidas por simetría y líquidos quirales de espín.

En segundo lugar, introducimos un conjunto de esquemas experimentales donde las interacciones de largo alcance son mediadas por una especie bosónica adicional atrapada en una red óptica, tanto en 2D como en 3D. En particular, mostramos que la interacción adicional con una cavidad puede dar lugar a una repulsión efectiva del tipo Coulomb, lo que abre la puerta a simular de manera analógica problemas de química cuántica, tomando átomos fermiónicos ultrafríos como electrones simulados. Además de explicar estos mecanismos, derivamos las condiciones operacionales para el simulador, lo probamos para átomos y moléculas sencillas, y analizamos cómo se aproxima el límite en el continuo a medida que la red óptica aumenta. Finalmente, comparamos nuestros resultados con los esperados en el continuo, donde los métodos utilizados en química cuántica pueden ser evaluados y puestos a prueba.

En resumen, nuestros resultados dibujan conexiones entre diferentes áreas de la física teórica y experimental donde la interacción entre la luz y la materia puede jugar un papel fundamental, y sugerimos cómo esto puede utilizarse para avanzar nuestra comprensión de la materia cuántica.

Acknowledgements

” *The first magician I ever saw as a boy placed a little red sponge in my hand and made a second one disappear. When I opened my hand two sponges appeared. I was spellbound because the illusionist made me believe that I created the miracle. Try to elicit a similar feeling with the people in your life.*

— **David Kwong**
(Extract from "Spellbound")

The book you now have on your hands (or screen) is not only a compilation of the research I have conducted over the last years, but also the result of a journey that has been shaped by many people, different countries and the first pandemic of my generation. Acknowledging these people as they deserve is a tremendous challenge, and I apologize in advance to those I missed. Here it is my best attempt to credit them.

First of all, I would like to thank Darrick and Alejandro for supervising this Thesis, and for their attention and support over these years. I was only an undergraduate when Darrick welcomed me in his group for the first time as a Summer Fellow. I still remember how impressed I felt by ICFO, the passion everybody showed in their work, and how much attention Darrick put on research, my questions and my education. Now that I am defending my PhD, I have witnessed the value of facing difficult questions until the deep (and usually beautiful) physical explanation is understood. Thank you for always having the door of your office open, and sharing your profound respect for science with me.

This vision of research has also been deeply influenced by Alejandro. First time we met was in the Spring of 2016, while he was a postdoc at the Max Planck Institute of Quantum Optics. My first contact with master equations was there, in the little whiteboard hanging in his office, where he trained my intuition with a mixture of brilliance, respect, and humility that I have not stopped seeing in him ever since. As I started getting more experienced and independent, I also had the privilege of witnessing his transition to a tenured scientist, building his own team back in Madrid. Despite the distance, having the chance to discuss with you at any point, throw wild ideas and receive feedback and support has been an invaluable help that goes way beyond science. With this thesis, I feel very honored to become your first "official" PhD alumnus. A big part of this, has been thanks to you.

This Thesis could neither be understood without the role played by Prof. Ignacio Cirac during the year he welcomed me in Garching at the beginning of my PhD. As a scientist, some of my most treasured memories are inevitably anchored to that sofa in his office where Alejandro, Tao and I would sit to dream about physical ideas that, at

the time, we didn't even know whether they would be feasible. Your long-term vision and care for science and those who make it is not only present in Chapters 6 and 7 of this book, but has also drawn a compass that influences my vision of research, as well as that of an entire generation of scientists, both back in Spain and worldwide.

Back in Barcelona, the project that gives rise to these results received the support from "la Caixa" Foundation (ID 100010434) through the fellowship LCF/BQ/ES18/11670016. This privilege did not only provide a level of independence and support beyond my wildest dreams, but has also been a great opportunity to meet other young scientists with very similar interests who have eventually become my friends. Thank you Anna and Joan for letting me share this part of the path with you and reflect my dreams on yours, regardless whether it was around some smoothies at the Sandwichez, or a concert from la Rosalia. Thank you also to the rest of our cohort for immediately making any major city in Spain way more welcoming, specially to Andrés, Pablo, Karla, Anika, Enrico, Miquel, Loïc, José, Llorenç, Iván, Yasmín... I could not be proudest of how much we have grown together over these years. Thank you also to Emilia, Gisela, Ana, Elisabeth... for being our most immediate support from the Foundation.

Doing science at ICFO has also been a tremendous learning experience. Thank you to all the inspiring people that have passed by the institute over these years and made it a stimulating space. First of all, to the members of the Theoretical Quantum-Nano Photonics group. To those who have accompanied me during these last years: Francesco, Stefano, Dani, Teresa, Giuseppe, Charlie, Daniel, Marcello, Loïc and Nikos; and to those who first welcomed me when I was an undergraduate: Marcos, Ana, James, Tommaso and Lukas. Going beyond the walls of our group, thank you Dani for all our discussions (the scientific and, especially, the non-scientific ones). I have learnt from you much more than what is found in Chapter 5 of this Thesis. Thank you also to my "office neighbors": Álvaro, David, Niels and Suchi for finding the time to enjoy a good paella by the beach, tapas in the Gothic quarter, or terrific Indian cuisine in your terrace when it was most needed. My work at ICFO would neither have been so enjoyable without the people who make our lives so much easier from behind the curtains. Thank you Mireia for welcoming at ICFO the very first time; María Jesús for arranging so many trips; Silvia for exposing me to the world of entrepreneurship; and Anne for finding me a place to stay in Barcelona, not only once, but twice. Thank you Laia, Ingrid, Natalia, Dolors, and your teams for liberating me from all sort of paperwork, and patiently answering my doubts. Thank you Fede, Lydia and the rest of the Outreach team for letting me accompany you in so many adventures, and even build a 9x9x9 LED cube to illustrate our ideas in the WMC (had I known the work it would involve, I would have suggested an even number of LEDs). Thank you Brook, Alina, Andrea, Tomas and all the Communication crew for your amazing talent and keeping me entertained during lock-down. Thank you Lluís for creating and nurturing such a stimulating environment for young scientist to grow into.

I am also very grateful to the people who have kept my company along the journey that culminates with this Thesis. Thank you Félix and Fran for being the first physicists I ever met, and making me think that I may one day become of them. My professors at Universidad de Cantabria, Universidad Complutense de Madrid and Perimeter Institute, for sharing your passion for education and exposing me to a world that has defined my life so much. To Rafa, Rosa, David, Armando, Lucas, Carmen and Guifré, for being my mentors and guide me through my first steps in

research. Thank you Johannes, Eduardo, Martí, Vero, Leo, Jordi, Miguel, Caroline, David... for all the ski trips, hiking adventures, and for allowing me to be part of your family during my time in Munich. Thank you Andrea for your high-esteem, and taking so much care of everyone in the group there. Thank you Adrián and Álvaro for carrying on our friendship beyond the cold weather of Perimeter, and Raimon for joining us to make the time in Barcelona so much more enjoyable.

My PhD time has also been inevitably influenced by the covid pandemic that drastically reduced the opportunities to travel and interact with other people. Fortunately, my family was safe and I could spend the months of highest uncertainty in Santander, surrounded by my loved ones, and doing science from the same room I left when I was 19 years old and moved to University. As restrictions allowed, life back in Barcelona started to slowly awake and the brunch crew became the best social bubble I could share my weekends with. Thank you Miguel, Marian, Natalia, Jess, Vicente, Agus, Isa and Noel for always finding the excuse to celebrate a pizza day, Carnaval, San Isidro, or las Campanadas, regardless whether it was at the right time or during the first week of December...I never expected to end up preparing so many of the cakes from the book you gave me. Thank you to Diego, Rafa, Rebe, Gema, Adrián... for being my closest friends after so many years, for making me feel home whenever I am back in Santander, and for all your visits over these years. You will always have a coach waiting for you wherever I am. Thank you Carlos and Mati for our crazy summer trips, it has been a gift to discover this part of the world with you. Thank you also David for making my life so much happier during the writing of this Thesis.

Finally, I need to thank my family. Gracias papá y mamá por regalarme una infancia donde poder sentirme tan feliz, querido y seguro. Gracias por proporcionarme la mejor educación que supisteis darme, y por seguir cuidándome con el mismo cariño ya de adulto, celebrando cada uno de mis logros como si fuesen vuestros. Gracias Raquel por ser mi confidente y ayudarme a cuidar de las personas que más queremos. Estoy muy orgulloso de la mujer en que te has convertido. Gracias a mis tíos y primos por perdonar mi ausencia en tantos cumpleaños, santos y aniversarios; y por siempre encontrar la excusa para reunirnos cuando estoy. Por último, gracias a mis abuelos por querernos de manera incondicional y formar una parte tan importante de mi vida. Pese a crecer con casi nada, trabajasteis duro para sacar adelante a unos hijos que pudieron incluso cursar estudios universitarios si lo desearon. Veros es el mejor ejemplo de sencillez, amor por los demás y por el trabajo bien hecho, que espero que también esté presente en estas páginas. Siendo el primer doctorado de la familia, esta tesis es vuestra.

List of Abbreviations

” He started to read the book he had bought (...) and the names of the people involved were very difficult to pronounce. If he ever wrote a book, he thought, he would present one person at a time, so that the reader wouldn't have to worry about memorizing a lot of names.

— Paulo Coelho
(Extract from "The alchemist")

BCS	Bardeen-Cooper-Schrieffer
BEC	Bose-Einstein condensate
BH	Bose-Hubbard
BO	Born-Oppenheimer
BOW	Bond order wave
CDW	Charge density wave
DFT	Density functional theory
DMRG	Density matrix renormalization group
ED	Exact diagonalization
GS	Gerchberg-Saxton
HF	Hartree-Fock
(I)FFT	(Inverse) fast Fourier transform
ITE	Imaginary time evolution
JC	Jaynes-Cummings
LCAO	Linear combination of atomic orbitals
QED	Quantum electrodynamics
RKKY	Ruderman-Kittel-Kasuya-Yosida
SLM	Spatial light modulator

Contents

Abstract	v
Acknowledgements	ix
1 Introduction	3
1.1 Outline of this Thesis	8
1.2 List of publications.	10
I Atom-light interactions	13
2 Preliminaries I: light-matter interaction	15
2.1 Single-atom coupling to light	16
2.1.1 Dressed energy-shift	17
Optical lattices	18
Intensity masks	18
Holographic potentials	19
2.2 Single-atom coupled to a cavity-mode	19
2.2.1 Jaynes-Cummings hamiltonian	19
2.2.2 The detuned Jaynes-Cummings ladder	20
2.2.3 Refined model considering dissipation: cooperativity	21
2.2.4 Small-volume cavity systems	22
Nanophotonic structures	23
Fibre cavities	23
2.2.5 Input-output formalism of an empty cavity.	24
2.3 Outlook	25
3 Single atom and photon optomechanical strong coupling	27
3.1 The system	29
3.1.1 Heuristic derivation of strong coupling condition	31
3.2 Role of the atomic motional wave function	32
3.2.1 Unconventional heating	33
3.3 Second-order time correlations	35
3.4 Finite temperature	39
3.5 Conclusions and outlook	43

II Atom-mediated interactions for cold atoms in optical lattices 45

4 Preliminaries II: ultracold atoms in optical lattices	47
4.1 Optical lattices	47
4.1.1 Dimensionality	48
4.2 Non-interacting particles in periodic lattices	48
4.2.1 Bloch functions and band structure	49
4.2.2 Wannier functions	50
4.3 Interacting atoms: Bose-Einstein condensates	51
4.3.1 Tight-binding Hamiltonian for deep lattices	52
Tunneling to neighboring sites	53
On-site potential	53
On-site interaction	54
4.4 Quantum simulators	54
4.4.1 Bose-Hubbard Hamiltonian	55
Superfluid phase	55
Mott-insulating phase	55
4.4.2 Generalized Bose-Hubbard models	56
4.5 Long-range interactions among trapped atoms	56
4.5.1 Dipole interactions	57
Polar molecules	58
Paramagnetic atoms	58
Rydberg atoms	58
4.5.2 Ionic systems	58
Ions in optical lattices	59
4.5.3 Engineered photon-mediated interactions	59
Nanophotonic structures	60
Optical cavities	60
4.6 Outlook: towards long-range interactions mediated by atoms	61
5 Tunable long-range interactions mediated by a Fermi gas	63
5.1 Effective fermion-mediated interactions	64
5.2 Knob I: additional trapping potential	67
5.2.1 Quantum simulation of frustrated phases	68
5.3 Knob II: dimensionality of the mediator	69
5.4 Conclusions	72
6 Toy-model simulators for quantum chemistry in 2D	73
6.1 Introduction	73
6.2 Discrete basis sets: atomic orbitals <i>vs.</i> grid basis	75
6.2.1 Linear combination of atomic orbitals.	77
6.2.2 Local or grid-discretized basis.	77
6.3 Simulating single-particle Hamiltonian in optical lattices	78
6.3.1 Electron kinetic energy	80
6.3.2 Nuclear attraction	80
6.4 Two-dimensional simulators	81
6.4.1 A single electron	81
6.5 Simulating electron repulsion in 2D optical lattices	84
6.5.1 General formalism	85
6.5.2 Scheme I: a single bosonic mediator	86
Single boson localized around one fermion	88

	Single boson localized around two fermions	88
6.5.3	Scheme II: N_e bosonic mediators	90
6.6	Conclusions and outlook	92
7	Towards 3D analog quantum chemistry simulation	93
7.1	Introduction	93
7.2	Nuclear attraction	94
7.3	Errors: discretization, finite-size, and mitigation strategies	98
7.4	Simulating electron repulsion in 3D optical lattices	100
7.4.1	Working conditions for the general formalism	101
7.4.2	Scheme I: Repulsion mediated by single atoms: non-Coulomb & non-scalable	102
7.4.3	Scheme II: Repulsion mediated by atoms subject to state-dependent potentials: Coulomb but non-scalable	106
7.4.4	Scheme III: Repulsion mediated by atomic spin excitations and cavity assisted transitions	110
	Derivation of the effective potential	110
	Working conditions	112
	Final potential and conditions	115
7.5	Numerical benchmark of the 3D analog simulator	116
7.5.1	He atom	116
7.5.2	Hydrogen molecule	117
7.5.3	HeH ⁺ molecule	119
7.6	Experimental implementation	120
7.6.1	Candidate atomic species	120
7.6.2	Measurement	121
7.6.3	Experimental considerations	122
7.7	Conclusion and outlook	123
8	Conclusions and perspectives	125
A	Additional notes on Chapter 3	129
A.1	Scattering approach for a single atom	129
A.2	Master equation simulation	131
B	Additional notes on Chapter 6	133
B.1	Scheme I: bound-state energy	133
B.1.1	Calculation of the integral in Eq. (6.30)	134
B.1.2	Calculation of the integral in Eq. (6.35)	134
B.2	Scheme II: Mediating atoms with two long-lived states	135
B.3	Numerical methods	137
B.3.1	Exact diagonalization	137
B.3.2	Imaginary time evolution (ITE)	138
C	Additional notes on Chapter 7	141
C.1	Discretization error scaling in 3D	141
C.1.1	Discretization of the integrals	141
C.1.2	Approximation of the kinetic term	142
C.2	Details on the perturbative analysis in Section 7.4.	142
C.2.1	Useful analytical expressions	142
C.2.2	Scheme I: Repulsion mediated by single atoms	143

- C.2.3 Scheme II: Repulsion mediated by atoms subject to state-dependent potentials 144
- C.2.4 Scheme III: Repulsion mediated by atomic spin excitations and cavity assisted transitions 146
- C.3 Numerical methods for multi-electronic systems. 148
 - C.3.1 A Hartree-Fock approximation 148
 - C.3.2 Numerical benchmarking of atomic Helium 150
 - C.3.3 Numerical benchmarking of H₂ 150
 - C.3.4 Numerical benchmarking of molecular HHe⁺ 151
- Bibliography** **153**

” *The problems of chemistry and biology can be greatly helped if our ability to see what we are doing, and to do things on an atomic level, is ultimately developed.*

— **Richard P. Feynman**

(Extract from "There is plenty of room at the bottom",
Engineering and Science 23, 22, 1960)

Chapter 1

Introduction

” *When you write, readers judge the significance of your problem not by the cost you pay, but by the cost they pay if you don't solve it. So what you think is a problem they might not. To make your problem their problem, you must frame it from their point of view, so that they see its cost to them.*

— **Wayne C. Booth, et al.**

(Extract from "The Craft of Research")

In Nature, systems dominated by the same physical laws behave alike, regardless how unsimilar they may look at a first glance. While this may look a superfluous observation, the ability to learn about a complex system by manipulating a more accessible one has enabled human creations that overcome the technical limitations of their time. For example, the Catalan architect Antoni Gaudí used inverted models formed by hundreds of hanging ropes to identify the optimal design for the cathedral he was projecting. Translating the tension of these ropes into the stress of his arcs, these forms shaped by nature corresponded to the design that better distributed the structural loads of his construction, as illustrated in Fig. 1.1(a-b). Decades later, the German architect Frei Otto relied on the shapes described by soap sheets to identify the most stable design for the surfaces that would cover the Olympic Stadium of Munich in 1972. As soap sheets naturally minimize the surface within a defined contour, the covers unveiled in this manner would be specially stable against any deformation, as Otto desired [see Fig. 1.1(c-d)]. But these simulations are not only limited to mechanical systems. For example, fluid equations are also challenging to solve, and the aerodynamic properties of cars and planes are often tested inside wind tunnels. Water tanks are also used to better understand the effect that the sea can have on the shores of city models built at scale.

Coming back to our present day, an architect who is able to compute the mechanical stress of her building on a desktop computer while visualizes the result in some virtual reality glasses may point out that some of these artefacts are just a distant memory of our history. However, still today, humankind faces problems that are fundamentally elusive to the classical computational capabilities we have. One of these challenges is the description of reality at very small scales, the one of electrons, atoms or molecules, which is dominated by the strange laws of quantum mechanics. Once the state of an electron or an atom is not fully determined, its computational complexity grows exponentially with the number of elements, which

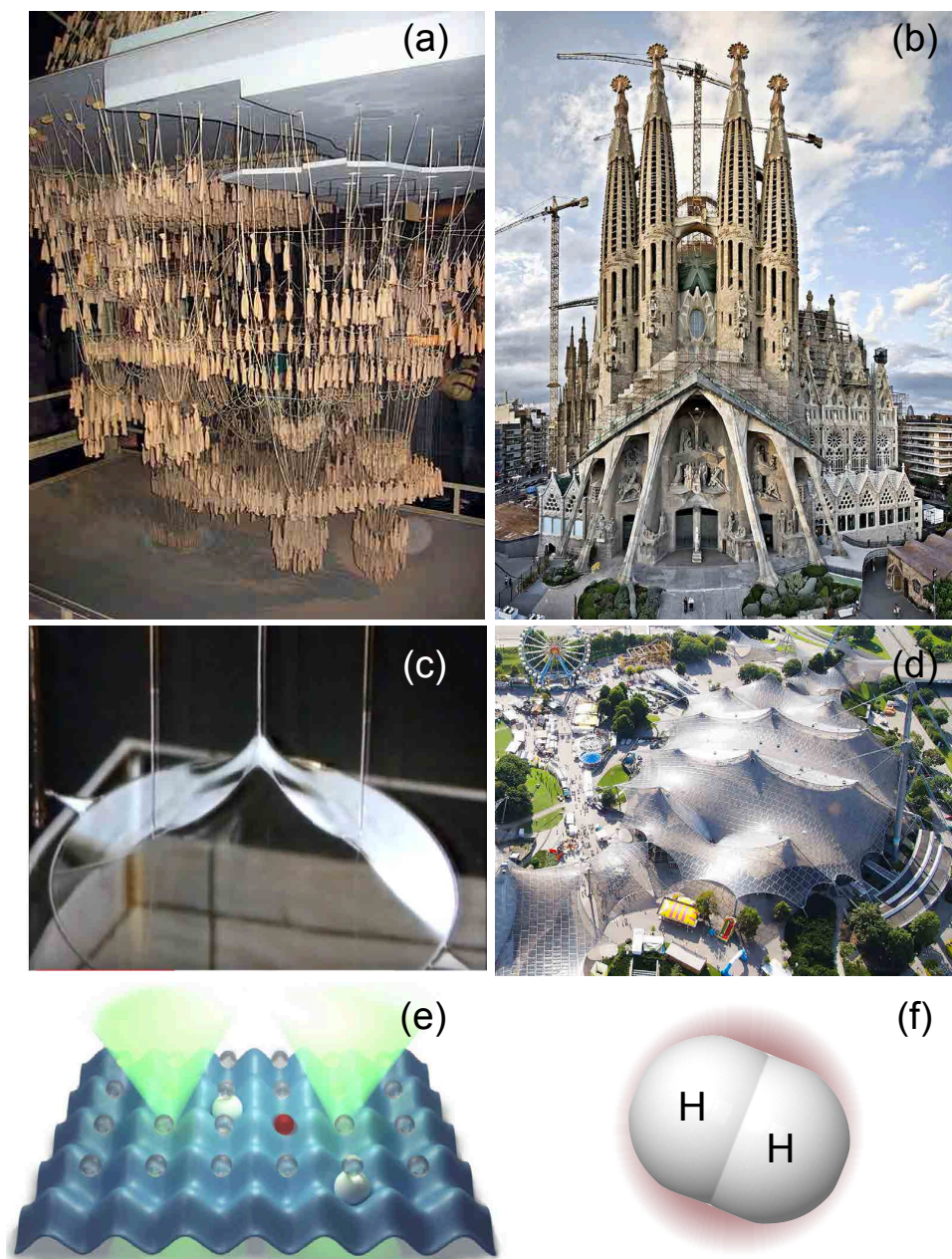


FIGURE 1.1: Example of analog simulators used in architecture (a,c) and quantum physics (e), together with their simulated counterparts, (b,d), and (f), respectively. (a) Funicular model developed by Antoni Gaudí for the cript of colonia Güell. (b) Highlight of the archs found at the Passion façade of Sagrada Familia (Barcelona). (c) Soap sheets subjected to an external force in some of its points. (d) Covers of the Olympic park of 1972 (Munich). (e) Two bosonic atoms (white) trapped in an optical lattice and attracted to two optical potentials (green). (f) Schematic representation of the electronic cloud of a H_2 molecule. *Credits: (a,b,d,f) ©Wikimedia. (c) ©Frei Otto - Spanning the future.*

soon becomes intractable for our largest classical supercomputers whenever more than a few hundred atoms are present. It then became obvious in the early 80s that,

” Nature isn’t classical, dammit, and if you want to make a simulation of nature, you’d better make it quantum mechanical.

— **Richard P. Feynman**

(Int. J. Theor. Phys. 21, 467, 1982)

This is, unlike the traditional models made of ropes or soap, any physical simulator we build to better understand the quantum world also needs to behave quantum mechanically.

Currently, different platforms are used to simulate quantum systems. These include molecules, ionic atoms, superconducting circuits, quantum dots, diamond nitrogen vacancies... Among these platforms, atomic systems stand out as one of the preferred ones [7]. The reason is that these systems have quantized internal degrees of freedom (electronic levels, nuclear spin...) with high coherence, and many optical transitions to initialize, engineer, and monitor them [8, 9]. Focusing on the simplest case of atomic Hydrogen, the energy difference between its lowest energy levels is $\sim 10^{15}$ Hz, which is in the order of the visible range of frequencies for light. The development of laser technologies starting in the late 60s provided coherent sources of light that awoke the field of quantum optics [10]. First experimental results revealed that photons in these lasers could hybridize with the internal structure of an atom. In 1977, Kimble reported non-classical effects on the light re-emitted by a sodium gas [11] and, one decade later, Rabi oscillations between a cavity photon and the excitation of atoms in an ensemble were observed [12–15].

This interaction of light with the effective dipole moment of an atom does not only influence its internal states, but also imparts radiation forces that can significantly influence its motion [16, 17]. Using sodium atoms, this allowed to decrease their kinetic energy in 1985 (cooling) [18], or trap them in a reduced region of space in 1986 [19], which deserved the 1997 Nobel Prize of Physics for Chu, Philips and Cohen-Tannoudji for the “*development of methods to cool and trap atoms with laser light.*”

Such a motional control enabled a wide range of technological advances [20]. By reducing atomic motion, one mitigates the room-temperature Doppler and collision energy shifts that widens the atomic levels. This reduction of momenta distribution also allows one to better control the time an ensemble of flying atoms interact with a fixed laser, which is the enabling mechanism behind the cold-atom fountains developed in 1989 [21]. The combination of cooling with these interferometry experiments allowed to measure the $|4, 0\rangle \leftrightarrow |3, 0\rangle$ transition of ^{133}Cs with a relative error smaller than 10^{-15} (20 times more accurate than previous setups), becoming the primary standard definition of a second [22]. In 1995, these cooling techniques were pushed to the limit of condensing an ensemble of bosonic atoms to their fundamental ground state, the Bose-Einstein condensate, achieving temperatures below $\sim 1\ \mu\text{K}$ [23, 24]. This soon deserved the 2001 Nobel prize to Ketterle, Cornell and Wieman “*for the achievement of Bose-Einstein condensation in dilute gases of alkali atoms, and for early fundamental studies of the properties of the condensates.*”

One could point out that these were effects appearing in ensembles of $10^5 - 10^7$ atoms, while a quantum control at the single-atom level would be desirable to simulate challenging quantum problems. Gaining this single-particle control was

highly non-trivial and, in the early days of quantum mechanics, it was even believed to be impossible. In the words of Schrödinger,

” We never experiment with just one electron or atom or (small) molecule. In thought-experiments we sometimes assume that we do; this invariably entails ridiculous consequences. (...) it is fair to state that we are not experimenting with single particles any more than we can raise *Ichthyosauria* in the zoo.

— Erwin Schrödinger
(J. Phil. Sci 3, 233, 1952)

Interestingly, the developed cooling techniques soon allowed to *rise Ichthyosauria in this zoo* [25, 26]. Starting with charged particles, individual ions were trapped in the early 90s by appropriately manipulating the incident electromagnetic fields [27, 28]. It was only one decade later that this control was extended to single neutral atoms [29], where non-homogeneous electric and/or magnetic fields are used to distort the atomic energy levels in a position-dependent manner.

Following a bottom-up description, the minimal example of light-matter interactions is the interplay between a single atom and a single photon. As it will be introduced in Chapter 2, the probability that an atom absorbs a resonant photon in free-space gets fundamentally upper bounded because of the finite cross-section of the atom and the diffraction limit for light [30, 31]. One way to push this interaction is by introducing the atom in a high-quality optical cavity, where the light-atom interaction gets enhanced by the number of photon round-trips. As mentioned above, the cavity field imparts effective forces that modifies atomic motion. Conversely, the resonance frequency of the cavity also gets modulated by the position of the atom, which defines an effective refractive index that depends on the region of the cavity where the atom is placed [32]. As a consequence, atomic position determines the probability that an incoming photon gets reflected and, with that, the overall population of the cavity field [33, 34]. In Chapter 3 we will focus on the resulting interplay between cavity field and atomic motion. In particular, we will derive optimal driving conditions that maximize this optomechanical coupling, and analyze experimental signatures that allow us to witness strong optomechanical effects between a single photon and a single atom.

Continuing the ladder towards synthetic quantum matter generation, the next goal is gaining the ability to build complex systems formed by several individual atoms. Nowadays, different techniques allow us to control the trapping of hundreds of atoms. The first realizations of ordered arrays of atoms with tunable geometries was enabled by optical lattices created by the interference of multiple-beams [35, 36], as atoms feel attracted to detuned light. Using holographic techniques, state-of-the-art dipole traps can engineer the individual trapping of hundreds of atoms in any arbitrary position of space [37]. The motional control provided by optical lattices soon allowed to build some of the first atomic quantum simulators, which addressed problems related to condensed matter physics. In the same manner that the ropes hung by Gaudí taught him about the arches of his building, atoms tunneling through different lattice sites simulated simple models about how electrons move in the lattice potentials described by crystalline structures. This was the case of the phase transition that had been predicted in the Fermi-Hubbard model, a minimal description used to describe high- T_c superconductivity [38]. As a proof-of-principle realization of such control, its bosonic version [39] was

experimentally realized in 2002 with a ^{87}Rb atom simulator in optical lattices [40] (see Section 4.4.1), and it was later implemented with fermionic atoms in 2008 [41].

Since then, the field has quickly developed over the last two decades, providing a deeper understanding of quantum phenomena that defeats the capabilities of state-of-the-art analytical or numerical methods. This is the case of many-body problems related to spin physics [42], quantum transport [43, 44] or thermalization [45–47] that can be addressed by atoms trapped in optical lattices. By tuning the geometry of these lattices one can induce hexagonal lattices where Dirac cones can appear [48], or even explore topological phase transitions, like the Haldane [49] or Harper-Hofstadter models [50]. Beyond this low-energy physics, the interplay between bosonic and fermionic mixtures [51, 52] can allow us to engineer artificial Gauge fields, which can address open questions in high-energy physics [53–55].

The richness of these models arises from the ability of atoms to interact with each other. Rather than having multiple copies of the same quantum phenomena, strongly correlated effects appear when the behaviour of each atom is influenced by the rest of them. The simplest interactions occur when this influence is local, for example, through collisions with a nearby atom or tunneling to a neighbouring occupied site of the lattice. Other problems, however, require longer-range interactions. This is the case of theoretical questions in quantum transport, thermalization [56], or quantum magnetism [57]. Arguably, one of the holy grails in this direction is quantum chemistry, where the electrons responsible for the molecular bounds experience Coulomb repulsion, which decays as $1/r$ with the distance. This long-range repulsion for electrons is naturally mediated by the exchange of virtual photons, and do not have a natural counterpart for neutral atoms in optical lattices.

The second part of this Thesis is precisely focused on developing strategies to mediate long-range interactions among neutral atoms trapped in optical lattices. Our approach focuses on replacing the virtual photon that mediates this interaction in real life by an additional mediating atomic species, similarly to how architects also got inspired by nature when designing their simulators. Different configurations for this additional species lead to a diverse range of scalings for the mediated potential. These range from exponentially attenuated interactions with an adjustable decaying length, in the case of the simplest schemes, to effective long-range Coulomb-like interactions for the most sophisticated setups [see Fig. 1.1(e-f)]. The toolbox offered by atomic long-range mediated interactions thus provides an interesting experimental roadmap, where simple configurations allow us to build simplified toy models where phenomena like frustrated phases of matter, molecular binding or dissociation can be studied in current devices. Their realization may well push the experimental state-of-the-art in cold atoms simulators to the more sophisticated configurations where real-life chemistry could be simulated in an analog way.

In the same way that the towers that Gaudí designed for the Sagrada Familia with just some ropes are now lifted under the guidance of the most sophisticated 3D *software*, quantum computers will surely follow the lead of analog simulators in the (hopefully not so distant) future that they admit error correction and a large-scale production. In the meantime, the advances made by our atomic models may allow us to keep exploring the quantum world and enable discoveries that, well sure, will survive beyond the paradigms in computation still to come.

1.1 Outline of this Thesis

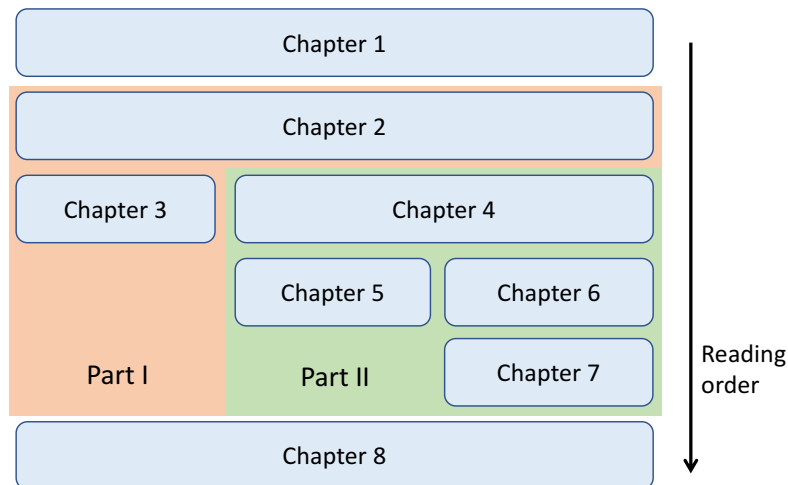
The content of this Thesis is structured in two different parts. Part I focuses on the motional control of single atoms coupled to an optical cavity. Part II develops different strategies capable of engineering long-range interactions among atoms trapped in optical lattices. Each of these parts is preceded by an introductory chapter (Chapters 2 and 4, respectively) that reviews several theoretical and background concepts we judge useful to better understand the subsequent parts of this Thesis. An expert reader in the field may then decide to skip such introductory chapters and dive directly into the original results of this Thesis, presented in the remaining Chapters 3, 5, 6 and 7. We now briefly summarize the content of each chapter,

- Chapter 2 introduces the basic notions of light-matter interaction at the single atom level. First, we describe how an external light-field can shift the natural energy levels of an atom and induce effective trapping potentials. Second, we review the Jaynes-Cummings Hamiltonian that governs the interaction of an atom with a quantized mode of an optical cavity, and introduce the concept of cooperativity. Finally, we present the input-output formalism that allows one to consider the interplay of this system with the environment.
- Chapter 3 shows how single atoms coupled to a cavity can offer unique opportunities as quantum optomechanical devices because of their small mass and strong interaction with light. In particular, we focus on the "*single-photon optomechanical strong coupling*" regime, where motional displacements on the order of the zero-point uncertainty are sufficient to shift the cavity resonance frequency by more than its linewidth. In many cavity QED platforms, however, this is unfeasible due to the large cavity linewidth. There, we propose an alternative route in such systems, which instead relies on the coupling of atomic motion to the much narrower cavity-dressed atomic resonance frequency. We discuss and optimize the conditions in which the scattering properties of single photons from the atom-cavity system become highly entangled with the atomic motional wave function. We also analyze the prominent observable features of this optomechanical strong coupling. This includes a per-photon motional heating that is significantly larger than the single-photon recoil energy, as well as mechanically-induced oscillations in time of the second-order correlation function of the emitted light.
- Chapter 4 shifts the focus to the study of ultracold atoms trapped in optical lattices. We first introduce the Bloch formalism that simplifies the analysis of this system, and review its success in the simulation of condensed matter problems, starting with the celebrated Bose-Hubbard model. We then motivate the impact that inducing long-range interactions among these atoms can have in the simulation of contemporary problems, such as quantum chemistry. Finally, we review the different strategies that are currently used to access extended interactions, and discuss the interest of further exploring atom-mediated interactions that could mimic Coulomb-like electronic repulsion.
- Chapter 5 shows that fermionic atoms in ultracold atomic mixtures can act as mediators, giving rise to long-range RKKY interactions characterized by the dimensionality and density of the fermionic gas. There, we propose several tuning knobs, accessible in current experimental platforms, that allow us to

further control the range and shape of the mediated interactions, extending the existing quantum simulation toolbox. In particular, we include an additional optical lattice for the fermionic mediator, as well as anisotropic traps to change its dimensionality in a continuous manner. This allows one to interpolate between power-law and exponential decays, introducing an effective cutoff for the interaction range, as well as to tune the relative interaction strengths at different distances. Finally, we show how this approach allows one to investigate certain frustrated regimes that were not previously accessible, where symmetry-protected topological phases as well as chiral spin liquids emerge.

- In Chapter 6, we propose an analog simulator for discrete two dimensional quantum chemistry models based on cold atoms in optical lattices. We first analyze how to simulate simple models, like the discrete versions of H and H_2^+ , using a single fermionic atom. We then show that a single bosonic atom can mediate an effective Coulomb repulsion between two fermions, leading to the analog of molecular hydrogen in two dimensions. We extend this approach to larger systems by introducing as many mediating atoms as fermions, and derive the effective repulsion law. In all cases, we analyze how the continuous limit is approached for increasing optical lattice sizes.
- Chapter 7 presents a new approach to the simulation of three-dimensional quantum chemistry problems in an analog way. Our method relies on the careful combination of two technologies: ultra-cold atoms in optical lattices and cavity QED. In the proposed simulator, fermionic atoms hopping in an optical potential play the role of electrons, additional optical potentials provide the nuclear attraction, and a single spin excitation over a Mott insulator mediates the electronic Coulomb repulsion with the help of a cavity mode. We also provide the operational conditions of the simulator and benchmark it with simple two-electron atoms (He) and molecules (H_2 and HeH^+).
- In Chapter 8, we finally summarize the main conclusion of this Thesis, and discuss some of the different research directions that it opens.

Based on the interconnection among different chapters, we propose the following reading order that we believe can accommodate the different interests of the reader:



Following this diagram, the content of a given chapter distills from those chapters represented immediately above. For example, a reader interested in Chapter 7, is recommended to firstly read through Chapters 1, 2, 4 and 6, so that the different ideas introduced along the text are naturally presented.

1.2 List of publications.

Finally, here we state the publications on which this Thesis is based, as well as which chapter(s) corresponds to the content of each publication.

- [1] J. Argüello-Luengo, A. González-Tudela, T. Shi, P. Zoller, J. I. Cirac, *Analogue quantum chemistry simulation*, *Nature* **574**, 215 (2019). Chapter 7.
- [2] J. Argüello-Luengo, A. González-Tudela, T. Shi, P. Zoller, J. I. Cirac, *Quantum Simulation of 2D Quantum Chemistry in Optical Lattices*, *Phys. Rev. Research* **2**, 042013 [Rapid Com.] (2020). Chapter 6.
- [3] J. Argüello-Luengo, T. Shi, A. González-Tudela, *Engineering analog quantum chemistry Hamiltonians using cold atoms in optical lattices*, *Phys. Rev. A* **103**, 043318 (2021). Chapters 6 and 7.
- [4] J. Argüello-Luengo, A. González-Tudela, D. González-Cuadra, *Tuning long-range fermion-mediated interactions in cold-atom quantum simulators*, *Phys. Rev. Lett.* **129**, 083401 (2022). Chapter 5.
- [5] J. Argüello-Luengo, D. E. Chang, *Optomechanical strong coupling between a single cavity photon and a single atom*, *New J. Phys.* **24** 023006 (2022). Chapter 3.

This first Chapter is also based on the outreach communication,

- [6] J. Argüello-Luengo, A. González-Tudela, *Simuladores cuánticos analógicos: Una herramienta para entender la materia que nos rodea*, *Revista Española de Física*, **35** (1) (2021).

Results portrayed in Fig. 5.3 are courtesy of D. González-Cuadra, as part of the collaboration in Ref. [4]. All the other figures and calculations appearing in this Thesis have been produced by the Author.

Part I

Atom-light interactions

Chapter 2

Preliminaries I: light-matter interaction

” *Whether you’re a writer, marketer, consultant, or lawyer: Your work is craft, and if you hone your ability and apply it with respect and care, then like the skilled wheelwright you can generate meaning in the daily efforts of your professional life.*

— **Cal Newport**

(Extract from "Deep work")

The interface between atoms and light allows one to access and manipulate their atomic internal degrees of freedom at the single-atom level. Due to the non-homogeneous spacing of atomic energy levels, the resulting interplay can also introduce nonlinearities in the scattered light, as an excited atom cannot absorb another resonant photon. The resulting quantum control of light and matter has enabled an enormous advance of fundamental science, including applications in quantum information [58], like the realization of gates and quantum memories for light [59]; metrology, like the exploration of fundamental limits using squeezed atomic states [60]; or, more recently, the realization of synthetic materials where light can induce exotic properties beyond those usually found in real materials, as it is the case of topological phenomena [53, 61–64].

This chapter will be devoted to introduce some of the notation and fundamental results that will vertebrate this Thesis. In particular, Section 2.1 describes how an external light-field can shift the natural energy levels of an atom, inducing an effective trapping potential that is proportional to the intensity of the field at each point of space. At low intensities, this electromagnetic field can be quantized, and the interaction with light occurs at the level of individual photons. Section 2.2 introduces the Jaynes-Cummings Hamiltonian that governs the interaction between an individual photon and a single atom, as well as the input-output formalism that facilitates the analysis of an open system, once the interplay with the environment is considered.

2.1 Single-atom coupling to light

As the most simple description of an atom, one can focus on two of its internal levels, denoted as $|\downarrow\rangle$ and $|\uparrow\rangle$, which are typically referred to as a ground and excited state. They are separated by energy $\hbar\omega_0$,

$$\hat{H}_A = \hbar\omega_0 |\uparrow\rangle \langle\uparrow|. \quad (2.1)$$

When addressed by a monochromatic laser field of frequency ω_l ,

$$\mathbf{E}(\mathbf{r}, t) = \varepsilon E_0(\mathbf{r}) \cos(\omega_l t), \quad (2.2)$$

these levels are connected through an optical dipole transition, where ε is the polarization vector of the field¹.

Since the wavelength of an optical field (in the order of hundreds of nm) is much longer than the size of the atom (typically a few angstroms), one typically neglects any spatial variation over the position of the atom \mathbf{r}_a . In this dipole approximation, the atom-field interaction reduces to [65],

$$\hat{H}_{A-F} = -\hat{\mathbf{d}} \cdot \mathbf{E}(\mathbf{r}_a), \quad (2.3)$$

where the position \mathbf{r}_e of the fundamental charge defines an effective dipole operator for the atom, $\hat{\mathbf{d}} = -e\mathbf{r}_e$. One should note that diagonal terms of the form $\langle\downarrow|\hat{\mathbf{d}}|\downarrow\rangle = \langle\uparrow|\hat{\mathbf{d}}|\uparrow\rangle = 0$ vanish, as there is no change in the parity, and only the term connecting the two atomic states, $\mathbf{d}_{\downarrow\uparrow} = \langle\downarrow|\hat{\mathbf{d}}|\uparrow\rangle$, is non-zero for a dipole-allowed transition.

Appropriately choosing its phase, the dipole matrix element can be taken to be real, so that the dipole operator in this reduced space writes as,

$$\hat{\mathbf{d}} = \mathbf{d}_{\downarrow\uparrow} (\hat{\sigma} + \hat{\sigma}^\dagger), \quad (2.4)$$

where $\hat{\sigma}^\dagger = |\uparrow\rangle \langle\downarrow|$ and $\hat{\sigma} = |\downarrow\rangle \langle\uparrow|$ are the creation and annihilation operators of an atomic excitation, respectively. After rewriting the electric field of Eq. (2.2) as $\mathbf{E}(\mathbf{r}, t) = \varepsilon E_0(\mathbf{r}) (e^{i\omega_l t} + e^{-i\omega_l t}) / 2$ and going to a frame rotating with the laser frequency, $U(t) = e^{-i\omega_l t \hat{\sigma}^\dagger \hat{\sigma}}$, we observe that some of the terms in the atom-field interaction (2.3) rapidly oscillate as $e^{\pm i(\omega_0 + \omega_l)t}$. Assuming that the two-level transition is being driven close enough to resonance, $|\Delta| = |\omega_l - \omega_0| \ll \omega_0 + \omega_l$ (which is consistent with our two-level description), one can follow a rotating wave approximation and neglect these terms.

The resulting interaction then takes the form,

$$\hat{H}_{A-F} = \frac{\hbar}{2} \left(\Omega^*(\mathbf{r}_a) \hat{\sigma} + \Omega(\mathbf{r}_a) \hat{\sigma}^\dagger \right), \quad (2.5)$$

where we define the **Rabi frequency** as,

$$\Omega(\mathbf{r}) \equiv -\frac{\langle\downarrow|\varepsilon \cdot \hat{\mathbf{d}}|\uparrow\rangle E_0(\mathbf{r})}{\hbar}, \quad (2.6)$$

¹Along this Thesis, we will use bold letters to indicate vectors.

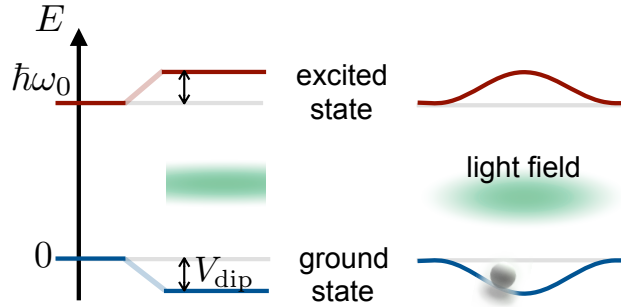


FIGURE 2.1: Schematic illustration of the energy shift (2.7) experienced by the ground and excited states of an atom due to an incident red detuned laser ($\Delta < 0$, represented in green) whose intensity is homogeneous (left) or follows a Gaussian distribution (right).

which characterizes the strength of the interaction between the two-level atom and the classical field.

2.1.1 Dressed energy-shift

When this interaction is weaker than detuning $|\Omega(\mathbf{r}_a)| \ll |\Delta|$, the atom-field interaction (2.5) effectively induces a dipole potential for the atom that can be derived to second order in perturbation theory as [66],

$$V_{\text{dip}} \approx \frac{\hbar|\Omega(\mathbf{r}_a)|^2}{4\Delta}(1 - 2\hat{\sigma}^\dagger\hat{\sigma}). \quad (2.7)$$

This shifts the ground and excited states in opposite directions, as represented in Fig. 2.1.

For an atom in the ground state, $\langle\hat{\sigma}^\dagger\hat{\sigma}\rangle \approx 0$, we observe that the shifted potential highly depends on the detuning between the laser and the atom.

- For a **red detuned** laser ($\Delta < 0$), the energy shift is $V_{\text{dip}} < 0$ and the atom feels attracted to the bright spots where the intensity field is greater.
- For a **blue detuned** laser ($\Delta > 0$), the energy shift is $V_{\text{dip}} > 0$ and those points of higher intensity fields induce a barrier that repels the atom from there.

While one could naively consider to reduce $|\Delta|$ to increase the strength of the mediated trapping potential (2.7), $V_{\text{dip}} \sim I/\Delta$, this would also further enhance the atomic scattering rate, which scales as $\Gamma_{\text{sc}} \sim I/\Delta^2$ [66]. Therefore, optical dipole traps usually operate at large detuning and high intensities to reduce the rate of atomic spontaneous emission for a certain trapping depth.

Regarding pressure conditions, trapped atoms are also very sensitive to collisions with the background gas, due to their low mass and typical trap depths. This motivates the high vacuum needed in typical experiments, where background pressures below 10^{-9} mbar are typically used to reduce the collision rate below 1 Hz [36].

Focusing now on the shape of this trapping potential (2.7), this can be engineered by controlling the intensity profile of the incoming field, $I(\mathbf{r}) \propto |\Omega(\mathbf{r})|^2$. Among the most useful choices followed to trap and manipulate atoms, we find the design of optical lattices and holographic potentials, which we introduce in the following.

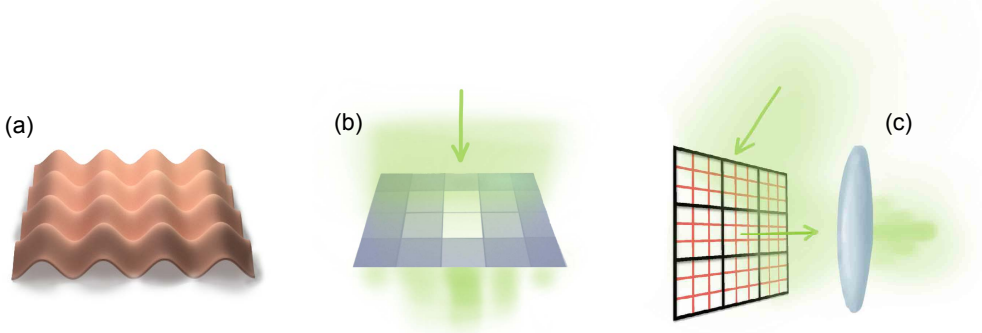


FIGURE 2.2: Schematic representation of (a) an optical lattice, (b) an intensity mask, (c) an holographic potential created by a SLM placed at the focal length of a lens (grey).

Optical lattices

The standing wave interference pattern that appears when a retroreflected laser beam interferes with itself is one of the simplest strategies to create an intensity profile that is static over time. In one dimension, this modulates the Rabi frequency as $\Omega(x) = \Omega_0 \sin(kx)$, which results into a trapping potential for the atomic ground-state of the form,

$$V_{\text{lat}}(x) = V_D \sin^2(kx), \quad (2.8)$$

whose strength depends on detuning following $V_D = \hbar\Omega_0^2/(4\Delta)$, as shown in Eq. (2.7).

Geometrically, this results into a periodic potential $V_{\text{lat}}(x+a) = V_{\text{lat}}(x)$, whose lattice spacing is half a wavelength, $a = \pi/k$ [see Fig. 2.2(a)]. The states and energies induced in the atomic system can be well described in terms of the Bloch theorem, as it will be presented in Section 4.2.1. Generalizing these potentials to higher dimensions, two and three-dimensional lattices can be engineered by superimposing retroreflected beams in different directions.

Going beyond periodic structures, further techniques allow one to independently engineer the intensity of the light field at different position. As we will show now, this offers the ultimate control to design the trapping potential that an atom feels at each point of space.

Intensity masks

As the trapping potential is directly given by the intensity field [see Eq. (2.7)], one simple way to modulate the effective profile in one and two-dimensional systems is by designing an appropriate intensity mask. In this manner, the homogeneous beam waist of a beam incident from an orthogonal direction gets selectively attenuated in different positions of space [see Fig. 2.2(b)]. In combination with a subjacent optical lattice, this allows to tailor the potential induced at each trapping site [67]. This ability to spatially modulate light can even be adjusted dynamically, which is of wide interest for problems related to transport or thermalization [43].

While intensity masks offer a good control on 1D and 2D problems, the need to drive in an orthogonal direction requires a further development for three-dimensional systems, where holographic techniques can be applied.

Holographic potentials

The idea behind holographic traps is conceptually simple: a monochromatic laser beam impinges on a spatial light-modulator (SLM), which imprints a non-uniform phase pattern on the incident field. The reflected laser beam is then focused with a high-numerical aperture lens to generate a given intensity pattern in its focal length [see Fig. 2.2(c)]. Advances in holographic techniques now allow for the non-trivial design of electric fields with any desired three-dimensional intensity pattern, $I(\mathbf{r})$. Through numerical procedures, like the Gerchberg-Saxton (GS) algorithm [68], one can calculate a phase profile that leads to the desired intensity profile.

The resulting high tunability in the induced 3D potential has made it possible to trap Rydberg atoms in exotic three-dimensional configurations [37], where the exploration of many-body physics is facilitated by the control in the position of individual atoms [69, 70]. In Section 4.3.1, we will follow this procedure to calculate the phase mask that leads to an attractive Coulomb-like potential for neutral atoms.

2.2 Single-atom coupled to a cavity-mode

The weak free-space interaction between photons and an atom is one of the main challenges one needs to overcome in order to access atomic quantum control using light. Focusing on the idealized vision of a two-level atom, its scattering length is given by, $\sigma_{sc} = 3\lambda^2/(2\pi)$ [71], where $\lambda = 2\pi c/\omega_0$ is the resonant wavelength. At the same time, the minimum area, A_{eff} , in which a light beam can be focused is limited by diffraction, $A_{eff} \sim \lambda^2$ [30, 31]. This then sets a limit on the probability that an atom in free space absorbs and rescatters a photon in the beam, $P = \sigma_{sc}/A_{eff}$, and state-of-the-art experiments with ions or neutral atoms are typically in the order of $P \sim 0.1$ [72].

In order to push this limit, different alternatives have been investigated over the last decades, including the use of tightly focused beams [30], or working with *atomic ensembles*, whose effective scattering probability in the detuned regime is enhanced by the number of atoms [73]. More recently, *nanophotonic* structures are being explored [72], where the use of evanescent fields allows us to go beyond the diffraction limit of propagating waves.

In this Section, we will focus on another predominant platform that enhances the interaction between atoms and light: *cavity quantum electrodynamics*. When the atom is placed between two mirrors that form a high-finesse optical cavity, the probability that light interacts with the atom is enhanced by the number of round-trips a photon can perform before escaping from the cavity, or spontaneously being emitted into free-space by the atom.

As cavities will play a prominent role in Chapters 3 and 7 of this Thesis, here we will introduce some key theoretical concepts, and we refer the reader to Refs. [74, 75] for a more extended introduction.

2.2.1 Jaynes-Cummings hamiltonian

At this point, we are interested in describing the interaction between a two-level atom and a single mode of the cavity that follows a normalized spatial mode profile $\mathbf{f}(\mathbf{r})$. The uncoupled Hamiltonian reads as,

$$\hat{H}_A + \hat{H}_F = \hbar\omega_0 |\uparrow\rangle \langle\uparrow| + \hbar\omega_c \left(\hat{a}^\dagger \hat{a} + 1/2 \right), \quad (2.9)$$

where ω_c is its resonance frequency and $\hat{a}^{(\dagger)}$ is the annihilation (creation) operator of the cavity mode, which follows a bosonic statistics.

The previous classical description of the field in Eq. (2.2) can now be generalized to its quantization inside the cavity, $\mathbf{E}(\mathbf{r}, t) = -\sqrt{\frac{\hbar\omega_c}{2\epsilon_0}} \mathbf{f}(\mathbf{r})\hat{a}(t) + \text{H.c.}$. The effective dipole interaction (2.3) now reads as,

$$\hat{H}_{\text{A-F}} = -\sqrt{\frac{\hbar\omega_c}{2\epsilon_0}} (\hat{\sigma}^\dagger + \hat{\sigma}) \mathbf{d}_{\downarrow\uparrow} \left[\mathbf{f}(\mathbf{r}_a) \hat{a} + \mathbf{f}^*(\mathbf{r}_a) \hat{a}^\dagger \right]. \quad (2.10)$$

Considering the rotating-wave approximation and defining the atom-field coupling term:

$$\hbar g(\mathbf{r}) = -\sqrt{\frac{\hbar\omega_c}{2\epsilon_0}} \mathbf{d}_{\downarrow\uparrow} \cdot \mathbf{f}(\mathbf{r}), \quad (2.11)$$

one arrives to the Jaynes-Cummings (JC) Hamiltonian [76],

$$\hat{H}_{\text{JC}} = \hbar\omega_0 |\uparrow\rangle \langle\uparrow| + \hbar\omega_c (\hat{a}^\dagger \hat{a} + 1/2) + \hbar g(\mathbf{r}_a) (\hat{\sigma}^\dagger \hat{a} + \hat{\sigma} \hat{a}^\dagger), \quad (2.12)$$

where counter-rotating terms have been neglected.

Note that the spatial mode profile is normalized, i.e., $\int d\mathbf{r} |\mathbf{f}(\mathbf{r})|^2 = 1$, and the spatial dependence of this coupling on atomic position can be expressed as $g(\mathbf{r}) = g_0 \tilde{f}(\mathbf{r})$, where $\tilde{f}(\mathbf{r})$ is a dimensionless mode profile with maximum modulus of order one. For a one-dimensional cavity, this can be modeled as a sinusoidal modulation $\tilde{f}(\mathbf{r}) \sim \sin(k_c x)$, with wavevector k_c . Due to its connection with the description of a classical field (2.5), g_0 is commonly referred to as the **single-photon Rabi frequency**.

2.2.2 The detuned Jaynes-Cummings ladder

An interesting observation at this point is that the JC hamiltonian (2.12) is block-diagonal in sectors of equal number of excitations, $N_{\text{exc}} = \langle \hat{a}^\dagger \hat{a} \rangle + \langle \hat{\sigma}^\dagger \hat{\sigma} \rangle$. Energy shifts within these sectors can then be treated similarly to the semiclassical description presented in Section 2.1.1.

For this, in the detuned regime $|\Delta| \gg g(\mathbf{r}_a)$, each pair of uncoupled states $|n, \downarrow\rangle$ and $|n-1, \uparrow\rangle$ gets dressed by the atom-cavity coupling and defines new states $|n, \downarrow\rangle'$ and $|n-1, \uparrow\rangle'$ with shifted resonance frequency, $E_{n,\alpha} = \langle n, \alpha |' H_{\text{JC}} | n, \alpha \rangle'$,

$$E_{n,\downarrow} \approx n\hbar\omega_c + n\hbar \frac{g^2(\mathbf{r}_a)}{\Delta_c}, \quad (2.13)$$

$$E_{n-1,\uparrow} \approx \hbar\omega_0 + (n-1)\hbar\omega_c - n\hbar \frac{g^2(\mathbf{r}_a)}{\Delta_c}, \quad (2.14)$$

for $\Delta_c = \omega_c - \omega_0$. As illustrated in Fig. 2.3, one then obtains a ladder of hybrid cavity-atom states with shifted energies that highly depend on the strength of g_0 and, therefore, on the atomic position inside the cavity. This strong dependence of the atom-cavity system on the position of the atom will dictate the optomechanical effects investigated in Chapter 3 that can appear once the emission of the cavity is considered.

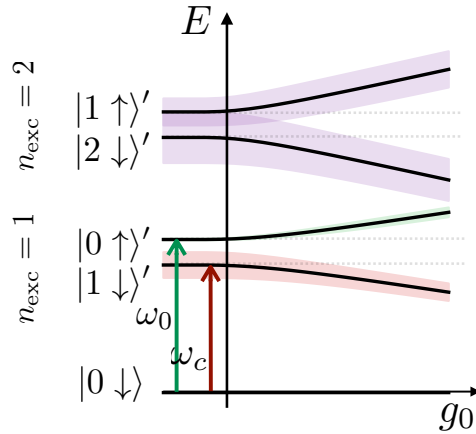


FIGURE 2.3: Schematic representation of the lowest energy levels of the JC Hamiltonian, showing up to 2 total excitations. The energy of the dressed eigenstates $|n_{\text{ph}}, \uparrow / \downarrow\rangle'$ experience a shift from the uncoupled levels $|n_{\text{ph}}, \uparrow / \downarrow\rangle$ that depends on the atom-cavity strength g_0 . The linewidth of these dressed levels is represented by shaded regions in the situation $\gamma \ll \kappa$.

2.2.3 Refined model considering dissipation: cooperativity

Up to this point, we have ignored any dissipative effect related to the coupling of the atom-cavity system and the rest of modes in the environment. This forces one to describe the atom-cavity system with a density matrix in order to account for mixed states. When the coupling to the environment can be described within Born-Markov conditions [77, 78], the dynamics of the atom-cavity density matrix is then given by the following master equation,

$$\partial_t \hat{\rho} = -\frac{i}{\hbar} [\hat{H}_{\text{JC}}, \hat{\rho}] + \kappa \mathcal{L}(\hat{a}, \hat{\rho}) + \gamma \mathcal{L}(\hat{\sigma}, \hat{\rho}), \quad (2.15)$$

where the Lindbladian, $\mathcal{L}(\hat{O}, \hat{\rho}) = \hat{O}\hat{\rho}\hat{O}^\dagger - \frac{1}{2}(\hat{O}^\dagger\hat{O}\hat{\rho} + \hat{\rho}\hat{O}^\dagger\hat{O})$, introduces the recycling term, $\hat{O}\hat{\rho}\hat{O}^\dagger$, needed to preserve the unitarity of the system [79]. Eq. (2.15) thus describes the evolution of the density matrix $\hat{\rho}$ accounting for cavity decay, with rate κ ; and atomic emission into modes different from the cavity one, with rate γ , which associated to jump operators \hat{a} and $\hat{\sigma}$, respectively.

While atomic spontaneous emission γ can be as narrow as a few MHz, cavity decay is typically several orders of magnitude larger in state-of-the-art experiments. In addition to the energy-shift described above, the hybridization with the cavity state further enhances the atomic emission rate, which, in the case of the single excitation space, $|0 \uparrow\rangle'$, increases as,

$$\tilde{\gamma}(\mathbf{r}_a) \approx \gamma + \kappa \frac{g^2(\mathbf{r}_a)}{\Delta_c^2}, \quad (2.16)$$

Such an enhancement of atomic emission from its free-space value γ is due to the change of vacuum modes introduced by the cavity, as firstly predicted by Purcell [80] and experimentally observed with Rydberg atoms [81], and strongly depends on the

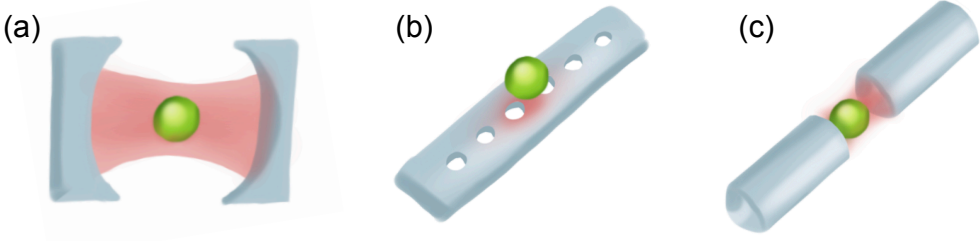


FIGURE 2.4: Schematic representation of an atom (green) optically coupled to (a) a Fabry-Perot cavity, (b) a photonic crystal, (c) a fibre cavity.

position of the atom through $g(\mathbf{r}_a)$. This enhanced emission rate is schematically represented in Fig. 2.3 in the form of wider coloured lines as g_0 increases.

An interesting figure of merit to compare the relevance of this atom-photon coupling over different cavity systems is the ratio between the energy shift g_0^2/Δ_c experienced by the dressed atomic state (2.13) and its enhanced atomic linewidth $\tilde{\gamma}$ (2.16). Maximizing over Δ_c , this ratio receives the name of **cooperativity** of the system,

$$C \equiv \frac{g_0^2}{\kappa\gamma}, \quad (2.17)$$

where $C \gg 1$ defines the strong coupling condition needed to resolve the dressed atomic line shift. Interestingly, written in terms of the atomic scattering length, cooperativity $C \propto N_{\text{trips}}\sigma_{\text{sc}}/A_{\text{eff}}$ can also be interpreted as the previously discussed probability of photon-atom interactions, P , now enhanced by the number of round trips the cavity photon can perform before leaking out the cavity, $N_{\text{trips}} = c/(\kappa L)$, where L is the cavity length [72]. While its meaning as a probability of interaction gets lost in the regime $C \gg 1$, it becomes a rather universal parameter to characterize the quality of cavity QED systems.

2.2.4 Small-volume cavity systems

Designing cavity systems of large cooperativity is desirable for a number of applications. As we have just motivated, cooperativity characterizes the enhanced probability of an atom interacting with a photon in the cavity, as well as the ability to resolve the atomic energy shift caused by this coupling. When two atoms are coupled to the same cavity mode, cooperativity also defines the error probability of exchanging a spin-excitation between them [82], which has important implications in quantum information communication.

Conventional Fabry-Perot cavities offer large cooperativities, in the range of $C \sim 10 - 100$ [see Fig. 2.4(a)]. These values are however hard to push experimentally, since the achievable mode volume for the light field, V_{eff} , gets lower bounded due to the penetration of the cavity-mode into the mirror coating. This fundamentally limits the atom-cavity coupling, $g_0 \propto V_{\text{eff}}^{-1/2}$, to a few 100 MHz [75]. To circumvent this limitation, several strategies are currently explored to further reduce the cavity mode volume in experimental setups where this is not fundamentally limited.

Nanophotonic structures

Nanophotonic structures offer a rich toolbox to control the propagation of light. One of the simplest structures is a **fibre**, whose high-refractive index core, surrounded by a lower index media (like air), allows the guidance of light through total internal reflection. In order to respect the diffraction limit $A_{\text{eff}} \gtrsim \lambda^2$, a significant evanescent field extends outside the fibre for sufficiently small fibre core radius, $r_{\text{fibre}} \lesssim \lambda$, which is attainable using heating-pulling techniques. Red-detuned fields allow to create attractive forces for atoms, while blue-detuned light (whose evanescent field remains closer to the fibre), prevents the atom from attaching to its surface [83]. By using counter-propagating beams, the resulting standing wave induces a periodic trapping potential for the atoms.

When photons propagating in a nanofibre find a defect, part of the transmitting light gets scattered at that point. A periodic distribution of defects can then lead to distinct dispersion relations, where the propagation of frequencies matching this pattern would be highly suppressed. Exploiting this idea, atoms can be trapped at the evanescent field of some guided modes tailored by the modulation of a dielectric material, [see Fig. 2.4(b)]. Their associated mode volumes can defeat the diffraction limit $V_{\text{eff}} \lesssim \lambda^3$, allowing for strong atom-cavity coupling in the range of 10 MHz for **whispering-gallery modes** [84] and in the order of GHz [85] for current experiments using **photonic crystal cavities** [86]. Despite the narrow atomic linewidth $\gamma \ll g$, the cavity decay of these systems $\kappa \gtrsim g$ sets their current cooperativity in the order of $C \sim 10$. Larger values could be achieved by trapping the atom closer to the nanophotonic structure. In that case, however, the experimental challenge is how to defeat the attractive Van-der-Waals forces [87, 88], which sets an experimental challenge to overcome the Van der Waals forces pulling the atom towards their surface.

Fibre cavities

Alternatively to this evanescent field trapping, directly coating a mirror surface at the tip of a fibre offers a refined frontier in cavity design [see Fig. 2.4(c)]. Recent advances even allow us to 3D print microscopic lenses at the tip [89]. Apart from facilitating a direct coupling with incoming light without the need of mode-matching optics, the mode-waist of these fibres ($\sim 1\mu\text{m}$) is one order of magnitude smaller than in macroscopic high-finesse cavities, which provides mode volumes that further approach the diffraction limit [90]. Atom trapping has been proved in these cavities, with state-of-the-art atom-cavity couplings in the order of several hundreds of MHz and cooperativities of order 10 [91, 92].

The achievement of experimental cavities with an enhanced atom-cavity coupling and large cooperativity offers an interesting avenue for research that we investigate in Chapter 3. In particular, we will analyze how sensitive the output of the cavity becomes to the position of the atom within the cavity field, and the fundamental consequences it has on the knowledge of the atomic motional state. In order to relate the output signal of the cavity to its input field, we now briefly introduce the input-output formalism widely used in open quantum systems.

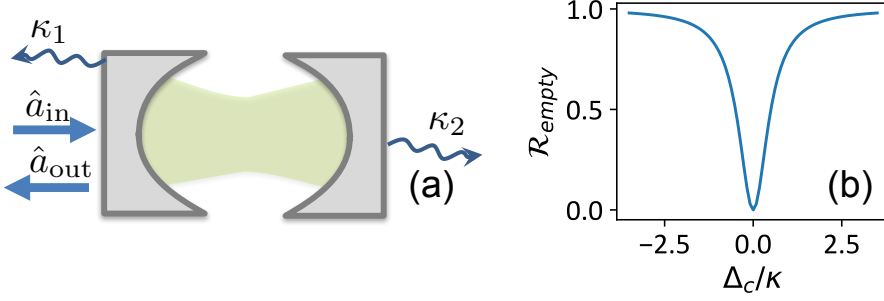


FIGURE 2.5: (a) Schematic representation of an empty cavity that is externally driven by input field \hat{a}_{in} and can decay through this driving channel (κ_1), or the rest of orthogonal modes (κ_2). (b) Reflectance of an empty cavity (2.20), as a function of laser-cavity detuning Δ_c for the balanced cavity configuration, $\kappa_1 = \kappa_2$.

2.2.5 Input-output formalism of an empty cavity.

Here, we review the input-output formalism that will allow us to analyze the reflectance of the cavity system introduced in Chapter 3. For this purpose, we will consider a two-sided empty cavity driven by a monochromatic input field of frequency, ω_l , where we distinguish the decay rate of the cavity into the port used to drive the system (κ_1), from the decay into transmission or absorption channels (κ_2), so that the total cavity decay rate reads as $\kappa = \kappa_1 + \kappa_2$, as illustrated in Fig. 2.5(a).

In particular, the input-output formalism [79, 93] allows us to express the field leaving the cavity through the channel associated to κ_1 , \hat{a}_{out} , in terms of the input field, \hat{a}_{in} , as,

$$\hat{a}_{\text{out}}(t) = \hat{a}_{\text{in}}(t) + \sqrt{\kappa_1} \hat{a}(t), \quad (2.18)$$

which satisfies, $[\hat{a}_{\text{in}}(t), \hat{a}_{\text{in}}^\dagger(t')] = \delta(t - t')$, and $\hat{a}_{\text{in}}^\dagger(\text{out}) \hat{a}_{\text{in}}(\text{out})$ has units of photon number per unit time.

The reflectance of the cavity, $\mathcal{R} = |r|^2$, measures which fraction of the incoming photons gets reflected through the output channel, where $r = \langle \hat{a}_{\text{out}} \rangle / \langle \hat{a}_{\text{in}} \rangle$. The above relation (2.18) allows us to calculate this quantity by solving the Heisenberg-Langevin equation of motion, $\partial_t \langle \hat{a} \rangle = \text{Tr}(\hat{a} \dot{\hat{\rho}})$, which, for the empty-cavity hamiltonian in the frame of the laser, $\hat{H}_c = -\hbar \Delta_c \hat{a}^\dagger \hat{a}$, writes as,

$$\partial_t \langle \hat{a} \rangle = -\frac{i}{\hbar} \langle [\hat{a}, \hat{H}_c] \rangle - \frac{\kappa}{2} \langle \hat{a} \rangle - \sqrt{\kappa_1} \langle \hat{a}_{\text{in}} \rangle, \quad (2.19)$$

where $\Delta_c = \omega_l - \omega_c$ is the laser-cavity detuning.

In the steady-state, $\partial_t \langle \hat{a} \rangle = 0$, one can relate the cavity field to the input as, $\langle \hat{a} \rangle = -i\sqrt{\kappa_1} / (\Delta_c + i\kappa/2) \langle \hat{a}_{\text{in}} \rangle$. The input-output relation (2.18) now allows us to express the reflectance of the cavity as a function of the driving frequency and cavity losses,

$$\mathcal{R}_{\text{empty}} = \left| 1 - \frac{i\kappa_1}{\Delta_c + i\kappa/2} \right|^2. \quad (2.20)$$

From here, one can observe that the incoming field gets perfectly reflected, $\mathcal{R} \rightarrow 1$, for highly detuned driving fields, $|\Delta_c|/\kappa \gg 1$. On the other hand, optimizing over

Δ_c , minimum reflectance occurs in resonance, $\Delta_c = 0$, where,

$$\mathcal{R}_{\text{empty, min}} = \left(1 - \frac{\kappa_1}{\kappa/2}\right)^2. \quad (2.21)$$

Interestingly, no reflection is found in resonance for the so-called **balanced-cavity configuration**, $\kappa_1 = \kappa_2 = \kappa/2$, as represented in Fig. 2.5(b).

2.3 Outlook

In this Chapter, we have introduced how the energy levels of an atom get modified by the effect of an external field, which can be conveniently used for optical trapping. In the presence of a cavity, the natural quantization of the cavity mode leads to the hybridization of the light and matter degrees of freedom, which can be described by the JC Hamiltonian in Eq. (2.12).

We have also motivated that the strength of this atom-cavity interaction, $g(\mathbf{r}_a)$, can highly depend on the position of the atom inside this cavity field. Furthermore, in systems with a large cooperativity, $C = g_0^2/(\kappa\gamma) \gg 1$, the linewidth of the system is narrow enough to resolve the energy shift of these levels. Following the input-output description in Eq. (2.18) just presented, we will show in Chapter 3 that the response of the cavity can then be effectively tuned in ($\mathcal{R} = 0$) or out of resonance ($\mathcal{R} = 1$) by just changing the position of the atom. This extreme sensitivity of the reflectance of the cavity to the position of a single atom has important consequences, as not only does the cavity response depend on the atom, but also the atomic motional state is influenced by the measurement of a reflected photon. This represents one of the minimal examples of the rich optomechanical effects that can appear in these systems, whose impact in state-of-the-art small-volume cavities is investigated in Chapter 3.

Chapter 3

Single atom and photon optomechanical strong coupling

/// *Just because you have an explanation doesn't mean it's the best explanation. Can you eliminate any unnecessary clutter or complexity? Can you find an entirely different approach that gives you deeper insight? Prove, prove, and prove again. Painters, sculptors, and poets do the same thing.*

— Paul Lockhart

(Extract from "Measurement")

In this Chapter we introduce **cavity optomechanics**, an emerging field with numerous exciting prospects for fundamental science and applications [34, 94]. Generically, such systems are characterized by some mechanical degree of freedom whose small displacement from the equilibrium position, x_0 , alters the resonance frequency of a cavity mode $\hbar\omega_c(x)\hat{a}^\dagger\hat{a}$, so that $\omega_c(x)$ now depends on the position of a resonator. This displacement, $\delta x = x - x_0$, can be quantized as $\delta\hat{x} = x_{\text{zfp}}(\hat{b} + \hat{b}^\dagger)$, where x_{zfp} is the mechanical zero-point motion. Expanding $\omega_c(x)$ to linear order in δx , one obtains a cubic coupling,

$$\hat{H}_{\text{OM}} = g_{\text{OM},0}\hat{a}^\dagger\hat{a}(\hat{b} + \hat{b}^\dagger), \quad (3.1)$$

between the operators associated to the annihilation(creation) of a phonon, $\hat{b}^{(\dagger)}$; or a cavity photon, $\hat{a}^{(\dagger)}$.

This cubic coupling between the motional and cavity degrees of freedom results in rich backaction effects once the cavity is driven that include sensing [95–98], cooling of the mechanical mode [99, 100], generation of squeezed light [101–103] or the creation of nonreciprocal devices [104]. The intuitive mechanism is illustrated in Fig. 3.1(a). When the cavity frequency at the equilibrium length is driven in resonance, the cavity field gets populated and those photons impart a radiation pressure on the cavity mirror (top). The resulting force pushes the mirror, changing the length of the cavity and modifying the energy of the cavity mode, $\omega_c(x)$. If the system now becomes out-of-resonance with the driving laser, the population of the cavity decreases (bottom), reducing the radiation force, which returns the mirror to its equilibrium position. Interestingly, this emission is not instantaneous, but

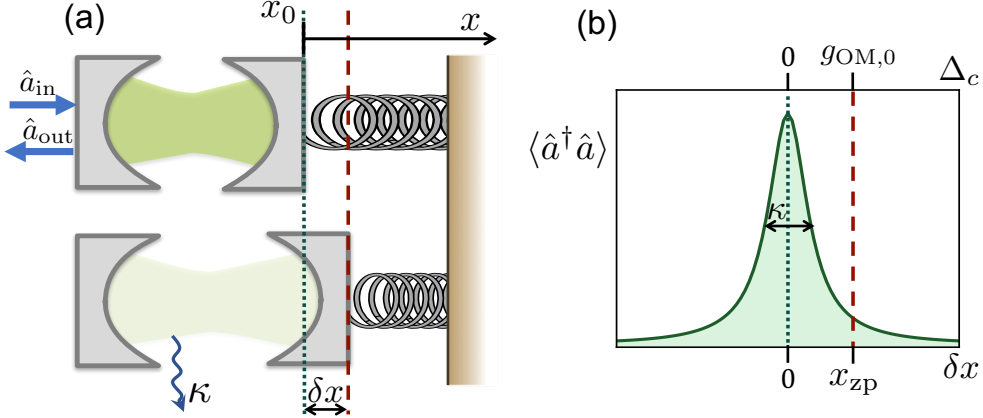


FIGURE 3.1: (a) Illustration of an empty cavity with one of its mirrors connected to a spring, where the displacement from the equilibrium length is $\delta x = x - x_0 = 0$ (top) and $\delta x > 0$ (bottom). A larger population of the cavity mode is schematically represented with a darker green color. (b) Qualitative dependence of the population of this field, $\langle \hat{a}^\dagger \hat{a} \rangle$, as one modifies the length of the cavity (lower axis), which changes the detuning with the driving laser, $\Delta_c(x) = \omega_l - \omega_c(x)$ (upper axis).

dictated by the decay time, $1/\kappa$, which defines the optomechanical properties of the system.

Therefore, a key figure of merit for these applications is the vacuum optomechanical coupling strength, $g_{OM,0} = (\partial\omega_c/\partial x) x_{zp}$, given by the product of the sensitivity of the cavity frequency to position displacements, and the zero-point motion of the resonator. In particular, the single-photon, single-phonon, strong coupling regime ensues when $g_{OM,0}$ exceeds the linewidth of the cavity κ , such that the optical response and dynamics change drastically at the level of individual quanta, x_{zp} , as illustrated in Fig. 3.1(b). For example, it has been proposed that the regime $g_{OM,0}/\kappa \gg 1$ can give rise to quantum optical nonlinearities [105, 106]. While a number of schemes have been proposed to reach this strong coupling regime [107–111], state-of-the-art optomechanical cavities remain at least two orders of magnitude away from reaching this regime [112, 113].

To circumvent this situations, optomechanical experiments are typically operated at strong driving. The cavity operator $\hat{a} \rightarrow \alpha + \delta\hat{a}$ then decomposes into a classical average field α , and a quantum fluctuation $\delta\hat{a}$, so that the interaction in Eq. (3.1) is dominated by the term,

$$\hat{H}_{OM} = g_{OM}(\delta\hat{a} + \delta\hat{a}^\dagger)(\hat{b} + \hat{b}^\dagger), \quad (3.2)$$

and the effective coupling strength $g_{OM} = g_{OM,0}\sqrt{N_{ph}}$ gets enhanced by the number of average cavity photons, $N_{ph} = |\alpha|^2$ so that, for a sufficiently strong driving, it can exceed the cavity linewidth and reach the (non-single photon) strong coupling regime ($g_{OM} \geq \kappa$). However, one can observe that the resulting linearized interaction in Eq. (3.2) misses the richness of the original cubic coupling dictated by optomechanics (3.1). For example, Gaussian states can only be transformed into other Gaussian states under the evolution of the quadratic interaction in Eq. (3.2). Current efforts then focus into manifesting the nonlinearities that can appear in the

single-photon strong coupling regime $g_{\text{OM},0}/\kappa \gg 1$.

To pursue this goal, atoms constitute an interesting candidate as an optomechanical element, due to their low mass and anomalously large optical response (i.e. a scattering cross section much larger than its physical size). In an atomic ensemble, the single-photon coupling strength gets enhanced by the number of atoms in the detuned regime, entering the strong coupling regime for sufficiently large ensembles [114–116]. In this Chapter, we show that the single-photon strong coupling regime can be realistically achieved using just a single atom coupled to a high-finesse cavity [75, 117–120]. While macroscopic cavity architectures allow for sufficiently small linewidths to reach the strong coupling regime [121–123], a number of emerging platforms introduced in Section 2.2.4 focus on achieving small mode volumes with a prohibitively large linewidth [84, 85, 92, 124–126]. Here, we show that optomechanical strong coupling effects can nonetheless emerge in these devices by working in a detuned atom-cavity regime and probing motional interactions on the narrower dressed atomic resonance of a single atom.

The enabling mechanism is based on the scattering properties of an incoming photon, which highly depend on its detuning to the dressed resonance frequency, (2.14), that in turn is sensitive to the atomic position within the cavity field, as introduced in Section 3.1. As a consequence, in Section 3.2 we will show that a scattered photon highly entangles with the resulting atomic motional state, carrying information about its position. This leads to a per-photon atomic heating larger than expected from single-photon recoil events and, as a more direct signature, we observe in Section 3.3 that detection of a reflected photon triggers motion-induced oscillations in time of the second-order correlation function of reflected light. In Section 3.4, we will show that these effects are observable in realistic systems, even for a non-zero initial motional temperature.

3.1 The system

Here we focus on the interaction of a single two-level atom with an optical transition between ground and excited states $|\downarrow\rangle, |\uparrow\rangle$, and a given mode of the electromagnetic field inside the cavity. The coherent interactions are described by the Jaynes-Cummings Hamiltonian (2.12),

$$\begin{aligned} \hat{H}_{\text{JC}} = & -(\Delta + \Delta_0)\hat{a}^\dagger\hat{a} - \Delta_0\hat{\sigma}^\dagger\hat{\sigma} \\ & + g(\hat{x})\left(\hat{\sigma}\hat{a}^\dagger + \text{H.c.}\right) - i\varepsilon\left(\hat{a}^\dagger - \hat{a}\right), \end{aligned} \quad (3.3)$$

where $\Delta = \omega_0 - \omega_c$ is the energy difference between the bare atomic and cavity resonance frequencies¹. Here, we also allow for an external laser drive of the cavity with $\Delta_0 = \omega_l - \omega_0$ representing the laser-atom detuning, and ε the driving amplitude, which we will generally consider weak enough to only produce a few excitations. $g(\hat{x}) = g_0 \sin(k_c \hat{x})$ denotes the position-dependent vacuum Rabi coupling strength, with k_c being the cavity mode wavevector. Importantly, we will treat the atomic position \hat{x} as a quantum dynamical degree of freedom, and assume that the atom is harmonically trapped with frequency ω_m and equilibrium position x_0 , as schematically illustrated in Fig. 3.2(a). As we introduced before, one can quantize the atomic motion around this point as $\delta\hat{x} = \hat{x} - x_0 = x_{\text{zp}}(\hat{b} + \hat{b}^\dagger)$, where

¹In the rest of this Chapter, we use the convention that $\hbar \equiv 1$.

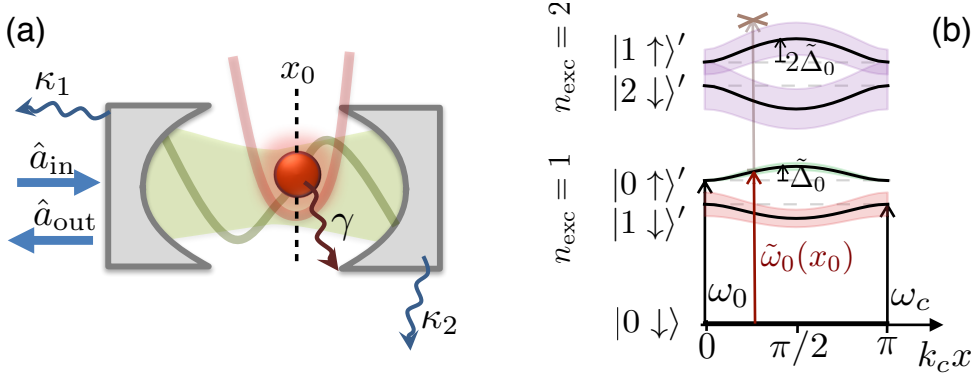


FIGURE 3.2: (a) A single atom is trapped in a harmonic oscillator potential of frequency ω_m centered at position x_0 , and coupled to a cavity mode. The cavity mode is externally driven with input field \hat{a}_{in} and can decay through this driving channel (κ_1), or other undetected routes (κ_2). In addition, the excited atom can spontaneously emit into free space at a rate γ . (b) Schematic representations of the lowest energy levels of the JC Hamiltonian in the absence of a drive [analogous to considering $\varepsilon = 0$ and $\omega_l = 0$ in (3.3)], showing up to 2 total excitations. For atomic positions away from the cavity nodes ($k_c x = 0, \pi$), the frequencies of the dressed eigenstates $|n_{\text{ph}}, \uparrow / \downarrow\rangle'$ experience a shift from the uncoupled levels $|n_{\text{ph}}, \uparrow / \downarrow\rangle$ that depends on atomic position, $\tilde{\Delta}_0 \approx g^2(x)/\Delta$. The linewidth of these dressed levels is represented by shaded regions in the situation $\gamma \ll \kappa$ explored in this work.

x_{zp} denotes zero-point motion fluctuations, and $\hat{b}^{(\dagger)}$ is the annihilation(creation) operator of phonons in the trap, $\hat{H}_{\text{trap}} = \omega_m \hat{b}^\dagger \hat{b}$.

Further including photonic losses from the cavity with decay rate κ , and atomic excited state spontaneous emission at a rate γ , one can describe the total evolution of the density matrix as,

$$\partial_t \hat{\rho} = -i [\hat{H}_{\text{JC}} + \hat{H}_{\text{trap}}, \hat{\rho}] + \kappa \mathcal{L}(\hat{a}, \hat{\rho}) + \gamma \mathcal{L}(e^{-ik_c \hat{x}} \hat{\sigma}, \hat{\rho}). \quad (3.4)$$

As compared to Eq. (2.15), here the $e^{-ik_c \hat{x}}$ term represents the recoil momentum that is imparted onto the atom upon spontaneous emission of a photon. Strictly speaking, the recoil along the x direction is a (non-uniform) random variable between $(-k_c, k_c)$, accounting for the possibility of a photon to be emitted in any direction [127]. As only one atom is present, the free-space direction of the emitted photon does not influence further interactions in the system and disregarding its angular component is sufficient to capture the salient physics and heating caused by atomic recoil [128, 129].

Here, we will consider the regime relevant to a number of cavity QED systems, where $\kappa \gg \gamma$ [84, 85, 126]. In order to access a strong optomechanical coupling, this motivates working in a detuned atom-cavity regime $|\Delta| \gg \kappa, g_0$ and focusing on the dressed atom-like excitation branch with narrower linewidth $\sim \gamma$. We will start by presenting some heuristic arguments to estimate the optimal conditions to reach this single-photon optomechanical strong coupling, which we will later show are rigorously correct. To simplify the discussion, we will also start by considering the case where the atom is initialized in the motional ground state, treating thermal states in Section 3.4.

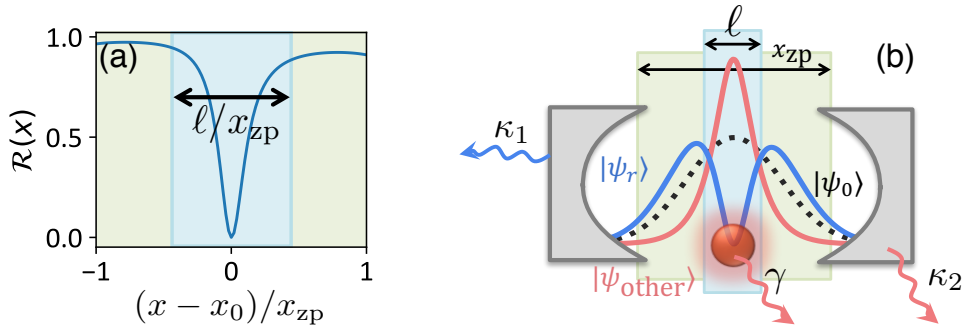


FIGURE 3.3: (a) In the studied configuration, reflectance is tuned to be null when the atom is placed at the center of the trap x_0 , with the spatial width of this reflection minimum given by ℓ . (b) After an incoming photon is scattered, the initial motional wave function $|\psi_0\rangle$ is strongly modified over the length ℓ , to the state $|\psi_r\rangle$ conditioned on the reflection of a photon, or the state $|\psi_{\text{other}}\rangle$ conditioned on scattering into other channels.

3.1.1 Heuristic derivation of strong coupling condition

One can start by considering a static atom with fixed position x . In the absence of a drive ($\varepsilon = 0$), one can block diagonalize the JC Hamiltonian (3.3) in the total number of excitations, $n_{\text{exc}} \equiv \hat{\sigma}^\dagger \hat{\sigma} + \hat{a}^\dagger \hat{a}$, as illustrated in Fig. 3.2(b) for up to $n_{\text{exc}} = 2$. In the limit of large atom-cavity detuning Δ , one of the single-excitation eigenstates $|0 \uparrow\rangle'$ is mostly an atomic excitation $|0 \uparrow\rangle$, but with a shifted resonance frequency (2.14), $\tilde{\omega}_0(x) \approx \omega_0 + \frac{g^2(x)}{\Delta}$, and broadened linewidth (2.16), $\tilde{\gamma}(x) \approx \gamma + \kappa \frac{g^2(x)}{\Delta^2}$, due to the interaction with the cavity [130]. We can consider the sensitivity of this resonance frequency to small (static) displacements δx that, to lowest order, yields a new resonance frequency $\tilde{\omega}_0(x_0 + \delta x) \approx \omega_0 + \frac{g_0^2}{\Delta} \left[\sin^2(k_c x_0) + \sin(2k_c x_0) k_c \delta x \right]$. The maximum sensitivity to a displacement δx then occurs halfway between a cavity node and anti-node, when $k_c x_0 = \pi/4$ [see Fig. 3.2(b)].

Although we take x to be static, one can nonetheless intuitively deduce a single-photon optomechanical strong coupling parameter, $\beta \equiv \frac{g_0^2 \eta}{\Delta \tilde{\gamma}(x_0)}$, which characterizes how much the dressed resonance frequency shifts if the atom is displaced by the zero-point motion, in units of the dressed linewidth. Optimizing over Δ , one observes that the maximum strong coupling parameter is dictated by the cooperativity of the system (2.17), $C \equiv g_0^2 / (\kappa \gamma)$, as $\beta_{\text{max}} = \eta \sqrt{C} / \sqrt{2}$, where $\eta \equiv k_c x_{\text{zfp}}$ is the Lamb-Dicke parameter.

We now derive the reflection coefficient of a weak monochromatic, coherent input field, as a function of atomic position. For this, we distinguish the decay rate of the cavity into the port used to drive the system (κ_1), from the decay into transmission or absorption channels (κ_2), so that the total cavity decay rate reads as $\kappa = \kappa_1 + \kappa_2$ [see Fig. 3.2(a)]. In particular, the input-output formalism [79, 93] allows us to express the field \hat{a}_{out} leaving the cavity through the channel associated to κ_1 in terms of the input field, \hat{a}_{in} , through the input-output relation (2.18),

$$\hat{a}_{\text{out}}(t) = \hat{a}_{\text{in}}(t) + \sqrt{\kappa_1} \hat{a}(t). \quad (3.5)$$

For an atom statically located in position x , one can now define $S_r(x)$ as the

steady-state reflection coefficient defined by the ratio between output and input fields [131, 132], which now depends on the coupling to the atom. Following a derivation analogous to Section 2.2.5, one obtains,

$$S_r(x) = \frac{\langle \hat{a}_{\text{out}} \rangle}{\langle \hat{a}_{\text{in}} \rangle} \approx 1 - \frac{i\kappa_1}{\Delta + \Delta_0 + i\kappa/2 - \frac{g(x)^2}{\Delta_0 + i\gamma/2}}, \quad (3.6)$$

and a corresponding reflectance, $\mathcal{R}(x) = |S_r(x)|^2$, as a function of the atomic position. We observe that in the atomless case ($g(x) = 0$), this reduces to the reflectance of an empty cavity shown in Eq. (2.20). Intuitively, efficient optomechanical coupling requires a large contrast in $\mathcal{R}(x)$ when the atom is displaced from position x_0 by a small amount, so that the event of detecting a reflected photon reveals significant information about the atomic position. Experimentally, one can optimize this by adjusting the driving frequency, the atom-cavity detuning, and the coupling to the detection channel, κ_1 . First, we choose to drive the atom-like resonance,

$$\Delta_0^* = \frac{g^2(x_0)}{\Delta^*}. \quad (3.7)$$

Expanding now the reflectance of the cavity around x_0 , $\mathcal{R}(x) = \mathcal{R}_0 + [(x - x_0)/\ell]^2$, one can enforce that the reflectance at position x_0 is exactly zero, $\mathcal{R}_0 = 0$, so that detection of a reflected photon ensures that the atom is not placed at that point. Imposing this, one obtains the optimal detuning,

$$\Delta^* = g(x_0) \sqrt{\frac{\kappa_1 - \kappa_2}{\gamma}}, \quad (3.8)$$

which corresponds to critical coupling, where the (dressed) atomic excited state decays equally into the cavity output, $(\kappa_1 \frac{g^2(x_0)}{\Delta^2})$, and other channels, $(\gamma + \kappa_2 \frac{g^2(x_0)}{\Delta^2})$. Maximizing the effective single-photon coupling parameter β as a function of κ_1 for the previous choice of parameters, one obtains $\kappa_1^* = 2\kappa_2$. This in turn yields the minimum displacement,

$$\ell^*/x_{zp} \equiv \sqrt{2}/(\eta\sqrt{C_{\text{in}}}), \quad (3.9)$$

over which the dressed atomic frequency shifts by $\tilde{\gamma}$, thus bringing the system off resonance with respect to the fixed external laser frequency [see Fig. 3.3(a)]. The fact that ℓ , representing the length scale over which a single photon can discriminate the atomic position, depends inversely with the square root of the intrinsic cooperativity $C_{\text{in}} \equiv g_0^2/\sqrt{\kappa_2\gamma}$ will play a prominent role in our following discussion. In particular, we observe that the maximum strong coupling parameter previously defined scales as $\beta^* \sim x_{zp}/\ell^*$.

3.2 Role of the atomic motional wave function

Previously, we have established that if the atom was a perfectly localized point particle, a photon would be reflected with an amplitude and phase given by $S_r(x)$.

Intuitively, once the atomic motional state is given by a wave function $|\psi_0\rangle = \int dx \psi_0(x) |x\rangle$, one might expect that the state upon scattering a single photon is given by $S_r |1_r\rangle |\psi_0\rangle + S_{\text{other}} |1_{\text{other}}\rangle |\psi_0\rangle$, where $|1_r\rangle$ denotes a reflected photon, and $|1_{\text{other}}\rangle$ denotes the scattering into some orthogonal channel (transmission or cavity absorption, see Appendix A.1). While $S_r |1_r\rangle |\psi_0\rangle = |1_r\rangle \int dx S_r(x) \psi_0(x) |x\rangle$ has the natural meaning that the amplitude and phase of the reflected photon depends on the atomic position, one can also observe that the atomic wave function conditioned on the detection of the reflected photon becomes,

$$|\psi_r\rangle = \frac{S_r |\psi_0\rangle}{|S_r |\psi_0\rangle|}, \quad (3.10)$$

where $S_r |\psi_0\rangle = \int dx S_r(x) \psi_0(x) |x\rangle$ and the denominator relates to the average reflectance of the cavity, $\mathcal{R} \equiv |S_r |\psi_0\rangle|^2 = \int dx \mathcal{R}(x) |\psi_0(x)|^2$. These results, which were up to now argued intuitively, can in fact be derived rigorously through an adiabatic elimination of the cavity degrees of freedom in the unresolved sideband regime, $\omega_m \ll \gamma, \kappa$ [123], where the dynamics of the atom-cavity interface is much faster than the mechanical evolution of the atom inside the trap and S_r defines a scattering matrix [131, 132] that is diagonal in the position basis (see Appendix A.1).

Intuitively, if the reflectance of the cavity was similar for different atomic positions, $\mathcal{R}(x) \approx \mathcal{R}$, reflection would reveal no information and the wave function would remain unaffected by detection, $|\psi_r\rangle \approx |\psi_0\rangle$. In contrast, if $S_r(x)$ contains any narrow spatial features, those features are now imprinted onto the atomic wave function itself. To quantify this, we observe that ℓ sets the characteristic width for the spatial features imprinted in the wave function [see Fig. 3.3(b)]. For an atom initially in the ground state of the trap, the effect of detection will then be large when this critical displacement is smaller than the zero-point motion of the atom, $\ell \ll x_{\text{zpt}}$, which corresponds to the strong coupling regime, $\eta \sqrt{C_{\text{in}}} \gg 1$.

3.2.1 Unconventional heating

As the initial atomic state $|\psi_0\rangle$ is modified by events associated to reflection or emission in other channels, its mechanical energy departs from the trap ground state energy. Following the example of Eq. (3.10), one can calculate the average number of phonons induced by a single incident photon, $\mathcal{J} = \mathcal{J}_r + \mathcal{J}_t + \mathcal{J}_a$, associated to scattering in the detection channel, cavity transmission/absorption, or atomic spontaneous emission, respectively, where

$$\mathcal{J}_\alpha = \langle S_\alpha \psi_0 | \hat{b}^\dagger \hat{b} | S_\alpha \psi_0 \rangle \quad (3.11)$$

for $\alpha \in \{r, t, a\}$. Note that for each of these emission mechanisms, \mathcal{J}_α then represents the number of phonons in the resulting atomic state $\langle S_\alpha \psi_0 | \hat{b}^\dagger \hat{b} | S_\alpha \psi_0 \rangle / \langle S_\alpha \psi_0 | S_\alpha \psi_0 \rangle$, weighted by the probability that this event occurs, $\langle S_\alpha \psi_0 | S_\alpha \psi_0 \rangle$.

For conventional scattering from a tightly trapped atom in free space, the characteristic number of phonons that an incoming photon can excite is characterized by the ratio between the single-photon recoil energy, ω_{rec} , and the mechanical frequency of the oscillator. When expressed in terms of the Lamb-Dicke parameter, this translates to a per-photon increase in phonons of $\eta^2 = \omega_{\text{rec}}/\omega_m$ [79].

In our coupled atom-cavity system, this heating effect can now be enhanced. Based on our previous analysis, we expect that the largest values of \mathcal{J} will appear

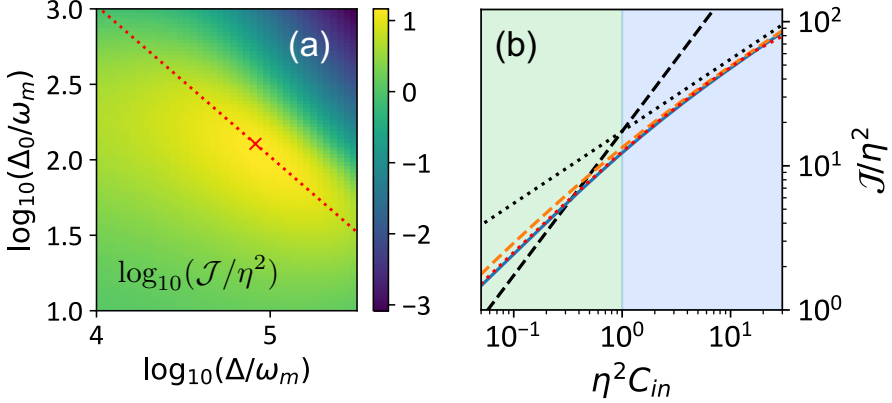


FIGURE 3.4: (a) Ratio of the per-photon increase in phonons (\mathcal{J}) of an atom in the cavity compared to the free-space result η^2 , for different choices of Δ and Δ_0 . Here $\kappa_1 = 2\kappa_2$ and $k_c x_0 = \pi/4$ (see main text). When not indicated otherwise, parameters compatible with Ref. [85] are used in the Figures: $g_0 = 2\pi \times 0.73$ GHz, $\omega_m = 2\pi \times 160$ kHz, $\gamma = 2\pi \times 6$ MHz, $\kappa_2 = 2\pi \times 3.9$ GHz, $\eta = 0.24$. The red dotted line follows a resonant driving with the dressed atomic frequency (3.7), and the crossed marker indicates the optimal atom-cavity detuning (3.8). (b) Value of \mathcal{J}/η^2 , maximized over free values of Δ and Δ_0 (orange dashed line), as compared to the result associated to Δ^* , Δ_0^* within our effective model (blue line), for increasing intrinsic cooperativity tuned by varying g_0 . The red dotted line corresponds to a master equation simulation of the open system (see main text). Dashed and dotted black lines follow the scalings $\mathcal{J} \sim \eta^2 C_{\text{in}}$ and $\mathcal{J} \sim \eta \sqrt{C_{\text{in}}}$ expected in the regimes $\eta^2 C_{\text{in}} \ll 1$ (coloured in green), and $\eta^2 C_{\text{in}} \gg 1$ (coloured in blue), respectively.

for the choices of cavity-laser and atom-cavity detunings derived in Eqs. (3.7,3.8). To validate this, in Fig. 3.4(a) we numerically calculate \mathcal{J}/η^2 for different detunings Δ_0 and Δ in a cavity satisfying $\kappa_1 = 2\kappa_2$. The rest of the parameters are compatible with current experimental platforms [85] where one can reach large intrinsic cooperativities in the order of $C_{\text{in}} \sim 23$, and a Lamb-Dicke parameter $\eta \sim 0.24$. In agreement with our derivation, we observe that a driving frequency in resonance with the dressed atomic frequency (red dotted line, Eq. (3.7)) corresponds to the region of larger heating ($\mathcal{J} \sim 10\eta^2$, associated to lighter colors), and that the atom-cavity detuning that produces maximal heating is compatible with the prediction of Eq. (3.8) (crossed marker).

In Fig. 3.4(b) we calculate \mathcal{J}/η^2 for the choices of Δ_0 and Δ predicted to maximize optomechanical coupling (Eqs. (3.7,3.8)), but now as a function of the intrinsic cooperativity C_{in} by allowing the vacuum Rabi coupling g_0 to vary, while maintaining the rest of the experimental parameters (ω_m , γ , κ_2 , η) as before. We observe that, for each value of intrinsic cooperativity, the heating that arises at the optimal parameters Δ_0^* and Δ^* (blue line) does match a fully numerical maximization of the average number of induced phonons over free values of Δ_0 , Δ (orange dashed line), quantitatively confirming our analysis.

While these calculations were based on the scattering matrix given in Eq. (3.6) and Appendix A.1, we additionally validate these results by performing a master equation simulation of the open system (red dotted line) in a truncated space of up to 2 photons and 50 phonons, where convergence is observed (see Appendix

Interestingly, we observe that the average number of induced phonons \mathcal{J} scales

differently with the intrinsic cooperativity in the weak ($\eta^2 C_{\text{in}} \ll 1$) and strong coupling regimes ($\eta^2 C_{\text{in}} \gg 1$), which can be understood from the phase $\varphi_a(x)$ of the scattering matrices $S_\alpha \sim e^{i\varphi_a(x)}$ that gets imprinted onto the atomic wave function. For the optimal parameters (3.7,3.8), we note that up to linear order in $\delta x/x_{\text{zp}}$ the imprinted phase associated to emission in undriven channels scales linearly as $\varphi_{t/a}(x) \sim \eta\sqrt{C_{\text{in}}}\delta x/x_{\text{zp}}$ [see Eq. (A.4)], which corresponds to an added momentum of $\eta\sqrt{C_{\text{in}}}/x_{\text{zp}} = \sqrt{2}/\ell$. Although $S_r(x)$ cannot be expressed as a phase term, atomic heating can only depend on the total cavity decay rate κ , and not on the specific channel contributing to this rate. Thus, as $\kappa_1 = 2\kappa_2$, it follows that the heating rate due to reflection is twice that of transmission/absorption, $\mathcal{J}_r \approx 2\mathcal{J}_t$.

Adding these three contributions in the weak-coupling limit, [$x_{\text{zp}} \ll \ell$, green shaded region of Fig. 3.4(b)], the imprinted momentum affects the entire wave function and the corresponding kinetic energy increase leads to a heating rate of $\mathcal{J}^{\ll} \sim (x_{\text{zp}}/\ell)^2 \sim \eta^2 C_{\text{in}}$. In contrast, in the strong optomechanical coupling limit ($x_{\text{zp}} \gg \ell$, blue shaded region), the phase imprinting only applies to a small region ℓ of the entire wave function, where the cavity is actually sensitive to the atomic position. This leads to a heating rate of $\mathcal{J}^{\gg} \sim (x_{\text{zp}}/\ell)^2 \cdot (\ell/x_{\text{zp}}) \sim \eta\sqrt{C_{\text{in}}}$, matching the scalings observed in Fig. 3.4(b) (black dashed and dotted lines, respectively). The fact that the per-photon heating rate could be one or two orders of magnitude larger than the expected free space result could be relevant to experiments that probe around the dressed atomic resonance frequency. Separately, we note that the enhanced heating of an atomic ensemble has been experimentally observed in a complementary regime, driving around the dressed cavity resonance of a detuned atom-cavity system [133].

3.3 Second-order time correlations

We now consider how the strong optomechanical coupling can manifest itself in the second-order time correlation of the reflected field,

$$g_{rr}^{(2)}(t) \equiv \frac{\langle \hat{a}_{\text{out}}^\dagger(0)\hat{a}_{\text{out}}^\dagger(t)\hat{a}_{\text{out}}(t)\hat{a}_{\text{out}}(0) \rangle}{\langle \hat{a}_{\text{out}}^\dagger(t)\hat{a}_{\text{out}}(t) \rangle \langle \hat{a}_{\text{out}}^\dagger(0)\hat{a}_{\text{out}}(0) \rangle}, \quad (3.12)$$

which quantifies the relative likelihood of detecting a reflected photon at time t , given the previous detection of a reflected photon at time $t = 0$.

We first present an approximate theory, based on the scattering matrix and the dynamics of the motional wave function following detection of a first reflected photon, $|\psi_r\rangle$ [see Eq. (3.10)]. This approach neglects contributions to $g_{rr}^{(2)}$ that arise from the anharmonicity $\sim \Delta$ of the JC ladder between $0 \rightarrow 1$ and $1 \rightarrow 2$ excitations [represented by the red arrows in Fig. 3.2(b)]. We will later show, by comparing with full master equation simulations, that the scattering matrix captures well important features of $g_{rr}^{(2)}(t)$ and, in particular, oscillations due to strong optomechanical coupling. For our previous choice of detunings [(3.7,3.8), ensuring $\mathcal{R}(x_0) = 0$], a central hole is imprinted in the conditional atomic motional state $|\psi_r\rangle$ [blue wave function in Fig. 3.5(a)], reducing atomic population at positions where reflection is more unlikely. Note that some of the other experimental parameters (κ_1/κ_2 and η) have been changed relative to previous figures to make the relevant effects more visible.

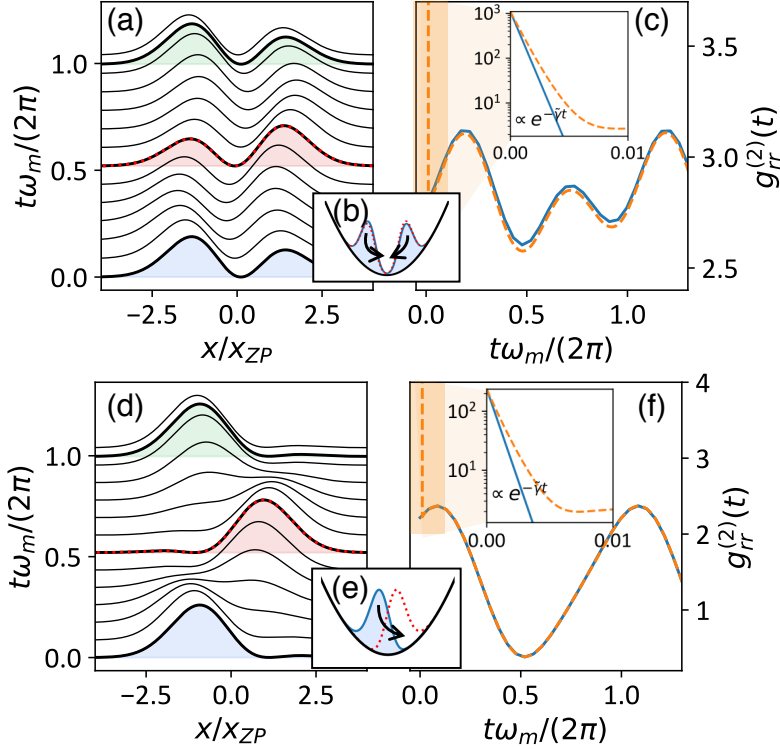


FIGURE 3.5: (a) Spatial probability distribution $|\psi_r(t)|^2$ following the detection of a reflected photon at $t = 0$, and under the assumption that the subsequent motional wave function only evolves under the external trapping potential for the configuration $\eta = 0.05$, $\kappa_1/\kappa_2 = 1.6$, marked with a red cross in Fig. 3.6(a). Later times are indicated by vertical shifts of the atomic density, and the wave function at times π/ω_m and $2\pi/\omega_m$ are coloured in red and green, respectively. Following Eqs. (3.7, 3.8), Δ_0 and Δ are chosen to satisfy $\mathcal{R}(x_0) = 0$. Rest of parameters as in Fig. 3.4. (b) Schematic representation of $|\psi_r|^2$ at time $t = 0$ (blue) and $t = \pi/\omega_m$ (dotted red). (c) Calculation of $g_{rr}^{(2)}(t)$ along this evolution, using the scattering matrix approach (blue line) and a master equation simulation of the cavity system (orange dashed line). The inset highlights the fast decay of $g_{rr}^{(2)}(t)$ at initial times revealed by the master equation (dashed line), compatible with a decay rate $\langle \tilde{\gamma}(x) \rangle$ (continuous line). (d-f) Analogous plots to (a-c), now for the case $\mathcal{R}(x_0 + x_{zp}) = 0$ (see text).

To approximate $g_{rr}^{(2)}(t)$, we consider the limit of a weakly driven cavity, such that the forces associated with the cavity field are negligible compared to the external trap. The subsequent dynamics of the atomic state are then dominated by the evolution purely in the trapping potential, $|\psi_r(t)\rangle = e^{-i\hat{H}_{\text{trap}}t}|\psi_r\rangle$ before further scattering events occur, as the atomic motion is highly isolated from its environment. Because of the overall mirror symmetry in $|\psi_r\rangle$ found for the discussed configuration, a revival of the wave function appears with periodicity in time π/ω_m as the atomic state evolves [red and green wave functions in Fig. 3.5(a), see also the illustration in Fig. 3.5(b)].

This time-evolving spatial distribution, combined with the sensitivity of the cavity response to the position of the atom, should result in a conditional time-dependent reflectance that manifests in $g_{rr}^{(2)}(t)$ as,

$$g_{rr}^{(2)}(t) \approx \frac{|S_r |\psi_r(t)\rangle|^2}{\mathcal{R}}, \quad (3.13)$$

which compares the reflectance of the cavity at time t after detection of a reflected photon to the initial reflectance \mathcal{R} of the cavity, considering that intermediate scattering events are unlikely over the observation time.

In Fig. 3.5(c) (blue curve), we plot the predicted $g_{rr}^{(2)}(t)$ from Eq. (3.13), for the spatial dynamics illustrated in Fig. 3.5(a). We observe a bunching effect immediately after detection of the first reflected photon, as detection projects the atomic state into a configuration compatible with that event. The same cavity response is expected whenever the state revives, which for the symmetric configuration presented above, occurs with periodicity π/ω_m .

To validate these results in the weakly driven regime, we have also performed a full master equation simulation of the driven system in Eq. (3.4) for a weak field input as described in Section 3.2 [orange dashed line in Fig. 3.5(c)]. We observe good agreement with the results provided by Eq. (3.13) at times $t > 1/\tilde{\gamma}$. At shorter times, we note an additional contribution to $g_{rr}^{(2)}(t)$ that can be interpreted from the anharmonicity Δ in the JC ladder of a motionless atom [see red arrows in Fig. 3.2(b)]. For large cooperativity, this detuning exceeds the linewidth of the cavity, $\Delta^*/\kappa \sim \sqrt{C_{\text{in}}}$ [see Eq. (3.8)], and favours the reflection of two-photon packages. In order to separate nonlinearities arising from motion versus the two-level structure itself, it is important to note that any transient feature arising in $g_{rr}^{(2)}(0)$ due to the (dressed) atomic state will decay at the cavity-enhanced atomic emission rate $\tilde{\gamma}$, as we further illustrate in the inset, which is much larger than typical atomic trap frequencies. Previous work on "single polariton optomechanics" involves adding a two-level atom as a third degree of freedom to an optomechanical system which explicitly allows for non-Gaussian states to be generated, [134, 135]. Here, although we also use an atom, the non-trivial time-dependent features in $g_{rr}^{(2)}(t)$ we observe beyond $t \gtrsim 1/\tilde{\gamma}$ can then be attributable to the single-photon strong coupling originated from atomic motion, rather than the two-level nature of the atom.

Regarding the significance of these time-dependent oscillations in $g_{rr}^{(2)}(t)$, we point out that they differ from oscillations in reflection that could be observed, for example, by applying a classical momentum kick on the atom. In particular, in the latter case, given an atom originally in a stationary state (such as the motional

ground state or a thermal state), an additional optical pulse (or a sudden variation in the trapping field) could induce motional oscillations in the atom. These would be already visible as temporal oscillations in the cavity output field $\langle \hat{a}_{\text{out}}^\dagger(t) \hat{a}_{\text{out}}(t) \rangle$, given a weak probe input. Note that these oscillations would only be significant if the kicking pulse contained many photons, given the small recoil energy of a single photon compared to the trapping frequency. In the presented scheme, the "kick" comes from the detection of just a single photon and the large conditional change that it imparts on the motional wave function, which is the essence of strong single-photon optomechanical coupling. Furthermore, the conditional nature of this effect causes these oscillations to appear in the higher-order correlation of $g_{rr}^{(2)}(t)$, rather than the unconditional reflectance itself.

Furthermore, the period of oscillations can be modified by tuning the driving frequency such that $\mathcal{R}(x_0 + x_{\text{zp}}) = 0$ (e.g. replacing $x_0 \rightarrow x_0 + x_{\text{zp}}$ in Eqs. (3.7, 3.8)). The detection of a reflected photon results in a conditional wave function whose probability amplitude is increased on one side of the trap, as illustrated in Fig. 3.5(d). After half a period, this state now oscillates to the opposite side of the trap [see Fig. 3.5(e)] which, in this configuration, manifests as antibunching [$g_{rr}^{(2)}(\pi/\omega_m) < 1$], restoring the natural periodicity $2\pi/\omega_m$ of the correlator $g_{rr}^{(2)}(t)$, as we show in Fig. 3.5(f).

We now discuss the approximate conditions desired to observe large contrast in the time-dependent oscillations in $g_{rr}^{(2)}(t)$. We begin by noting that our previous strong coupling conditions, based on achieving an effective length ℓ/x_{zp} as small as possible [see Eq. (3.9)], do not directly translate into large oscillations in $g_{rr}^{(2)}(t)$. In particular, large oscillations require a large difference between the unconditional and conditional reflectances. Note that in the best case scenario, the detection of a reflected photon completely conditions the atomic wave function to reflect a second photon, resulting in a conditional reflectance of unity. Thus, one wants to avoid that this unconditional reflectance is already too close to unity, $\mathcal{R} \rightarrow 1$. This large unconditional reflectance would occur, for example, if $\ell/x_{\text{zp}} \rightarrow 0$, such that the atom is effectively never in the narrow spatial width $\sim \ell$ where the reflection would differ from unity, resulting in $g_{rr}^{(2)}(0) \rightarrow 1$.

To better interpret how intermediate situations may be optimal, one can explore a simplified uniform response in reflectance $\mathcal{R}(x) = 1 - (1 - \mathcal{R}_0)\Theta[\ell - |x|]$ for a homogeneous mechanical state $|\psi(x)|^2 = (2x_{\text{zp}})^{-1}\Theta[x_{\text{zp}} - |x|]$; where $\Theta[x]$ denotes the step function that is 1 for $x > 0$ and 0 otherwise. In this toy model, one obtains that the maximum value of $g_{rr}^{(2)}(0)$ occurs when $\ell(1 + \mathcal{R}_0) \sim x_{\text{zp}}$, which defines an optimal (non-zero) length for each choice of \mathcal{R}_0 . The optimal configuration is a balanced cavity ($\mathcal{R}_0 = 0$), where one would desire $\ell \sim x_{\text{zp}}$.

To further illustrate this, in Fig. 3.6(a) we calculate the scattering matrix approximation to $g_{rr}^{(2)}(0)$ (3.13), using the same parameters for g_0 , γ , and κ_2 as in the experiment of Ref. [85] and Fig. 3.4(a). However, we now allow the Lamb-Dicke parameter (experimentally tunable through the intensity of the trapping potential) and the output port decay rate κ_1 to vary. Choosing for each set of η and κ_1 the atom-cavity detuning that minimizes $\mathcal{R}(x_0)$, and driving in resonance with the dressed atomic frequency for an atom positioned at x_0 , we heuristically observe that the largest values of $g_{rr}^{(2)}(0) \sim 3$ appear in a region compatible with $\ell(1 + \mathcal{R}_0) = 6x_{\text{zp}}$ (red continuous line), which aligns with the intuition built from

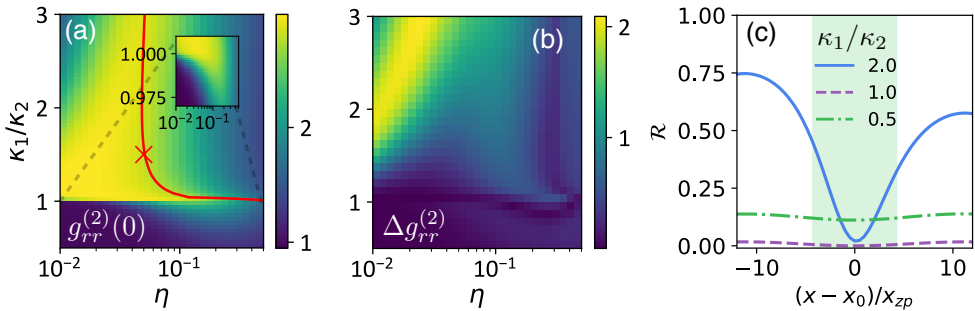


FIGURE 3.6: (a) Scattering matrix calculation of $g_{rr}^{(2)}(0)$ when driving in resonance the dressed atomic frequency for the configuration $\mathcal{R}_0 = 0$ as defined in Eqs. (3.7,3.8), as one varies the Lamb-Dicke parameter η and the ratio κ_1/κ_2 . For $\kappa_1 < \kappa_2$, where it is not possible to obtain $\mathcal{R}_0 = 0$, we numerically maximize $g_{rr}^{(2)}(0)$ as a function of Δ . Rest of experimental parameters as in Fig. 3.4. Red line follows the relation $\ell(1 + \mathcal{R}_0) = 6x_{zp}$, and red marker indicates the configuration $\kappa_1/\kappa_2 = 1.6$, $\eta = 0.05$ explored in Fig. 3.5. The inset zooms into the region of ratios $\kappa_1/\kappa_2 \approx 1$. (b) For the same parameter choices as (a), we illustrate the overall variation along a full mechanical oscillation, $\Delta g_{rr}^{(2)} \equiv \max_t g_{rr}^{(2)}(t) - \min_t g_{rr}^{(2)}(t)$. (c) Reflectance of this atom-cavity system as a function of the position of a motionless atom trapped in an harmonic potential centered at x_0 with Lamb-Dicke parameter $\eta = 0.07$ and different values of κ_1/κ_2 (see legend). Coloured area indicates the region $|x - x_0| < \ell$.

our toy model. In Fig. 3.6(b) we further show the overall variation of $g_{rr}^{(2)}(t)$ along a full mechanical oscillation, $\Delta g_{rr}^{(2)} \equiv \max_t g_{rr}^{(2)}(t) - \min_t g_{rr}^{(2)}(t)$, observing that the largest values $\Delta g_{rr}^{(2)} \sim 2$ appear in a region compatible to those with larger $g_{rr}^{(2)}(0)$.

Here, one can also see a sharp change in $g_{rr}^{(2)}(0)$ around $\kappa_1 = \kappa_2$, that is more evident as $\eta < 0.1$ [see inset in Fig. 3.6(a)]. In this latter regime, the effective atomic displacement over which the reflectance of the cavity varies $\ell/x_{zp} \sim (\eta\sqrt{C_{in}})^{-1}$ becomes much larger than the characteristic spread of the atomic state and, therefore, the response of the cavity becomes less sensitive to the position of the atom, as illustrated in Fig. 3.6(c). For $\kappa_1/\kappa_2 \geq 1$, the fact that no reflection occurs for an atom at the center of the trap ($\mathcal{R}_0 = 0$) defines a high relative difference in the response of $\mathcal{R}(x)$ that highly discriminates this central position when a reflected photon is detected (see blue and purple lines). This translates into a large response $g_{rr}^{(2)}(0) \sim 2$ even if the absolute variation of $\mathcal{R}(x)$ along the zero-point motion of the atom is very reduced as κ_1 approaches κ_2 (purple line). However, when the cavity leakage through the undetected channel exceeds the emission in the driven port ($\kappa_1 \ll \kappa_2$) there is no possible choice of atom-cavity detuning that allows for \mathcal{R}_0 to vanish (green line, see Eq. (3.8)). As a consequence, the relative difference in reflectance gets suppressed in this regime, $\Delta\mathcal{R}/\mathcal{R}_0 \ll 1$, and detection of a reflected photon barely provides any information about the atomic position, which leads to the observed values $g_{rr}^{(2)}(0) \sim 1$ when $\eta \ll 1$.

3.4 Finite temperature

In a real experimental situation, limitations in cooling or atom transport can prevent the atom from being prepared in its motional ground state. Instead, here we

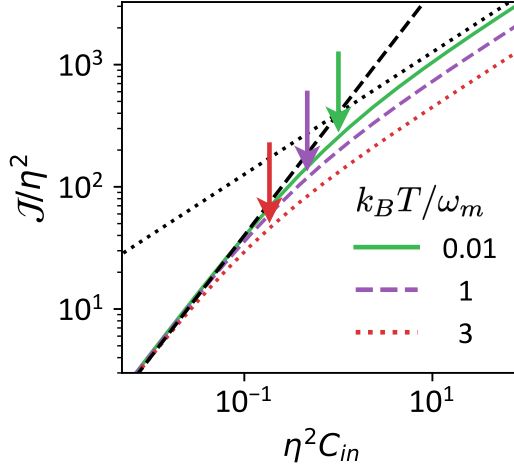


FIGURE 3.7: Average number of induced phonons per photon, normalized by the free-space expectation, \mathcal{J}/η^2 , for an atom in a thermal state ρ_T associated to temperatures $k_B T/\omega_m = 0.01, 1, 3$ (see legend), and increasing values of atom-cavity coupling. The rest of parameters are chosen as in Fig. 3.5(a). We observe that the transition between the weak ($\mathcal{J} \propto \eta^2 C_{\text{in}}$, black dashed line) and strong coupling limits ($\mathcal{J} \propto \eta \sqrt{C_{\text{in}}}$, black dotted line) appears at the critical effective length [$\ell = x_T$] marked with coloured arrows.

describe the situation where the motional state is given by a thermal density matrix at temperature T ,

$$\hat{\rho}_T = \frac{e^{-\hat{H}_{\text{trap}}/(k_B T)}}{Z}, \quad (3.14)$$

where k_B is the Boltzmann constant and $Z = \text{Tr}(e^{-\hat{H}_{\text{trap}}/(k_B T)})$ the partition function. An important consequence is that its steady-state position uncertainty $x_T \equiv \sqrt{\text{Tr}(\hat{x}^2 \hat{\rho}_T)}$ becomes temperature broadened as $x_T/x_{\text{zpt}} \approx \sqrt{2n_{\text{ph}} + 1}$, where $n_{\text{ph}} \equiv \text{Tr}(\hat{b}^\dagger \hat{b} \hat{\rho}_T)$ is the thermal phonon number that approximates $n_{\text{ph}} \approx k_B T/\omega_m$ in the limit $n_{\text{ph}} \gg 1$.

In analogy to the role played by x_{zpt} in the zero-temperature limit, x_T represents the characteristic temperature-dependent length of the system, and strong optomechanical coupling is expected to occur when $x_T \sim \ell$. To illustrate this, in Fig. 3.7 we calculate the average number of additionally induced phonons caused by a single photon as the intrinsic cooperativity increases, where each contribution can be obtained from the scattering matrix description as $\mathcal{J}_\alpha = \text{Tr}(\hat{b}^\dagger \hat{b} S_\alpha \hat{\rho}_T S_\alpha^\dagger)$. Note that phonons already present in the thermal state now need to be subtracted from the number of phonons in the final conditional state, so that the net number of phonons added is $\mathcal{J} = \mathcal{J}_r + \mathcal{J}_t + \mathcal{J}_a - \text{Tr}(\hat{b}^\dagger \hat{b} \hat{\rho}_T)$. Presenting the calculation for three different temperatures, we observe for each of them that $x_T = \ell$ (marked with arrows) defines the crossover, where \mathcal{J} changes in scaling from $\eta^2 C_{\text{in}}$ to $\eta \sqrt{C_{\text{in}}}$. While this transition point occurs at smaller values of $\eta^2 C_{\text{in}}$ as temperature is increased, the magnitude of the strong coupling effect also decreases, as evidenced by the decreased heating \mathcal{J}/η^2 .

One can also analyze the effect that temperature has on the second-order correlations previously discussed. In Fig. 3.8 we use the scattering matrix formalism to calculate $g_{rr}^{(2)}(t)$ for different initial thermal states. For this, we assume that the dynamics of the thermal state conditioned to reflection of an initial photon, $\hat{\rho}_{T,r} = S_r \hat{\rho}_T S_r^\dagger / \text{Tr}(S_r \hat{\rho}_T S_r^\dagger)$, is dominated by the evolution purely in the trapping potential, $\hat{\rho}(t) = e^{-i\hat{H}_{\text{trap}}t} \hat{\rho} e^{i\hat{H}_{\text{trap}}t}$, so that one can approximate the second-order correlator as $g_{rr}^{(2)}(t) \approx \text{Tr}(S_r \hat{\rho}_{T,r}(t) S_r^\dagger) / \text{Tr}(S_r \hat{\rho}_T S_r^\dagger)$.

The fact that the characteristic width of the state, x_T , now depends on temperature yields some interesting phenomena. First, although Eq. (3.13) was formally derived assuming a pure initial state, one can see that $g_{rr}^{(2)}(0)$ only in fact depends on the position probability distribution, suggesting that the purity of the state is irrelevant. Thus, one might expect $g_{rr}^{(2)}(0)$ to be independent of temperature, as long as the trapping frequency is adjusted so that the effective Lamb-Dicke parameter $\tilde{\eta} = \eta x_T / x_{\text{zp}}$ remains constant. This independence is illustrated in Fig. 3.8(a), where we plot $g_{rr}^{(2)}(0)$ as a function of temperature and $\tilde{\eta}$.

However, the thermal nature of the state is expected to play a role in the subsequent dynamics of $g_{rr}^{(2)}(t)$. To investigate this, in Fig. 3.8(b) we show the second-order correlation function associated to time $t' = \pi / (2\omega_m)$ (the two reflected photons are separated by a quarter of the mechanical oscillation period). At this time delay, we see that $g_{rr}^{(2)}(t')$ does retain a temperature dependence for fixed $\tilde{\eta}$, and tends toward 1 at larger temperatures.

To understand this, note that following the detection of the first reflected photon, evolution under \hat{H}_{trap} during a time $t' = \pi / (2\omega_m)$ causes the position quadrature to fully transform to momentum, and vice versa. In particular, the spatial width of this conditioned state at time t' , $\text{Tr}(\hat{x}^2 \hat{\rho}_{T,r}(t')) / x_{\text{zp}}^2$, equals the width in momenta at initial time, $\text{Tr}(\hat{p}^2 \hat{\rho}_{T,r}(0)) / p_{\text{zp}}^2$, where $p_{\text{zp}} \equiv 1 / (2x_{\text{zp}})$. On the other hand, the resulting increase in kinetic energy due to the momentum imparted by detection for fixed $\tilde{\eta}$ is given by $\sim \ell^{-2} \sim n_{\text{ph}}^{-1}$. This becomes negligible compared to the kinetic energy of the thermal state $\sim n_{\text{ph}}$. It then follows that $\text{Tr}(\hat{p}^2 \hat{\rho}_{T,r}(0)) \approx \text{Tr}(\hat{p}^2 \hat{\rho}_T)$ in the regime $n_{\text{ph}} \gg 1$, which leads to the observed limit $g_{rr}^{(2)}(t') \rightarrow 1$. Thus, by fixing $\tilde{\eta}$, the overall variation of $g_{rr}^{(2)}(t)$ in the limit $n_{\text{ph}} \gg 1$ then oscillates between the result $g_{rr}^{(2)}(0)$ also expected at zero temperature, to the value $g_{rr}^{(2)}(t') \sim 1$ appearing for $n_{\text{ph}} \gg 1$ after one quarter of the mechanical period, as we plot in Fig. 3.8(c). As a consequence, higher temperature can in fact lead to greater contrast in the temporal oscillations of the second-order correlation function.

Finally, in Fig. 3.8(d), we plot $g_{rr}^{(2)}(\pi / \omega_m)$ as a function of atom-laser detuning and temperature. Here, we fix the trapping frequency ω_m to yield a (zero-temperature) Lamb-Dicke parameter of $\eta = 0.05$. We observe that after half a mechanical oscillation, bunching and antibunching occur for driving frequencies that satisfy the conditions $\mathcal{R}(x_0) = 0$ (green dashed line) and $\mathcal{R}(x_0 \pm x_T) = 0$ (red dotted line), respectively. The latter condition now depends on the temperature of the state through the temperature-broadened x_T , so that driving frequencies associated to bunching and antibunching separate as the temperature increases. Taking now the limit of large temperature, we observe that second-order correlations tend to the Poissonian result $g_{rr}^{(2)} = 1$ as the change in the wave

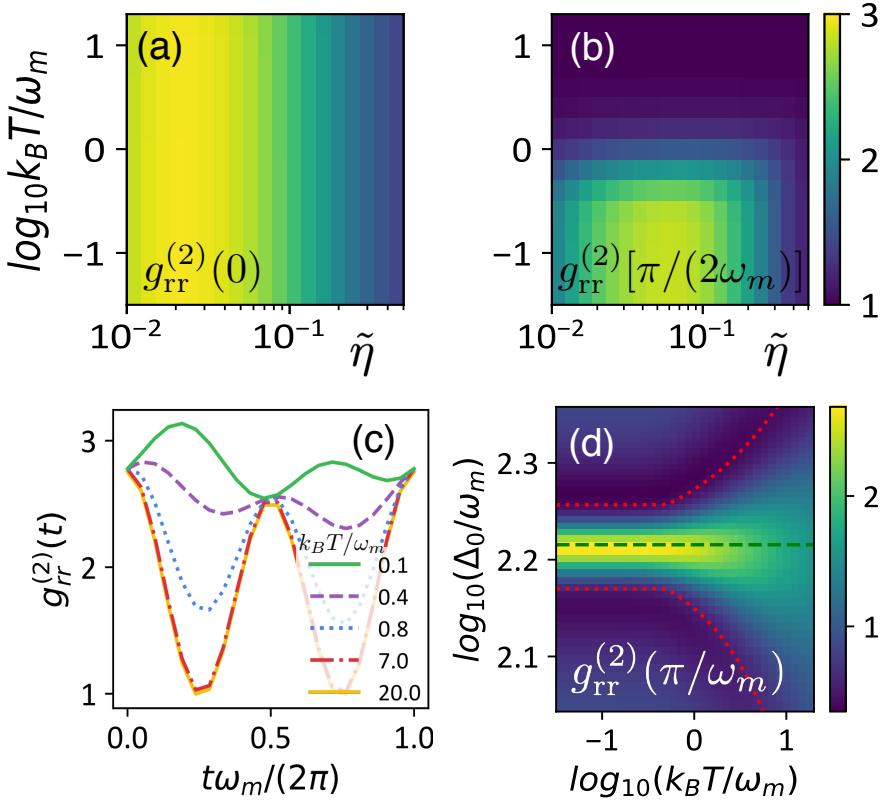


FIGURE 3.8: Value of the second-order time correlation function at times $g_{rr}^{(2)}(0)$ (a) and $g_{rr}^{(2)}[\pi/(2\omega_m)]$ (b), as a function of the temperature T of the initial thermal state and the effective Lamb-Dicke parameter, $\tilde{\eta} = \eta x_T / x_{zp}$, for fixed coupling ratio $\kappa_1 / \kappa_2 = 1.6$ and the rest of parameters chosen as in Fig. 3.6. (c) Evolution of $g_{rr}^{(2)}(t)$ associated to five different values of temperature for the choice of effective Lamb-Dicke parameter $\tilde{\eta} = 0.05$. (d) Second-order time correlations half a mechanical oscillation away from initial detection, $g_{rr}^{(2)}(\pi/\omega_m)$, for different driving frequencies and temperatures of the initial atomic thermal state, and fixed $\eta = 0.05$. Bunching (light yellow) prevails for driving resonant with the atom-like frequency, $[\mathcal{R}(x_0) = 0]$ (green-dashed line, Eq. (3.7)), while antibunching (dark blue) appears for a detuning compatible with $[\mathcal{R}(x_0 \pm x_T) = 0]$ (red dotted lines, see text). Calculations are performed within the scattering matrix model (see main text), observing convergence when allowing for up to 150 phonons in the explored range of temperatures. The rest of parameters are chosen as in Fig. 3.4.

function, restricted to a region ℓ , is less significant when the temperature increases and the atom is more spread. Still, we note that deviations from the Poissonian result $g_{rr}^{(2)} = 1$ of order 40% can be readily observable for phononic occupations in the order of $n_{\text{ph}} \approx 7$, compatible with Ref. [85].

3.5 Conclusions and outlook

Taking advantage of the narrow linewidth of a single atom, we have shown that it is possible to reach the single-photon strong coupling regime of optomechanics, even when the cavity linewidth is prohibitively large. We have shown that this optomechanical strong coupling can give rise to anomalously large motional heating, and to motionally-induced oscillations in the second-order correlation function of the light reflected from the cavity.

From the perspective of utilizing atom-cavity systems to realize coherent spin-photon interfaces, such as for quantum information processing, our work shows that there is the possibility to get strongly entangled with other undesired degrees of freedom, in the form of phonons. It is therefore important to specifically account for this effect when analyzing and optimizing protocols, especially in systems with high cooperativity and large spatial variations of the vacuum Rabi splitting, $g(x)$. On the other hand, such a platform would be unique in enabling the study of quantum optomechanics in the strong coupling regime. For example, it would be interesting to investigate how to exploit such systems to realize strongly non-Gaussian dynamics. Separately, with the possibility to scale atom-cavity interfaces to multiple atoms and/or cavities [85], it might be possible to observe interesting strongly correlated optomechanical states at the many-body level [136].

Part II

Atom-mediated interactions for cold atoms in optical lattices

Chapter 4

Preliminaries II: ultracold atoms in optical lattices

” The problem with surprise is that you have to lay out a trail for the audience to follow all the while you’re keeping slightly ahead. You don’t want them to be bored, but neither do you want them to be confused, and unfortunately there are many ways to do both.

— **Stephen Sondheim**

(Extract from "Look, I made a hat")

Along the first part of this Thesis, we have illustrated some of the striking consequences that can appear when light and matter intimately interact with each other. In particular, Section 2.1.1 described how a strong classical driving field can manipulate the energy levels of a two-level atom, inducing an energy shift that is proportional to the intensity of the beam. In Section 4.1 of this Chapter, we illustrate how this principle can be used to engineer optical lattices. Once atoms are trapped in such a periodic potential, the resulting band-structure of the spectrum admits a convenient description based on Bloch theory that we introduce in Section 4.2. In particular, deep lattices admit a tight-binding description (Section 4.3), where contact interactions among trapped bosons naturally simulate the local repulsion described in the Bose-Hubbard (BH) model, which we introduce in Section 4.4. In Section 4.5 we review different strategies that have been pushed forwards in order to engineer long-range interactions in this system, and we finally motivate in Section 4.6 the long-range tunability of interactions that is desired for relevant simulations in, e.g., analog quantum chemistry, which is the scope of the second part of this Thesis.

4.1 Optical lattices

An interesting experimental configuration is the one created by two counterpropagating fields of the same polarization, which create a standing wave whose amplitude is spatially modulated as $I(\mathbf{r}) = I_0 \sin^2(\mathbf{k}\mathbf{r})$. Experimentally, such a superposition can be obtained by retroreflecting the beam with an orthogonal mirror. For a standing wave formed in the x direction, the wavevector is $\mathbf{k} = k\mathbf{u}_x$, whose modulus $k = 2\pi/\lambda$ is dictated by its wavelength, λ . This induces a periodic

optical potential perceived by the atom (2.8),

$$V_{\text{lat}}(x) = V_D \sin^2(kx), \quad (4.1)$$

where V_D is the depth of the resulting optical lattice, which scales with the intensity of the beam and atomic detuning as I_0/Δ , (see Eq. (2.7)).

In the context of atomic trapping, it is the detuning Δ between the driving frequency and the atomic transition what determines whether the resulting forces pull the atom towards the maxima (red-detuned) or the minima (blue-detuned) of the intensity profile. In either case, atoms reduce their potential energy by being placed at the minima of the induced potential, which receives the name of *sites* of the lattice and are separated by a distance $a = \lambda/2$.

4.1.1 Dimensionality

A rich variety of geometries is possible when considering additional incoming fields. For example, one can extend the one dimensional potential in Eq. 4.1 to two and three dimensions by adding additional pairs of laser beams on these extra axes. Interference patterns would however appear if these lasers were coherent with each other. To prevent this, one can use orthogonal polarization for beams in different directions or lasers whose polarization axes rotate at different frequencies. Alternatively, it is also possible to rely on slightly, but sufficiently different driving frequencies, so that any possible interference pattern disappears when time averaging [137].

Manipulating the direction, phase, intensity, frequency and polarization of the incoming beams, one can virtually engineer any desired lattice geometry (Kagome [138], incommensurate [139], moire [140]...), even dynamically. In particular, using a sufficiently large confining potential in one direction of a 3D (2D) optical lattice one can effectively bring all relevant energies of the system below the energy needed to create an excitation in this trap, effectively creating an array of independent 2D (1D) lattices. In connection with the periodic potentials appearing in, e.g., crystalline structures, this offers a clean playground to explore phenomena associated to condensed matter Hamiltonians. As compared to them, the engineered optical lattice does not support phononic modes that may distort the potential, and the presence of defects is negligible.

4.2 Non-interacting particles in periodic lattices

In the following, we will derive a minimal model for the dynamics of atoms trapped in periodic optical potentials. This simplified description in terms of localized wavefunctions will allow us to derive most of the salient properties of the system, and will evidence the close connection between the resulting dynamics and relevant Hamiltonians appearing in areas such as condensed matter physics.

Indeed, one of the of the main lessons extracted from solid state physics is that electrons moving in periodic potentials are well described by energy bands. As opposed to free space, their spectrum is not continuous, but forbidden regions appear as a consequence of the interaction between the electrons and periodically distributed atoms of the material. Inspired by this understanding, an analysis based

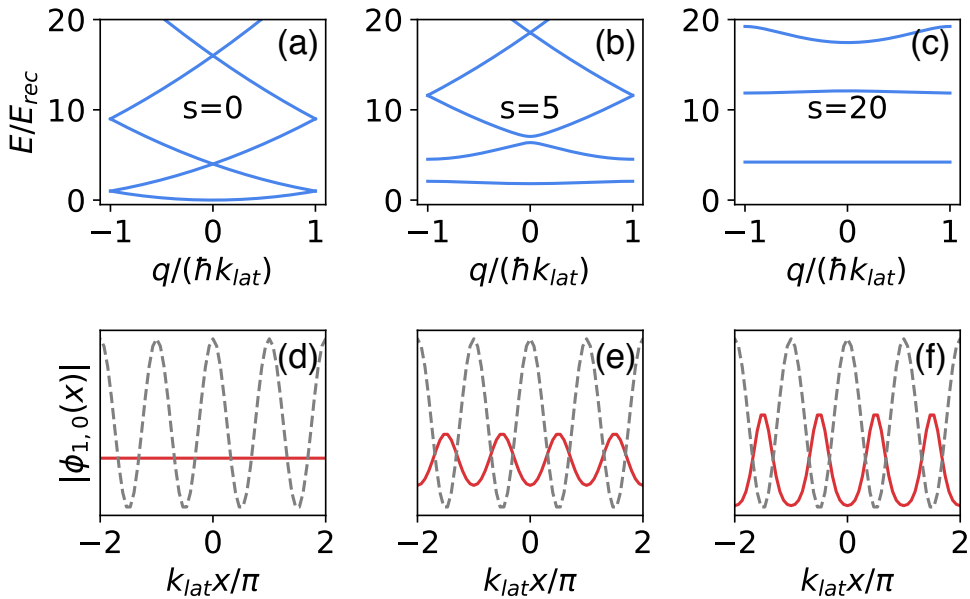


FIGURE 4.1: (a-c) Dispersion relation of an atom in a periodic potential for increasing depth of the lattice, $s = V_D / E_{\text{rec}}$. (d-f) Lowest energy Bloch function associated to quasimomentum $q = 0$ (red line). As the lattice depth increases from $s = 0$ (a,d) to $s = 20$ (c,f), atomic population concentrates at the minima of the lattice, represented in dashed grey lines as a reference. Numerically, it is calculated by expanding $V(r)$ and $u_{n,q}(r)$ on its first Fourier components with momenta $\alpha \cdot (2k)$, for $\alpha = -\alpha_{\text{max}}, \dots, \alpha_{\text{max}}$ [141], and restricting to $\alpha_{\text{max}} = 5$ already provides good convergence when only interested for the lowest band.

on Bloch theory can provide a good description of the effects that appear in atoms trapped in optical lattices.

4.2.1 Bloch functions and band structure

In order to derive these bands, let us characterize the states emerging in the single-particle sector due to the periodic potential $V_{\text{lat}}(\mathbf{r})$. Since $V_{\text{lat}}(\mathbf{r} + \mathbf{R}) = V_{\text{lat}}(\mathbf{r})$ for $\mathbf{R} = \sum_{\alpha \in \{x,y,z\}} n_{\alpha} \mathbf{a}_{\alpha}$, where $\mathbf{a}_{\alpha} = a_{\alpha} \mathbf{u}_{\alpha}$, $n_{\alpha} \in \mathbb{Z}$, and a_{α} is the lattice spacing in direction α . Now, we can use the Bloch-theorem to write the single-particle eigenstates $\hat{H}\phi_{n,\mathbf{q}}(\mathbf{r}) = \varepsilon_{n,\mathbf{q}}\phi_{n,\mathbf{q}}(\mathbf{r})$ of $\hat{H} = -\hbar^2 \nabla^2 / (2m) + V_{\text{lat}}(x)$ as follows:

$$\phi_{n,\mathbf{q}}(\mathbf{r}) = u_{n,\mathbf{q}}(\mathbf{r})e^{i\mathbf{q}\mathbf{r}}, \quad (4.2)$$

where \mathbf{q} is the quasimomentum in the reciprocal space, $u_{n,\mathbf{q}}(\mathbf{r})$ is a function with the same periodicity as $V_{\text{lat}}(\mathbf{r})$, and n is denoting the index of the energy band $E_n(\mathbf{q})$. Note that quasimomenta is only unique up to a vector of the reciprocal lattice, \mathbf{k} , which allows us to restrict \mathbf{q} to the first Brillouin zone.

The properties of these functions are highly determined by the depth of the potential. This is commonly expressed in terms of the recoil energy of the atom,

$$E_{\text{rec}} = \frac{\hbar^2 k^2}{2m}, \quad (4.3)$$

which defines the kinetic energy imprinted by a single incoming photon, where m is the atomic mass. The depth of the optical lattice is then typically expressed through the dimensionless quantity, $s = V_D/E_{\text{rec}}$. In Fig. 4.1(a-c) we illustrate the band structure associated to different potential depths for a 1D sinusoidal potential.

For vanishing depth [(a), $s = 0$], we observe that there are no gaps and the spectrum consists of free particles moving in a parabolic dispersion relation defined by q . As the lattice depth increases (b), this dispersion is no longer quadratic and increasing gaps appear, reducing the band widths. In the limit of very deep lattices [(c), $s \gg 1$], the spectrum is nearly degenerate in q and energy levels converge to the discrete levels of a quantum harmonic oscillator localized at each lattice site.

In Fig. 4.1(d-f) we represent the lowest-energy Bloch function for quasimomentum $q = 0$. For a vanishing lattice (a), it just corresponds to a free-wave. As the strength of the optical lattice dominates kinetic energy (b-c), its wavefunction concentrates around the minima of the lattice, while still being delocalized over the entire system. Note that for two and three dimensional sinusoidal potentials, the problem is separable in each direction. Therefore, Bloch functions on each dimension can be calculated separately, and the energy of the band is the sum of the independent contributions.

4.2.2 Wannier functions

As we have just observed, atomic wavefunctions concentrate at the potential minima of the lattice in the limit where the trapping potential depth is much larger than the recoil energy ($s \gg 1$). While Bloch functions (4.2) delocalize over the entire lattice, it will be useful to introduce a description based on Wannier functions localized in each lattice site when calculating local properties. The Wannier function of a site \mathbf{j} for the n -th band can be obtained from $\phi_{n,\mathbf{q}}(\mathbf{r})$ as follows:

$$w_{n,\mathbf{j}}(\mathbf{r}) = \frac{1}{\sqrt{N}} \sum_{\mathbf{q} \in \text{BZ}} \phi_{n,\mathbf{q}}(\mathbf{r}) e^{-i\mathbf{j}\mathbf{q}} \quad (4.4)$$

where N is the total number of sites and \mathbf{q} runs over the first Brillouin zone.

In Fig. 4.2 we represent the Wannier function associated to the lowest energy band. For small lattice depth (a,b), two side lobes are visible, indicating a non-vanishing probability of finding the atom in the adjacent site. As depth increases (c), these wings are exponentially suppressed, reducing the tunneling to adjacent sites and adopting a Gaussian-like shape centered at individual sites, as it occurs for the eigenfunctions of a quantum harmonic oscillator.

Let us now remind several properties of these functions:

- Using the properties of the Bloch modes of Eq. (4.2), it can be seen that $w_{n,\mathbf{j}}(\mathbf{r}) = w_{n,0}(\mathbf{r} - \mathbf{j})$. That is, the Wannier functions between the different sites only differ on a lattice translation.
- The Wannier functions depends on the choice of the Bloch phase in Eq. (4.2), but for simple Bravais lattice like the cubic one, it can always be chosen such that $w_{n,\mathbf{j}}(\mathbf{r}) \in \mathbb{R}$ [142, 143].

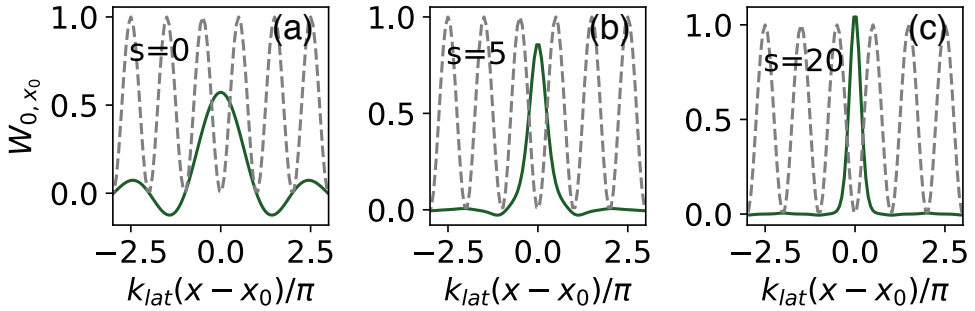


FIGURE 4.2: Wannier function associated to the lowest band of a periodic potential for increasing depth of the lattice, ranging from $s = 0$ (a), to $s = 20$ (c).

- The Wannier functions form a complete basis of space, i.e,

$$\int d\mathbf{r} w_{n,j}(\mathbf{r}) w_{n',j'}(\mathbf{r}) = \delta_{nn'} \delta_{j,j'}. \quad (4.5)$$

- As the lattice potential is separable in the three directions, the Wannier function can be written: $w_{n,j}(\mathbf{r}) = w_{n,j}(x)w_{n,j}(y)w_{n,j}(z)$.
- Finally, in the strong-confinement limit, $s \gg 1$, atoms only probe the positions close to the minima. There, the periodic potential (4.1) can be expanded as an harmonic trap, $V_{\text{lat}}(\mathbf{r}) = V_D \pi^2 r^2 / d^2$, where $r = |\mathbf{r}|$. This allows one to obtain an analytical expression for the Wannier functions in terms of the eigenstates of an harmonic potential with trapping frequency,

$$\omega_{t,\alpha} = \frac{2\sqrt{V_D E_{\text{rec}}}}{\hbar}, \quad (4.6)$$

with $\alpha = x, y, z$, which provides an energy estimate for the energy separation between the different bands appearing in the structure.

While we have focused so far on a description of non-interacting particles, the use of Wannier functions can also provide a good description of interacting particles deeply trapped in optical lattices. In the following, we will introduce the properties of gases formed by interacting bosons, and the natural tight-binding description that arises for deep lattices.

4.3 Interacting atoms: Bose-Einstein condensates

When several atoms are trapped in the same lattice, one also needs to consider the interactions that arise between them. It can be difficult to capture the exact manner two atoms interact depending on their relative separation. However, in the limit of low energy finite-range collisions, they can be well characterized by the leading s -wave scattering amplitude, a_s . This allows us to describe the physics of the system by simply adjusting our model to have the same scattering length as the exact atom-atom interaction [144].

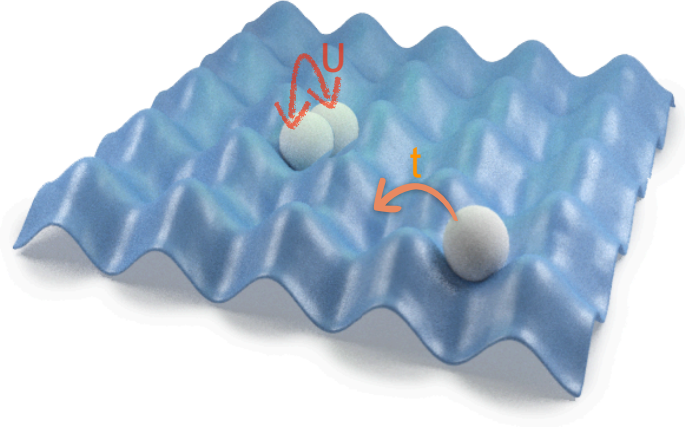


FIGURE 4.3: Schematic representation of a 2D optical lattice (blue) where trapped atoms (white) can tunnel to neighbor sites with rate t , and on-site energy U is associated to the double occupation of a lattice site.

In the grand canonical ensemble, the Hamiltonian describing bosonic atoms in an external trapping potential can be written in second quantization as,

$$\begin{aligned} \hat{H}_b = \int d\mathbf{r} \hat{\Psi}^\dagger(\mathbf{r}) \left(-\frac{\hbar^2}{2m} \nabla^2 + V_{\text{lat}}(\mathbf{r}) + V_{\text{aux}}(\mathbf{r}) \right) \hat{\Psi}(\mathbf{r}) \\ + \frac{2\pi a_s \hbar^2}{m} \int d\mathbf{r} \hat{\Psi}^\dagger(\mathbf{r}) \hat{\Psi}^\dagger(\mathbf{r}) \hat{\Psi}(\mathbf{r}) \hat{\Psi}(\mathbf{r}) \end{aligned} \quad (4.7)$$

where $\hat{\Psi}^\dagger(\mathbf{r})$ is a bosonic field operator creating an atom in position \mathbf{r} and $V_{\text{aux}}(\mathbf{r})$ denotes any additional external slowly varying potential.

When the gas is trapped in a deep lattice, the projection of this Hamiltonian in the localized Wannier functions centered at the different sites of the optical lattice leads to one of the simplest non-trivial models for interacting bosons in a periodic lattice: the BH Hamiltonian, which we will sequentially introduce in the following.

4.3.1 Tight-binding Hamiltonian for deep lattices

When cold atoms are placed in a sufficiently deep optical lattice, one typically assumes that the atoms are prepared in their motional ground state and interband transitions are negligible [38, 39, 145]. In this limit, the atomic field operator $\hat{\Psi}(\mathbf{r})$ can be expanded as a sum of wavefunctions localized at the sites of the optical lattice,

$$\hat{\Psi}(\mathbf{r}) = \sum_{\mathbf{j}} w_{\mathbf{j}}(\mathbf{r}) \hat{b}_{\mathbf{j}}, \quad (4.8)$$

where we drop the band-index n , and we define the annihilation (creation) operators $\hat{b}_{\mathbf{j}}^{(\dagger)}$ of a bosonic state at site $\mathbf{j} \in \mathbb{Z}^3$, which also obeys commutation rules $[\hat{b}_{\mathbf{i}}, \hat{b}_{\mathbf{j}}^\dagger] = \delta_{\mathbf{i},\mathbf{j}}$. Projecting the atomic Hamiltonian in this basis, one obtains the second quantized Hamiltonian [146]:

$$\hat{H}_b = - \sum_{\mathbf{i}, \mathbf{j}} t_{\mathbf{i}, \mathbf{j}} \hat{b}_{\mathbf{i}}^\dagger \hat{b}_{\mathbf{j}} + \sum_{\mathbf{i}} \varepsilon_{\mathbf{j}} \hat{n}_{\mathbf{i}} + \frac{U}{2} \sum_{\mathbf{i}} \hat{n}_{\mathbf{i}} (\hat{n}_{\mathbf{i}} - 1), \quad (4.9)$$

where $\hat{n}_{\mathbf{i}} = \hat{b}_{\mathbf{i}}^\dagger \hat{b}_{\mathbf{i}}$ counts the number of bosonic atoms in state σ placed at the lattice site \mathbf{i} . Regarding the rest of terms, $t_{\mathbf{i}, \mathbf{j}}$ defines the tunneling between the sites $\{\mathbf{i}, \mathbf{j}\}$, $\varepsilon_{\mathbf{j}}$ a position dependent energy shift caused by the external potential $V_{\text{aux}}(\mathbf{r})$, and U is the on-site interaction that acts whenever two or more atoms occupy the same site, as we detail in the following.

Tunneling to neighboring sites

The strength of tunneling amplitude matrix $t_{\mathbf{i}, \mathbf{j}}$ of Eq. (4.9) is given by¹,

$$t_{\mathbf{i}, \mathbf{j}} = \int d\mathbf{r} w_{\mathbf{i}}(\mathbf{r}) \left[-\frac{\hbar^2}{2m} \nabla^2 + V_{\text{lat}}(\mathbf{r}) \right] w_{\mathbf{j}}(\mathbf{r}). \quad (4.10)$$

In the strong-confinement limit previously discussed, $s \gg 1$, Wannier functions are strongly localized around the minima of the lattice, such that only nearest neighbour contributions appear in practice. The strength of the nearest neighbour hopping terms in a regular lattice, $t \equiv t_{\langle \mathbf{i}, \mathbf{j} \rangle}$, can be estimated by approximating the Wannier functions as a Gaussian of variance $s^{-1/2} k^{-2}$ [147], which gives the result [146],

$$t \approx E_{\text{rec}} \sqrt{\frac{4}{\pi}} s^{3/4} e^{-2\sqrt{s}}, \quad (4.11)$$

The kinetic part of the ultra-cold fermionic atoms in optical lattices is then approximated as,

$$\hat{T}_f = -t \sum_{\langle \mathbf{i}, \mathbf{j} \rangle} \hat{b}_{\mathbf{j}}^\dagger \hat{b}_{\mathbf{i}}, \quad (4.12)$$

which relates to the width of the lowest Bloch band as $4Dt = \max \varepsilon_{0, \mathbf{q}} - \min \varepsilon_{0, \mathbf{q}}$, where D is the dimension of the lattice.

On-site potential

The effect of an external potential $V_{\text{aux}}(\mathbf{r})$ is characterized by a position dependent shift, $\varepsilon_{\mathbf{j}}$, proportional to the intensity of the beam at each of the individual lattice sites. Its expression in terms of the Wannier functions reads as,

$$\varepsilon_{\mathbf{j}} = \int d\mathbf{r} |w_{\mathbf{j}}(\mathbf{r})|^2 V_{\text{aux}}(\mathbf{r}). \quad (4.13)$$

In order to induce the auxiliary potential $V_{\text{aux}}(\mathbf{r})$, one can rely on the intensity-dependent energy shifts experienced by the atom when shine by a detuned laser. Retroreflected beams provide periodic potentials (as used to create the optical lattice),

¹We set the on-site tunneling term $t_{\mathbf{i}, \mathbf{i}}$ as the energy reference because it is a constant energy terms in all sites [146].

and more complex profiles can be obtained by further engineering the light intensity at each site of the lattice. As introduced in page 18, this can be achieved for 1D and 2D systems with an intensity mask that filters an homogeneous beam that is shine orthogonally to the lattice. Digital mirror devices even allow to modulate this mask over time, providing a high tunability of the induced potential [43]. Such control of the light intensity at each site of the lattice is however harder to achieve in three-dimensions, where holographic techniques can be used for this purpose, as we will describe in Section 7.2.

On-site interaction

Finally, we have the scattering interaction caused by atomic collisions in the same lattice site that, for a deep lattice, expands as [146],

$$U = \frac{4\pi a_s \hbar^2}{m} \int d\mathbf{r} |w_j(\mathbf{r})|^4 \approx \sqrt{\frac{8}{\pi}} s^{3/4} k a_s E_{\text{rec}}. \quad (4.14)$$

In the case of collisions between two different types of atoms, the same expression can be derived by replacing the corresponding interspecies scattering length and reduced mass. Note that the scattering length a_s can be either a positive or negative variable [148, 149]. This defines situations where atoms will favourably spread over different lattice sites ($a_s > 0$) or will tend to condensate at the same minima ($a_s < 0$). Feshbach resonances further allow one to experimentally control both the sign and amplitude of a_s by using an external magnetic field, B [150],

$$a_s = a_{\text{bg}} \left(1 - \frac{\Delta_s}{B - B_0} \right). \quad (4.15)$$

Here, a_{bg} denotes the background scattering length, and Δ_s and B_0 are the resonance width and position, respectively, which can be determined experimentally for each pair of colliding atoms.

4.4 Quantum simulators

At this point, one could argue that typical distances in solid-state crystals are of the order of 0.1 nm, while the sites spacing of optical lattices are usually in the order of μm . Also, atoms are much heavier than electrons. As a consequence, in order to map the electronic properties occurring in solid-state at temperatures of hundreds of Kelvin, one needs to cool atoms below a few nK [151, 152]. Remarkably, thanks to the advances in atomic cooling, control and measurement techniques that we reviewed in Chapter 2, single atoms are nowadays easier to observe and manipulate than single electrons are, offering a rich platform to explore problems arising from diverse fields, ranging from condensed matter [40] to high-energy physics [51, 153] or quantum thermalization [154].

4.4.1 Bose-Hubbard Hamiltonian

Historically, simulating the BH model [39],

$$\hat{H}_b = -t \sum_{\langle i,j \rangle} \hat{b}_i^\dagger \hat{b}_j + \sum_i \varepsilon_j \hat{n}_i + \frac{U}{2} \sum_i \hat{n}_i (\hat{n}_i - 1), \quad (4.16)$$

was the first experimental success of cold atoms in optical lattices [40], as it naturally maps to the tight-binding Hamiltonian (4.9) of a repulsive Bose gas in a homogeneous optical lattice.

The competition between the repulsive interaction and the kinetic term of the Hamiltonian leads to a phase transition that was originally studied for the superfluid-insulator transition in liquid helium [155]. On the one hand, a Bose gas is a superfluid that presents long-range coherence. Once in an optical lattice, the restriction of the bosonic dynamics to a nearest-neighbor tunneling leads to a non-trivial situation that distinguishes between two phases.

Superfluid phase

In the limit where tunneling dominates over atom-atom interactions ($t \gg U$), the energy of the system is minimized when all N atoms independently occupy an extended state. This leads to the delocalized single-particle product state,

$$|\Psi_{\text{SF}}\rangle_{U=0} \propto \left(\sum_{i=1}^M \hat{b}_i^\dagger \right)^N |0\rangle, \quad (4.17)$$

that spreads over all M lattice sites and is characterized by long-range phase coherence.

Mott-insulating phase

As the interaction forces dominate ($U \gg t$), fluctuations in the occupation number become energetically unfavourable, and the lowest energy-state is reached for an homogeneous fixed occupation of every lattice site. For a commensurate filling $n = N/M$, this corresponds to,

$$|\Psi_{\text{MI}}\rangle_{t=0} \propto \prod_{i=1}^M \left(\hat{b}_i^\dagger \right)^n |0\rangle. \quad (4.18)$$

The critical ratio U/J where this phase transition occurs has been theoretically analyzed [39, 155] and experimentally observed [40], and is proportional the number of first-neighbours in the lattice. When compared to the gapless superfluid phase, one interesting property of the Mott phase is that an energy gap $\sim U$ opens as one crosses the quantum critical point, separating $|\Psi_{\text{MI}}\rangle_{t=0}$ from any uneven occupation of the lattice sites.

Starting from a superfluid configuration, the Mott-insulating phase can be experimentally prepared by adiabatically increasing the depth of the optical lattice up to values in the order of $s \sim 20$ [40]. A relevant configuration in our work will be the unitary occupation of the lattice $n = 1$, where the number of trapped atoms matches the amount of available lattice sites. While imperfections may appear

during its preparation (empty or double-occupied sites), current experiments are able to achieve unitary fillings of order 99.9% [156].

4.4.2 Generalized Bose-Hubbard models

Current research focuses on extending this successful implementation of the BH model to richer scenarios also accessible in optical lattices. Among others, these investigations include,

- **Different dimensional systems.** By increasing the depth of the lattice in a particular direction, one can restrict the problem into a 2D or 1D scenario [157, 158], where different transition points are expected. Other exotic geometries can also be considered by wisely choosing the beams configuration, including triangular [159–162], Kagome lattices [138, 163, 164] or honeycomb [165] lattices, which allows one to simulate particular crystalline structures where, e.g. Dirac points appear [48, 166].
- **Disordered systems.** Disorder plays a core role in condensed matter, as can prevent the appearance of long-range coherence in the system. This is responsible for effects like the Anderson localization of otherwise superfluid extended states. The engineering of random optical potentials [167, 168] or additional incommensurate ones [139, 169] allows one to explore the transitions between the localized states originated from Anderson localization, and those expected in the Mott insulating phase as the trapping depth increases [170].
- **Internal structure of the atom.** The atomic internal state can determine its trapping depths (and, therefore, tunneling rate), as well as the atom-atom interactions [171]. This defines effective spin Hamiltonians where quantum problems related to magnetism [172, 173], quantum dynamics [174, 175] or lattice gauge theories [51, 153] can be simulated.
- **Extended BH models** Another interesting generalization of Hubbard models is the engineering of atom-atom interactions that extend beyond nearest-neighbor sites, which will be the scope of the second part of this Thesis. In the next Section, we will further motivate its interest, and review some of the strategies followed in state-of-the-art experiments to obtain extended interactions.

4.5 Long-range interactions among trapped atoms

While interactions among atoms sitting in different sites are exponentially suppressed in the case of highly localized Wannier functions ($s \gg 1$), different mechanisms can lead to longer-range interactions. The range and scaling of these interactions can lead to the appearance of metastable states, modifying not only the spectrum, but also the stability of these phases. For example, nearest-neighbor couplings can stabilize checker-board patterns, associated to fractional filling factors [176, 177]. Long-range interactions between ultra-cold atoms are also known to be the source of many exotic many-body phenomena. These include new magnetic [178, 179] or supersolid phases [180–182] that can exist in extended Hubbard models, as well as topologically ordered states [63, 183], or roton spectra [184, 185], that can appear when long-range interactions are tuned.

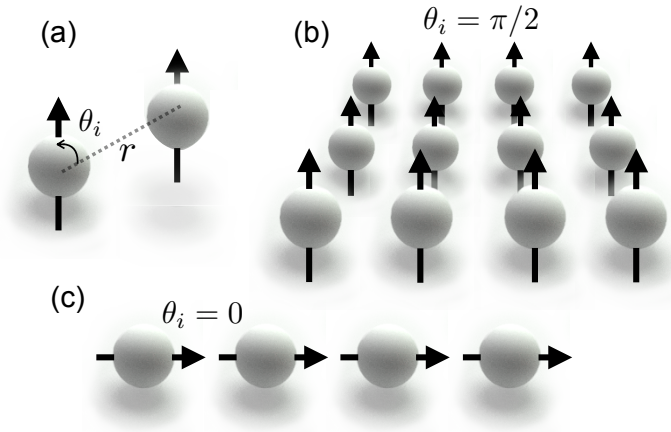


FIGURE 4.4: (a) Schematic representation of two dipoles separated by distance r , and forming an angle θ_i with the line that separates them. (b) 2D array of dipoles oriented with angle $\theta_i = \pi/2$ from the plane that contains them. (c) 1D array of dipoles aligned with the common axis, $\theta_i = 0$.

Long-range interactions in Bose-Fermi mixtures have allowed the observation of soliton trains [186–189], or quantum droplets, originated from the balance between attractive long-range (dipolar) and repulsive contact interactions [190, 191], which have also been observed with purely contact interactions [192]. As we will show in Chapters 6 and 7 of this Thesis, long-range interactions experienced by fermionic atoms can also be harnessed to build analog quantum chemistry simulators [1–3]. Unfortunately, these interactions do not appear naturally between neutral atoms, since they generally interact through the (local) elastic collisions introduced in Eq. (4.14). This is the reason why finding ways to engineer and control such long-range atomic interactions is one of the most pressing issues in atomic physics nowadays. Here, we review some of the strategies experimentally available and motivate the approach introduced in the rest of this Thesis.

4.5.1 Dipole interactions

Atoms and molecules with a permanent dipole moment (electric or magnetic) interact with each other through dipole-dipole potentials of the form [193],

$$V(\mathbf{r}_1, \mathbf{r}_2) = \frac{V_{DD}}{r^3} (\cos \theta_{12} - 3 \cos \theta_1 \cos \theta_2), \quad (4.19)$$

where $r \equiv |\mathbf{r}_1 - \mathbf{r}_2|$ is the distance between the two particles and $\theta_{12} = \theta_1 - \theta_2$ represents the angle difference between the two dipoles, where θ_i is the angle formed by the dipole and the line connecting their centers [see Fig. 4.4(a)].

While the overall potential scales as $\sim r^{-3}$, these anisotropic interactions highly depend on the relative orientation of the dipoles. Homogeneous interactions can still be identified in some reduced geometries. For example, atoms in a plane with their dipole moment equally oriented normally to the plane experience an homogeneous repulsive potential V_{DD}/r^3 [see Fig. 4.4(b)]. Similarly, atoms in a one-dimensional array with dipolar moments aligned with their common axis attract each other with a potential, $2V_{DD}/r^3$ [see Fig. 4.4(c)].

The strength of these interactions is determined by the dipole moments involved, $V_{DD} = \mu_1\mu_2/(4\pi\epsilon_0)$, whose magnitude highly depends on the physical origin of the dipole [194], as we will discuss now.

Polar molecules

In heteronuclear molecules, one can find permanent electric dipole moments in the order of a few Debyes ($\mu \sim 1D \sim 10^{-30} \text{ C} \cdot \text{m}$). This leads to dipole interactions that can exceed typical scattering forces in cold atomic gases by two orders of magnitudes. Current techniques enable to cool down molecules to ultralow temperatures, which has been a longstanding challenge due to the complexity of the molecular internal structure introduced by its rotational and vibrational modes [195]. At the same time, these additional degrees of freedom, combined with the tunability accessible in optical lattices and the non-linearity introduced by long-range interactions, offer promising perspectives for their use in quantum simulation and computation [196].

Paramagnetic atoms

Atomic species like Cr or Dy can have large magnetic moments of order $5 \mu_B$ in the presence of a magnetic field. While these magnetic forces are typically weaker than electric dipole or contact interactions [197], the interplay with optical lattices at large filling allows for non-negligible effects, where magnetic dipole exchange enters as an additional degree of freedom. Using ^{52}Cr [198, 199] or ^{168}Er [200], the role played by the spin axis and long-range interactions has been explored in many-body problems, such as the extended BH model.

Rydberg atoms

Atoms in a largely excited state typically have their valence electron hundreds of Amstrongs away from their nuclei. This induces a large electric dipole that scales quadratically with the principal quantum number n of this electron, which results into dipole interactions $V_{DD} \propto n^4$ [201]. The resulting energy shift caused by the dipolar potential once a Rydberg atom is populated can prevent a second atom from getting excited within a range of influence in the order of $10 \mu\text{m}$. This is the, so-called, Rydberg blockade radius [202]. For dense atomic clouds, hundreds of atoms fit within this blockade radius, and such a strong nonlinear behaviour offer interesting possibilities in the construction of quantum gates [203, 204], memories [205, 206] or single-photon sources [207]. Its combination with optical lattices [208, 209] or tweezers [69] allows one to further control the atomic positions enabling the simulation of fundamental many-body models.

The main source of decoherence introduced by this Rydberg mechanism is the reduced lifetime of the Rydberg states, of the order of $100\text{s } \mu\text{s}$. A way of overcoming this limitation is the use of Rydberg dressing techniques which are currently being pursued experimentally [210].

4.5.2 Ionic systems

While in this Thesis we will focus on manipulating neutral atoms, it is worth mentioning the interesting physics that appears when an ensemble of ions is cooled

to temperatures below mK. Being charged particles, strong electrostatic forces can be imparted through external electric field. However, Gauss's law prevents a stable ion trap from being based on static electromagnetic fields (Earnshaw's theorem). This can be circumvented by other trapping techniques. For example Paul traps rely on time-averaged oscillating electric fields, while Penning traps uses a combination of electric and magnetic fields [27, 28]. Once at equilibrium, this trapping potential is balanced by the Coulomb repulsion between the ions, defining crystal structures whose collective vibrational modes describe a quantum motional degree of freedom widely used for quantum simulation. Increasing the trapping force in one or two of the directions, one can further constrain the trapped ensemble, so that 1D or 2D crystal of hundreds of atoms are formed. The coupling between the internal state of these ions to the motional degrees of freedom of the crystal leads to an effective spin-spin interactions, $\sum_{i,j} J_{ij} \hat{\sigma}_i^\dagger \hat{\sigma}_j$, that exhibits a long-range scaling $J_{ij} \propto |\mathbf{r}_i - \mathbf{r}_j|^{-\alpha}$ with a power-law that can be tuned between values $0 < \alpha < 3$ [211, 212]. Such an experimental tunability allows one to study the role that long-range interactions can have in quantum phenomena ranging from quantum magnetism [57] to quantum transport or thermalization [56].

Ions in optical lattices

Going beyond this common trapping, optical dipole traps have recently been adapted to ions [213]. In this scenario, Coulomb forces are typically orders of magnitude larger than optical forces, and any stray electric field needs to be detected and compensated [214]. The extension to optical lattices benefits from the scalability and versatility of these platforms [215], and allows to defeat the temperature limits imposed by micromotion in electrostatic traps [216], while still allowing for trapping lifetimes of 3 s nowadays [217], comparable to atoms under similar conditions.

Because of strong Coulomb repulsion, ions in optical lattices are typically separate by many sites [218], and the interplay of this long-range interaction with a periodic potential can lead to a quantum phase transition [219]. The motional control of these ions also constitutes an interesting platform for digital quantum simulation [220, 221] and, choosing a common lattice spacing, hybrid ion-atom systems can also be engineered [222]. Introducing this ionic array in an optical cavity, further allows to engineer the range of the arising interactions through photon-mediated effects [223], as we will introduce in the following.

4.5.3 Engineered photon-mediated interactions

One of the first lessons in electromagnetism is that a virtual photon exchanged between two charged particles can induce a long-range interaction between them. The more separated they are, the more unlikely it is for this mediating photon to propagate from one particle to the other, which translates into Coulomb forces that decay with the distance and whose scaling highly depends on the media the mediator propagates through.

Regarding neutral atoms, photons emitted by an excited state rarely interact with another atom before decaying into free-space, which is the origin of weak Van-der-Waals forces, $\sim r^{-6}$. However, by controlling the environment atoms are coupled to, one can manipulate this process, enhancing the probability that an emitted photon reaches other atoms and gaining a rich tunability of the resulting interactions [72].

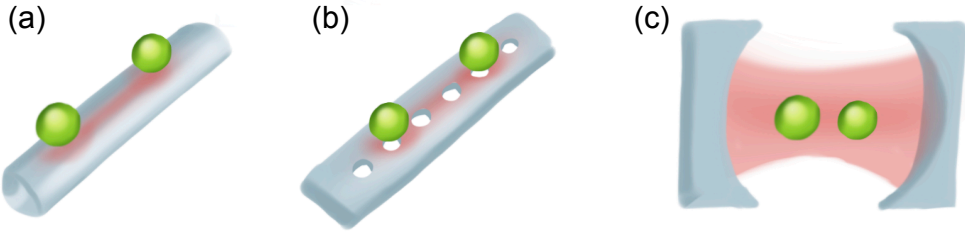


FIGURE 4.5: Schematic representation of the atom-atom interaction mediated by (a) an optical fibre, (b) a photonic crystal, (c) a Fabry-Perot cavity.

Some of the structures previously introduced can then be used to mediate atom-atom interactions.

Nanophotonic structures

As introduced in Sec. 2.2.4, atoms coupled to the evanescent field of a nanophotonic structure can defeat the diffraction limit, offering an interesting opportunity for light-matter coupling and, therefore, atom-atom interactions mediated by light [see Fig. 4.5(a)]. Being trapped so close to its surface (typically ~ 200 nm), the decay of an atom into a **fibre** can in principle represent $\sim 30\%$ of the total atomic emission [224], while ratios one order of magnitude smaller are found in current experiments [225, 226]. This decay allows for an effective infinite-range spin-spin interaction that is dictated by the separation between atoms in positions x_i and x_j through the phase accumulated by the mediating photon, $\propto \exp(ik_0|x_i - x_j|)\hat{\sigma}_j^\dagger\hat{\sigma}_i$, where k_0 is the wavevector that better couples to the atomic transition [227]. This is responsible for collective effects, including superradiant emission or nearly perfect reflectance of the fibre, which is highly influenced by the accumulated phase between the atoms [228–230].

Some of the challenges of this interaction is that coherent spin exchange cannot be decoupled from collective dissipative processes. Applications in quantum information or quantum simulation would highly benefit from the ability to further engineer the dispersion relation of these fibres, which is one of the main opportunities offered by **photonic crystals** once a periodic distribution of defects is tailored [see Fig. 4.5(b)]. Similarly to electrons propagating in periodic materials, the resulting dispersion relation shows a rich band structure, with band-gap frequencies at which photons cannot propagate [231]. This offers an interesting perspective from the point-of-view of mediated interactions. For atomic transitions tuned inside a band-gap of the structure, photon propagation inside the crystal is overall exponentially suppressed. When this frequency is close enough to the band-edge, a significant propagation between nearby atoms is still possible before these exponential tails appear [88, 232], allowing for an effective spin-spin exchange interaction over long distances where fundamental many-body problems can be addressed [233].

Optical cavities

Among the long-range interactions mediated by photons, we should finally point to the infinite-range interactions appearing in optical cavities [see Fig. 4.5(c)]. As

introduced in Section 2.2, the numerous round-trip photons experience in high-cooperativity cavities allow one to effectively couple all atoms dressed by a cavity mode. The combination with optical lattices allows one to explore the competition between short-range interactions caused by on-site collision and the long-range interaction mediated by the cavity mode, where collective effects can stabilize self-organized supersolid phases [234]. Recently, the interplay of this infinite-range interaction with a magnetic field gradient aligned along the cavity axis has enabled further tuning the distance-dependence of interactions in motionally fixed atomic arrays by temporally modulating the intensity of the drive field [235], which opens a new avenue for quantum simulation.

4.6 Outlook: towards long-range interactions mediated by atoms

In Table 4.1 we summarize the different strategies introduced in Section 4.5 to induce long-range interactions among atoms trapped in optical potentials. Their scaling ranges from the all-to-all forces present in cavities, to exponentially suppressed interactions for atoms tuned at the band-gap of photonic crystals. The strength of these atom-atom interactions at an optical distance of 500 nm is also diverse, ranging from a few Hz for the case of weak dipole interactions appearing in paramagnetic atoms, to several GHz in the case of strong Rydberg or ionic forces.

Interactions		Scaling	Nearest-neighbor strength V_1/h
Dipole interactions	Polar molecules	$\sim r^{-3}$	~ 1 kHz
	Paramagnetic atoms	$\sim r^{-3}$	~ 1 Hz [200]
	Rydberg atoms	$\sim r^{-3}$	~ 0.1 GHz ($n = 20$) ~ 100 GHz ($n = 40$) [201]
Ionic interactions	Ion-ion	$\sim r^{-1}$	~ 100 GHz
	Ion-neutral atom	$\sim r^{-4}$	~ 100 Hz [222]
Photon-mediated	Optical nanofibre	$\sin(kr)$	~ 0.1 -1 MHz [226]
	Photonic crystals		~ 10 MHz [85]
	Optical cavities	$\sin(kr)$	$\sim 0.1 - 1$ KHz [235]

TABLE 4.1: Summary of the long-range scalings presented in Section 4.5 for different mediating mechanisms. The nearest-neighbor strength is estimated for an interatomic separation of 500 nm.

The second part of this Thesis will be devoted to engineer in a lattice atom-atom forces capable of simulating the electronic repulsion present in a chemical bound. As we will see, this translates into a number of requirements,

- The simulated atoms should be fermionic to emulate the statistics of electronic systems.
- These atoms should be able to tunnel from one lattice site to another to mimic the electron dynamics.

- Every pair of atoms should repel each other following a long-range Coulomb-like scaling that decays inversely with their separation, as $1/r$.
- In order to mimic the natural ratios between the kinetic and repulsive energy of electrons within a finite lattice, the strength of this repulsion needs to be comparable to the tunneling rate, which is typically in the order ~ 100 kHz.

One can see, however, that none of the systems above satisfies all these conditions. Only ions provide the correct Coulomb-like scaling, but their strong repulsive forces highly exceeds the kinetic energy-scales of atoms trapped in optical lattices, and ordered arrays beyond 1D have not yet been reached. Driven strategies of cavity systems, such as Ref. [235], may lead to the desired scaling by considering an appropriate choice of the input field, but the tunneling responsible for the fermionic dynamics is not present in such system.

In the second part of this Thesis, we will investigate whether contact interactions with an additional atomic species can mediate long-range interactions among trapped atoms that satisfy the four desired features presented above. In particular,

- In Chapter 5, the additional atomic species will be a Fermi gas trapped in a harmonic potential, which leads to an oscillatory effective potential that can be highly tuned by both the geometry of the trap or the use of additional laser fields.
- In Chapter 6, we will consider additional bosonic atoms trapped in an optical lattice as a mediator. By appropriately accessing some of its internal levels, we will show that different effective interactions can be obtained, ranging from polynomially decaying to an exponential scaling with a tunable decay length.
- In Chapter 7, we will show that the infinite range interactions that can be mediated by an additional cavity leads to an effective Coulomb-like repulsive potential that satisfies the four conditions needed for electronic simulation. We will derive the equivalence between this system and electronic configurations in chemistry, and numerically benchmark its performance with simple molecular configurations.

Chapter 5

Tunable long-range interactions mediated by a Fermi gas

” Fui distraída todo el camino, pensando en que siempre se mueve uno en el mismo círculo de personas por más vueltas que parezca dar.

— Carmen Laforet
(Extract from "Nada")

We have just introduced how the exchange of mediating particles can lead to the long-range interactions that appear in nature. Here we explore the orthogonal direction that consists in using fermionic atoms in atomic mixtures as mediators [178, 180, 181, 185, 188, 236–244]. Such fermion-mediated interactions have been predicted [178, 241, 245] to lead to the Ruderman-Kittel-Kasuya-Yosida (RKKY)-type interactions appearing in solids [246–248], which have a power-law, oscillating nature, fixed by the dimensionality and density of the Fermi gas. With the recent experimental observation of these interactions [188, 243], a timely question that has been scarcely explored [185] is how they can be further tuned to explore new phenomenology with them.

In this Chapter, we take advantage of the flexibility offered by ultracold atomic platforms to control the range and shape of long-range fermion-mediated interactions, going beyond the conventional RKKY ones encountered in solid-state systems. This allows us to design a quantum simulation toolbox that can be used to prepare, for instance, frustrated phases that are not accessible using other approaches. This Chapter is organized as follows. First, in Section 5.1 we review how to derive the effective fermion-mediated RKKY interactions for a Fermi-Bose mixture of ultracold atoms. In Section 5.2, we introduce an additional optical potential for the Fermi gas and show how the range of the interactions can be interpolated from a power law to an exponential decay by tuning the ratio between the periodic potential and the confining harmonic trap. This also allows one to select the ratios between interactions at different distances within a non-vanishing range. We then show how, for a hardcore bosonic chain immersed in the fermionic cloud, the resulting interactions can be used to prepare frustrated phases with non-trivial topological properties. Finally, we consider in Section 5.3 an extra tuning knob by continuously changing the dimensionality of the cloud using different trapping

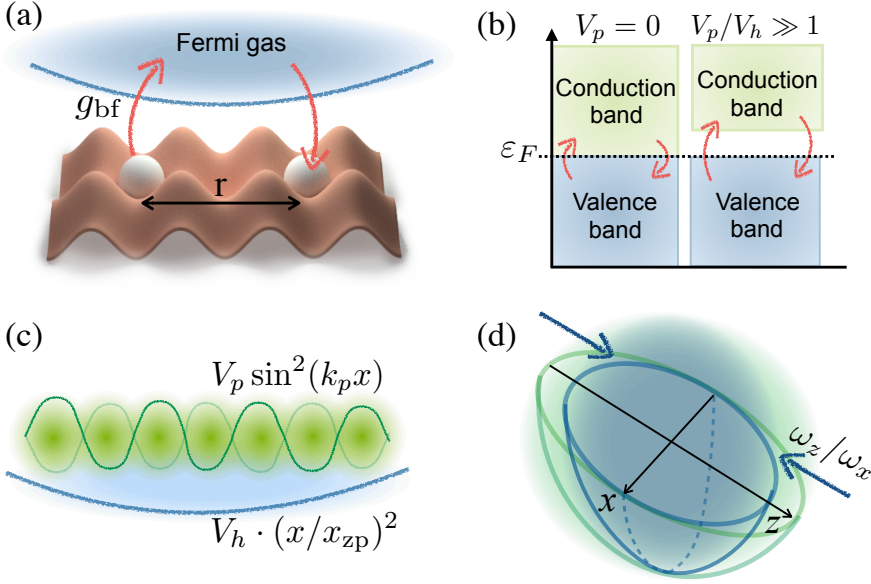


FIGURE 5.1: (a) Two bosonic atoms (white) separated by distance r and trapped in an optical lattice (red) experience an effective long-range interaction mediated by a Fermi gas trapped in an harmonic potential (blue). (b) The contact Bose-Fermi interactions (g_{bf}) virtually populates the conduction band of the Fermi gas. (c) An additional oscillatory potential induces a gap between the valence and conduction gap, exponentially damping the mediated interactions. (d) By controlling the strength of the trapping potential in an orthogonal direction, ω_z/ω_x , one can continuously tune the dimension of the Fermi gas from 1D to 2D, introducing additional modulating frequencies as will be shown in Fig. 5.4.

intensities in each spatial direction. As we will illustrate, this control allows one to further tune the interaction ratios.

5.1 Effective fermion-mediated interactions

Let us consider an atomic mixture as depicted in Fig. 5.1(a), where one species corresponds to non-interacting spinless fermions trapped by an harmonic potential,

$$V(x, y, z) = \frac{m_f}{2} \left[\omega_x^2 x^2 + \omega_y^2 y^2 + \omega_z^2 z^2 \right]. \quad (5.1)$$

The fermionic Hamiltonian reads as, $\hat{H}_f = \sum_n \varepsilon_n \hat{c}_n^\dagger \hat{c}_n$, where $\hat{c}_n^{(\dagger)}$ is the (creation) annihilation operators associated with the n -th eigenstate of this oscillator, with energy ε_n . For concreteness, we assume that the other atomic species is bosonic and it is trapped in an optical lattice, $V_{\text{lat}}(\mathbf{r})$, with fixed lattice spacing d . While Pauli blocking prevents s-wave interactions among spin-polarized fermion, one can still account for boson-boson and boson-fermion collisions. This leads to a bosonic Hamiltonian of the form,

$$\hat{H}_b = \int d\mathbf{r} \hat{\phi}^\dagger(\mathbf{r}) \left(\frac{-\hbar^2}{2m_b} \nabla^2 + V_{\text{lat}}(\mathbf{r}) \right) \hat{\phi}(\mathbf{r}) + g_{bb} \int d\mathbf{r} \hat{\phi}^\dagger(\mathbf{r}) \hat{\phi}^\dagger(\mathbf{r}) \hat{\phi}(\mathbf{r}) \hat{\phi}(\mathbf{r}), \quad (5.2)$$

and a Bose-Fermi density-density interaction,

$$\hat{H}_I = g_{bf} \int d\mathbf{r} \hat{\phi}^\dagger(\mathbf{r}) \hat{\psi}^\dagger(\mathbf{r}) \hat{\phi}(\mathbf{r}) \hat{\psi}(\mathbf{r}) \quad (5.3)$$

where the field operator $\hat{\phi}(\mathbf{r})$ [$\hat{\psi}(\mathbf{r})$] describes the annihilation of a boson [fermion] and g_{bb} (g_{bf}) is the bosonic (interspecies) coupling constant, which is experimentally tunable through magnetic Feshbach resonances [see Eq. (4.15)].

Below the Fermi temperature, the N fermionic atoms are occupying all states up to the Fermi energy, $\varepsilon_F = \varepsilon_N$, and the state can then be written as $|\Omega\rangle = \prod_{n=1}^N \hat{c}_n^\dagger |0\rangle$. In the regime where fermionic timescales are much faster than the bosonic ones and their interaction is weak, one can take $\hat{H}_0 = \hat{H}_b + \hat{H}_f$ as the unperturbed Hamiltonian and \hat{H}_I as a perturbation, obtaining an effective potential for the bosons [178],

$$\hat{H}_{\text{eff}} = \varepsilon_F + \hat{H}_b + G \iint d\mathbf{r} d\mathbf{r}' F_{\mathbf{r},\mathbf{r}'} \hat{\phi}^\dagger(\mathbf{r}) \hat{\phi}^\dagger(\mathbf{r}') \hat{\phi}(\mathbf{r}) \hat{\phi}(\mathbf{r}'), \quad (5.4)$$

where $G = 2m_f g_{bf}^2 k_F^4 / \hbar^2$ and $x_{\text{zp}} = [\hbar / (2m\omega_x)]^{1/2}$. Here, the last term arises from the second-order perturbation $\sum_{m \neq i} |\langle m | \hat{H}_I | i \rangle|^2 / (E_m - \varepsilon_F)$, where the initial state $|i\rangle = |\Omega\rangle |\{r_b\}\rangle$ belongs to the ground-state manifold of \hat{H}_0 for bosonic atoms placed in positions $\{r_b\}$, and $|m\rangle = \hat{c}_m^\dagger \hat{c}_n |\Omega\rangle |\{r_b\}\rangle$ is a particle-hole excited state outside the manifold, with energy E_m . Note that due to the conservation of fermionic parity, fermions need to be exchanged twice to generate a potential, unlike photons, which can be exchanged only once. This has important implications for the sign and shape of $F_{\mathbf{r},\mathbf{r}'}$ [249]. Interestingly, this mediated potential only depends on the bosonic separation $F_{\mathbf{r},\mathbf{r}'} \approx F(|\mathbf{r} - \mathbf{r}'|)$.

Numerically, this perturbative sum is calculated by considering all possible combinations of hole and particle states that are below and above the Fermi energy, respectively. For a Fermi gas with N atoms trapped in a 1D harmonic potential of frequency ω_x , this can be numerically calculated as,

$$F_{1D}(r) = 2 \sum_{m=0}^{N-1} \sum_{n=N}^{\Lambda} \frac{\varphi_m(0) \varphi_n(0) \varphi_n(r/x_{\text{zp}}) \varphi_m(r/x_{\text{zp}})}{n - m}, \quad (5.5)$$

where Λ is the upper numerical cutoff for energies in the conduction band, and we observe convergence of the infinite sum for $\Lambda \approx 4N$. Here, $\varphi_n(x)$ denotes the wavefunction of the n -th eigenstate of the trap in position x , whose energy for a harmonic trap is $E_n = (n + 1/2)\hbar\omega_x$, and is dictated by [250],

$$\varphi_n(x) = \frac{e^{-(x/2)^2} H_n(x/\sqrt{2})}{(2\pi)^{1/4} \sqrt{2^n n!}}, \quad (5.6)$$

where $H_n(x)$ denotes the Hermite polynomial of order n . To simplify this calculation for high orders n , one can observe in Eq. (5.5) that these wavefunctions only need to be evaluated at the position of the mediated atoms. To facilitate this, one can rely on a recurrence relation that reduces the calculation of $\varphi_n(x)$ for a given n to the evaluation of the lowest order ones. Defining $R_n(x) = H_n(x/\sqrt{2})/\sqrt{2^n n!}$ one

has [251],

$$\begin{aligned} R_0(x) &= 1, \\ R_1(x) &= \sqrt{2}x, \\ R_{n+1}(x) &= \sqrt{\frac{2}{n+1}}xR_n(x) - \sqrt{\frac{n}{n+1}}R_{n-1}(x). \end{aligned} \quad (5.7)$$

This numerical calculation can be directly extended to the 2D case by considering the appropriate energies and states. Since it will be useful to interpret the results of this Chapter, let us now review here the properties of a free Fermi gas with energy dispersion $\varepsilon_{\mathbf{k}}^0 = \frac{\hbar^2|\mathbf{k}|^2}{2m_f}$, which provides a first approximation in the limit $N \gg 1$. Analytical expressions in this limit can be found in all spatial dimensions [247, 252, 253]. For example, in the one-dimensional case ($N\omega_x \ll \omega_{y,z}$), $F(r)$ expands in the limit $k_F r \gg 1$ as [252]:

$$F_{1D}(r) \propto \frac{-1}{k_F r} \left(\cos(2k_F r) + \frac{\sin(2k_F r)}{2k_F r} \right), \quad (5.8)$$

whereas in the two-dimensional case ($\omega_x = \omega_z \ll \omega_y/N$), it expands as [253]:

$$F_{2D}(\mathbf{r}) \propto -\frac{1}{k_F^2 r^2} \left(\sin(2k_F r) - \frac{\cos(2k_F r)}{4k_F r} \right). \quad (5.9)$$

In both dimensions, interactions share some common features: i) the fermion-mediated interactions are attractive in the limit $r \rightarrow 0$, regardless of the sign of g_{bf} . The mean-field intuition is that, for $g_{bf} > (<)0$, the Fermi gas tends to avoid (be attracted to) the bosons, reducing (increasing) the fermionic density, and thus, the bosons feel more attracted to this place. ii) Asymptotically, they lead to longer range interactions $\sim r^{-1}$ (1D) and $\sim r^{-2}$ (2D) than dipolar ones ($\sim r^{-3}$). iii) The interactions oscillate with an effective length inversely proportional to the Fermi momentum, $k_F = \sqrt{2m_f \varepsilon_F}$. Thus, choosing the wavevector of the bosonic optical lattice potential k_L , one can induce (anti-)ferromagnetic interactions if $k_L = (2)k_F$, or incommensurate ones ($k_L/k_F \in I$).

For a sufficiently deep optical lattice for the bosons, only its lowest motional band gets populated. Wannier functions $w_{\mathbf{j}}(\mathbf{r})$ centered at the lattice sites \mathbf{j} become a convenient description for the bosonic fields, $\hat{\phi}(\mathbf{r}) = \sum_{\mathbf{j}} w_{\mathbf{j}}(\mathbf{r}) \hat{b}_{\mathbf{j}}$. Projecting in this basis the effective Hamiltonian (5.4), one obtains an extended BH model,

$$\hat{H}_{\text{eff}} = -t_b \sum_{\langle \mathbf{j}, \mathbf{j}' \rangle} \hat{b}_{\mathbf{j}}^\dagger \hat{b}_{\mathbf{j}'} + \frac{U_b}{2} \sum_{\mathbf{j}} \hat{n}_{\mathbf{j}}^b (\hat{n}_{\mathbf{j}}^b - 1) + \sum_{\mathbf{j}, \mathbf{j}'} v_{\mathbf{j}, \mathbf{j}'} \hat{n}_{\mathbf{j}}^b \hat{n}_{\mathbf{j}'}^b, \quad (5.10)$$

with nearest-neighbor tunneling strength t_b and on-site interaction $U_b = g_{bb} \int d\mathbf{r} |w_{\mathbf{j}}(\mathbf{r})|^4$, where $t_b, \max |v_{\mathbf{j}, \mathbf{j}'}| \ll \hbar\omega_{x,y,z}$ to satisfy the previous perturbative treatment. Here, $\hat{b}_{\mathbf{j}}^{(\dagger)}$ are the (creation) annihilation operators of a bosonic atom on site \mathbf{j} , $\hat{n}_{\mathbf{j}}^b = \hat{b}_{\mathbf{j}}^\dagger \hat{b}_{\mathbf{j}}$ is the bosonic number operator, and the effective

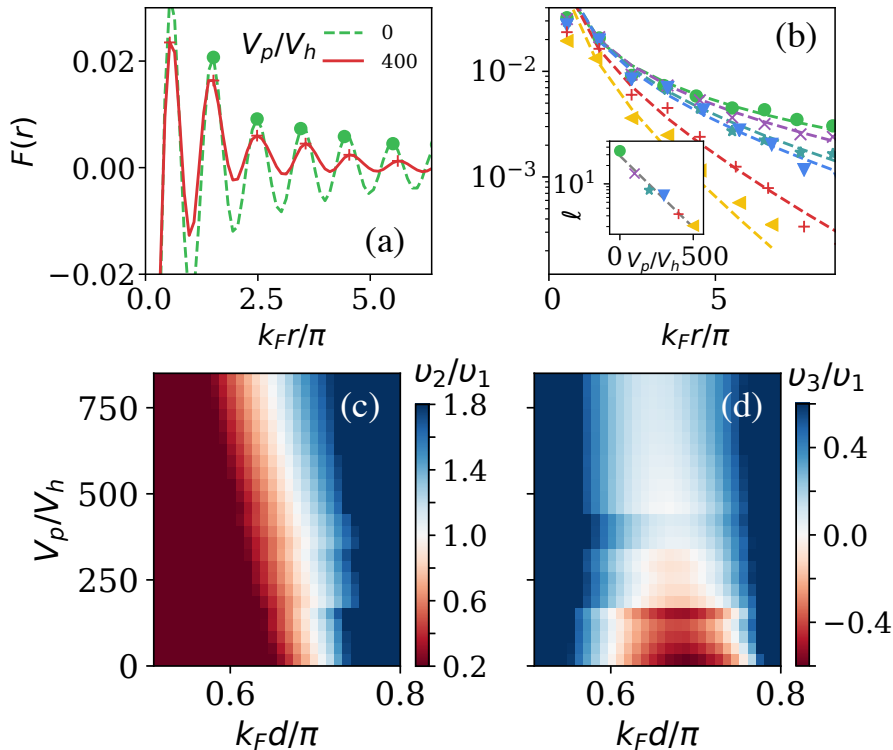


FIGURE 5.2: (a) Effective potential between two atoms in one dimension mediated by a Fermi gas trapped in an harmonic trap with (green) and without (red) an extra periodic trap of strength $V_p/V_h = 400$. Markers indicate the oscillation maxima. (b) Value of the maxima for increasing values of V_p/V_h from 0 (green) to 500 (yellow). The inset shows the decay length ℓ of a fitted Yukawa interaction, $\sim \exp[-k_F r / (\pi \ell)] / r$. (c-d) Strength of the second v_2/v_1 (c) and third v_3/v_1 (d) neighbour interactions as a function of V_p/V_h and the effective lattice spacing $k_F d$. Here, the bosonic Wannier function $w_j(\mathbf{r})$ is approximated by a Gaussian distribution with, $x_{\text{width}}/d = 0.17$, consistent with a lattice wavelength $\lambda = 784.7$ nm for ^{87}Rb [254] (see the main text).

potential $v_{j,j'}$ terms can be obtained from the perturbed potential (5.4) as,

$$v_{j,j'} = G \iint d\mathbf{r} d\mathbf{r}' F(|\mathbf{r} - \mathbf{r}'|) |w_j(\mathbf{r})|^2 |w_{j'}(\mathbf{r}')|^2. \quad (5.11)$$

5.2 Knob I: additional trapping potential

We now show how the range of the effective interactions can be controlled by adding a periodic potential $V_p \sin^2(k_p x)$ to the previous fermionic trap in the 1D case, $V(x) = V_h \cdot (x/x_{\text{zp}})^2$, where $V_h = \hbar\omega_x/4$, as illustrated in Fig. 5.1(c). In the following, we fix the number of fermionic atoms, while we vary the ratio V_p/V_h by modifying the depth of the periodic potential. It is expected that a value of $V_p \neq 0$ opens up a gap in the energy dispersion of the fermionic excitations, introducing a cutoff in the interaction range if the Fermi energy lies within the band gap [see

Fig. 5.1(b)]. This is guaranteed by choosing an appropriate wavevector k_p for the fermionic optical lattice, so that the oscillatory potential maximally hybridizes with the highest occupied state. As this N -th eigenstate of the quantum harmonic oscillator has $N - 1$ nodes extended over an average width $\sqrt{\langle x^2 \rangle} \sim \sqrt{N}x_{zp}$, this translates into the scaling $k_p x_{zp} \sim \sqrt{N}$.

Along the Figures in this Chapter, we have considered parameters compatible with an atomic mixture of fermionic ${}^6\text{Li}$ and bosonic ${}^{87}\text{Rb}$ [255]. In particular, we consider a Lithium Fermi gas formed by $N = 200$ atoms optically trapped with frequency $\omega_x = 2\pi \times 200 \text{ Hz}$, whose associated Fermi temperature is $T_F \sim 1 \mu\text{K}$ [242]. Rubidium atoms are trapped in an optical lattice with wavelength $\lambda = 784.7 \text{ nm}$ and an optical depth that is 12 times larger than recoil energy. Temperatures in the order of $T \sim 100 \text{ nK}$ are experimentally accessible [242], and they only populate the motional ground-state of each lattice site, as required by the tight-binding description. Approximating the resulting Wannier function as a Gaussian, the associated width corresponds to 0.17 times the lattice spacing, $d = \lambda/2$ [254]. As desired, this leads to a tunneling rate that is one order of magnitude smaller than the fermionic trapping frequency ω_x , and the associated tunneling time $\sim 10 \text{ ms}$ allows for hundreds of tunnelling events during the typical coherence times of these experiments. The coherence length for the fermionic system can be estimated as $L_{\text{coh}} = \hbar v_s / (k_B T) \sim 10 \mu\text{m}$ [256], which allows the mediating process to take place over ~ 20 sites of the lattice. Here, $v_s = \hbar k_F / m_f$ denotes the sound velocity for phonons at the Fermi level, and longer coherence lengths could be achieved by further reducing the temperature.

In Fig. 5.2(a), we show the fermion-mediated interaction appearing in a 1D Fermi gas for two values of V_p/V_h corresponding to the pure harmonic case ($V_p/V_h = 0$, dashed green) and a ratio $V_p/V_h = 400$ (solid red). We observe how the periodic potential tends to (exponentially) cut the range of the interaction, inducing a purely positive potential for distances $k_F r > 2$. In Fig. 5.2(b), we plot the maximum relative values of the fermion-mediated interactions at the oscillations for increasing values of V_p/V_h , where it is more evident the transition from a power-law decay for small V_p/V_h , to an exponentially decaying Yukawa-like interaction when V_p/V_h is large. We can therefore control the effective interaction range, given by the exponential decay length ℓ , which is exponentially reduced by V_p/V_h , as $\ell \sim e^{-\alpha V_p/V_h}$ (inset).

Besides, playing with the effective lattice separation of the bosonic species $k_F d$ (which can be controlled through the frequency of the harmonic trap, adjusting k_p accordingly), one can identify diverse choices of induced interactions, as we illustrate in Figs. 5.2 (c-d). There, we see for example that there are regions for V_p/V_h and $k_F d$ (coloured in white) where the potential for the nearest and next-nearest neighbours coincide $v_2 \approx v_1$, while interactions among longer distance atoms are very weak, $v_3/v_1 \approx 0$. This is important because such potentials can be the source of frustrated quantum many-body phases, as we explain below.

5.2.1 Quantum simulation of frustrated phases

To illustrate the last point, we analyze the phase diagram of a 1D chain of hardcore bosons ($U_b/t_b \rightarrow \infty$) whose interactions are mediated by a 1D Fermi gas. The

different phases can be distinguished using the structure factor,

$$S(q) = \frac{1}{L^2} \sum_{i,j} \langle \delta \hat{n}_i^b \delta \hat{n}_j^b \rangle e^{iq(r_i - r_j)}, \quad (5.12)$$

where $\delta \hat{n}_i^b = \hat{n}_i^b - \rho$ and $\rho = 1/L \sum_i \langle \hat{n}_i^b \rangle$ is the bosonic density.

Using a density-matrix renormalization group (DMRG) algorithm [257] with fixed bond dimension $D = 200$, we calculate the ground state of a periodic chain with $L = 60$ sites and half-occupation, $\rho = 1/2$. The choice of parameters in Fig. 5.3 is consistent with the state-of-the-art Bose-Fermi mixtures [242, 243] detailed above. In particular, the interaction among the two atomic species is characterized by a scattering length $a_{\text{bf}} \sim 25 a_B$ [255], which can be externally controlled through Feshbach resonances. This allows for mediated interactions of order, $|v_1| + |v_2| \sim t_b$, as needed for the model studied in this section.

Fig. 5.3(b) shows how, for $V_p/V_h = 0$, $S(q)$ develops a clear peak at a certain value q_0 that varies with $k_F d$. The value at the peak $S_{\text{max}} = S(q_0)$ can be used as an order parameter, revealing in this case a staircase structure where every step corresponds to a charge density wave (CDW) phase with long-range order in the atomic density. For each of them, the order is characterized by the momentum q_0 , and we labeled these phases as CDW_q . As an example, we depict in Fig. 5.3(a) the real-space density for CDW_π . In Fig. 5.3(c), we can observe how the situation changes as we increase the value of V_p/V_h . If the amplitude of the periodic potential is sufficiently large, a disordered phase emerges between the different CDW_q phases, where $S(q)$ vanishes at all momenta. This is an example of a frustrated phase [258], where the density order melts due to quantum fluctuations enhanced by competing interactions in a region where the different density orders are close in energy. Instead, a bond order develops [Fig. 5.3(a)], characterized by a non-zero value of the order parameter $B = 1/L \sum_j (-1)^j \langle \hat{B}_j \rangle$, with $\hat{B}_j = \hat{b}_j^\dagger \hat{b}_{j+1} + \text{H.c.}$ (Fig. 5.3(e)). This bond-order wave (BOW) is a strongly-correlated phase that cannot be accessed through the conventional RKKY interactions [181], since it requires comparable nearest and next-nearest neighbor interactions, while further-range interactions should vanish. This guarantees, in particular, that the classical energies corresponding to CDW_π and $\text{CDW}_{\pi/2}$ patterns are similar, thus enhancing frustration, while keeping the energy of CDW_q much higher. While this situation can be achieved for spinfull fermions with dipolar interactions [259], spinless particles require $v_2/v_1 \approx 0.5$ [260], which is achieved here by varying the amplitude of the periodic potential, V_p , as shown previously. Similarly to the fermionic case [259], here the BOW phase possesses non-trivial topological properties. These are characterized by both a non-zero quantized value of the Berry phase [261] [Fig. 5.3(d)], calculated here through from the entanglement spectrum as explained in Ref. [262], and the emergence of localized protected states at the boundaries [Fig. 5.3(f)]. We note that similar topological effects are observed in non-frustrated BOW phases induced instead by dynamical optical lattices [263–269].

5.3 Knob II: dimensionality of the mediator

Let us finally provide another way of tuning the interactions that is unique of atomic systems, enabled by the possibility to control the effective dimensionality of the

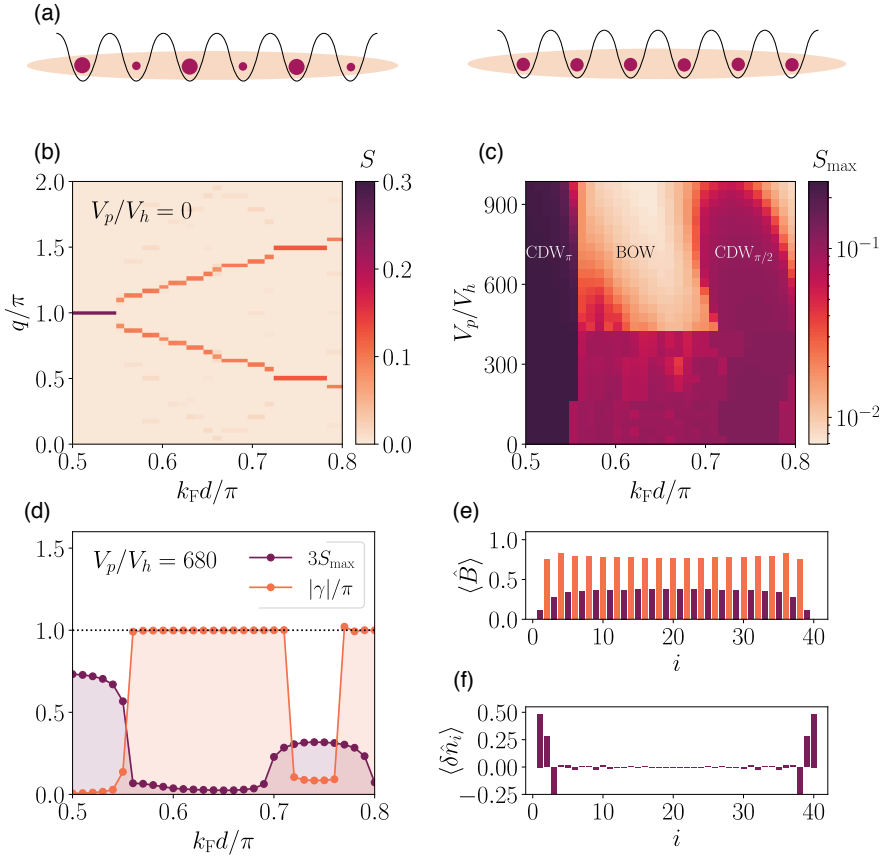


FIGURE 5.3: (a) Real-space configuration of the CDW_π (left), where spheres of different sizes correspond to an alternating atomic occupation, and frustrated BOW (right) with a dimerized bond structure. (b) $S(q)$ as a function of $k_F d$ for a chain with $L = 60$ sites and bosonic density $\rho = 1/2$, for $V_p = 0$. The phase diagram presents a staircase structure, where every step corresponds to a CDW_q characterized by a peak in $S(q)$. (c) Value of S at the peak, S_{\max} as a function of $k_F d$ and V_p/V_h , showing how the CDW orders melt for sufficiently large values of V_p/V_h , giving rise to a frustrated BOW. (d) S_{\max} and Berry phase γ as a function of $k_F d$ for $V_p/V_h = 680$, showing the non-trivial topological nature of the BOW phase. Real-space configuration of the BOW phase for $L = 40$, showing (e) dimerized bonds and (f) localized edge-states at the boundaries. Parameters as in Fig. 5.2. DMRG calculations are courtesy of D. González-Cuadra, as part of the collaboration in Ref. [4].

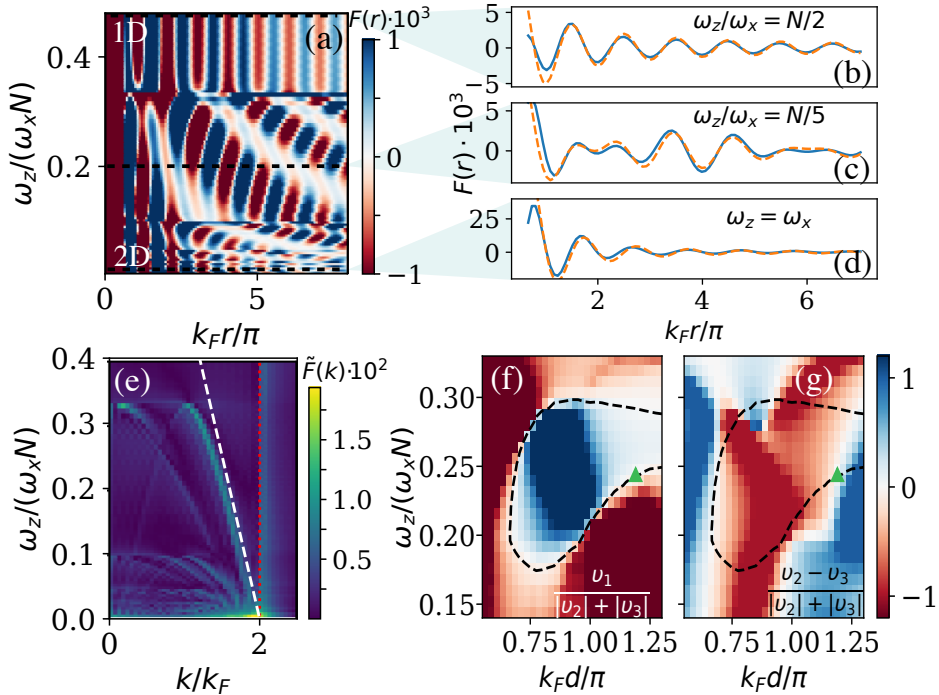


FIGURE 5.4: (a) Mediated potential $F(r)$ as a function of the anisotropy ratio $\omega_z/(N\omega_x)$ and effective atomic separation $k_F r$. Repulsive (attractive) forces are represented in red (blue). (b-d) Value of $F(r)$ for three anisotropy ratios (blue) indicated in (a) with black dashed lines, compared to the expected analytical results (5.8,5.9) (orange). (e) Cosine transform of $F(r)$ as a function of $\omega_z/(N\omega_x)$, where the dotted lines correspond to the frequencies $2k_F$ (red) and \tilde{k}_1 (white). (f,g) Relation between the nearest-neighbor potentials $v_{1,2,3}$ of a kagome lattice with lattice spacing d , as a function of $\omega_z/(\omega_x N)$ and $k_F d$. Dashed contour follows $v_1 = 0$. Here we took $N = 250$ and the rest of the parameters as in Fig. 5.2.

fermionic gas. In particular, by superimposing three independent standing-wave potentials, each ω_i in Eq. (5.1) can be controlled independently for the three orthogonal directions by modifying their intensity [see Fig. 5.1(d)]. Starting from $\omega_x = \omega_y = \omega_z$ and increasing ω_y , one can go smoothly from a 3D fermionic gas to an effective 2D one for $\omega_{x,z} \ll \omega_y/N$ [157, 158]. Similarly, increasing ω_z connects the 2D and the 1D case. Since the power-law exponent of $F(r)$ depends on the dimension D as $1/r^D$, one expects that this method interpolates between different integer values.

Let us now explore the effect of this dimensional crossover in the effective interactions $F(r)$ for the two-to-one dimensional transition, while we maintain the bosons in 1D. Fig. 5.4(a) shows $F(r)$ as a function of the anisotropy ratio $\omega_z/(\omega_x N)$ and $k_F d$, together with some cuts at the 1D / intermediate / 2D regimes in Figs. 5.4(b-d). Note that the dependence on N is introduced because the crossover is expected in the limit $\omega_z/\omega_x \sim N$, where the energy of the highest-energy state in the x -direction is not enough to induce an excitation in the z -axis, and the interaction becomes effectively 1D. We observe that the interpolation is more intricate than initially expected. While in the limits $\omega_z/(\omega_x N) \gg (\ll) 1$ one recovers the expected 1D (2D) RKKY-type interactions, the intermediate dimensions acquire additional

beating oscillations due to the presence of different harmonics in the potentials. This is more evident in Fig. 5.4(e), where we plot the corresponding cosine transform $\tilde{F}(k)$. The frequency $2k_F$ appears in all intermediate dimensions and, through a careful analysis, we observe that additional frequencies appear associated to discrete values $\tilde{k}_n = 2k_F[1 - n\omega_z/(\omega_x N)]$. The larger the value of ω_z/ω_x , the smaller is the contribution associated to smaller frequencies (as longer effective lengths that cannot fit the constrained direction vanish). In particular, in the range $\omega_z/(\omega_x N) \in (0.1, 1/3)$, only contributions associated to \tilde{k}_0 and \tilde{k}_1 are dominant, leading to a smooth beating between the two frequencies in the potential, as we fit in Fig. 5.4(c) (dashed line).

Despite the apparent complexity of the fermion-mediated interactions within this dimensional crossover, they might lead to the appearance of novel many-body phases difficult to obtain otherwise. For example, recent works have shown how chiral spin liquids can appear for hardcore bosons in kagome lattices with long-range interactions where the second and third neighbor terms are similar and the nearest neighbor interaction cancels, i.e., ($v_2 \approx v_3$ and $v_1 = 0$) [179], a regime that is typically hard to access with conventional approaches. In Fig. 5.4(f,g), we make a search whether such regime would be accessible through this dimensional crossover and find that, indeed, there are configurations where $v_1 \approx 0$ (see contour line), while $v_2 \approx v_3$ (green marker). Although further analysis is required, specially to account for the effect of further-range interactions in the phase diagram, our results show a promising avenue to investigate magnetic frustration and spin liquids states in 2D ultracold atomic mixtures using the emergent tunable long-range interactions.

5.4 Conclusions

In this Chapter, we have provided two strategies to control fermion-mediated interactions in ultracold atomic mixtures by modifying the fermionic confinement potential. First, we have added an extra periodic potential to open a gap in the fermionic band. Then, we have continuously modified the effective dimension of the fermionic gas by using anisotropic traps. In both cases, we have characterized the emergent long-range interactions, obtaining a very versatile control over their range and shape. Finally, we have considered different examples where this extended quantum simulation toolbox can lead to the exploration of frustrated quantum many-body phases that are not easily accessible with other approaches. Given the recent experiments in this direction [188, 243], and the relatively simple tools that our proposal demands, we expect these results to be relevant for near-future experiments on the topic.

Chapter 6

Toy-model simulators for quantum chemistry in 2D

” A clerk stands on top of the shelf with a wheeled base that is kept at the center of the sphere. After we set up the model universe to correspond to the current state of the real universe, the motion of the model thereafter should be an accurate simulation of the future, including the motion of the sun. After the clerk records the movements of the sun, we will have a precise calendar. This is the dream of hundreds of civilizations before us.

— Cixin Liu

(Extract from "The Three-Body Problem")

6.1 Introduction

Solving quantum chemistry problems, which generally imply obtaining the ground state energy of many electrons interacting with both the nuclei and among themselves through Coulomb interactions, is an extremely challenging task. Even if one considers the nuclei positions $\{\mathbf{R}_\alpha\}_{\alpha=1}^{N_n}$ fixed due to their larger mass (the Born-Oppenheimer approximation, BO), and focuses only on the electronic degrees of freedom, these problems still involve many interacting electrons, whose associated Hilbert space grows exponentially with the number of electrons (N_e).

One way to circumvent this exponential *explosion* [270] consists in using the electron density instead of the wavefunction. For instance, DFT [271, 272] has enabled a better description and understanding of both static [273–276] and dynamic [277] properties of a large variety of molecules. The capability of such computational methods, whose main challenge is to address electronic correlations, are however sometimes hard to assess. Educated guesses of such functionals have already allowed one to study the properties of large molecules [278]. Unfortunately, there is no unambiguous path for improving these functionals [279–289], which are known to fail in certain regimes [279].

A complementary route consists in projecting the quantum chemistry Hamiltonian in a basis set [290, 291] with a finite number of elements N_o . The typical choices

for the basis are linear combinations of atomic orbitals with Slater- or Gaussian-type radial components. These methods generally provide good accuracies with small N_o . However, the quality of the solution ultimately depends on the basis choice. On top of that, the Hilbert space of the projected Hamiltonian still grows exponentially with N_o , which complicates their solution if large basis sets are required, especially for non-equilibrium situations.

In parallel to these developments, the last few years have witnessed the emergence of an alternative route to study chemistry problems based on using quantum systems to perform the computation. This idea was first proposed by Feynman as a way of preventing the exponential explosion of resources of quantum many-body problems [270], formalized later by Lloyd [292], and first exported into the quantum chemistry realm by Aspuru-Guzik *et al* [293]. First algorithms used Gaussian orbital sets and phase-estimation methods to obtain ground-state molecular energies [294]. Despite the initial pessimistic scaling of the gate complexity with the number of orbitals (polynomial, but with a large exponent [295]), recent improvements through the use of more efficient algorithms [296] or different basis sets, e.g., plane-waves [297–299], have reduced significantly the gate scaling complexity. Since these algorithms typically assume fault-tolerant quantum computers that will not be available in the near-future, in the last years there has also been an intense effort on hybrid variational approaches more suitable for current noisy quantum computers [300–304]. However, these will be ultimately limited by the available ansätze that can be obtained with current devices, as well as on the optimization procedure [305, 306].

The previously described efforts (see Ref. [307] for an introductory review) fall into what is called the **digital quantum simulation** framework, in which the fermionic problem is mapped into qubits and the Hamiltonian evolution is performed stroboscopically. Here, we will introduce a complementary route to study these problems, showing how to simulate in an analog way the quantum chemistry Hamiltonian using a discretized space (or grid) basis representation [308]. These representations have been generally less used in the literature due to the large basis sets required to obtain accurate results. However, they have recently experienced a renewed interest [309–311] due to their better suitability for DMRG methods [312]. In our case, we will use this grid representation because it is well suited for describing fermions trapped in optical lattice potentials, where the fermionic space is naturally *discretized* in the different trapping minima of the potential.

As introduced in Chapter 4, simulators based on ultracold atoms have already addressed condensed matter questions that the most advanced classical computers cannot compute [43, 45]. In all these addressed problems, the key feature is that their interactions are either local or short-range, which is ideally suited for the existing simulators. On the contrary, analog simulation of quantum chemistry now requires engineering long-range (Coulomb) interactions between fermionic particles, and no system has been identified so far fulfilling such requirement. This is why current efforts concentrate in digital simulation.

In this Chapter, we propose and analyze a scheme for **analog quantum chemistry simulation** that can be implemented with present technology. Our approach uses ultracold atoms to address lattice models, where the electron-electron interaction can take different forms. While not exactly reproducing all aspects of the real quantum chemistry scenario, this simulator still retains the most relevant

ingredients, enabling the observation of the most representative phenomena in quantum chemistry. Furthermore, it offers a suitable platform to benchmark computational methods in that field. In particular, it allows us to extend the benchmarking offered by DMRG beyond 1D. Previous analog simulators based on fermionic atoms trapped in optical lattices have been proposed to emulate the molecular potentials of benzene-like molecules [313] or simulate ultrafast dynamics in strong-fields [314, 315]. In contrast to them, the presented proposal allows us to go beyond the local interactions naturally found in cold atoms, simulating the non-local fermionic repulsion that appears in typical quantum chemistry problems.

This Chapter is structured as follows:

- In Section 6.2, we introduce the different parts of the quantum chemistry Hamiltonians projected in finite basis sets. We discuss both the grid basis representation that we use in our analog simulation and the widely-used combination of atomic orbitals, emphasizing the similarities and the differences between these two approaches.
- In Section 6.3, we review how to obtain the single-particle parts of the quantum chemistry Hamiltonian. This is, the kinetic term and nuclear attraction of fermionic atoms in an optical lattice.
- In Section 6.4, we start by presenting the trivial situation of a single fermion moving in an attractive Coulomb-like potential, which allows us to introduce a natural definition of the Rydberg energy and Bohr radius in 2D.
- In Section 6.5, we then analyze different strategies to obtain an effective repulsion between the fermionic atoms.
- Finally, in Section 6.6, we summarize our findings and point to further directions of work, some of which will be explored in Chapter 7.

6.2 Discrete basis sets: atomic orbitals vs. grid basis

Problems in quantum chemistry typically require to either calculate the electronic structure of a complex molecule in equilibrium, $\hat{H}_e |\Psi\rangle_e = E_e |\Psi\rangle_e$, or its time-evolution in an out-of-equilibrium situation: $i\partial_t |\Psi(t)\rangle_e = \hat{H}_e |\Psi(t)\rangle_e$. These problems are generally operated using the BO approximation where each nucleus is classically treated as a fixed particle of charge $Z_\alpha e$. The BO-electronic Hamiltonian for a molecule with N_e electrons and a given nuclei configuration $\{\mathbf{R}_\alpha\}_{\alpha=1}^{N_n}$ reads as, $\hat{H}_e^c = \hat{H}_{\text{kin}}^c + \hat{H}_{\text{nuc}}^c + \hat{H}_{e-e}^c$, where¹,

$$\hat{H}_{\text{kin}}^c = -\frac{\hbar^2}{2m_e} \sum_j \hat{\nabla}_j^2, \quad (6.1)$$

$$\hat{H}_{\text{nuc}}^c = -\frac{e^2}{4\pi\epsilon_0} \sum_{\alpha=1}^{N_n} Z_\alpha V_C(\hat{\mathbf{r}}_j, \mathbf{R}_\alpha), \quad (6.2)$$

$$\hat{H}_{e-e}^c = \frac{e^2}{8\pi\epsilon_0} \sum_{i \neq j=1}^{N_e} V_C(\mathbf{r}_i, \mathbf{r}_j), \quad (6.3)$$

¹Here, upper-index, c , is used to distinguish this continuum electronic Hamiltonian from the discretized terms later appearing in the simulator.

where, m_e , and e denote the electronic mass and charge, respectively, and ϵ_0 is the vacuum permittivity. Here $V_C(\mathbf{r}_1, \mathbf{r}_2) = \frac{1}{|\mathbf{r}_1 - \mathbf{r}_2|}$ is the pair-wise Coulomb potential between the charged particles (electrons and nuclei), and, $\hat{H}_1^c = \hat{H}_{\text{kin}}^c + \hat{H}_{\text{nuc}}^c$, is the single-electron part of the Hamiltonian, which contains both the electron kinetic energy (6.1) and the electron-nuclei attraction (6.2), whereas Eq. (6.3) corresponds to the electron-electron repulsion. When discussing chemistry parameters, the natural unit of length is conveniently given by the Bohr Radius, $a_0 = (4\pi\epsilon_0\hbar^2)/(m_e e^2)$, and the unit of energy is the Hartree energy², $E_h = \hbar^2/(m_e a_0^2)$.

Since the molecular electrons are indistinguishable (up to the spin degree of freedom), for computational purposes it is typically more convenient to write a **second-quantized version** of the Hamiltonian that already takes into account the fermionic statistics of the particle. There is a general recipe to do it [250, 316]: first, one needs a set of single-particle states $\mathcal{B} = \{|\phi_i\rangle\}$, that can be used to define an abstract Hilbert space of states $|n_1, n_2, \dots\rangle$, denoting that there are n_i electrons occupying the i -th single-particle states. With these states, one can then define annihilation(creation) operators, $\hat{c}_i^{(\dagger)}$ that denote the annihilation(creation) of a fermionic particle in the i -th single-particle state. This labelling already accounts for the different spin states and the fermionic statistics of the particle through their anticommutation rules: $\{\hat{c}_i, \hat{c}_j^\dagger\} = \delta_{ij}$, and $\{\hat{c}_i, \hat{c}_j\} = \{\hat{c}_i^\dagger, \hat{c}_j^\dagger\} = 0$. With these operators, one can define the field operators,

$$\hat{\Psi}(\mathbf{r}) = \sum_i \phi_i(\mathbf{r}) \hat{c}_i, \quad (6.4a)$$

$$\hat{\Psi}^\dagger(\mathbf{r}) = \sum_i \phi_i^*(\mathbf{r}) \hat{c}_i^\dagger, \quad (6.4b)$$

which can be used to write the Hamiltonian in the following form:

$$\hat{H}_e = \int d\mathbf{r} \hat{\Psi}^\dagger(\mathbf{r}) \hat{H}_1^c \hat{\Psi}(\mathbf{r}) + \frac{1}{2} \iint d\mathbf{r} d\mathbf{r}' \hat{\Psi}^\dagger(\mathbf{r}) \hat{\Psi}^\dagger(\mathbf{r}') \hat{H}_{e-e}^c \hat{\Psi}(\mathbf{r}') \hat{\Psi}(\mathbf{r}). \quad (6.5)$$

If the basis \mathcal{B} of single-particle states is complete (i.e., it is infinite dimensional), the mapping between the first-quantized Hamiltonian of Eqs. (6.1-6.3) and the second-quantized one of Eq. (6.5) would be exact. However, this is generally not practical since the associated Hilbert space will still be infinite. For these reasons, the typical approach consists in projecting the Hamiltonian in the subspace spanned by the tensor product of a finite-dimensional discrete basis set, \mathcal{B}_t , and solving the problem within that subspace. The prototypical bases chosen are built out of (linear combinations) of atomic orbitals centered around the nuclei position, labeled as linear combination of atomic orbitals (LCAO) basis sets [290]. However, for our analog quantum chemistry simulation it will be more adequate to use an alternative representation based on a grid discretization of the continuum in a finite set of points. In what follows, we discuss how the second-quantized electronic Hamiltonian looks in both cases, and highlight their main differences.

²For comparison, note that the Hartree energy is twice the Rydberg energy, Ry.

6.2.1 Linear combination of atomic orbitals.

Here, the basis set is composed of $N_o (> N_e)$ single-particle (orthonormal) atomic orbitals, $\mathcal{B}_t = \{|\phi_i\rangle\}_{i=1}^{N_o}$, so that the Hamiltonian reads as,

$$\hat{H}_e^{\text{LCAO}} = \sum_{i,j=1}^{N_o} t_{ij} \hat{c}_i^\dagger \hat{c}_j + \sum_{i,j,k,l=1}^{N_o} \frac{V_{ijkl}}{2} \hat{c}_i^\dagger \hat{c}_j^\dagger \hat{c}_l \hat{c}_k, \quad (6.6)$$

where the parameters of the discrete Hamiltonian t_{ij} and V_{ijkl} can be computed from Eqs. (6.1-6.3) using the real space representation of the orbitals, $\phi_i(\mathbf{r}) = \langle \mathbf{r} | \phi_i \rangle$, as follows:

$$t_{ij} = \int d\mathbf{r} \phi_i^*(\mathbf{r}) \hat{H}_1^c \phi_j(\mathbf{r}), \quad (6.7a)$$

$$V_{ijkl} = \iint d\mathbf{r} d\mathbf{r}' \phi_i^*(\mathbf{r}) \phi_j^*(\mathbf{r}') \hat{H}_{e-e}^c \phi_l(\mathbf{r}') \phi_k(\mathbf{r}), \quad (6.7b)$$

The number of t_{ij} and V_{ijkl} parameters scales with the size of the \mathcal{B}_t basis as N_o^2 and N_o^4 , respectively, while their value depends on the particular states chosen. Convenient choices widely-used in quantum chemistry are linear combinations of Gaussian or exponential type-orbitals localized around the nuclei [290, 291]. The former are particularly appealing since the properties of Gaussian functions can simplify substantially the calculations of t_{ij}, V_{ijkl} , which can become a bottleneck if large basis sets are required.

An advantage of this approach is that the number of orbitals required typically scales proportionally with N_e . Besides, it is a variational method that provides an unambiguous path to reach the true ground state energy by increasing N_o . This is why these representations have been the most popular ones in current approaches for digital quantum simulation [307]. On the down side, the accuracy of the solution will depend on the particular molecular structure, since the basis sets are composed of functions with fixed asymptotic decays that might not be suitable to, e.g., describe diffuse molecules [317–322].

6.2.2 Local or grid-discretized basis.

This option consists in writing the continuum Hamiltonian \hat{H}_e in grid points, whose coordinates write as $\mathbf{j} = (j_x, j_y, j_z)$, for $j_{x,y,z} \in \mathbb{Z}$. To do it, one can approximate the derivatives of the kinetic energy term in Eq. (6.1) by finite-differences, and evaluate the potentials at the grid points [291, 308]. This ultimately results in a second-quantized Hamiltonian, \hat{H}_e^{grid} , with the following shape,

$$\hat{H}_e^{\text{grid}} = - \sum_{\mathbf{i}, \mathbf{j}, \sigma} J_{\mathbf{i}, \mathbf{j}} \hat{c}_{\mathbf{i}, \sigma}^\dagger \hat{c}_{\mathbf{j}, \sigma} \quad (6.8a)$$

$$- \sum_{n=1}^{N_n} \sum_{\mathbf{j}, \sigma} V_{\text{nuc}}(\mathbf{j}, \mathbf{R}_n) \hat{c}_{\mathbf{j}, \sigma}^\dagger \hat{c}_{\mathbf{j}, \sigma} \quad (6.8b)$$

$$+ \frac{1}{2} \sum_{\mathbf{i}, \mathbf{j}, \sigma, \sigma'} V_{e-e}(\mathbf{i}, \mathbf{j}) \hat{c}_{\mathbf{i}, \sigma}^\dagger \hat{c}_{\mathbf{j}, \sigma'}^\dagger \hat{c}_{\mathbf{i}, \sigma} \hat{c}_{\mathbf{j}, \sigma'}, \quad (6.8c)$$

where $\hat{c}_{\mathbf{j},\sigma}^{(\dagger)}$ are now the local operators creating an electron with spin σ at site position \mathbf{j} , satisfying the fermionic commutation rules stated above. The kinetic energy coefficients $J_{i,\mathbf{j}}$ (6.8a) depend on the expansion order chosen to approximate the Laplacian, and decay with the separation between sites $|\mathbf{j} - \mathbf{i}|$. Along this Thesis, we will use the simplest finite difference formula for the second order derivative:

$$\frac{d^2 f(x)}{dx^2} \approx \frac{f(x+a) - 2f(x) + f(x-a)}{a^2}, \quad (6.9)$$

which means that only nearest neighbour hoppings (and on-site energy) will appear in the kinetic energy term of Eq. (6.8a), and $J_{i,\mathbf{j}} \equiv 0$ for the rest of the hopping terms. Here, a , denotes the spacing between the discretized points. The nuclei-attraction term V_{nuc} (6.8b) induces a position-dependent energy shift on the discretized electron orbitals coming from the attraction of the nuclei. Finally, the electron-electron repulsion V_{e-e} (6.8c) translates into long-range density-density interactions between the localized fermionic states. In the limit where $N \rightarrow \infty$ and $a \rightarrow 0$, the Hamiltonian \hat{H}_e^{grid} (6.8a-6.8c) converges to the continuum one, \hat{H}_e^c (6.1-6.3).

This method typically requires larger basis sets to obtain accurate results [308] compared to LCAO ones. However, the number of interaction terms $V_{e1}(\mathbf{n}, \mathbf{m})$ scales quadratically with the size of the basis because only density-density interaction terms appear. This can yield dramatic improvements when applying tensor-network methods, which motivates the renewed interest they have experienced in the last years [309–311]. Besides, from the analog quantum simulation perspective, such density-density interactions appear more naturally than the four-index interactions appearing in LCAO approaches.

A potential disadvantage is that these methods are generally not variational. That is, increasing N_o might sometimes yield a larger energy than the one of smaller basis sets. This has been identified as a problem of underestimation for the kinetic energy when using the finite-difference approximation of the derivatives (6.9) [323]. However, there are constructive ways of making the kinetic operator variational using different approximations of the kinetic energy [323]. Along Chapters 6 and 7, however, we will stick to the simple finite-difference formula of Eq. (6.9) because of its simplicity.

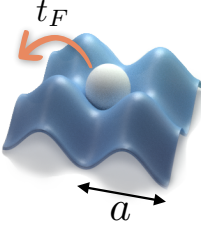
In what follows, we explain how to simulate the different parts of the quantum chemistry Hamiltonian projected in a grid basis using ultra-cold atoms trapped in optical lattices. The reason for choosing this platform is that fermionic atoms with (at least) two internal atomic states can be used to describe electrons without the need to encode these operators into qubits, simplifying the Hamiltonian simulation, as already pointed out in earlier proposals [313–315]. We start by considering the single-particle part of the Hamiltonian in Section 6.3. In Section 6.4, we particularize it to the 2D case, and then we explain how to obtain the electron repulsion in Section 6.5.

6.3 Simulating single-particle Hamiltonian in optical lattices


Fermionic atoms hopping in a deep optical lattice naturally follow a grid description associated to the sites of the lattice, whose mapping to the discretized quantum

Electronic molecular Hamiltonian

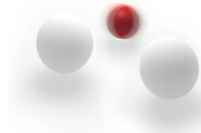
Kinetic term



Nuclear attraction



Electronic repulsion



$$-t_F \sum_{\langle i,j \rangle} f_i^\dagger f_j - V_0 \sum_{j,n} \frac{Z_n}{\|\mathbf{j} - \mathbf{r}_n\|} f_j^\dagger f_j + \sum_{i,j} \frac{V_0}{\|\mathbf{i} - \mathbf{j}\|} f_i^\dagger f_i f_j^\dagger f_j$$

FIGURE 6.1: Fermionic atoms, playing the role of electrons, are trapped in a periodic 2D cubic potential. Their hopping simulates the kinetic energy term of the electrons, and they are subject to additional optical potentials which emulate the nuclear interaction.

chemistry Hamiltonian in Eq. (6.8) is explored in the following. Similarly to the bosonic system introduced in Section 4.3, the dynamics of ultra-cold fermionic atoms trapped in an optical lattice can be described by a second-quantized Hamiltonian. Following the techniques introduced in Section 4.2, one typically assumes that the atoms are prepared in the motional ground state of each trapping minimum, and that interband transitions are negligible [38, 39, 145]. With these assumptions, the field operators $\hat{\Psi}_f(\mathbf{r})$ can be expanded in terms of Wannier functions centered at each lattice site (see Section 4.2.2),

$$\hat{\Psi}_f(\mathbf{r}) = \sum_{j,\sigma} w_j(\mathbf{r}) \hat{f}_{j,\sigma}, \quad (6.10)$$

where we define the annihilation(creation) operators $\hat{f}_{j,\sigma}^{(\dagger)}$ of a fermionic state with spin σ at site \mathbf{j} , which also obey anti-commutation rules $\{\hat{f}_{i,\sigma}, \hat{f}_{j,\sigma'}^\dagger\} = \delta_{i,j} \delta_{\sigma,\sigma'}$. With these operators, the second-quantized Hamiltonian (4.9) for the fermions, \hat{H}_f , can be expressed as,

$$\hat{H}_f = \hat{H}_{\text{kin}} + \hat{H}_{\text{nuc}}, \quad (6.11)$$

which accounts for the tunneling of the fermionic atoms to neighbor sites, and the on-site interaction with an external potential (see Fig. 6.1). In what follows, we analyze both terms, and explain how to make them match exactly those of the quantum chemistry Hamiltonian \hat{H}_e^{grid} , corresponding to Eqs. (6.8a)-(6.8b), respectively.

6.3.1 Electron kinetic energy

Particularizing Eq. (6.7a) to the basis of Wannier functions, the kinetic part of the ultra-cold fermionic atoms in a deep optical lattices is approximated as a nearest-neighbour tunneling,

$$\hat{H}_{\text{kin}} = -t_f \sum_{\langle i,j \rangle, \sigma} \hat{f}_{i,\sigma}^\dagger \hat{f}_{j,\sigma}, \quad (6.12)$$

where the kinetic term t_f is dictated by the depth of the optical lattice (4.11). This gives exactly the electron kinetic energy terms of Eq. (6.8a) using the finite-difference approximation of the derivative of Eq. (6.9), up to a constant energy shift $2t_f$ that commutes with the complete Hamiltonian and can be subtracted. Note that, because of the larger effective mass of the fermions compared to the real electron systems, this dynamics will occur at a much slower timescale (ms) compared to electronic systems (fs). This can facilitate the observation of real-time dynamics of the simulated chemical processes, something very difficult to do in real chemistry systems.

6.3.2 Nuclear attraction

Following the BO approximation, we consider that the electronic dynamics is much faster than the nuclear one, such that their equations can be decoupled. Then, we desire that these fermionic atoms are subjected to an external potential that induces the attraction to N_{nuc} "nuclei" that we consider placed in fixed positions" $\{\mathbf{R}_n\}_{n=1\dots N_{\text{nuc}}}$ during the calculation of the electronic Hamiltonian. This allows us to induce them with an on-site interaction of the form,

$$\hat{H}_n(\{\mathbf{R}_n\}) = - \sum_{n=1}^{N_{\text{nuc}}} \sum_{\mathbf{j}, \sigma} Z_n V(|\mathbf{j} - \mathbf{R}_n|) \hat{f}_{\mathbf{j},\sigma}^\dagger \hat{f}_{\mathbf{j},\sigma}, \quad (6.13)$$

where Z_n is the atomic number of nucleus n , and $V(r)$ is the attractive nuclear potential.

In 2D lattices, this potential can be obtained by combining the light shift induced by an external laser orthogonal to the lattice and a fully programmable intensity mask (4.13), such that $\epsilon_{\mathbf{j}} = V_{\text{aux}}(\mathbf{j}) = \sum_n Z_n V(|\mathbf{j} - \mathbf{r}_n|)$. This can be obtained, e.g., by using a digital mirror device (shown in grey in Fig. 6.2) [43], as introduced in Section 2.1.1. This externally induced potential can eventually mimic the effect of inner-shell electrons as well. In order to prevent the divergence in the origin, positions \mathbf{R}_n of the nuclei are shifted half a site from the lattice nodes in the y direction. For consistency of our model, the maximum energy difference between the different sites, that is of the order $\Delta\epsilon_{\text{max}} = Z_{\text{max}} V_0$, should be much smaller than the trapping depth (2.8), V_D , of the overall potential $\Delta\epsilon_{\text{max}} \ll V_D$, such that the tunnelings t_f are not affected by it. We also need $\Delta\epsilon_{\text{max}} \ll \hbar\omega_t$, so that it does not create interband transitions (see [324–327] where similar effects were considered due to the existence of confinement potentials). Both limits can be satisfied in the regime of parameters we are interested in.

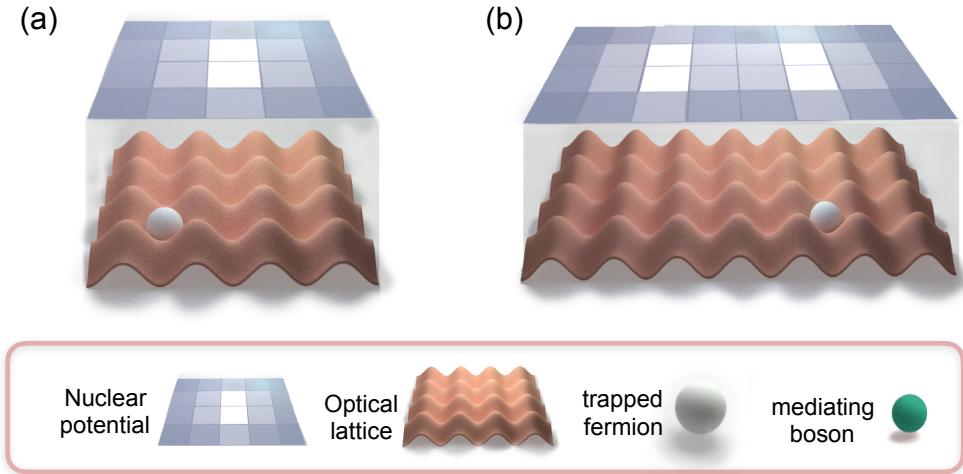


FIGURE 6.2: Fermionic atoms (white) play the role of the molecular electrons. They hop in a 2D lattice (red), where the nuclear potential is imprinted (blue). For a single simulated electron, this pattern can lead to, e.g., atomic hydrogen ((a), one nucleus) or H_2^+ ((b), two nuclei). For more than one fermionic atom, two different schemes are proposed to mediate an effective repulsion between them.

6.4 Two-dimensional simulators

For the sake of clarity, we will now discuss several scenarios, with increasing experimental difficulty, for the simulation of quantum chemistry problems in 2D discrete lattices of size $N \times N$. We start with simple one-electron systems: the analogous of the hydrogen atom, and the H_2^+ molecule. Then, we show how to simulate two electron problems, here exemplified by the H_2 molecule. Finally, we show how these systems can be scaled-up to more electrons, although with a different dependence of the repulsion with the distance.

6.4.1 A single electron

We consider now the simplest situation of simulating atomic hydrogen. To begin with, we consider the attractive Coulomb potential on its standard form³, $V_{\text{nuc}}(\mathbf{j}) = V_0/|\mathbf{j}|$, for moderate finite lattice sizes and a unique nucleus, $Z_1 = 1$, centered in the lattice site $\mathbf{R}_1 = (\lfloor N/2 \rfloor, \lfloor N/2 \rfloor + 1/2)$. The reason for choosing this case is two fold: first, it can be simulated directly using the Hamiltonian of Eq. (6.13) imposing $N_n = 1$, since one does not require the electron interactions. Second, it is fully understood analytically in the continuum limit, which allows us to easily benchmark our results and define the natural units of our system.

In order to gain intuition, one can compare this discretized Hamiltonian to the continuum limit, where an analytical solution is also known in 2D [328]. As a consequence of the reduced dimensionality, electrons get closer to the nuclei than in the 3D case [329], and energy levels correspond to $E_n^* = \frac{-Ry^{(2D)}}{(n-1/2)^2}$, for $n = 1, 2, \dots$. In

³We assume that the lattice and nuclei positions are normalized to the lattice constant a , such that V_0 has units of energy.

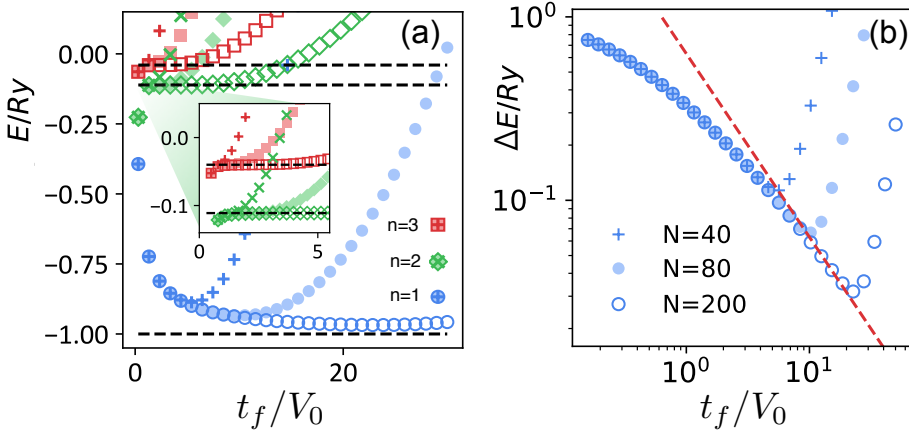


FIGURE 6.3: (a) Lower part of the spectrum for the discretized 2D atomic hydrogen Hamiltonian in Eq. (6.11) for different values of the effective Bohr radius t_f/V_0 , calculated through exact diagonalization (ED, see Appendix B.3.1). For clarity, only the lowest-energy state is shown for the energy levels $n = 1, 2, 3$. As more lattice sites are involved in the simulation (t_f/V_0 increases), the spectrum approaches the value in the continuum (horizontal lines for $n = 1, 2, 3$). This is valid up to a critical Bohr-radius in which finite-size effects become relevant and the solution deviates from this behaviour. This critical value appears earlier for smaller sizes ($N = 40$ for crossed markers) than for bigger systems ($N = 80$, coloured marker, and $N = 200$, edged marker). (b) The energy difference ΔE between the ground-state of the discretized Hamiltonian in Eq. (6.11), and the one in the continuum decreases polynomially before finite-size effects become relevant. Larger system sizes can follow this scaling up to more precise solutions. Dashed line follows the scaling $(t_f/V_0)^{-1}$.

that limit, one can also identify,

$$a_0^{(2D)}/a = t_f/V_0 \quad \text{and} \quad Ry^{(2D)} = V_0^2/t_f, \quad (6.14)$$

which are the equivalent Bohr radius (a_0), and Rydberg energy (Ry), for the 2D discrete model⁴. The first ultimately determines the size of the orbitals and thus how the continuum limit is recovered. In particular, it is needed that the orbitals fit in the lattice (to avoid finite size effects), and that this Bohr radius occupies several lattice sites (to reduce discretization errors). This leads to the following conditions,

$$1 \ll t_f/V_0 \ll N. \quad (6.15)$$

By controlling at will this ratio with the lasers creating the optical potentials (t_f/V_0), one can effectively choose the Bohr radius of the discrete Hydrogen atom (a_0/a) and, consequently, of the simulated molecules when more nuclei are present. This will be an important asset of our simulation toolbox since it will allow one to minimize the errors coming from discretization and finite-size effects. In Fig 6.3(a) we show the lower part of the spectrum for the discretized Hamiltonian (6.11) for different values of t_f/V_0 and N . First, we observe that we have quantized levels,

⁴As compared to the three-dimensional case studied in Chapter 7, $Ry^{(2D)} = 4Ry^{(3D)}$, and $2a_0^{(2D)} = a_0^{(3D)}$. Along the rest of this Chapter, we will omit the (2D) labelling.

and thus the discrete model qualitatively reproduces the continuous one. In fact, this can be observed with small lattices ($N = 40$).

From this calculation, we observe several features of the grid discretized basis that we are choosing to represent the quantum chemistry Hamiltonian. For example, when $a_0/a \lesssim 1$, all the states deviate from the expected energy. This is not surprising because in this regime, all the fermionic density is expected to concentrate around one trapping minimum, such that discretization effects become large. In the opposite regime, when the Bohr radius becomes comparable with system size, $a_0/a \sim N$, the energies also deviate from the continuum result, since the discrete Hydrogen atom does not fit in our system. Only in the intermediate regime one can minimize both errors and approximate well the correct energy. Note, however, that the optimal range of a_0/a depends on the particular orbital considered. For example, the ground state s orbital ($n = 1$) is more sensitive to discretization effects since it has a larger fraction of atomic density close to the nucleus, while larger orbitals are more sensitive to finite size effects because their spatial extension grows with n .

In Fig. 6.3(b) we observe that the discretized solutions of the Hamiltonian approach the analytical result following the scaling,

$$\frac{\Delta E}{\text{Ry}} \propto \frac{V_0}{t_f}. \quad (6.16)$$

To analyze this effect, it is useful to have some insights on how the discretization of the space affects the convergence to the continuum solution. A back-of-the-envelope dimensional analysis can be presented for the 2D case, where we consider the ground-state electronic wave-function, $\psi_0(r) = a_0^{-1} \sqrt{2/\pi} e^{-r/a_0}$. For the two main sources of discretization errors, the calculation of the energy terms is based on integrals that are discretized as a Riemann sum. The difference between this sum and the continuum limit is defined to first order by the second derivative of the integrand. For the Coulomb term, this reads as, $V_0 \sum_j \partial_x^2 (|\psi(\mathbf{r}_j)|^2/r)$. This sum does not converge in the continuum limit for the 2D case, and the leading order error corresponds to the diverging term, that is dictated by our choice of the cutoff for the position closest to the nuclei. Normalizing by the Rydberg energy, this error terms scales as $(t_f/V_0)^{-1}$ in 2D. As we numerically observe in Fig. 6.3(b), this dominates the scaling of the 2D setup when the effective Bohr radius increases.

Let us now explore a system with a single fermion and two equal nuclei, $Z_{1,2} = 1$, separated by d/a lattice sites, $\mathbf{j}_{1,2} = (\lfloor N/2 \pm d/(2a) \rfloor, \lfloor N/2 \rfloor + 1/2)$, i.e. the analog of H_2^+ . This internuclear separation measured in number of lattice sites can be directly expressed in terms of the Bohr radius as $d/a_0 = (d/a) \cdot (V_0/t_f)$, and therefore compared to tabulated values [330]. In Fig. 6.4(a) we plot the energy of the ground state as a function of the distance. We obtain a molecular potential, as it is expected for H_2^+ , already for the moderate size $N = 40$. Increasing t_f/V_0 favors accuracy, up to the point where finite-size effects appear. At this point the difference in energies to the continuum (dashed line) deviates from the aforementioned scaling $\Delta E \propto (t_f/V_0)^{-1}$, which identifies the optimal configuration for our finite system and a given choice of d/a_0 . In Fig. 6.4(b) we illustrate this effect by showing that a given internuclear separation d/a_0 , can be calculated with different values of integer lattice-site separations d/a by tuning the effective Bohr radius a_0/a accordingly. In

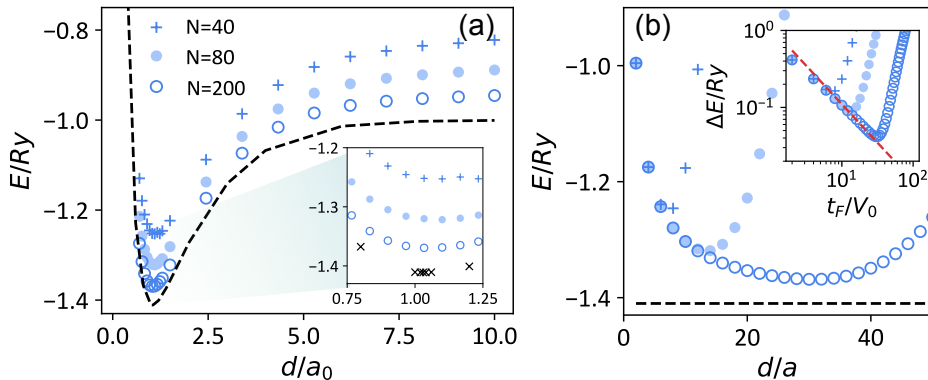


FIGURE 6.4: (a) Ground-state energy of the 2D hydrogen cation (H_2^+) for different lattice sizes N and internuclear distance d/a_0 (see Text for the optimal choice of the lattice separation). The inset zooms into separation close to equilibrium. Dashed line (black crosses in the inset) follows an accurate solution for this 2D cation [330]. (b) Ground-state energy of H_2^+ calculated for fixed $d/a_0 = 1$ and increasing effective Bohr radius t_f/V_0 . The energy of the calculated ground-state decreases up to a critical size at which finite-size effects appear. This critical size is larger for bigger lattice sizes. In the inset, the difference in energies to the tabulated value -1.41 Ry (black dashed line) reveals the scaling $(t_f/V_0)^{-1}$ (red dashed line). Markers represent the same sizes as in (a).

Chapter 7 we will introduce an error mitigation strategy that further allows us to increase the precision of measurements limited by finite size effects.

6.5 Simulating electron repulsion in 2D optical lattices

Let us now explore the non-trivial situation where two fermionic atoms emulate two electrons and the interelectronic repulsion between them needs to be mediated. This is the most complicated part of the simulation since it requires to describe long-range density-density interactions between ultra-cold fermionic atoms, whose interactions are typically local. That is, they only interact when their wavefunctions overlap significantly (i.e., same site). The key idea consists in using an auxiliary atomic species trapped together with the fermions such that the long-range interactions are effectively mediated by it. For concreteness, we assume to be in the regime where on-site interactions between the fermions are negligible⁵ and this auxiliary atom to be a boson, although this will not play a big role for the physics that will be discussed along this Chapter. These auxiliary atoms need to be trapped in an optical lattice of similar wavelength than the one of the fermions⁶, and it should be able to interact locally with the fermions through on-site collisions. These are described by a Hamiltonian [see Eq. (4.14)]:

$$\hat{H}_{f\text{-aux}} = U \sum_j \hat{f}_j^\dagger \hat{f}_j \hat{b}_j^\dagger \hat{b}_j, \quad (6.17)$$

⁵This regime, $U = 0$, can be obtained by, e.g., tuning the scattering length using Feshbach resonances [see Eq. (4.15)].

⁶It would also be sufficient that the period of the auxiliary atom lattice is larger and commensurate with the fermionic one.

where $\hat{b}_j^{(\pm)}$ is the annihilation(creation) operator associated to the bosonic atoms at the j site. We consider that the bosonic optical lattice can have a different size than the fermionic one, i.e., having N_M lattice sites per side. These atoms will have an internal dynamics described by a mediator Hamiltonian, \hat{H}_{aux} , which depends on the particular optical lattice configuration chosen, and ultimately determines the effective interactions induced in the fermionic atoms. Thus, the idea consists in properly engineering \hat{H}_{aux} such that the effective fermionic interactions lead to the desired long-range potential,

$$\hat{H}_{e-e} = \sum_{\mathbf{i}, \mathbf{j}} V(|\mathbf{i} - \mathbf{j}|) \hat{f}_{\mathbf{i}}^\dagger \hat{f}_{\mathbf{i}} \hat{f}_{\mathbf{j}}^\dagger \hat{f}_{\mathbf{j}}, \quad (6.18)$$

where the particular shape of $V(|\mathbf{i} - \mathbf{j}|)$ depends on the chosen scheme/configuration.

For notational simplicity from now on, we will omit the fermionic spin degree of freedom in \hat{f}_j , but since the fermion-auxiliary atom interactions in Eq. (6.21) are assumed to be equal for both spin states, so will be the effective fermionic repulsion.

6.5.1 General formalism

Our approach to calculate the effective fermionic interactions is based on the separation of energy scales between the fermionic dynamics, \hat{H}_f , and the rest of the Hamiltonian, $\hat{H}_{f-\text{aux}} + \hat{H}_{\text{aux}}$. In particular, we will assume that $\|\hat{H}_f\| \ll \|\hat{H}_{f-\text{aux}} + \hat{H}_{\text{aux}}\|$, such that we can consider the fermions fixed in the auxiliary atomic timescales. Thus, if we have N_e fermions placed in positions $\{\mathbf{j}\} \equiv \mathbf{j}_1, \dots, \mathbf{j}_{N_e}$ we can make the following ansatz for the full atomic mixture wavefunction,

$$|\Psi_{f-\text{aux}}(\{\mathbf{j}\})\rangle = |\mathbf{j}_1, \dots, \mathbf{j}_{N_e}\rangle_f \otimes |\varphi(\mathbf{j}_1, \dots, \mathbf{j}_{N_e})\rangle_{\text{aux}}. \quad (6.19)$$

In this way, one can first solve the problem for the auxiliary atoms degrees of freedom within a fixed fermionic configuration $\{\mathbf{j}_i\}_{i=1}^{N_e}$:

$$\left[\hat{H}_{f-\text{aux}}(\{\mathbf{j}\}) + \hat{H}_{\text{aux}} \right] |\varphi_{m, \{\mathbf{j}\}}\rangle_{\text{aux}} = E_{m, \text{aux}}(\{\mathbf{j}\}) |\varphi_{m, \{\mathbf{j}\}}\rangle_{\text{aux}}, \quad (6.20)$$

where the index m denotes the possible eigenstates within the same fermionic configuration, and where $\hat{H}_{f-\text{aux}}(\{\mathbf{j}\})$ (6.21) reads as,

$$\hat{H}_{f-\text{aux}}(\{\mathbf{j}\}) = U \sum_{\{\mathbf{j}\}} \hat{b}_{\mathbf{j}_i}^\dagger \hat{b}_{\mathbf{j}_i}. \quad (6.21)$$

Note that $\sum_{\{\mathbf{j}\}}$ indicates a sum now only over the fermionic positions.

Once the auxiliary atom problem of Eq. (6.20) is solved, we divide the bosonic Hilbert space for each fermionic configuration distinguishing between the contribution of one of the eigenstates, $|\varphi_{s, \{\mathbf{j}\}}\rangle_{\text{aux}}$ with eigenenergy $E_{s, \text{aux}}(\{\mathbf{j}\})$, and the rest of states, which we label as $|\varphi_{m, \{\mathbf{j}\}}^\perp\rangle_{\text{aux}}$, with $m = 1, \dots, \bar{N}_M - 1$. Here, $\bar{N}_M = N_M^D$ indicates the number of mediating atoms in a D -dimensional regular optical lattice. Then, one can calculate the effective fermionic Hamiltonian resulting

from the dressing of such particular eigenstate $|\varphi_{s,\{j\}}\rangle_{\text{aux}}$ by projecting in this space all possible fermionic configurations. The resulting effective Hamiltonian for the fermions reads as,

$$\begin{aligned} \hat{H}_{\text{eff}} &= \sum_{\text{all}\{j\}} \langle \varphi_{s,\{j\}} | \left[\hat{H}_f + \hat{H}_{f-\text{aux}} + \hat{H}_{\text{aux}} \right] | \varphi_{s,\{j\}} \rangle_{\text{aux}} \\ &\approx -t_f \mathcal{F} \sum_{\langle i,j \rangle} \hat{f}_i^\dagger \hat{f}_j - \sum_{\alpha=1}^{N_n} \sum_j \frac{Z_\alpha V_0}{|\mathbf{j} - \mathbf{R}_\alpha|} \hat{f}_j^\dagger \hat{f}_j + \sum_{\text{all}\{j\}} E_{s,\text{aux}}(\{j\}) |\{j\}\rangle \langle \{j\}|, \end{aligned} \quad (6.22)$$

where we see how the auxiliary atomic state has two effects over the fermionic Hamiltonian. First, the fermionic kinetic energy gets renormalized by the Franck-Condon coefficient:

$$\mathcal{F} = \langle \varphi_{s,\{j\}} | \varphi_{s,\{i\}} \rangle_{\text{aux}}. \quad (6.23)$$

This is, the overlap between the bosonic states for two fermionic configurations $\{j\}, \{i\}$ in which all the fermions have the same position, except one that is displaced to a nearest neighbour position. As we will see, \mathcal{F} can be considered independent of the particular position occupied by the fermions.

Second, and more importantly, a position-dependent energy-term which, in principle, depends on all the fermion positions, being therefore $2N_e$ -body operator. However, when $E_{s,\text{aux}}(\{j\})$ can be written as a sum of pairwise contributions, i.e.,

$$E_{s,\text{aux}}(\{j\}) = \sum_{\substack{m,n=1, \\ m \neq n}}^{N_e} V(\mathbf{j}_m - \mathbf{j}_n), \quad (6.24)$$

so that the term of Eq. (6.22) reduces to a density-density operator,

$$\hat{H}_{\text{eff}} \approx \hat{H}_f + \sum_{\substack{m,n=1, \\ m \neq n}}^{N_e} V(\mathbf{j}_m - \mathbf{j}_n) \hat{f}_{j_m}^\dagger \hat{f}_{j_n}^\dagger \hat{f}_{j_m} \hat{f}_{j_n}, \quad (6.25)$$

which would mimic the Coulomb potential found in the quantum chemistry Hamiltonian of Eq. (6.3) if $V(\mathbf{j}_m - \mathbf{j}_n) = V_0/|\mathbf{j}_m - \mathbf{j}_n|$, with $V_0 > 0$ in order to be repulsive.

In the following, we will present two different schemes aimed at inducing an effective long-range repulsion among fermions trapped in a 2D lattice. These simple schemes will later be instrumental in Chapter 7 to obtain an effective Coulomb-like repulsion in 3D. There, we will apply this same general formalism and discuss in greater detail the conditions needed for this derivation to be valid, as well as candidate experimental implementations.

6.5.2 Scheme I: a single bosonic mediator

First, we start with a simple scheme where we use an additional bosonic atom trapped in an optical lattice potential with the same geometry as the fermions. In this scheme, we only consider one of the bosonic internal states, $|b\rangle$ and, as they coexist in the same lattice sites, elastic scattering processes between the bosonic and

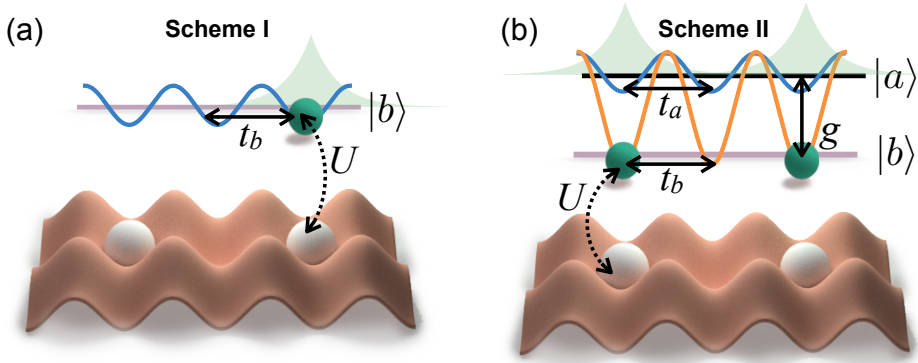


FIGURE 6.5: (a) A single atom (green) is used. It tunnels with constant t_b through a lattice with the same spacing as the fermionic one. There is an on-site repulsion with strength U when the mediating atom occupies the same site as the fermion. (b) We use as many mediating atoms as electrons need to be simulated (2 in the case of the figure). The on-site repulsion with the fermions now appears in a different internal level b , whose tunneling is slower as compared to level a , using a state-dependent lattice. Both levels are coherently coupled with coupling constant g .

fermionic atoms occupying the same position can induce an on-site repulsion U , as in Eq. (6.17). This boson is also allowed to tunnel at a rate t_b to nearest-neighboring sites [see Fig. 6.5(a)],

$$\hat{H}_{I,\text{aux}} = -t_b \sum_{\langle i,j \rangle} \hat{b}_i^\dagger \hat{b}_j, \quad (6.26)$$

where $\hat{b}_j^{(\dagger)}$ represents the annihilation(creation) of auxiliary atoms at positions \mathbf{j} , and t_b is their effective tunneling amplitude to the nearest neighbouring site.

Note that this Hamiltonian can be easily diagonalized in momentum space by introducing periodic boundary conditions, so that $\hat{H}_{I,\text{aux}}$ reads as,

$$\hat{H}_{I,\text{aux}} = \sum_{\mathbf{k}} \omega_{\mathbf{k}} \hat{b}_{\mathbf{k}}^\dagger \hat{b}_{\mathbf{k}}, \quad (6.27)$$

where $\hat{b}_{\mathbf{k}}^\dagger = \frac{1}{(2\pi)^{D/2}} \sum_{\mathbf{j}} \hat{b}_j^\dagger e^{i\mathbf{k}\mathbf{j}}$, and $\hat{b}_{\mathbf{k}} = \frac{1}{(2\pi)^{D/2}} \sum_{\mathbf{j}} \hat{b}_j e^{-i\mathbf{k}\mathbf{j}}$, are the atomic creation and annihilation operators in momentum space, and $\omega_{\mathbf{k}} = -2t_b \sum_{\alpha=x,y} \cos(k_\alpha)$ their corresponding eigenenergies for a given momentum vector $\mathbf{k} = (k_x, k_y)$ in units of a^{-1} , with $k_\alpha \in \{2j\pi/\bar{N}_M \text{ for } j = 1 \dots \bar{N}_M\}$, and $\alpha \in \{x, y\}$.

For the purpose of this section, we will focus on a single auxiliary atom present in the lattice. In this case, one can write an ansatz for its wavefunction $|\varphi_{m,\{\mathbf{j}\}}\rangle_{\text{aux}} = \sum_{\mathbf{k}} \varphi_{m,\{\mathbf{j}\}}(\mathbf{k}) \hat{b}_{\mathbf{k}}^\dagger |\text{vac}\rangle$ that can be used to find their corresponding eigenenergies,

$$\left[U \sum_{\{\mathbf{j}\}} \hat{b}_j^\dagger \hat{b}_j + \hat{H}_{I,\text{aux}} \right] |\varphi_{m,\{\mathbf{j}\}}\rangle_{\text{aux}} = E_m(\{\mathbf{j}\}) |\varphi_{m,\{\mathbf{j}\}}\rangle_{\text{aux}}. \quad (6.28)$$

In what follows, we analyze first the case of having a single fermion in the system

where we will see the emergence of a bound state of the auxiliary atom around the fermionic position [331–333].

Single boson localized around one fermion

If only a single fermion is present at the system at position \mathbf{j}_0 , then Eq. (6.28) leads to the following equation:

$$\omega_{\mathbf{k}} \varphi_{I,\mathbf{j}_0}(\mathbf{k}) + U \varphi_{I,\mathbf{j}_0}(\mathbf{0}) = E_{I,B} \varphi_{I,\mathbf{j}_0}(\mathbf{k}), \quad (6.29)$$

where $\varphi_{I,\mathbf{j}_0}(\mathbf{j}) = \overline{N}_M^{-1} \sum_{\mathbf{k}} e^{-i\mathbf{k}\mathbf{j}} \varphi_{I,\mathbf{j}_0}(\mathbf{k})$ describes the single boson localized around the fermion and its bound state energy $E_{I,B}$ is determined by

$$U^{-1} = \frac{1}{\overline{N}_M} \sum_{\mathbf{k}} \frac{1}{E_{I,B} - \omega_{\mathbf{k}}}, \quad (6.30)$$

which has a bound-state solution for the auxiliary atom whose energy lies above the scattering spectrum, i.e., $E_{I,B} > 4t_b$. Its associated wavefunction in the position representation, $|\varphi_{I,\mathbf{j}_0}\rangle = \sum_{\mathbf{r}} \varphi_{I,\mathbf{j}_0}(\mathbf{r}) \hat{b}_{\mathbf{r}}^\dagger$ reads as,

$$\varphi_{I,\mathbf{j}_0}(\mathbf{r}) = \frac{1}{\overline{N}_M \sqrt{\mathcal{N}}} \sum_{\mathbf{k}} \frac{e^{i\mathbf{k}\cdot(\mathbf{r}-\mathbf{j}_0)}}{E_{I,B} - \omega_{\mathbf{k}}}, \quad (6.31)$$

with $\mathcal{N} = \frac{1}{\overline{N}_M} \sum_{\mathbf{k}} \frac{1}{(E_{I,B} - \omega_{\mathbf{k}})^2}$, where we have used the normalization relation, $\frac{1}{\overline{N}_M} \sum_{\mathbf{k}} |\varphi_{I,\mathbf{j}_0}(\mathbf{k})|^2 = 1$, and $\overline{N}_M = N_M^D$ denotes the number of sites in the optical lattice of the mediator.

The resulting effective Hamiltonian can now be mapped into the general expression of Eq. (6.22) by projecting on the bound state energy surface. Interestingly, the overlap of the bosonic bound states defines the effective Franck-Condon coefficient (6.23),

$$\mathcal{F} = \frac{1}{\overline{N}_m \mathcal{N}} \sum_{\mathbf{k}} \frac{e^{-i\mathbf{k}_x}}{(E_{I,B} - \omega_{\mathbf{k}})^2}, \quad (6.32)$$

of the bound boson-fermion pair, which renormalizes the original fermionic tunneling t_f . Since the only effect of this term is to renormalize the kinetic energy, we will omit the tilde labelling throughout this Chapter, $\tilde{t}_f = t_f \mathcal{F} \rightarrow t_f$.

Single boson localized around two fermions

Let us now explain what occurs in the case where two fermions are placed at positions $\{\mathbf{j}_1, \mathbf{j}_2\}$. Solving the time-independent Schrödinger Eq. (6.28), one obtains,

$$\omega_{\mathbf{k}} \varphi_{\lambda,\mathbf{j}_{1,2}}(\mathbf{k}) + C_1 e^{-i\mathbf{k}\mathbf{j}_1} + C_2 e^{-i\mathbf{k}\mathbf{j}_2} = E_{\lambda} \varphi_{\lambda,\mathbf{j}_{1,2}}(\mathbf{k}), \quad (6.33)$$

with parameters, $C_{\alpha} = \frac{U}{N} \sum_{\mathbf{k}} e^{i\mathbf{k}\mathbf{j}_{\alpha}} \varphi_{\lambda}(\mathbf{k})$. Here, one can find not only one, but two bound-state solutions, i.e., with energies $E_{\pm}(\{\mathbf{j}\}) > 4t_b$, and whose wavefunction in

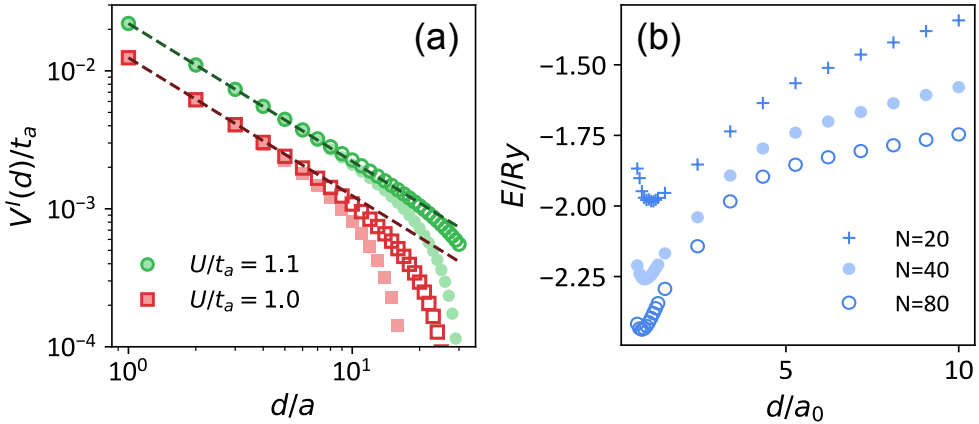


FIGURE 6.6: (a) Energy of the single-boson bound state described by the first scheme Eq. (6.26) as the number of sites $|\mathbf{j}_{12}| = d/a$ separating two fermions is modified. Here, we use an imaginary time evolution method (ITE, see Appendix B.3.2 for details). Dashed lines follow the scaling $V_{I,0}/(d/a)$. (b) Ground state energy of the simulated Hamiltonian for H_2 for different lattice sizes and the effective potential $V_I(d)$.

momentum space reads as,

$$\varphi_{\pm, \mathbf{j}_{1,2}}(\mathbf{k}) \propto \frac{e^{-i\mathbf{k}\mathbf{j}_1} \pm e^{-i\mathbf{k}\mathbf{j}_2}}{E_{\pm}(\{\mathbf{j}\}) - \omega_{\mathbf{k}}}. \quad (6.34)$$

When transforming these expressions into real space, one can see that they correspond to the combination of states localized around the fermionic positions $\{\mathbf{j}\}$. However, as explained in the previous section [see Eq. (6.24)], what governs the effective induced interaction between fermions is the spatial dependence of the eigenenergies $E_{\pm}(\{\mathbf{j}\})$, which can be calculated from,

$$U^{-1} = \frac{1}{N_M} \sum_{\mathbf{k}} \frac{1 \pm e^{i\mathbf{k}\cdot\mathbf{j}_{12}}}{E_{I\pm}(\{\mathbf{j}\}) - \omega_{\mathbf{k}}}, \quad (6.35)$$

where $\mathbf{j}_{12} = \mathbf{j}_1 - \mathbf{j}_2$. The shape of this energy depends on both the symmetric/antisymmetric character of the wavefunction, and whether the solution is found above/below the scattering spectrum ($\omega_{\mathbf{k}}$), which can be tuned by modifying U/t_b . By numerical inspection, we observe that to obtain a repulsive interaction we must use the symmetric state and tune the parameters such that $E_{I+}(\{\mathbf{j}\}) > \omega_{\mathbf{k}}$. Equating (6.30) and (6.35), the energy of the symmetric bound-state can be expressed as,

$$E_{I,+}(\{\mathbf{j}\}) \approx E_{I,B} + V_I(\mathbf{j}_{12}), \quad (6.36)$$

where $E_{I,B}$ is the bound-state energy associated to a single fermion [see Eq. (6.30)] and,

$$V_I(\mathbf{j}_{12}) \approx \frac{1}{N_B N_M} \sum_{\mathbf{k}} \frac{e^{i\mathbf{k}\cdot\mathbf{j}_{12}}}{E_{I,B} - \omega_{\mathbf{k}}}. \quad (6.37)$$

For separations $|\mathbf{j}_{12}| \ll 0.06 e^{2\pi t_b/U} \ll N$, the resulting effective spatial dependence $V_I(\mathbf{j}_{12})$ admits an approximate solution in 2D (see Appendix B.1),

$$V_I^{2D}(d) \approx V_{I,0}^{2D} / |\mathbf{j}_{12}|, \quad (6.38)$$

where $V_{I,0}^{2D} \approx 6.4e^{-2\pi t_b/U} t_b$. This simple scheme then mediates an effective repulsion between the two fermionic atoms that scales with their separation as $1/|\mathbf{j}_1 - \mathbf{j}_2|$, matching the dependence of the distance of 3D molecular interactions, but now restricted to 2D, as we also mimic for the nuclear potential⁷. We illustrate the spatial dependence of this potential and its effect in the 2D H_2 molecule in Figs. 6.6(a-b), respectively. There, one can observe molecular potentials even for relatively small lattices and assess the error. The continuum limit is obtained in a regime similar to the H_2^+ molecule case. Let us also mention here that when $t_b > 0$, there is an additional checkerboard phase pattern in the spatial dependence $V_I(\mathbf{j}_{12})$ that appears because the closer energy modes of the upper band-edge of $\omega_{\mathbf{k}}$ have $\pm\pi$ -momenta. Therefore, if one wants the fermion not to be sensitive to it, we require the spacing of the auxiliary atom lattice to be half the one of the fermions. Another option consists on working with an excited energy band that shows $t_b < 0$ [334], so that this checkerboard phase pattern does not appear.

As one increases the number of fermionic atoms, one can however see that this mediated pairwise repulsion does not hold when more than two fermions are present. To reach this scalability for $N_e > 2$, let us now introduce a second scheme for the bosonic mediator.

6.5.3 Scheme II: N_e bosonic mediators

One of the problems of the previous proposal is the impossibility of independently tuning the strength and range of the interactions, since there is only a single tunable parameter (U/t_b). Here, we will show how to harness the latest advances in state-dependent optical lattices [335–339] to gain that tunability. This proposal is scalable, at the price of modifying the scaling of the repulsive interaction.

The idea consists of assuming that one can engineer two very different potentials for two long-lived states of the auxiliary atoms that we label as a and b (see Fig. 6.5(b) for a scheme), such that when the atoms are in state b , they tunnel at a much slower rate, t_b , than when they are in state a , i.e., $t_a \gg t_b$. These states can be either the hyperfine states of an Alkali specie, or the metastable excited states of alkaline-earth ones, as we will detail more in Section 7.6. What is important is that these states can be coherently coupled either through a two-photon Raman transition or a direct one with effective coupling amplitude g and detuning Δ . Like this, the global internal dynamics for the auxiliary atom is described by the following Hamiltonian:

$$\begin{aligned} \hat{H}_{\Pi,\text{aux}} = & \Delta \sum_{\mathbf{j}} \hat{b}_{\mathbf{j}}^\dagger \hat{b}_{\mathbf{j}} - t_a \sum_{\langle i,j \rangle} \hat{a}_i^\dagger \hat{a}_j + g \sum_{\mathbf{j}} (\hat{b}_{\mathbf{j}}^\dagger \hat{a}_{\mathbf{j}} + \text{H.c.}) \\ & - t_b \sum_{\langle i,j \rangle} \hat{b}_i^\dagger \hat{b}_j + \frac{W}{2} \sum_{\mathbf{j}} \hat{b}_{\mathbf{j}}^\dagger \hat{b}_{\mathbf{j}}^\dagger \hat{b}_{\mathbf{j}} \hat{b}_{\mathbf{j}}. \end{aligned} \quad (6.39)$$

⁷Note that this choice of nuclear potential differs from the one encountered in a flatland world, in which Coulomb's law leads to interactions that scale as $\propto \log(r)$.

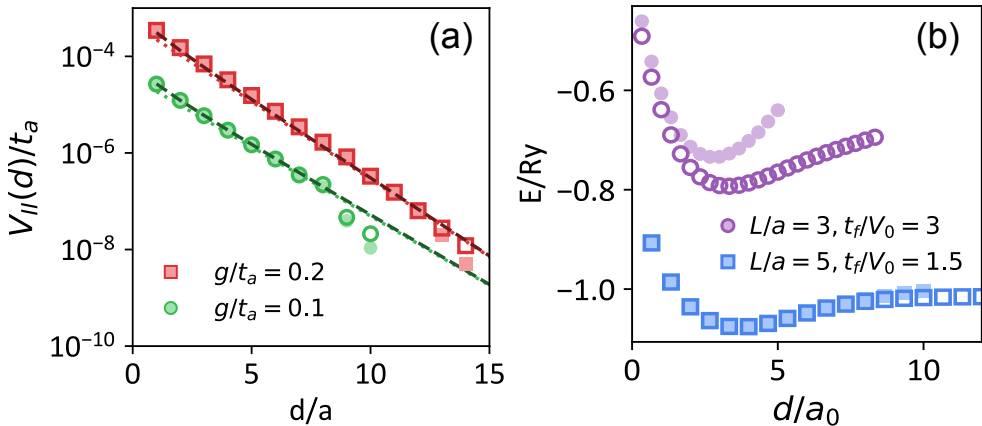


FIGURE 6.7: (a) Calculation of the repulsion mediated by the second scheme (6.39) between two fixed fermions separated d/a sites (markers), using ITE. Dashed lines follows the analytical approximation of Eq. (6.40). Edged markers corresponds to $N = 80$ and coloured ones to $N = 40$. Here, $U = 4.1 t_a$. (b) Molecular potential for a "pseudomolecule" of hydrogen, where both nuclear attraction and electronic repulsion follow the exponential scaling (6.40). Here, edged markers represent $N = 60$, coloured ones $N = 30$, and $L_{II}/a = (2\sqrt{\delta_{II}}/t_a)^{-1}$.

Using this Hamiltonian, one can solve again Eq. (6.28) for two fermions in a configuration $\{j\}$, but now replacing $\hat{H}_{I,aux} \rightarrow \hat{H}_{II,aux}$. Still, if one increased the number of fermionic atoms in the lattice while maintaining a single mediating boson, one would see that not all interactions among pairs of fermions are equally weighted, precluding scalability. Intuitively, it is more favourable for the mediating atom to localize among the pair of fermions that are closer to each other, rather than in an equal superposition, so that not all interaction are equally considered. We will provide more evidence in Section 7.4.3 for a 3D example.

To prevent this effect, here we include as many mediating bosonic atoms as electrons need to be simulated [see Fig. 6.5(b)]. In particular, we are interested in the regime in which both levels are weakly coupled $g \ll \Delta$, and when the atomic states trapped in the a lattice hop faster than in any of the other levels [339]: $t_a \gg t_b \gg t_f$, which to trace-out the effect of the mediating atoms and write an effective Hamiltonian for the fermions (6.25). By using as many bosonic atoms as fermions, the hard-core boson repulsion, $W \gg t_b$, leads to a bound state in which all fermionic sites are equally occupied, getting a configuration in which the repulsion among each pair of atoms is equally weighted, as required by Eq. (6.18). For this configuration, the pair-wise mediated interaction scales as,

$$V_{II}^{2D}(d) \approx V_{II,0}^{2D} e^{-2d\sqrt{\delta_{II}}/(a\sqrt{t_a})}, \quad (6.40)$$

for $d\sqrt{\delta_{II}}/(a\sqrt{t_a}) \gg 1$, where $V_{II,0}^{2D} \approx \frac{g^4}{8\pi t_a^2 \delta_{II}}$, and $\delta_{II} = U - 4t_a + \mathcal{O}(g^2/\Delta)$, (see Appendix B.2).

While this exponential scaling differs from the molecular Hamiltonian observed in nature, the model already captures the key features of the interactions appearing in molecular chemistry: nuclear attraction and electronic repulsion. It is then expected to reveal some of the features of chemical systems, including their

electronic correlations. In Fig. 6.7(a), we show the effective repulsive potential induced by the second scheme for different values of detuning δ_{II} , which is tunable and can be used to control the characteristic length of the interaction. This repulsion can then delocalize over several sites and allows one to design non-local interactions. In Fig. 6.7(b), we illustrate the effect that this modified effective repulsion controlled by δ_{II} has on two fermionic atoms hopping in the lattice, whose dependence on the distance is also mimicked by the tunable attractive nuclear interaction. This leads to a molecular potential of a "pseudomolecule" of hydrogen, where the bonding length and dissociation limit are observed.

6.6 Conclusions and outlook

To sum up, in this Chapter we have shown how ultracold atoms moving in 2D optical lattices can be used to simulate simplified models for quantum chemistry in today's experimental setups. We have observed that early experiments with a few simulating atoms can pursue the timely goal of describing the simplest discretized versions of an atom and a molecule, with repulsive interactions that are experimentally accessible with state-of-the-art setups. Such simulators open up a number of possibilities for further research. First, they provide an experimental platform for which numerical methods used in quantum chemistry can be adapted and benchmarked. Lessons learnt from these simulators, could then be transferred back into improved algorithms for quantum chemistry. Second, one of the main challenges of these discretized 2D simulators is that their solutions approach the continuum result slower than in the 3D case. Fully characterizing this scaling may well lead to improved protocols that are less sensitive to the system size. In fact, we will introduce some of these protocols in the next Chapter, where we extend these schemes to three dimensions.

Chapter 7

Towards 3D analog quantum chemistry simulation

” True originality consists in returning to the origin. Those who seek out the laws of Nature in order to fashion new works collaborate with the Creator. Those who copy do not.

— Antoni Gaudí

(Catalan architect, 1852-1926)

In this Chapter, we show how to extend the previous two-dimensional toy simulations for quantum chemistry to a three-dimensional simulator that mimics both the attractive and repulsive forces appearing in real-life chemistry. For this purpose, we bridge two paradigmatic systems, namely, ultra-cold atoms in optical lattices [133, 145, 338] and cavity QED [95, 114, 340–342]. The key ingredient to mediate the required long-range Coulomb-like interaction is to trap another atomic species in the Mott insulator regime, with several internal states such that its spin excitations mediate effective forces between the simulated electrons. While the setup is discrete and finite, we show that precise results can be obtained for simple molecules with moderate lattice sizes.

7.1 Introduction

As introduced in Section 6.1, one of the main goals of quantum chemistry is to obtain the low energy behaviour of N_e electrons and several nuclei when the positions, \mathbf{R}_α , of the nuclei are fixed. Using a cubic discretization in real space associated to the $\bar{N} = N^3$ sites of a cubic optical lattice, the electronic Hamiltonian to solve contains the three terms, $\hat{H}_{\text{qc}} = \hat{H}_{\text{kin}} + \hat{H}_{\text{nuc}} + \hat{H}_{e-e}$, associated to the kinetic energy of the electrons (6.12), their attraction to the nuclei (6.13) and electron-electron repulsion (6.18), respectively. In 3D, the connection of the length/energy scales of the discrete Hamiltonian \hat{H}_{qc} and the continuum three-dimensional one is now given by,

$$a_0^{(3D)}/a = 2t_f/V_0 \quad \text{and} \quad \text{Ry}^{(3D)} = V_0^2/(4t_f), \quad (7.1)$$

where $a_0^{(3D)}$, a and $R_y^{(3D)}$ are the Bohr radius, lattice spacing, and Rydberg energy, respectively¹. Thus, for the simulator to work, one needs to be in a regime,

$$(a) \ 1 \ll 2t_f/V_0 \ll N/N_e^{1/3},$$

such that the first inequality prevents discretization effects, and the second guarantees that the molecule fits in the volume of the simulator.

Following the discussion in Section 6.3, our three-dimensional simulator will be based in the following ingredients: i) cold spin-polarized fermionic atoms hopping in a 3D optical potential to play the role of electrons [145]. In particular, we consider spinless fermions, and the spin degree of freedom can be included using an extra internal level [343]. ii) Additional potentials to emulate the nuclei attraction. Since this is a single-particle Hamiltonian, it can be created through optical Stark-Shifts with an adequate spatial modulation. For example, in Section 7.2 we show that one can use holographic techniques with judiciously optimized phase masks to engineer a Coulomb-like spatial potential at the fermionic positions in 3D. In Section 7.3, we further analyze the errors associated to the discretization and finite-size of the lattice, and present a strategy that helps mitigating those limitations. iii) The most difficult part is to simulate \hat{H}_{e-e} (6.18), since it involves repulsive interactions between the fermions with a $1/r$ dependence. Inspired by how virtual photons mediate Coulomb interactions in QED, in Section 7.4 we extend the strategies introduced in Chapter 6 to mediate effective repulsion between the simulated fermions, now in 3D. We show that a spin excitation of another atomic species forming a Mott insulator can mediate the desired Coulomb forces between fermions. We devote Section 7.5 to benchmark the simulation of simple atoms and molecules (He, H₂ and HeH⁺), and analyze the role of finite-size effects for state-of-the-art lattice sizes. In Section 7.6, we finally discuss some practical issues about the implementation of these ideas.

7.2 Nuclear attraction

Following Section 6.3.2, the nuclear attraction term \hat{H}_{nuc} can be simulated by a position dependent shift ε_j , whose expression in terms of the Wannier functions reads as (4.13),

$$\varepsilon_j = \int d\mathbf{r} |w_j(\mathbf{r})|^2 V_{\text{aux}}(\mathbf{r}) \approx V_{\text{aux}}(\mathbf{j}). \quad (7.2)$$

Thus, in order to match the nuclear attraction term of the quantum chemistry Hamiltonian in Eq. (6.2), we *just* require that $V_{\text{aux}}(\mathbf{r})$ has the shape of the nuclear Coulomb attraction, at least, at the optical lattice minima \mathbf{j} where the fermions can hop. To obtain that, one can add a red-detuned spatially shaped electric field beam, $\mathbf{E}_\alpha(\mathbf{r})$, for each of the nuclei we want to simulate, such that the induced light-shift generates an optical potential with the shape,

$$V_{\text{aux}}(\mathbf{j}) = - \sum_{\alpha=1}^{N_n} \frac{|\mathbf{E}_\alpha(\mathbf{j})|^2}{\delta_\alpha} \approx - \sum_{\alpha=1}^{N_n} \frac{Z_\alpha V_0}{|\mathbf{j} - \mathbf{R}_\alpha|}, \quad (7.3)$$

¹Note that different factors appear when compared to the 2D case (6.14) due to the additional third dimension. In the rest of this Chapter, we will omit the (3D) label.

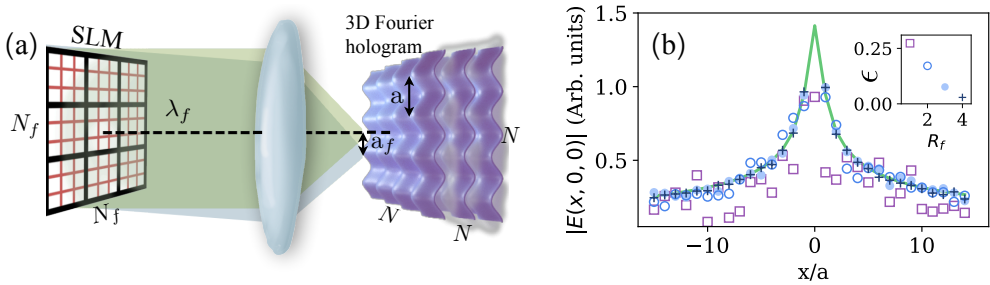


FIGURE 7.1: (a) Schematic representation of the holographic approach. A monochromatic laser beam with wavelength λ_f is reflected into a spatial light-modulator (SLM) which imprints a complex phase pattern in a two-dimensional grid with $N_f \times N_f$ sampling points. A lens creates a 3D Fourier hologram in a volume around its focal point where the fermionic optical lattice of $N \times N \times N$ sites and spacing a is placed. The minimum distance in which the electric field can be modulated in the 3D hologram, a_f , depends on the optical properties of the setup, but it is always lower-bounded by the diffraction limit of light $a_f \geq \lambda_f/2$. As shown in Ref. [344], intensity of the field at each point is determined by the Fourier Transform of the phase mask in the corresponding direction. (b) Linear cut of one of the calculated electric field amplitude at the center of the lattice after the iteration process of the GS algorithm for refining factors $R_f \in (1 - 4)$ (see text for definition). Green line follows the desired Coulomb potential, $V_0/|\mathbf{r}|$, and different markers are used for each refining factor, as indicated in the inset. *Inset* shows the average normalized error for 30 random initializations of the algorithm.

where V_0 is the overall energy scale of the potential controlled by the intensity of the laser and/or detuning δ_α .

The non-trivial part here consists in obtaining the electric fields $\mathbf{E}_\alpha(\mathbf{r})$ with the desired intensity pattern, $|\mathbf{E}_\alpha(\mathbf{r})|^2$, as the intensity masks introduced in the 2D case (see Section 6.3.2) cannot be directly extended to three dimensions. One alternative is harnessing the advances in 3D holographic techniques that allow one to shape the electromagnetic field in a given volume by imprinting complex phase patterns in a two-dimensional grid and using Fourier optics to propagate them to the position of the optical lattice [345]. These 3D holograms have already enabled, for example, trapping Rydberg atoms in exotic three-dimensional (3D) configurations [37].

As introduced in Section 2.1.1, holographic techniques allow one to engineer three-dimensional intensity patterns at will [345]. For this, a monochromatic laser beam with wavelength λ_f is shine into a SLM that imprints a non-uniform phase pattern in a grid with $N_f \times N_f$ pixels. As schematized in Fig. 7.1(a), the reflected laser field is then focused with a high-numerical aperture lens to generate the desired potential. The minimum spatial resolution (a_f) in which the electric field can be modulated depends on both the optical setup and the wavelength of the incident laser λ_f , but it will always be lower bounded by the diffraction limit of light $a_f \geq \lambda_f/2$. This motivates the use of high numerical aperture lenses [31, 346, 347] to reduce the waist of the holographic beam. We will label as $R_f = a/a_f$ to the ratio between the interatomic distance in the optical lattice and the spatial resolution of the hologram.

The first step to design 3D holograms consists in finding the appropriate phase pattern that should be imprinted in the $N_f \times N_f$ grid of the SLM to obtain the desired electric field intensity. Fortunately, there are many constructive algorithms to do it [348–350]. Inspired by the original GS algorithm [68, 344, 351, 352], here we follow the one of Ref. [344], which is adapted to modulating 3D electric fields in

discrete points of space. This algorithm initially starts by a random set of phases in the $N_f \times N_f$ grid, and then iteratively looks for a solution that both approximates a given intensity pattern at the fermionic positions, V_j^0 , with the only restriction of satisfying Maxwell's equations. That is, the \mathbf{k} -components of the beam of monochromatic light λ_f need to lie in the Ewald sphere of radius $k_f = 2\pi/\lambda_f$. The convergence of the solution can be monitored using the dimensionless factor:

$$\epsilon = \frac{1}{N} \sum_j \left| \frac{V_j - V_j^0}{V_j^0} \right|, \quad (7.4)$$

where V_j is the electric field intensity in position j obtained at an iteration of the algorithm and V_j^0 the targeted one. A key element for the convergence of the algorithm is the number of sampling points N_f of the grid, which for simplicity we will assume to be proportional to the number of optical lattice positions $N_f = R_f N$, choosing R_f as the proportionality factor. Like this, if $R_f > 1$ the hologram can find solutions where the electric field intensity is modulated also within the fermionic positions, which will facilitate the convergence of the algorithm.

In Fig. 7.1(b) we plot the result of applying this algorithm [344] for several (integer) values of R_f for the case of a single nucleus at the central position of the lattice. That is, when V_j^0 should have a Coulomb shape potential around the origin². We apply the GS algorithm to find the phase mask for a given (integer) R_f until the improvement of the relative error ϵ from one iteration to the next is below 10^{-4} . Then, we plot in the main panel a linear cut of the 3D electric field amplitude at the final iteration V_j (with markers) compared to the targeted one V_j^0 (in solid green line), and its corresponding relative error ϵ in the inset. In purple squares we plot the case $R_f = 1$ where we observe that the agreement with the desired potential leads to a final error above 10%. However, as we increase the number of sampling points N_f using larger R_f , the algorithm is able to find better solutions, as clearly indicated by the decrease of the final relative error as R_f increases. For example, with $R_f = 4$ (blue crosses), the potential finally obtained captures the desired intensity profile at the positions of the fermions, obtaining a normalized relative error of $\epsilon \approx 0.02$. The most obvious way to increase R_f consists in either increasing the optical lattice period or using smaller wavelengths for the focused holographic laser. One option is to use alkaline-earth atoms which have a level structure that combines telecom transitions with ultraviolet (400 nm) ones (1.4 μm) [353], although we recognize that going to large R_f will be experimentally challenging and will require the use of innovative ideas, e.g., developing novel tweezers techniques [31]. For this reason, in Section 7.3 we will discuss the impact of imperfect potential in the precision of the simulators, showing how already $\epsilon \sim 0.1$ can provide energy errors smaller than 1% for the simplest case of atomic hydrogen.

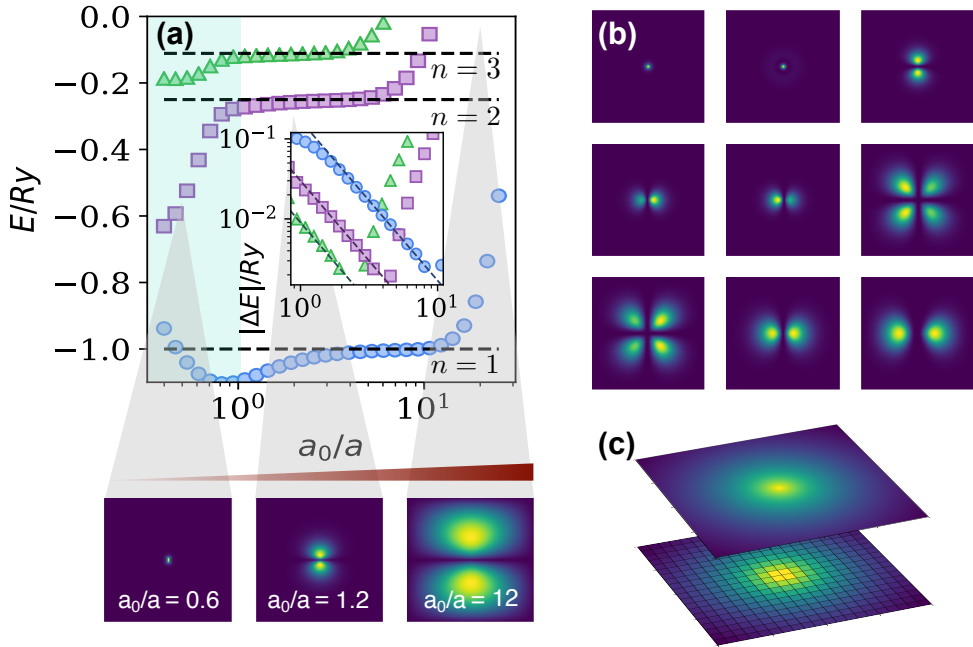


FIGURE 7.2: (a) Lowest-energy states for a cubic lattice of $N = 100$. of the continuum (dashed black lines) and the discrete Hydrogen atom Hamiltonian \hat{H}_f (color markers), associated to the principle quantum number $n = 1, 2, 3$. Their energy depends on the effective Bohr radius. Once atomic orbitals occupy more than a single site, $a_0/a > 1$, the spectrum approaches the analytical result $E_n = Ry/n^2$ (dashed lines), up to a critical size for which the finiteness of the lattice becomes relevant. For $n = 1$, these finite-size effects appear at around $a_0/a \approx 10$ for the present size. *Inset*, shows the difference between the calculated and analytic energy associated to these curves. Dashed line follows the scaling expected from discretization effects, shown in Eq. (7.6). (b) Axial cut in the central positions of the lattice is represented for the first 9 eigenstates of \hat{H}_{qc} for $t_f/V_0 = 2$, $N = 150$. (c) Appropriately choosing the Bohr radius, we show how the same orbital can be obtained with $N = 1000$ (up, $t_f/V_0 = 150$) or $N = 20$ (down, $t_f/V_0 = 3$), where the discretization of the system is more noticeable.

7.3 Errors: discretization, finite-size, and mitigation strategies

Up to now, we have shown that the dynamics of ultra-cold fermionic atoms in deep optical lattices ($s \gg 1$), and with an appropriate shaping of $V_{\text{aux}}(\mathbf{r})$ can mimic the single-particle part of the chemistry Hamiltonian (6.11),

$$\hat{H}_f = -t_f \sum_{\langle i,j \rangle} \hat{f}_i^\dagger \hat{f}_j - \sum_{\alpha=1}^{N_n} \sum_j \frac{Z_\alpha V_0}{|\mathbf{j} - \mathbf{R}_\alpha|} \hat{f}_j^\dagger \hat{f}_j. \quad (7.5)$$

Before showing how to simulate the electron repulsion part of the 3D quantum chemistry interactions in Eq. (6.18), in this section we will further provide intuition on how the chemistry energies and length scales translate into the cold-atom simulation, and which are the errors appearing due to two competing mechanisms: discretization and finite size effects, taking as a case of study the Hydrogen atom. Identifying the discretized [see Eq. (7.5)] and continuum Hamiltonians [see Eqs. 6.1-6.3], one obtains the natural correspondence of units shown in Eq. (7.1). There, we see that the effective Bohr radius in units of the lattice constant a_0/a , is defined by the ratio t_f/V_0 . In order to illustrate it, we plot in Fig. 7.2 the lowest energy spectrum of the discrete Hydrogen atom as a function of the effective Bohr radius a_0/a . The black dashed lines are the expected energies in the continuum Hamiltonian, i.e., $E_n = \text{Ry}/n^2$, whereas in the different colors are the different numerical energies for a fixed system size of $N = 100$ sites.

As we discussed for the 2D case in Fig. 6.3, here we see that by increasing the ratio t_f/V_0 and making the lattice larger, one approaches the continuum limit (dashed line), as intuitively expected. The optimal choice of t_f/V_0 does however depend on the atomic state one wants to represent. This dependence of the convergence to the continuum limit on the particular atomic and molecular orbital will be a commonplace of this method, and it also occurs for other basis representations [291]. In spite of this, by analyzing the sources of errors one can extract some general conclusions that can provide valuable information when performing the experiments:

- **Discretization effects.** Analyzing numerically the convergence to the correct result in Rydberg units: $\Delta E = |E - E_\infty|$ (see inset in Fig. 7.2), we found an heuristic scaling of the error given by:

$$\frac{\Delta E_{\text{dis}}}{\text{Ry}} \propto \left(\frac{a}{a_0}\right)^2 \propto \left(\frac{V_0}{t_f}\right)^2, \quad (7.6)$$

where the proportionality factor depends on the particular orbital studied. The observed quadratic scaling is more favourable than the one encountered in the 2D case, $(V_0/t_f)^{-1}$ (6.16). This can be justified by considering the errors introduced by the discretization of the derivative and the integrals in the

²As done previously, we always consider that the nuclei are centered in a position separated half-a-lattice constant away from the lattice sites to avoid the divergent behaviour. This will introduce an error in our simulation, as we will consider more in detail in the next subsection.

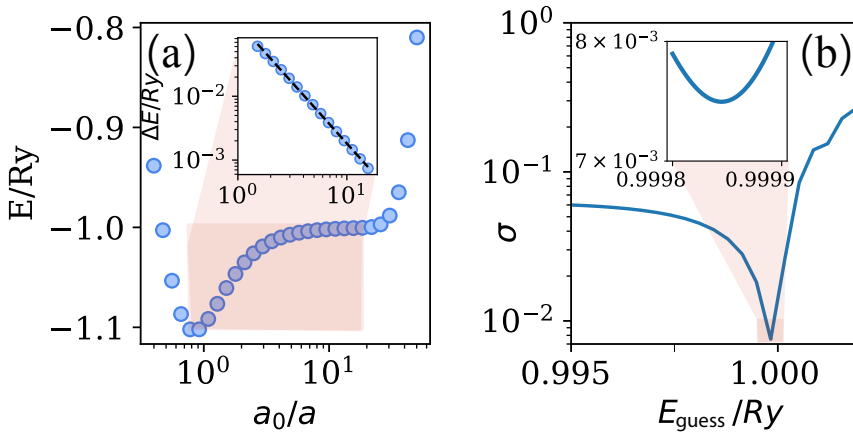


FIGURE 7.3: (a) Ground state of the discretized Atomic Hamiltonian depicted in Fig. 7.2, for different values of the effective Bohr radius and $N = 250$. Inset: example of the fitting of the energy difference to the continuum value $\Delta E = E - E_\infty$, following a polynomial regression of the form $\Delta E/\text{Ry} = c \cdot (a_0/a)^b$ for fitting parameters, c and b . In this example we have chosen the continuum value E_∞ to be 1Ry . The best candidate for the value in the continuum needs to be calculated, as one generally does not know it a priori. (b) More systematically, here we show the standard deviation σ in the determination of the fitting parameter b for different candidate values of E_{guess} . We identify the best choice of $E_{\text{guess}}/\text{Ry}$ as the one with the smallest deviation, E_∞ . In this simple example, one extrapolates the numerical result $E_\infty = 0.9998\text{Ry}$ (see inset), for the energy of $1s$ orbital. This is, a precision of 0.01% for this simple scenario, gaining one order of magnitude with respect to the precision one can directly achieve before finite-size effects appear.

kinetic and potential energy term, respectively, leading both to the same scaling presented in Eq. (7.6) (see Appendix C.1).

- **Finite size effects.** These errors can be associated to the part of the electron density that cannot be fitted within our system size. Since the Hydrogen orbitals decay exponentially with the principal quantum number n , one can estimate that the errors due to finite size effect decay exponentially with the ratio between the system size and the size of the orbitals, i.e., $\propto e^{-Na/(na_0)}$.

Even though these estimates were based on the Hydrogen atom, one can already extract important conclusions for the simulation of larger molecules. On the one hand, one can estimate the error scaling with electron density. Since each level with principal quantum number n can fit $2n^2$ electrons, an atom/molecule with N_e electrons is expected to occupy a maximum quantum number $n_{\text{max}} \propto N_e^{1/3}$, such that its estimated size will be $\sim N_e^{1/3} a_0/a$ sites. Thus, following Eq. (7.6), the discretization errors for such distances will scale with $\Delta E_{\text{dis}}/\text{Ry} \propto \rho_e^{2/3}$, where $\rho_e = N_e/\bar{N}$ is the electron density.

On the other hand, we can design an **extrapolation method** to obtain the energies with accuracies beyond the particular system size chosen and, importantly, without an *a priori* knowledge of the exact result. We illustrate the method in Fig. 7.3 for the ground state of Hydrogen, and in Section 7.5 we apply it as well to the case of multi-electron systems. The key steps go as follows: first, one calculates (or measures in the case of an experiment) the ground state energy for a fixed system

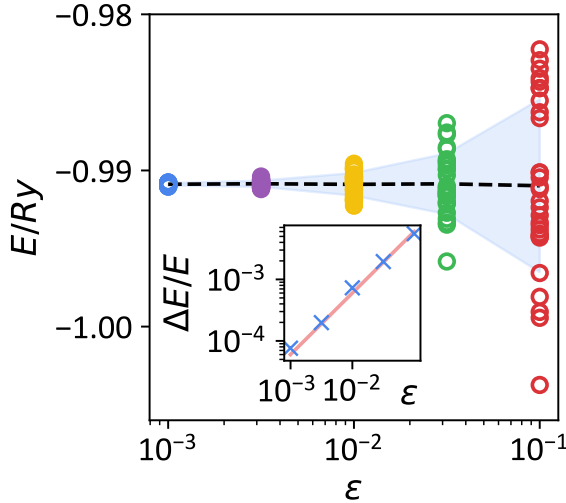


FIGURE 7.4: Ground-state energy of the 3D Hydrogen-like Hamiltonian for increasing values of the average normalized error of the nuclear potential, ϵ . 30 random iterations are considered for each choice of ϵ , showing the average value (dashed line) and standard deviation (coloured region). Inset: the relative error in the resulting energy follows a linear scaling with the normalized nuclear potential error, $\Delta E/E \approx 0.06\epsilon$ (red line). Parameters: $N = 60$, $t_f/V_0 = 1$.

size N and for several ratios a_0/a (panel a). Then, one defines $\Delta E/\text{Ry} = (E - E_{\text{guess}})/\text{Ry}$ for several values of E_{guess} (panel b) and fit the resulting function to a polynomial regression $\Delta E/\text{Ry} = c(a_0/a)^b$, with free fitting parameters b and c . We identify the right choice of the guess energy as the one with smallest standard deviation σ (panel c), that we will say it is the one of the continuum limit $E_\infty \equiv E_{\text{guess}}(\sigma_{\min})$. Using this procedure for a system size $N = 250$, we obtain $E_\infty = 0.9998\text{Ry}$, which is one order of magnitude better than the result one would obtain without extrapolation for this size (i.e., directly looking at the minimum value of E for that system size). For completeness, we also check that this value of E_∞ also leads to an exponent factor compatible with $b = -2$ (not shown), which is the error scaling consistent with Eq. (7.6). In Section 7.5, this will be the criterion used to identify the best estimation for atomic and molecular energies beyond the discretization of the lattice.

In addition to the errors caused by discretization and finite size effects, in Fig. 7.4 we further benchmark energy deviations in the Hydrogen ground-state caused by a relative normal error ϵ in the induced nuclear potential (see Section 7.2). For lattice size $N = 60$, we observe that $\epsilon \sim 0.1$ (compatible with $R_f = 2$ in Fig. 7.1), already provides an accuracy in the retrieved energy of order 1%.

7.4 Simulating electron repulsion in 3D optical lattices

In what follows, we will make use of the general formalism previously introduced in Section 6.5.1. First, we will devote Section 7.4.1 to motivate how working conditions can be derived from it. Next, in Sections 7.4.2 and 7.4.3 we will extend to 3D the two simplified setups previously introduced in Section 6.4, which will result

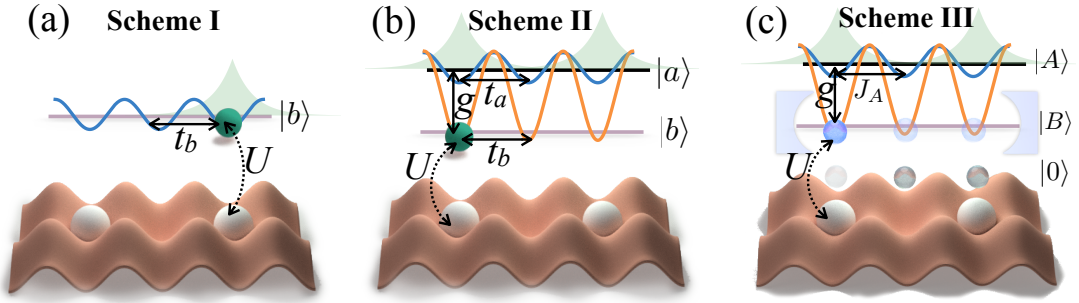


FIGURE 7.5: Schemes presented in this Chapter, to induce repulsion among fermionic cold atoms (white) trapped in a three-dimensional optical lattice (red, pictorially represented in a lower dimension for simplicity). (a) In *Scheme I* (Section 7.4.2), repulsion is induced by a single mediating atom (green) in a given internal state $|b\rangle$. This mediating atom tunnels with rate t_b , and experiences an on-site interaction with occupying the same lattice site as the fermionic atom. This induces a non-Coulomb and non-scalable repulsion for more than two fermionic atoms. (b) In *Scheme II* (Section 7.4.3), one relies on a second internal level of the mediating atom to reach the Coulomb-like potential. Both levels $|a\rangle$ and $|b\rangle$ are coupled with rate g , and tunneling rate depends on their state. (c) In *Scheme III* (Section 7.4.4) we use a different approach to achieve the Coulomb repulsion among an arbitrary number of atoms. Here, rather than a single atom, the mediating species is in a Mott phase, with exactly one atom occupation per site (translucent gray). While these atoms are fixed, an atomic excitation (coloured blue) $|A\rangle$ can propagate to a neighboring site through magnetic exchange. They are also coupled with rate g to another internal level $|B\rangle$, that is subject to a Raman-assisted cavity-mediated collective interaction, J_c , and a on-site repulsion U with fermionic atoms.

in slightly different repulsive potentials from the targeted one. Extending the discussion of the previous Chapter, a complete proposal is discussed in Section 7.4.4, where we also derive and numerically benchmark its perturbative working conditions. The motivation for this incremental discussion is two-fold: first, it allows one to understand the role of all the ingredients required in the final proposal; second, even though the models discussed in Sections 7.4.2 and 7.4.3 do not provide a fully scalable Coulomb-like interaction, they can be used as simpler, but still meaningful, experiments that can simulate chemistry-like behaviour and guide the way to the full proposal.

7.4.1 Working conditions for the general formalism

Previously, we introduced in Section 6.5.1 a general formalism to describe how the energy of the auxiliary species $E_{s,\text{aux}}(\{\mathbf{j}\})$ depends on the position of the fermions, $\{\mathbf{j}\}$, as it creates a bound-state, $|\varphi_s(\{\mathbf{j}\})_{\text{aux}}\rangle$, around them as a consequence of a contact interaction, $\hat{H}_{f\text{-aux}}$ (6.21). Let us now summarize then the conditions to achieve the needed fermionic repulsion:

- There should be one eigenstate $|\varphi_s(\{\mathbf{j}\})_{\text{aux}}\rangle$ from the Hamiltonian of Eq. (6.20), whose energy can be written as:

$$E_{s,\text{aux}}(\{\mathbf{j}\}) = \sum_{\substack{m,n=1, \\ m \neq n}}^{N_e} \frac{V_0}{|\mathbf{j}_m - \mathbf{j}_n|}, \quad (7.7)$$

where $V_0 > 0$ determines the strength of the effective repulsion between the electrons.

- For self-consistency, $|\varphi_s(\{\mathbf{j}\})_{\text{aux}}\rangle$ needs to be the dominant state of the Hilbert space of the auxiliary atoms dressing the fermionic configuration $\{\mathbf{j}\}$, so that the total state writes as $|\Psi\rangle = \sum_{\{\mathbf{j}\}} \psi(\{\mathbf{j}\}) |\{\mathbf{j}\}\rangle_f |\varphi_s(\{\mathbf{j}\})_{\text{aux}}\rangle$. Also, the different parts of the Hamiltonian ($\hat{H}_f, \hat{H}_{f\text{-aux}}, \hat{H}_{\text{aux}}$) should not couple significantly this state to the orthogonal ones $|\varphi_m^\perp(\{\mathbf{r}\})_{\text{aux}}\rangle$ of any given fermionic configuration. This means that, if any of the Hamiltonian parts \hat{H}_α connect $|\varphi_s(\{\mathbf{j}\})_{\text{aux}}\rangle$ to an state $|\varphi_m^\perp(\{\mathbf{r}\})_{\text{aux}}\rangle$, the transition should be prevented by a large enough energy gap between them, denoted by $\Delta_{m,r}$. Like this, we can upper-bound the error introduced by such couplings using perturbation theory:

$$\varepsilon_\alpha = \sum_{\text{all}\{\mathbf{r}\}} \sum_m \left| \frac{f \langle \{\mathbf{r}\} |_{\text{aux}} \langle \varphi_{m,\{\mathbf{r}\}}^\perp | \hat{H}_\alpha | \Psi \rangle}{\Delta_{m,r}} \right|^2, \quad (7.8)$$

which should of course satisfy:

$$\varepsilon_\alpha \ll 1, \quad (7.9)$$

for all $\alpha = f, f - \text{aux}, \text{aux}$. This provides a second working condition for the dynamics to be governed by the effective fermionic repulsion Hamiltonian of Eq. (6.18).

In what follows, we will introduce sequentially the different schemes for the interaction of the mediating atoms in 3D, \hat{H}_{aux} , until we obtain the desired repulsive, pair-wise, Coulomb potential between the fermionic atoms. If not particularly interested in the details, the reader may skip this part and jump into the resulting Yukawa-like potential of Eq. (7.43), as well as the working conditions (b-d) summarized in page 115.

7.4.2 Scheme I: Repulsion mediated by single atoms: non-Coulomb & non-scalable

Let us assume initially the simplest level configuration for the auxiliary atomic state. That is, it has only a single ground state level subject to an optical potential with the same geometry as the fermionic one, $\bar{N}_M = N_M^3$ sites, but with different tunneling rate [see Fig. 7.5(a)]. The resulting auxiliary Hamiltonian in this case reads as Eq. (6.26),

$$\hat{H}_{\text{I,aux}} = -t_b \sum_{\langle i,j \rangle} \hat{b}_i^\dagger \hat{b}_j, \quad (7.10)$$

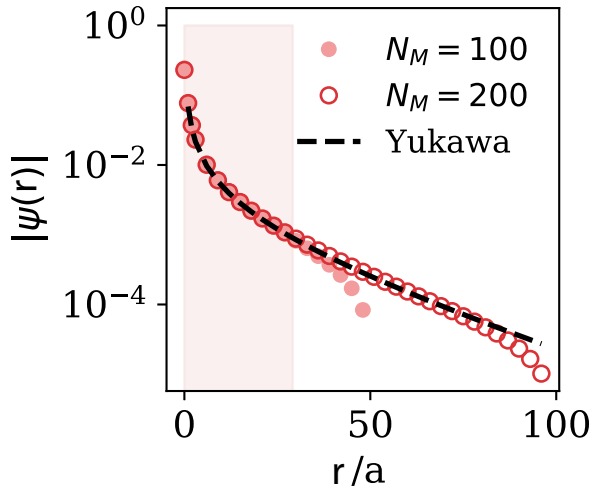


FIGURE 7.6: Radial wavefunction of the mediating auxiliary atom placed at $\mathbf{j}_0/a = \lfloor N_M/2 \rfloor [1, 1, 1]$ for lattice size $N_M = 100, 200$ and $U = 4t_b$. Displacements are studied in the x -axis, $\mathbf{j} = \mathbf{j}_0 + [r, 0, 0]$. Dashed line follows the Yukawa potential in Eq. (7.11). Shaded region indicates the region $r/a \leq L_I$ where Coulomb potential applies. Here, L_I is calculated using Eq. (7.12).

Extending to 3D the derivation in Section 6.5.2, we will see how this bound state can mediate a repulsive interaction when two or more fermions are hopping in a three-dimensional lattice that, unfortunately, does not have the correct spatial dependence presented in Eq. (7.7).

Single fermion

In this first scheme, one can obtain a closed expression for the bosonic bound-state as in Eq. (6.31). Taking the continuum limit, $N_M \rightarrow \infty$, to replace the summation by an integral, and making a quadratic expansion of the energy dispersion around the band-edges (see Appendix C.2.1), one obtains an analytical expression for the wavefunction that reads in 3D as,

$$\varphi_{B, \mathbf{j}_0}(\mathbf{r}) \propto \frac{e^{-|\mathbf{j}-\mathbf{j}_0|a/L_I}}{|\mathbf{j}-\mathbf{j}_0|}. \quad (7.11)$$

That is, a Yukawa-type localization around the fermionic position \mathbf{j}_0 with a localization length given by $L_I/a = \sqrt{E_{I,B}/t_b - 6}$ that, to leading order in t_b/U , reads as (see Appendix C.2.2),

$$L_I/a = (3.176 - 4\pi t_b/U)^{-1}. \quad (7.12)$$

Interestingly, this localization length can be tuned with the experimental parameters, i.e., changing U/t_b , and be made very large. In particular, the bound state can display a $1/r$ shape over the whole fermionic lattice as long as $L_I/a \gg N$.

These analytical formulae can be numerically benchmarked by solving Eq. (6.31) for the case of a single fermion and a finite 3D lattice size. This is done in Fig. 7.6

where we plot the spatial dependence of the numerically obtained wavefunction for two different system sizes: $N_M = 100$ and $N_M = 200$, represented with filled and empty circles, respectively, together with the Yukawa shape (in dashed black) predicted from Eq. (7.11). We have chosen $U/t_b = 4$ such that the expected length is $L_I/a \approx 29$, indicated by the shaded red region of the figure. From this figure we can extract two conclusions: first, the spatial wavefunction displays, as expected from Eq. (7.11), an approximate $1/r$ decay for short distances, i.e., $r < L_I$ (shaded red area). Second, for larger distances the spatial wavefunction follows the Yukawa shape of Eq. (7.11) until it becomes closer to the border. Thus, to observe the $1/r$ decay for the whole fermionic space we require that $N \ll L_I/a \ll N_M$.

An additional condition comes from reducing the coupling to non-orthogonal states, i.e., the condition of Eq. (7.9). In this case, only \hat{H}_f contributes as follows,

$$\varepsilon_f = \sum_m \left| \frac{t_f \langle \varphi_{m,j_0+1}^\perp | \varphi_{B,j_0} \rangle}{\Delta_{m,j_0+1,j_0}} \right|^2 \leq \frac{t_f^2}{\mathcal{N}_B \bar{N}_M} \sum_{\mathbf{k}} \frac{1}{(E_{I,B} - \omega_{\mathbf{k}})^4} \quad (7.13)$$

such that the condition $\varepsilon_f \ll 1$ translates into,

$$t_f/t_b \ll (a/L_I)^2, \quad (7.14)$$

providing the working condition that guarantees the separation of energy scales between the fermionic and auxiliary atom dynamics. Here, $j_0 + 1$ denotes a nearest-neighbor of j_0 , and we have made use of the calculations in Appendix C.2.2. This energy separation guarantees that the auxiliary atom will immediately follow the fermion as it hops through the lattice. As we already explained in the previous section, this auxiliary atom dressing renormalizes as well the fermion hopping by the Franck-Condon coefficient [see Eq. (6.23)]. For the nearest-neighbour hoppings, that are the only non-negligible ones in this case, this coefficient reads

$$\mathcal{F}_I = \langle \varphi_{B,j_0+1} | \varphi_{B,j_0} \rangle \approx e^{-a/L_I} \quad (7.15)$$

so that the fermionic hopping is less affected the more delocalized the auxiliary atom wavefunction is.

Two fermions

When two fermions are present at positions $\{\mathbf{j}_1, \mathbf{j}_2\}$, the energy of the auxiliary bound-state depends on their separation, $\mathbf{j}_{12} = \mathbf{j}_1 - \mathbf{j}_2$, as in Eq. (6.37)

$$V_I(\mathbf{j}_{12}) \approx \frac{1}{\mathcal{N}_B \bar{N}_M} \sum_{\mathbf{k}} \frac{e^{i\mathbf{k}\mathbf{j}_{12}}}{E_{I,B} - \omega_{\mathbf{k}}}, \quad (7.16)$$

which is the term that induces a position-dependent interaction between the fermions [see Eq. (7.7)]. Note as well the similarity between $V_I(\mathbf{j}_{12})$ and the bound-state wavefunction of the single-fermion case (Eq. (6.31)). Thus, we can also take the continuum limit of this expression to transform the sums into integrals and make a parabolic expansion of $\omega_{\mathbf{k}}$ to obtain an analytical formula of $V_I(\mathbf{j}_{12})$. In the long-distance limit, that is, when $|\mathbf{j}_{12}| \gg L_I/a$, the potential shows the same Yukawa

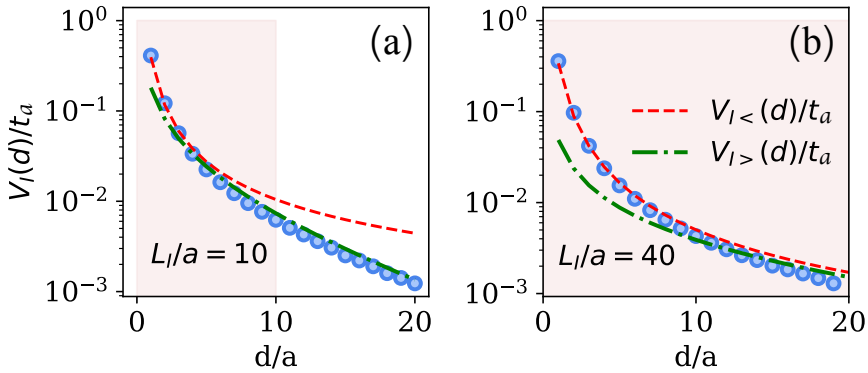


FIGURE 7.7: Comparison between the numerical calculation of $V_I(d)$ obtained from equating Eqs. (6.30) and (6.35) (round markers), as compared to the analytical expansions (7.17) (dashed lined) and (7.18) (dotted-dashed line), valid in the regimes $d/L_I \ll 1$ (coloured region) and $d/L_I \gg 1$, respectively. Parameters: $N_M = 120$.

shape,

$$V_{I,>}(\mathbf{j}_{12}) = V_{I,>}(|\mathbf{j}_{12}|) \approx \frac{2at_b}{|\mathbf{j}_{12}| \cdot L_I} e^{-|\mathbf{j}_{12}|a/L_I}. \quad (7.17)$$

Unfortunately, in the opposite limit, i.e., $|\mathbf{j}_{12}| \ll L_I/a$, where the shape should display the desired $1/|\mathbf{j}_{12}|$ profile, Eq. (7.16) expands as (see Appendix C.2.2),

$$V_{I,<}(\mathbf{j}_{12})/t_b \approx \frac{0.322}{|\mathbf{j}_{12}|^2} + \frac{0.724a}{|\mathbf{j}_{12}| \cdot L_I}. \quad (7.18)$$

In Fig. 7.7, these analytical expressions are numerically benchmarked by solving the bosonic Hamiltonian (6.28) in a finite system for two fermions separated by an increasing number of sites, and two different values of L_I . There, we observe how the energy spatial decay never displays the desired $1/|\mathbf{j}_{12}|$ scaling but rather the $1/|\mathbf{j}_{12}|^2$ predicted by Eq. (7.18). The intuition behind this limitation is that we do not have enough tunable parameters since U/t_b controls both the strength and the range of the interaction (L_I). Thus, when L_I is tuned to be large enough, the correction to the energy $E_{\pm}(\{\mathbf{j}\})$ is so strong that it induces a different spatial dependence from the $1/r$ shape.

For completeness, let us also mention that as the two fermions separate, the auxiliary atom wavefunction approximates a superposition of the single-boson density of Eq. (6.31) centered at each position, such that the Franck-Condon coefficient of Eq. (6.23) approximates as $\mathcal{F}_I \approx 0.5 \left(1 + e^{-a/L_I}\right)$. Additionally to the error in Eq. (7.13) caused by the coupling to states in the band due to \hat{H}_f , the condition on t_f/t_b derived for the single fermion case now includes an additional contribution given by Eq. (7.9) due to the coupling to the antisymmetric

bound-state. This additional contribution reads as,

$$\left| \frac{t_f \langle \varphi_{-(\mathbf{j}_1+1, \mathbf{j}_2)} | \varphi_{+(\mathbf{j}_1, \mathbf{j}_2)} \rangle}{E_+(\mathbf{j}_1, \mathbf{j}_2) - E_-(\mathbf{j}_1+1, \mathbf{j}_2)} \right|^2 \approx \left| \frac{t_f (1 - \mathcal{F}_1)}{4V_1(d)} \right|^2 \ll 1, \quad (7.19)$$

where, for $d/a \gg 1$, we have approximated $\langle \varphi_{-(\mathbf{j}_1+1, \mathbf{j}_2)} | \varphi_{+(\mathbf{j}_1, \mathbf{j}_2)} \rangle \approx 0.5(1 - \mathcal{F}_1)$. From the definition of the Franck-Condon coefficient [see Eq. (7.15)], in the limit $L_1/a \gg 1$, this can be approximated as $0.5a/L_1$. We observe that since the gap between the symmetric and antisymmetric state is given by $2V_1(|\mathbf{j}_{12}|)$, the condition becomes more demanding as the two fermions separate, since $V_1(|\mathbf{j}_{12}| \rightarrow \infty) \rightarrow 0$.

Ensuring that the symmetry of state is preserved irrespective of the fermionic positions will be one of the main motivations to introduce the cavity-assisted hoppings required for the model discussed in Section 7.4.4.

More than two fermions

Although we have just showed in the previous section that this auxiliary atom configuration will not be able to deliver the desired Coulomb potential for two fermions, let us here consider the general situation with N_f fermions to see that an additional complication arises, that is, that the eigenenergy $E_+(\{\mathbf{j}\})$ does not correspond to a pair-wise sum. Instead, the auxiliary atomic excitation tends to localize more strongly around those fermions closer to each other, making the proposal non-scalable. To illustrate this effect, in Fig. 7.8 we plot an example of a numerically calculated energy $E_+(\{\mathbf{j}\})$ when three fermions are placed in a triangular geometry and move the distance of one of them such that it goes from an equilateral configuration to an isosceles one. We plot the ratio between the population in the fermionic sites at the apex of the triangle, compared to one of the positions of the base (η in the figure). There, we observe that the population only becomes equal in the equilateral superposition.

Having identified the problems associated to this simple auxiliary atom configuration, in the next subsections we will show how, by adding complexity to the internal dynamics of the auxiliary atom, one can solve these limitations.

7.4.3 Scheme II: Repulsion mediated by atoms subject to state-dependent potentials: Coulomb but non-scalable

To further tune the strength and range of the interactions, we now consider the second mediating scheme described in Eq. (6.39). For this, we use two long-lived energy levels of the mediator, that we call a and b , separated by an energy difference Δ . Level b experiences an on-site repulsion U when occupying the same site as a fermion, while the atoms in level a live on a shallow lattice that allows them to move with tunneling rate t_a . Both levels are coupled through a Raman (or direct) transition of strength g [see Fig. 7.5(b)].

As compared to the previous derivation in Section 6.5.3, here we consider that only one auxiliary atom is present (rather than having as many mediating atoms as fermions). One can then write the following ansatz for the auxiliary atom

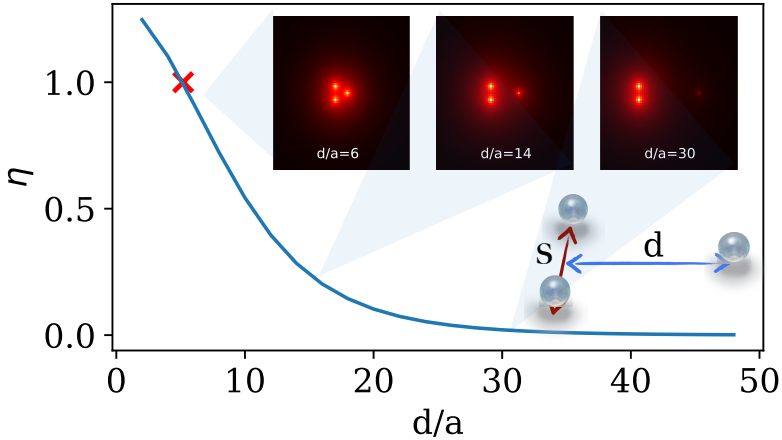


FIGURE 7.8: Asymmetry between the population of the bound state of Hamiltonian for a configuration of three simulating atoms. Here we choose an isosceles distribution, of fixed base s/a , and variable height d/a (see inserted scheme). Continuous line follow the ground state obtained with exact diagonalization for different values of d/a . η denotes the ratio between the population of the bath in the apex site, and one of the vertices of the base. A value 1, indicating the desired symmetric superposition between the three atoms, is only achieved in the equilateral configuration (red cross). Panels show axial cuts of the population in bath b for geometrical configurations $d/a = 6, 14$, and 30 (from left to right). Qualitatively, one observes that the symmetric superposition at the three vertices is less enforced as triangle sides become more unequal. (Parameters: $L_I/a = 10$, $s/a = 6$, $N_M = 120$).

wavefunction:

$$|\varphi_{\Pi,m}(\{\mathbf{j}\})\rangle_{\text{aux}} = \sum_{\mathbf{k}} \left(\varphi_{m,\{\mathbf{j}\}}^a(\mathbf{k}) \hat{a}_{\mathbf{k}}^\dagger + \varphi_{m,\{\mathbf{j}\}}^b(\mathbf{k}) \hat{b}_{\mathbf{k}}^\dagger \right) |\text{vac}\rangle. \quad (7.20)$$

Under these conditions, we find that there is again a symmetric bound state in bath b localized around the fermions, whose associated eigenenergy $E_{\Pi,+}(\mathbf{j})$ leads to repulsive spatially-dependent interactions. Since $t_b \ll t_a$, the spatial dependence is dominated by the hopping in the a -bath. In order to obtain an analytical expression for $E_{\Pi,+}(\mathbf{j})$, we will further assume that $g \ll t_a$ and that $t_b = 0$. Note that even if one takes originally $t_b = 0$, one does still obtain an effective tunnelling through the a bath given by $t_b \approx g^2 t_a / \Delta^2$, that we will neglect to get the analytical expression. These assumptions allow us to obtain $E_{\Pi,+}(\mathbf{j})$ using second-order perturbation theory. For two fermions, this leads to,

$$E_{\Pi,+}(\{\mathbf{j}\}) \approx E_{\Pi,B}^{(2)} + \frac{g^2}{N_M} \sum_{\mathbf{k}} \frac{e^{i\mathbf{k} \cdot \mathbf{j}_{12}}}{E_{\Pi,B}^{(0)} - \omega_{\Pi,\mathbf{k}}}, \quad (7.21)$$

where $\omega_{\Pi,\mathbf{k}} = -2t_a \sum_{\alpha=x,y,z} \cos(k_\alpha)$ is the energy-dispersion ruling the propagation of the a modes, and $E_{\Pi,B}^{(0)} = U + \Delta$, $E_{\Pi,B}^{(2)} = E_{\Pi,B}^{(0)} + \frac{g^2}{N} \sum_{\mathbf{k}} \frac{1}{E_{\Pi,B}^{(0)} - \omega_{\Pi,\mathbf{k}}}$ are the bound-state energies for the single-fermion case in this atomic configuration calculated to 0-th/2-nd order, respectively (see Appendix C.2.3 for more details on the calculation).

As we did for the previous model, one can obtain a formula for the spatial

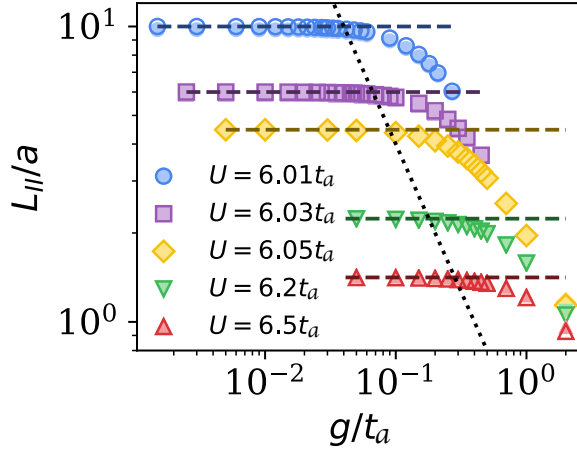


FIGURE 7.9: Effective Yukawa-type length obtained from fitting the exponentially decaying wavefunction in bath a (shaded marker), and the state energy, $(E_{\text{II,B}}^{(0)}/t_a - 6)^{-1/2}$, (contoured marker) for different values of on-site interaction U/t_a . Dashed lines follow the leading-order approximation $L_{\text{II}}^{(0)}/a = (E_{\text{II,B}}^{(0)}/t_a - 6)^{-1/2}$, and the dotted line indicates the critical coupling strength g/t_a when second-order corrections in the population a -modes are 1% larger than the leading order. Here, $N_M = 100$.

dependence by taking the continuum limit of (7.21) and expanding $\omega_{\mathbf{k}}$ around its band-edges. This yields to,

$$V_{\text{II}}(\mathbf{j}_{1,2}) = E_{\text{II},+}(\mathbf{j}_{1,2}) - E_{\text{II,B}}^{(2)} \approx V_{\text{II}} \frac{e^{-|\mathbf{j}_{12}|a/L_{\text{II}}^{(0)}}}{|\mathbf{j}_{12}|}, \quad (7.22)$$

where $V_{\text{II}} = g^2/(4\pi t_a)$ is the strength of the repulsive interaction, and $L_{\text{II}}^{(0)}/a = (E_{\text{II,B}}^{(0)}/t_a - 6)^{-1/2}$ is its range, which can be calculated from the 0-th order energy expression (see Fig. 7.9 and the discussion below it).

From Eq. (7.22) we can already see that this atomic configuration solves one of the problems of the previous proposal of section 7.4.2, that is, that now one can tune independently the strength V_{II} and its range L_{II} . This enables going to a regime where L_{II} is bigger than the fermionic system size, i.e., $L_{\text{II}} \gg N$, while still keeping the $1/r$ -dependence such that the two-fermion repulsion has a truly Coulomb-like shape in all space.

Now, let us see the working conditions, based on the discussion around Eq. (7.9), where this effective repulsion works.

- Let us first bound the corrections introduced by the fermion hopping Hamiltonian \hat{H}_f . Focusing on the two-fermion case, these contributions are:

$$\varepsilon_f = \left| \frac{t_f}{U} \right|^2 + \left| \frac{a}{L_{\text{II}}} \frac{t_f}{4V_{\text{II}}(d)} \right|^2 \ll 1, \quad (7.23)$$

where the first term corresponds to the coupling to states $\hat{b}_j^\dagger |\text{vac}\rangle$ in positions not occupied by a fermion, and the second term corresponds to the

antisymmetric state whose population in level b is approximately $(\hat{b}_{j_1}^\dagger - \hat{b}_{j_2}^\dagger) / \sqrt{2} |\text{vac}\rangle$, analogously to Eq. (7.19). As it occurred in the previous model, ensuring the right symmetry for the mediating state becomes more demanding as the two fermions separate. From the definition of the Bohr-radius [see Eq. (7.1)], larger orbital sizes require to increase the effective length of the Yukawa potential so that, in the worst-case-scenario where the fermions are maximally separated, $(a_0/a) (Na/L_{\text{II}}) \ll 1$ is still satisfied.

- The correction introduced by $\hat{H}_{\text{II,aux}}$ can be bounded by (see Appendix C.2.3 for details):

$$\varepsilon_{\text{aux}} \leq \frac{V_{\text{II}} L_{\text{II}}}{t_a a} \ll 1, \quad (7.24)$$

which guarantees that the population in the a modes remains small, such that the second-order expansion used in Eq. (7.21) holds.

- Besides, as aforementioned, it is desirable that the localization length L_{II} is independent of the particular fermionic configuration. However, by solving numerically Eq. (6.28) with $\hat{H}_{\text{II,aux}}$ for a single fermion, we find that the length of the bound state, which will afterwards mediate the interaction, can depend on the ratio g/t_a , and thus on $V_{\text{II}}(d)$. This is shown explicitly in Fig. 7.9 where we plot the L_{II} obtained by a numerical fitting of the bound-state shape as a function of g/t_a and for several U/t_a , and compare it with $L_{\text{II}}^{(0)}$ (dashed black lines). There, we observe how indeed $L_{\text{II}}^{(0)}$ matches well the numerically obtained value until a critical g/t_a where it starts to deviate. We numerically observe that L_{II} deviates significantly from $L_{\text{II}}^{(0)}$, when the population in a -mode deviates from its first-order expansion terms (in dashed black). Using that intuition, we can then estimate the conditions for the L_{II} -independence of parameters by imposing that the higher-order terms in the a -modes are smaller than the first order ones, which yields the following inequality (see Appendix C.2.3)

$$V_{\text{II}}/t_a \ll (a/L_{\text{II}})^2 \quad (7.25)$$

From an energy perspective, we see that this bound obtained from the population of atoms in level a , dictates that the mediated repulsion, $E_{\text{II},+}(\{j\}) - E_{\text{II},B}^{(2)}$, needs to be smaller than the energy-gap, $E_{\text{II},B}^{(2)}/t_a - 6$, defining $L_{\text{II}}^{(0)}$. This condition also ensures that the higher-order corrections to the bound-state energy dependent on the fermionic configuration can be neglected.

Under these conditions, this experimental setup allows us to simulate faithfully a quantum chemistry interaction for two-electron problems. Unfortunately, this proposal inherits the same problems of scalability than the previous one: when more than two fermions are present, the bound state tends to localize more strongly in the position of the closest ones (remember Fig. 7.8), and $E_{\text{II},+}$ cannot be written as a pairwise potential. In the 2D case, this was solved by considering as many mediating atoms are fermions in the lattice (Section 6.5.3). However, the resulting pairwise repulsion would not lead to the desired Coulomb-like potential in 3D. In the next section, we will then consider a different approach based on cavity-assisted

interactions.

7.4.4 Scheme III: Repulsion mediated by atomic spin excitations and cavity assisted transitions

Here, we finally introduce all the ingredients required to obtain the repulsive, pair-wise, $1/r$, potential needed for quantum chemistry simulation. The previous analysis of the simplified setups will allow us for a more intuitive understanding of the role of the different elements, and we will numerically benchmark through exact calculations the working conditions of the simulator. This proposal requires [see Fig. 7.5(c)]:

- Three long-lived states that we label as a, b, c , subject to different state-dependent potentials, such that they can only hop when they are in the a state.
- The auxiliary atoms should be initialized in a Mott-insulating state $|\text{Mott}\rangle = \prod_i \hat{c}_i^\dagger |\text{vac}\rangle$ with unit filling. Like this, instead of working with atomic excitations directly, as we did in the previous two subsections, the second-quantized operators \hat{A}_j, \hat{B}_j will denote single-spin excitations over the Mott-state, i.e.,

$$\hat{A}_j^\dagger |\text{Mott}\rangle = \left(\prod_{i \neq j} \hat{c}_i^\dagger \right) \hat{a}_j^\dagger |\text{vac}\rangle, \quad (7.26a)$$

$$\hat{B}_j^\dagger |\text{Mott}\rangle = \left(\prod_{i \neq j} \hat{c}_i^\dagger \right) \hat{b}_j^\dagger |\text{vac}\rangle, \quad (7.26b)$$

- We also demand controllable cavity-assisted transitions that can be engineered to transfer excitations between levels c and b [340, 354, 355]. These transitions induce a long-range interaction term, J_c/\bar{N}_M , where we already include explicitly the inverse volume dependence of the cavity-assisted couplings. Besides, we still keep the local Raman assisted transitions between the a and b levels already used in section 7.4.3, with strength g and detuning Δ .

Summing up all these ingredients, the internal dynamics of the auxiliary atoms will be ruled by the following Hamiltonian,

$$\hat{H}_{\text{III,aux}} = \frac{J_c}{\bar{N}_M} \sum_{i,j} \hat{B}_i^\dagger \hat{B}_j + \Delta \sum_j \hat{B}_j^\dagger \hat{B}_j + J_A \sum_{\langle i,j \rangle} \hat{A}_i^\dagger \hat{A}_j + g \sum_j (\hat{A}_j^\dagger \hat{B}_j + \text{H.c.}), \quad (7.27)$$

where J_A is the super-exchange coupling strength, which can be tuned from positive to negative [356, 357] and here will be considered to be $J_A > 0$. Note that, apart from the first term describing cavity-assisted transitions, this Hamiltonian for the spin excitation is formally identical to the mediating Hamiltonian $\hat{H}_{\text{II,aux}}$ of Eq. (6.39).

Derivation of the effective potential

To show the scalability of the proposal, we study directly the case when N_e fermions are present in the system with positions $\{\mathbf{j}\} = \{\mathbf{j}_1, \dots, \mathbf{j}_{N_e}\}$. Inspired by the previous sections, we study the fermion interaction induced when only a single spin excitation is present in the system, which is initially symmetrically distributed

among all fermionic positions:

$$|\varphi_+^{(0)}\rangle = \frac{1}{\sqrt{N_e}} \sum_{\{\mathbf{j}\}} \hat{B}_{\mathbf{j}}^\dagger |\text{Mott}\rangle. \quad (7.28)$$

From Eq. (7.27), it can be shown that the commutator $[\hat{H}_{\text{III,aux}}, \sum_{\mathbf{i}} (\hat{B}_{\mathbf{i}}^\dagger \hat{B}_{\mathbf{i}} + \hat{A}_{\mathbf{i}}^\dagger \hat{A}_{\mathbf{i}})] = 0$, such that the number of spin excitations in this Hamiltonian is conserved, allowing us to remain in the single excitation subspace of the Hamiltonian $\hat{H}_{\text{III,aux}}$. Thus, all the possible wavefunctions are captured by the following ansatz,

$$|\varphi_{\text{III,m}}(\{\mathbf{j}\})\rangle_{\text{aux}} = \sum_{\mathbf{k}} \left(\varphi_{m,\{\mathbf{j}\}}^A(\mathbf{k}) \hat{A}_{\mathbf{k}}^\dagger + \varphi_{m,\{\mathbf{j}\}}^B(\mathbf{k}) \hat{B}_{\mathbf{k}}^\dagger \right) |\text{Mott}\rangle. \quad (7.29)$$

Then, in order to obtain an analytical expression of the energy of the symmetric configuration $E_{\text{III,+}}(\{\mathbf{j}\})$ including the energy shift of the fermions, $\hat{H}_{f-\text{aux}}(\{\mathbf{j}\}) + \hat{H}_{\text{III,aux}}$, we apply perturbation theory using:

$$\hat{H}_0 = \Delta \sum_{\mathbf{j}} \hat{B}_{\mathbf{j}}^\dagger \hat{B}_{\mathbf{j}} + U \sum_{\{\mathbf{j}\}} \hat{B}_{\mathbf{j}}^\dagger \hat{B}_{\mathbf{j}}, \quad (7.30)$$

as the unperturbed Hamiltonian. At this level, there is a degeneracy of the order of the number of fermions, that the cavity will break. Then, we include

$$\hat{H}_{\text{cav}} = \frac{J_c}{\bar{N}_M} \sum_{\mathbf{i},\mathbf{j}} \hat{B}_{\mathbf{i}}^\dagger \hat{B}_{\mathbf{j}}, \quad (7.31)$$

$$\hat{H}_A = J_A \sum_{\langle \mathbf{i},\mathbf{j} \rangle} \hat{A}_{\mathbf{i}}^\dagger \hat{A}_{\mathbf{j}} + g \sum_{\mathbf{j}} (\hat{A}_{\mathbf{j}}^\dagger \hat{B}_{\mathbf{j}} + \text{H.c.}), \quad (7.32)$$

as the two perturbations over it. Using perturbation theory, we find that the eigenenergy of the unperturbed state $|\varphi_+^{(0)}\rangle$, with energy $\hat{H}_0 |\varphi_+^{(0)}\rangle = E_{\text{III,B}}^{(0)} |\varphi_+^{(0)}\rangle = (U + \Delta) |\varphi_+^{(0)}\rangle$, is perturbed to first order by the \hat{H}_{cav} leading to: $E_{\text{III,B}}^{(1)} = U + \Delta + \rho_M J_c$, where $\rho_M = N_e / \bar{N}_M$ is the fermionic density. The cavity then breaks the degeneracy between the symmetric/antisymmetric wavefunctions, creating an energy difference $\rho_M J_c$ between them. To the next order, \hat{H}_A leads to an additional correction of the energy, which introduces the desired spatial dependence,

$$E_{\text{III,+}}^{(2)}(\{\mathbf{j}\}) \approx E_{\text{III,B}}^{(1)} + \frac{g^2}{N_e \bar{N}_M} \sum_{\mathbf{k}} \frac{|e^{i\mathbf{k} \cdot \mathbf{j}_1} + \dots + e^{i\mathbf{k} \cdot \mathbf{j}_{N_e}}|^2}{E_{\text{III,B}}^{(1)} - \omega_{\text{III,k}}}, \quad (7.33)$$

where $\omega_{\text{III,k}} = 2J_A \sum_{\alpha=x,y,z} \cos(k_\alpha)$ is the eigenenergy of the Hamiltonian $J_A \sum_{\langle \mathbf{i},\mathbf{j} \rangle} \hat{A}_{\mathbf{i}}^\dagger \hat{A}_{\mathbf{j}}$ using periodic boundary conditions. In that equation, we observe that \hat{H}_A delocalizes the auxiliary A -spin excitations providing the position dependent part of $E_{\text{III,+}}^{(2)}(\{\mathbf{j}\})$, which can be broken into a constant and a sum of pair-wise contributions that have the same shape as the one in Eq. (7.21). In the continuum

limit, $N_M \rightarrow \infty$, the pair-wise contributions can again be written as an integral that yields:

$$E_{\text{III},+}^{(2)}(\{\mathbf{j}\}) \approx E_{\text{III},\text{B}}^{(2)} + V_{\text{III}} \sum_{\mathbf{i},\mathbf{j}} \frac{e^{-|\mathbf{i}-\mathbf{j}|a/L_{\text{III}}}}{|\mathbf{i}-\mathbf{j}|}, \quad (7.34)$$

where, to second order, $E_{\text{III},\text{B}}^{(2)} = E_{\text{III},\text{B}}^{(1)} + \frac{g^2}{\mathcal{N}} \sum_{\mathbf{k}} \frac{1}{E_{\text{III},\text{B}}^{(0,1)} - \omega_{\mathbf{k}}}$. Here, L_{III} is the effective length of the Yukawa-Type potential, now given by, $L_{\text{III}} = a \left(E_{\text{III},\text{B}}^{(1)} / J_A - 6 \right)$, and $V_{\text{III}} = \frac{g^2}{2\pi J_A N_e}$ its strength (see Appendix C.2.4).

Working conditions

For self-consistency in the derivation of $E_{\text{III},+}^{(2)}(\{\mathbf{j}\})$, in Eq. (7.34), we must impose that the corrections to the unperturbed state, $|\varphi_+^{(0)}\rangle$, due to different elements of the Hamiltonian are small [Eq. (7.9)]. We introduce these contributions one by one:

- The cavity Hamiltonian \hat{H}_{cav} tends to delocalize the auxiliary atomic excitations beyond the fermion positions, which does not occur when the fermion-auxiliary atom interaction is large enough. Using Eq. (7.9), we find that the cavity-mediated population of other symmetric states rather than $|\varphi_+^{(0)}\rangle$ is upper bounded by:

$$\varepsilon_{\text{cav}} = \left| \frac{\sqrt{\rho_M} J_c}{U - J_c} \right|^2, \quad (7.35)$$

such that one sufficient condition to satisfy $\varepsilon_{\text{cav}} \ll 1$ is:

$$J_c \ll U. \quad (7.36)$$

This is numerically confirmed in Fig. 7.10(a), where we study the triangular fermionic configuration discussed in Fig. 7.8 using now the Hamiltonian $\hat{H}_{f-\text{aux}}(\{\mathbf{j}\}) + \hat{H}_{\text{III},\text{aux}}$. For illustration, we plot the weight of the wavefunctions in the fermionic positions, i.e., $W = \sum_{\mathbf{i} \in \{\mathbf{j}\}} |\varphi_{m,\{\mathbf{j}\}}^A(\mathbf{i})|^2$ (black dashed line), as a function of J_c/J_A for a fixed U and for several values of g/J . There, we observe that $W \approx 1$ when Eq. (7.36) is satisfied, irrespective of the particular choice of the rest of parameters.

- As it occurred in subsection 7.4.3, the hoppings in \hat{H}_A connect $|\varphi_+^{(0)}\rangle$ with two different set of states: (i) it dresses it with some population in the A -modes; and (ii) it takes it out of the symmetric sector. One can upper bound the corrections due to these two processes by $\varepsilon_A = \varepsilon_{A,i} + \varepsilon_{A,ii}$, where:

$$\varepsilon_{A,i} = \frac{g^2}{N_e \overline{N}_M} \sum_{\mathbf{k}} \left| \frac{e^{i\mathbf{k} \cdot \mathbf{j}_1} + \dots + e^{i\mathbf{k} \cdot \mathbf{j}_{N_e}}}{E_{\text{II},\text{B}}^{(0)} - \omega_{\text{II},\mathbf{k}}} \right|^2 \leq \frac{g^2 L_{\text{III}}}{8\pi a J_A^2} N_e \ll 1, \quad (7.37)$$

assuming the desired condition $d/L_{\text{III}} \ll 1$ for any pair of fermions, so that the

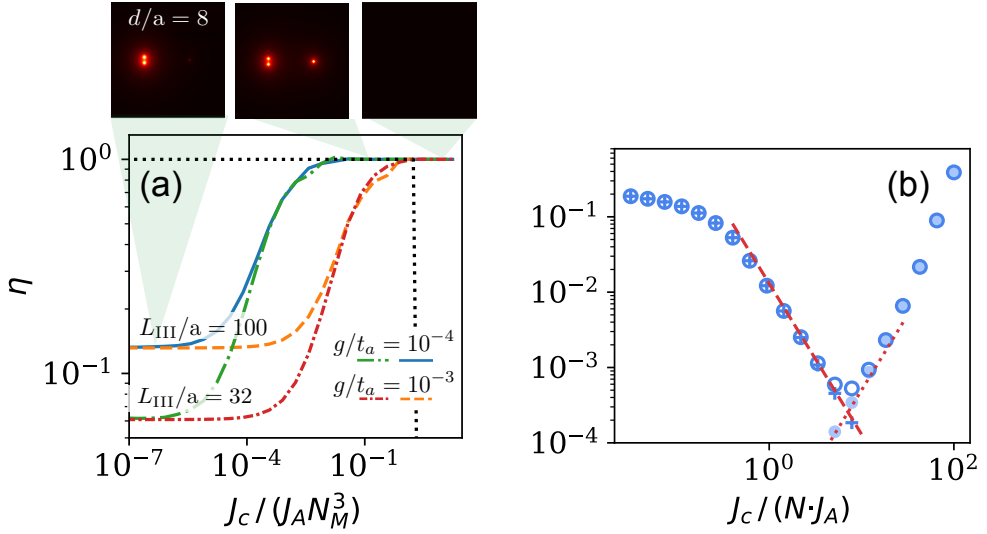


FIGURE 7.10: (a) Exact diagonalization calculation of the bound state associated to Hamiltonian (7.27) for three fermions in the isosceles configuration illustrated in Fig. 7.8. We represent the ratio η between the population in bath a of the fermion at the apex of the triangle, and one vertex of the base, as a function of the population in the cavity coupling strength. The no-cavity limit ($J_c/J_A = 0$) is determined by the fermionic geometry and effective length L_{III}/a . As the cavity interaction increases, inequality (7.39) defines the lower cavity strength limit at which the population of the bath is equal for each of the fermionic positions. The black dotted line shows the total population of atoms in level A at the position of the three vertices (W as defined in the main text), which is close to 1 for $J_c < U$, and quickly decays to an uniform distribution among all sites when the cavity interaction dominates the on-site interaction with the fermion $J_c > U$. Inset: population of bath a for different values of cavity interaction. Note in the last inset that all the bath is equally populated when the cavity strength overpasses the on-site interaction U . Parameters: $U = 2J_A$, $\Delta_c = 10J_A$, $N_M = 160$, $s/a = 6$, $d/a = 24$. (b) Population of the mediating atom ground-state on contributions not corresponding to the leading-order ground-state, $(\hat{B}_{j_1} + \hat{B}_{j_2}) \hat{f}_{j_1} \hat{f}_{j_2} / \sqrt{2}$, for any combination of j_1, j_2 (contoured marker), see main text. Here we use an exact diagonalization of the ground-state energy for a minimal model where two fermions are hopping on a 1D lattice, are attracted by two nuclei separated 8 lattice sites, repel each other with an effective potential V_0/d (being d the interfermionic separation) and experience an on-site interaction U with a bosonic species connected to a cavity mode (i.e. the terms associated to the fermionic dynamics and population in state b of the Hamiltonian (7.27)). Plus markers show the total population of the antisymmetric states of the form $(\hat{B}_{j_1} - \hat{B}_{j_2}) \hat{f}_{j_1} \hat{f}_{j_2} / \sqrt{2}$ and coloured markers the population of sites not occupied by the fermions, $\hat{B}_j \hat{f}_{j_1} \hat{f}_{j_2}$ for $j \notin \{j_1, j_2\}$. These are compared to the scaling predicted by the first-order analytical predictions given by Eq. (7.39) (red dashed line) and Eq. (7.35) (dotted line), respectively. Note that the dynamics in level a is not included in this minimal model.

Parameters: $N = 50$, $V_0 = 1/4J_A$, $U = 4000J_A$.

Coulomb scaling prevails over the exponential decay. One observes that the final inequality scales as $g^2/J_A^2 \lesssim a/L_{\text{III}}$, similarly to the two-fermion condition we encountered in the previous scheme [see Eq. (7.24)].

The other contribution coming from the antisymmetric states is prevented by the energy gap between the symmetric/antisymmetric sector induced by the cavity-assisted transitions ($\rho_M J_c$), and it can be upper bounded by,

$$\varepsilon_{A,ii} = \left(\frac{V_{\text{III}}}{\rho_M J_c} \right)^2 G(\{\mathbf{j}\}), \quad (7.38)$$

where $G(\{\mathbf{j}\})$ is a function that solely depends on the particular fermionic configuration (see Appendix C.2.4). Interestingly, $G(\{\mathbf{j}\}) \equiv 0$ in the case where all the fermions are equally spaced or when there are only two fermions, while in general it can always be upper-bounded by $|G(\{\mathbf{j}\})| \leq (N_e/2 - 1)$. Then, the inequality to be satisfied when many fermions are present reads as,

$$\varepsilon_{A,ii} \leq \left(\frac{V_{\text{III}}}{\rho_M J_c} \right)^2 \frac{N_e}{2} \ll 1. \quad (7.39)$$

This condition is also numerically benchmarked for the triangular configuration of three fermions represented in Fig. 7.10(a). As in Fig. 7.8, we plot the ratio of the weight of the wavefunction in the basis positions compared to the apex (η , see scheme in Fig. 7.8), showing how they only become equal in the limit when Eq. (7.39) is satisfied.

- Besides, an extra condition appears to avoid that \hat{H}_f connects the mediating state with the rest of the subspace [see Eqs. (7.8-7.9)]. We can upper bound this contribution coming from the antisymmetric distribution of spin excitations at the fermionic positions by (see Appendix C.2.4),

$$\varepsilon_f \approx \frac{a}{L_{\text{III}} N_e} \left(\frac{t_f}{\rho_M J_c} \right)^2 \ll 1. \quad (7.40)$$

Testing this inequality numerically in a three-dimensional model is an outstanding challenge as it involves the three-dimensional Hilbert space of both the fermion and spin excitations in the a and b levels. Instead, in Fig. 7.10(b), we test Eq. (7.40) in a minimal model of two fermions hopping in a 1D lattice for different values of the cavity coupling J_c . We observe a qualitative good agreement with the scaling $\propto (t_f/J_c)^2$ before the error introduced by an excessive cavity strength appears [Eq. (7.35)].

- Also, as it occurred in the previous section, there is an additional condition to force that L_{III} does not vary depending on the fermionic configuration, as this will imply that the effective repulsive potential will change as the fermions hop into the lattice. Making an energy argument analogous to the derivation used in Eq. (7.25), one would desire $|E_{\text{III},+} - E_{\text{III},B}^{(1)}| \ll (a/L_{\text{III}})^2 J_A$. This bound will highly depend on the particular fermionic configuration. An (unrealistic) upper bound for electronic repulsion would correspond to the case where all fermions are as close to each other as they can be, while respecting their fermionic character. In the limit of many simulated electrons, this scales as

$V_{\text{III}} N_e^{5/3} \ll (a/L_{\text{III}})^2 J_A$. This, however, does not make use of the entire allowed space for the fermions. A more realistic bound should take into consideration that fermions will distribute over the entire lattice for the optimal simulation. One can then approximate the repulsive energy as $|E_{\text{III},+} - E_{\text{III},\text{B}}^{(1)}| \approx \frac{V_{\text{III}}}{2^{1/3}} (N_e - 1)^{2/3} \sum_{\mathbf{j}} \rho(\mathbf{j})^{4/3}$, where $\rho(\mathbf{j})$ denotes the fermionic density in site \mathbf{j} . This estimation can then be particularized for any atomic/molecular level of interest. As a back-of-the-envelope calculation, considering an homogeneous density $\rho(\mathbf{r}) \approx \rho_e$, one obtains,

$$\frac{V_{\text{III}}}{2^{1/3}} (N_e - 1)^{2/3} N_e^{4/3} / N \ll (a/L_{\text{III}})^2 J_A. \quad (7.41)$$

The left-hand side of this estimation corresponds to the repulsion of an homogeneous distribution of N_e atoms in a cubic lattice of N sites per side. Intuitively, one can see that its scaling $\propto N_e^2/N$ corresponds to the previous unrealistic scaling $N_e^{5/3}$ of a cubic array of distance 1, corrected by the new characteristic length, $N_e^{1/3}/N$, when all the lattice is occupied.

- Finally, there is an additional condition that only involves the localization length L_{III} of the Yukawa-type potential and the sizes of the fermionic/auxiliary atom lattice. That is,

$$N \ll L_{\text{III}}/a \ll N_M, \quad (7.42)$$

whose intuition is clear: the length of the Yukawa potential has to be larger than the number of sites of the fermionic optical lattice (N), such that the fermions repel with a $1/r$ -scaling, but smaller than the auxiliary atomic optical lattice, in order not to be distorted by finite size effects. In particular, one can relax the condition of Eq. (7.41), aimed to ensure that the effective length in the Yukawa potential is constant regardless the fermionic configuration, and impose instead that the smallest and largest of them are contained within this range $[N, N_M]$.

Final potential and conditions

In summary, after the elimination of the cavity mode and Mott insulator described in Eq. (7.27), the effective interaction mediated by this scheme III describes a fermion-fermion potential (7.34) that follows a Yukawa form [358] with a constant energy shift C :

$$V(r) \approx C + \frac{V_0}{r/a} e^{-r/L}, \quad (7.43)$$

where $L/a = \sqrt{J/(U + \Delta + \rho_M J_c - 6J)}$ is the localization length, which can be tuned with Δ , and $V_0 = \frac{g^2}{2\pi J N_e}$ is the strength of the potential repulsion. Here, $\rho_M = N_e/\bar{N}_M$ and we omit the, III, labelling from now on. This mapping between the simulator and the grid representation of the quantum chemistry Hamiltonian holds as long as,

$$\begin{aligned} & \text{(b) } J_c \ll U, \\ & \text{(c) } t_f \ll J_c \rho_M, \text{ and } V_0 \sqrt{N_e} \ll J_c \rho_M, \\ & \text{(d) } V_0 N_e^2 \ll J_A N (a/L)^2. \end{aligned}$$

Here, condition (b) enforces that the a excitation localizes symmetrically only around the position of the fermions (7.36); (c) guarantees that neither the tunneling of the fermions (7.39) nor the interaction with the b -excitations (7.40) spoils the effective interaction; and (d) ensures that the Yukawa potential does not depend on the fermionic positions (7.41). Furthermore, to obtain a truly Coulomb repulsion, the length L must be larger than the fermionic lattice of size N , but smaller than the Mott insulator size. This is, the condition (7.42):

$$(e) N \ll L/a < N_M.$$

When all (a-e) inequalities are satisfied, the exact solution in the continuum limit is recovered for $N \rightarrow \infty$. Thus, we can conclude that the finite size of the simulator is what ultimately limits the precision of the simulation.

7.5 Numerical benchmark of the 3D analog simulator

After having explained how to simulate all the elements of the quantum chemistry Hamiltonian in a grid basis representation [Eqs. (6.12, 6.13 6.18)], here we illustrate the performance of our simulator for two-electron systems for moderate system sizes using numerical simulations. In particular, we study in detail the simulation of the He atom (subsection 7.5.1), which we will use to illustrate how to explore the physics of different spin symmetry sectors; and the H_2 and HeH^+ molecules (subsection 7.5.3) to illustrate molecular physics for the case of equal and unequal nuclei charges.

For this purpose, we will use directly the effective repulsion in Eq. (6.18), with an effective potential $V(\mathbf{i} - \mathbf{j}) = V_0/|\mathbf{i} - \mathbf{j}|$ given by Eq. (7.43) in the limit where the simulator conditions are satisfied. Despite the apparent simplicity of the problem, obtaining the ground state energy of \hat{H}_{eff} for two fermions with, e.g., exact diagonalization methods, poses already an outstanding challenge since the number of single-particle states in a grid basis scales with the number of fermionic lattice sites \bar{N} . To obtain the results that we will show in the next subsections, we have then adopted an approach reminiscent of Hartree-Fock (HF) methods, where the Hamiltonian is projected in a basis that combines atomic states calculated from the single-particle problem, together with electronic orbitals that interact with an average charge caused by the rest of electrons (see Appendix C.3 for more details). Let us remark that these are just numerical limitations to benchmark the simulator, that would be free from these calculations details.

7.5.1 He atom

The first system we consider is the case of the He atom. This corresponds to a system with a single nucleus with $Z_1 = 2$, such that one just requires a single spatially-shaped laser beam to mimic the nuclear potential, and two simulated electrons [see Fig. 7.11(a)]. Let us note that since \hat{H}_{eff} does not couple the position and spin degree of freedom, one can solve independently the problems where the spin degrees of freedom are in a singlet (antisymmetric) or triplet states (symmetric), which will result in spatially symmetric/antisymmetric wavefunctions, traditionally labeled as para- and orthohelium, respectively.

In Fig. 7.12(a,b) we plot the ground state energy of the He atom as a function of the effective Bohr radius presented in Eq. (7.1). Note that there is no closed solution

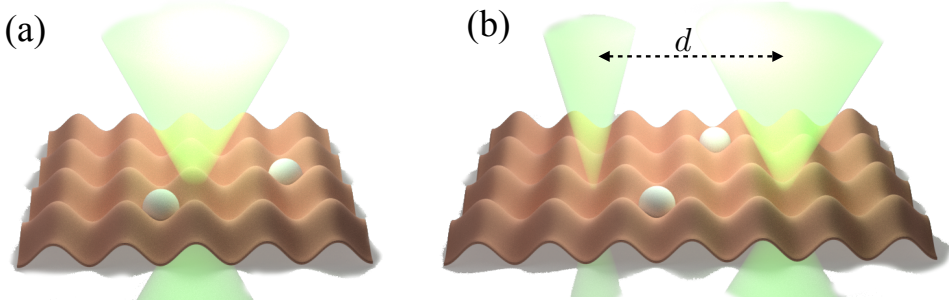


FIGURE 7.11: (a) Configurations corresponding to the simulation of atomic He, where a nuclear potential centered in the lattice is induced using holographic techniques 4.3.1, and two fermionic atoms trapped in the lattice play the role of two electrons. (b) The configuration is modified to simulate HeH^+ , where one tailors the attraction due to the distinct Hydrogen (left) and Helium (right) nuclear charges, separated, in this scheme, by $d/a = 3$ sites.

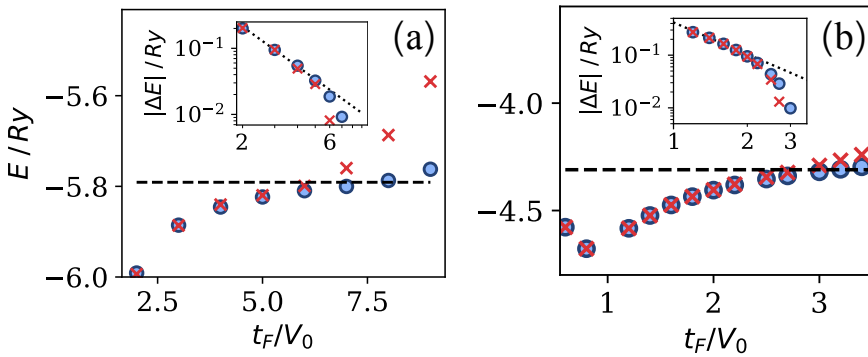


FIGURE 7.12: Ground state energy of the discretized Hamiltonian associated to atomic He, in the ortho (a), and parahelium sectors (b). Following the extrapolation method, dashed lines indicate the values $E_{\text{para,He}}^{\infty} = -5.79$ Ry and $E_{\text{ortho,He}}^{\infty} = -4.31$ Ry, respectively, for which the scaling of the energy error as $(a_0/a)^{-2}$ is observed (insets). Round (crossed) markers correspond to $N = 100$ ($N = 75$).

even for this very simple system, and our simulator, which is compared to numerical results with no relativistic or QED corrections [359]. Furthermore, we use the extrapolation strategy explained in Section 7.3 based on the scaling of the error $\Delta E/\text{Ry} \propto (a_0/d)^{-2}$ to obtain the expected energy that will come out from the simulation, yielding $E_{\text{para,He}}^{\infty} = -5.79$ Ry, and $E_{\text{ortho,He}}^{\infty} = -4.31$ Ry. Their relative error to the tabulated values [359], -4.3504 Ry and -5.8074 Ry, is therefore of 0.3% and 0.9%, respectively, for the benchmarking done with a system of size $N = 100$. Note that the bigger error corresponds to orthohelium, whose orbitals are larger and thus, more affected by the discretization of the lattice.

7.5.2 Hydrogen molecule

One of the features of interest in molecular physics is the molecular potential. That is, how the ground state energy of the molecule varies as a function of the distance d between the nuclei. This curve already provides useful information, such as its

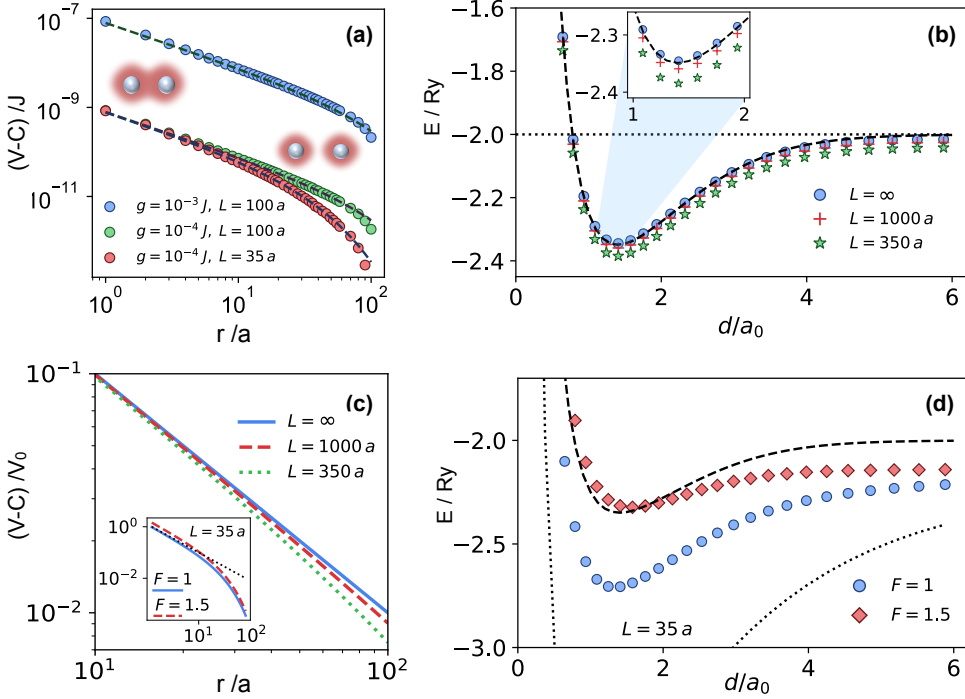


FIGURE 7.13: (a) Energy of the single-excitation bound state of Hamiltonian in Eq. (7.27) for two fixed fermions as a function of their separation, r . We choose $\Delta = 2J$, $N_M = 200$, $J_c = J$, such that (a-e) inequalities are satisfied. The Yukawa potential of Eq. (7.43) corresponding to each configuration of parameters is plotted with dashed lines. (b) We use this effective interaction to calculate the molecular potential associated to an analog simulator of H_2 of size $N = 75$. For each internuclear separation, we choose t_f/V_0 giving optimal accuracy (see Supplementary Information section 3), ranging from $t_f/V_0 = 4.2$ to $t_f/V_0 = 2.3$ in the dissociation limit (dotted line). Molecular orbitals are included in the projective basis until convergence is observed. For a Coulomb potential (blue dots), the result agrees with an accurate solution in the nonrelativistic regime [360, 361] (dashed line). As L decreases, the exponential decay in the Yukawa potential prevails, underestimating Coulomb repulsion and lowering the molecular potential. (c) This underestimation of the repulsive potential is stressed when violating $N \ll L/a$ (see inset). (d) Changing the ratio between the amplitude of the nearest-neighbor electronic and nuclear potentials, F , one can explore artificial repulsive interactions that form pseudomolecules in more relaxed experimental conditions. The dotted line here represents the limit of zero-repulsion in the absence of a mediating excitation.

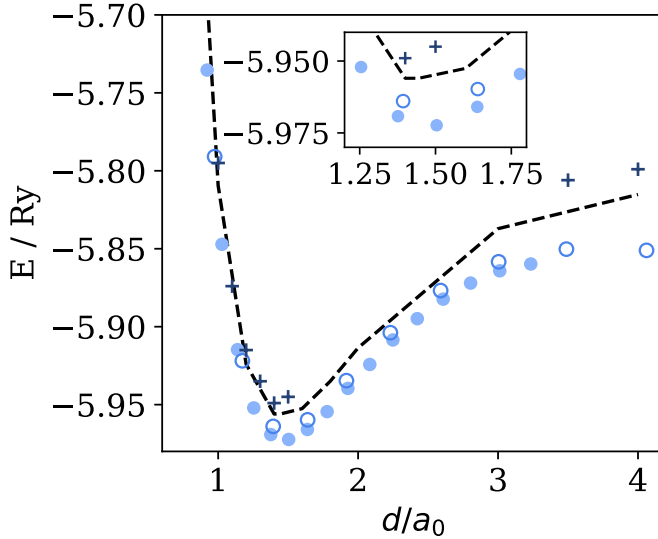


FIGURE 7.14: Molecular potential of HeH^+ as a function of the lattice size calculated for a finite lattice of $N = 75$ (coloured markers) and $N = 100$ (contoured markers). Crossed markers follow the mitigation strategy using these sizes, and described in Section 7.3. Black dashed line follows the molecular potential beyond discretization numerically calculated [362]. Inset zooms around the position of the minimum.

equilibrium molecular position (if any) as well as its dissociation energy. In our simulator, in order to always maintain the nuclei half a site away from the nodes of the lattice (to avoid a divergent value of the potential) we choose integer values of d/a .

In Fig. 7.13 we analyze the accuracy for the simplest molecule, H_2 . First, we compute exactly the energy of the spin excitation that mediates the fermionic repulsion, as a function of the interfermionic separation [see Fig. 7.13(a)]. We show that it reproduces the $1/r$ behavior over a wide range of values of g/J and L . In Fig. 7.13(b) we compute the molecular potential with $N = 75$ by using a Yukawa electronic potential with different lengths L . We observe excellent qualitative agreement for all L 's considered in the figure, and a quantitative matching when $L/a \gg N$. Remarkably, even if $L/a \lesssim N$, valuable information can still be extracted by adjusting other experimental parameters, as shown in Fig. 7.13(d). This illustrates how one can increase the strength of the electron repulsion V_0 to compensate the underestimation of the potential at long distances, and obtain a pseudomolecular potential that is qualitatively similar to the one expected with Coulomb interactions, as represented in Fig. 7.14.

7.5.3 HeH^+ molecule

Now, we study the two-electron molecule He^+-H , which has two nuclei, one with charge $Z_1 = 1$ (the one corresponding to the H atom) and another one with $Z_2 = 2$ (the one corresponding to the He cation). Thus, the simulator requires two spatially-shaped laser beams, one with twice the intensity of the other, such that its induced potential is twice as big [see Fig. 7.11(b)].

In Fig. 7.14 we plot the molecular potential that could be obtained with our simulator for two different system sizes $N = 75$ and $N = 100$. As we did before, for each value of d/a_0 , we choose the optimal discrete Bohr radius, a_0/a , using the extrapolation strategy introduced in Section 7.3. Notice that this molecular potential needs to include nuclear repulsion, and its minimum corresponds to the distance at equilibrium. The energy at this point, $E_{\min, \text{HeH}^+}^\infty = -5.95$ Ry, which is in agreement with the numerical value -5.95740408 Ry reported in Ref. [362]. As the separation increases, we observe that the error of the finite simulator increases, since the finiteness of the lattice is more restrictive when more sites need to separate the nuclear position. We also observe that the continuum result obtained with the mitigation approach still tends to the dissociation limit corresponding to ortho-Helium, discussed in the Section 7.5.1.

7.6 Experimental implementation

Here, we provide further details and candidates for the experimental implementation of some of the key ingredients of the proposal introduced in Section 7.4.4.

7.6.1 Candidate atomic species

This proposal is based on the interplay between two atomic species: (i) Fermionic atoms: they have two internal levels, which play the role of the electronic spin. (ii) Mediating atoms: they must have three levels available: $|0\rangle$ for the ground state in the Mott insulator; $|b\rangle$ with the spin excitation; $|a\rangle$ with the state that tunnels and induces the effective repulsion.

Over the last years, many atomic species have been trapped, condensed, and used in experiments with optical lattices. For illustration, let us give a particular example based on fermionic and bosonic alkaline-earth atoms. These atoms offer a rich internal structure, with long-lived excited metastable states 3P_0 and 3P_2 . As a particular choice, one can consider ^{87}Sr as a simulator for electrons. Its nuclear spin is $I = 9/2$ and, similarly to Ref. [343], one can encode the spin of the simulated electron into nuclear states, $|\uparrow\rangle \equiv |^1S_0, m_I = -9/2\rangle$ and $|\downarrow\rangle \equiv |^1S_0, m_I = -7/2\rangle$. This information is therefore protected from the electronic transitions used in the rest of the proposal.

One can now use one of its bosonic isotopes, ^{88}Sr for the mediating atoms [363]. We assign the long-lived states 1S_0 , 3P_0 , and 3P_2 as levels $|0\rangle$, $|b\rangle$, and $|a\rangle$, respectively. Since there exists a magic wavelength that makes the trapping of the states S and one of the P equal, it is possible to choose nearby frequencies that provide basically the same lattice period for all states with the appropriate conditions [339]. Apart from that, an additional laser driving the 1S_0 level off resonance can be used to induce the external potential (with the holographic techniques explained in the previous chapters). Note that the isotope shift is sufficiently large in those atoms so that this can be negligible even in the case that the level 1S_0 is chosen as $|0\rangle$. The cavity can be tuned close to the $^3P_0 \rightarrow ^3S_1$ resonance, without affecting the other states, and two-photon Raman transitions can couple the levels 3P_0 and 3P_2 appropriately. Also, note that having nuclear spin 0 is not a problem in this case, as the mediated electronic repulsion is spin-independent. By choosing an isotope of Sr, an optical lattice with the same spacing can be engineered at the bosonic state 1S_0 , with similar choices to the fermionic atoms.

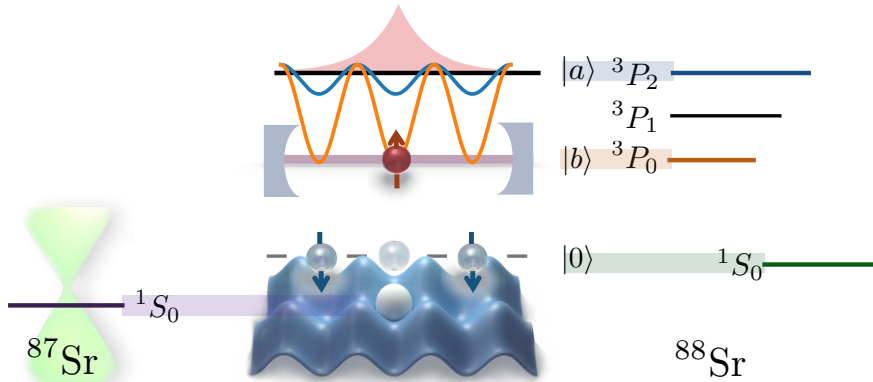


FIGURE 7.15: Schematic correspondence between the lowest-energy metastable states of ^{87}Sr and ^{88}Sr , as compared to the relevant energy levels of the hopping fermions and mediating atoms of the Mott, respectively.

Furthermore, the lattice depth and spacing in $3P_2$ can be independently controlled by, e.g., using magic wavelengths [364], and its scattering length can be tuned using, e.g., non-resonant light [365].

Apart from alkaline-earth atoms, there are interesting experiments with fermionic and bosonic mixtures of Alkali atoms with similar (or displaced) potentials, for instance, in Refs. [366, 367]. Moreover, there are on-going experiments with fermionic ^6Li and bosonic ^{23}Na atoms to simulate dynamical gauge fields [368]. An advantage is that ^6Li has spin $1/2$ in the ground state and thus act as a spin-full electron. Another alternative is to use mixtures of two types of atomic elements, e.g., Li-Yb, as it is also being pursued in experiments with optical lattices [369–371].

7.6.2 Measurement

From the chemistry perspective, all relevant quantities can be expressed in terms of the fermionic density. This is for example the key idea used in DFT methods [272]. One possibility then consists on performing a 3D spatial tomography of the N_e electron and reconstruct the fermionic density. This is very complex in practice, but with gas microscope techniques (see Ref. [372], for instance) could be feasible.

An alternative would be measuring the energy of the system. In addition to constructing molecular potentials, scanning the energy at different nuclear configurations can provide additional information, such as the value of molecular forces (Hellmann-Feynman theorem [290]). For this, three elements need to be simultaneously measured: the kinetic energy $\langle K \rangle$, the nuclear attraction $\langle V_{\text{nuc}} \rangle$, and the electronic repulsion $\langle V_{e-e} \rangle$; such that the total energy writes as $E = \langle K \rangle + \langle V_{\text{nuc}} \rangle + \langle V_{e-e} \rangle$. Using sudden quenches of the Hamiltonian, such contributions can be independently converted into kinetic energy. One can then perform a time of flight measurement of the fermionic atoms expelled from the lattice, using for example ionization or fluorescence techniques. As one can observe, the measured quantities will not correspond to eigenstates of the original Hamiltonian and this will give some variance in the measurement proportional to the number of fermions. One could then repeat this procedure to gain statistically significance. Once the equilibrium point of the molecular potential is identified, the

procedure can also be highly simplified as only measuring $\langle K \rangle$ is needed to read the total energy at that point, based on the virial theorem for molecules [373].

7.6.3 Experimental considerations

A reliable simulation of the quantum chemistry Hamiltonian needs that our simulator, described by Eq. 6.22, satisfies a set of inequalities (a-e). We are however aware that there will be other experimental imperfections that may impose extra conditions and that will have to be analyzed in detail to optimize the performance of the simulation. Among the more relevant ones are:

- **Finite temperature** leads to thermal fluctuations which may spoil the simulation. Thus, these fluctuations will lead to defects in the Mott insulator (see below), and may also influence the internal states of the atoms. The latter, however, can typically be very well controlled in atomic systems as we just need the atoms to be initially in a polarized state, which is reasonably easy to prepare [374].
- **Dephasing** can be originated by fluctuations in the transitions or due to gravitational or magnetic fields (as internal levels are being used). This would spoil the potential of the system as a quantum simulator. However, the first effect is small in the case of microwave or Raman transitions, and the second and third can be controlled in the conditions already used for condensed matter simulations [43, 45].
- **Inexact fermionic filling.** Since fermions play the role of electrons, an inexact number of fermionic atoms hopping in the lattice translates into an erroneous effective charge in the simulated molecule. These errors can be possibly post-selected by measuring the number of fermionic atoms after the simulation is performed.
- **Defects in the Mott insulator.** The absence of Mott particles in a given lattice site will locally modify the effective fermion potential. Fermions hopping to this site cannot mediate its repulsive interaction through spin-excitations, perturbing the simulated molecular orbital around this position. Importantly, the defects will not affect the potential far from the fermion such that the final performance of the simulation will scale with the density of defects rather than their number.
- **Spatial inhomogeneities of cavity coupling.** In the final simulator Hamiltonian of Eq. (7.27), we have assumed that the $|b\rangle$ -excitations couple homogeneously to the cavity mode. In general, there might be some inhomogeneities that translates in a Hamiltonian:

$$\frac{J_c}{N_M} \sum_{ij} J_{ij} \hat{B}_i^\dagger \hat{B}_j. \quad (7.44)$$

The fluctuations of J_{ij} around 1 will induce an extra decoherence timescale, $\Gamma_{c,inh}$, that must be smaller than our simulator parameters as well. In state-of-the-art experiments, optical cavities at visible wavelengths and cavity mode-waist of $\sim 500 \mu m$ are already available [375–377], which would roughly allow for $\sim 10^4$ local minima of the standing wave sitting in a homogeneous region.

- **Cavity & atom losses.** Even though the cavity-induced interactions are

mediated by a virtual population of photons, cavity decay introduces extra decoherence into the system due to the emission of these virtual photons. Moreover, the atomic excited states, also virtually populated, may as well decay into free space, introducing losses. The decay time of these excitations then needs to be larger than the slower tunneling time, $\kappa, \gamma \gg t_f$, which, following condition (e), sets a lower bound for the cooperativity of the cavity QED system, introduced in Section 2.2.3.

- **Three-body losses.** Since we have fermions and there can be at most one atom per lattice site, these type of losses should be small.

From these qualitative arguments, we see that most of the possible errors of the simulation are either already under control in current experiments [43, 45] or scale in an intensive way as the ratio between the number of simulated electrons and the number of available sites in the simulator.

7.7 Conclusion and outlook

Summing up, in this Chapter we have shown how to simulate 3D quantum chemistry Hamiltonians in an analog fashion using ultra-cold fermionic atoms in optical lattices. In particular, we have sequentially introduced several results, such as: i) A discussion of the physics of the holographic potentials required to obtain the nuclear attraction term. ii) The introduction of several setups to obtain fermionic repulsion that runs from Coulomb-like in the most sophisticated configuration to an exponential scaling (with a controllable decay length). Still these simpler schemes, where the emergent interactions are not fully Coulomb-like, can already be used as intermediate, but meaningful, experiments to observe chemistry-like behaviour, and to benchmark existing numerical algorithms. iii) An extrapolation strategy which allows us to obtain the expected energies in the continuum limit beyond the limitations imposed by the finite size of the simulator and, importantly, without an *a priori* knowledge of the expected energy. This approach could also guide other systems simulating chemistry problems in a lattice. iv) A numerical benchmark of the working conditions of the simulator. v) An illustration of the simulator capabilities for two-electron systems like the He atom or the H_2 and HeH^+ molecules. vi) Finally, a candidate experimental implementation.

We emphasize again that some of the elements and conditions required in this proposal are beyond the state-of-the-art, as it requires the combination of technologies that have only been built independently of each other so far. However, the rapid progress of analog quantum simulation may well lead to the realization of the present ideas in the near future, motivated by its potential impact in the determination of chemical structures, the understanding of reaction mechanisms, or the development of molecular electronics. We then expect that the results in this Chapter can stimulate both theoretical and experimental research, even before the realization of a fully-fledged analog simulator for quantum chemistry.

Chapter 8

Conclusions and perspectives

” *One never notices what has been done; one can only see what remains to be done.*

— Marie Skłodowska Curie
(Letter to her brother, 1894)

Throughout this Thesis, we have analyzed different scenarios where light changes the natural interactions atoms have in free space. In particular, we have investigated some of the interesting opportunities it offers in the simulation of quantum problems related to condensed matter physics and quantum chemistry.

Following a bottom-up approach, the first part of this Thesis has focused on investigating this light-matter interplay at the minimal level of a single photon and a single atom. In particular, Chapter 3 reveals that single-photon strong optomechanical effects are attainable in contemporary single-atom experiments, and could manifest as an increased heating rate due to the leaked information about the position of the atom, as well as mechanically-induced oscillations of the second-order correlation function for emitted light.

The second-part of the Thesis has continued with the analysis of neutral atoms trapped in an optical lattice. Going beyond the contact interactions that naturally appear in this platform, we have introduced different strategies to induce long-range interactions mediated by an additional atomic species in the form of a Fermi gas (Chapter 5), individual bosonic atoms (Chapters 6 and 7) or a Mott insulator (Chapter 7). For each of them, we have considered the application of these mediated forces in the simulation of quantum problems that range from bond-ordering in condensed matter (Section. 5.2.1), to molecular dissociation in quantum chemistry (Section 7.5.2).

Taking this work as a basis, there are many interesting directions that one can pursue. A particularly appealing one in the near-term is to continue simplifying the ingredients required for the realization of mediated long-range repulsion among neutral atoms, even at the cost of not simulating real materials or chemical interactions. In this second direction, Fig. 8.1 provides a tentative roadmap of experiments with increasing complexity (as moving to the bottom right of the table) towards complete analog chemistry simulation. For instance, first experiments could be performed with spinless fermions in one and two spatial dimensions. Another simplification might come from non-Coulomb nuclear potentials, e.g., in

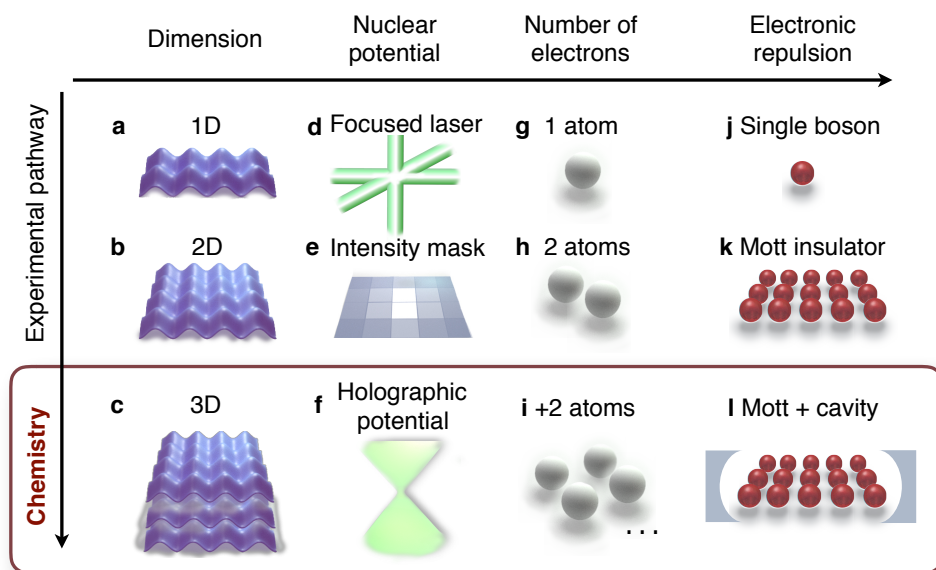


FIGURE 8.1: Schematic representation of the simplifications that can be considered for the different interactions of the system. The lowest line (c,f,i,l) corresponds to the full proposal in Chapter 7, leading to the chemical interactions we observe in nature. Chemistry in lower dimensions could be considered by restricting the optical lattice in such directions (a,b). The holographically created Coulomb potential could be replaced by, e.g., the Gaussian profile of a focused laser (d), giving a different scaling for electron-nuclei attraction. In 1D and 2D lattices one can also rely on an intensity mask (e). First implementations with single atoms (g) would allow to observe simple electronic orbitals (such as the energy levels of Hydrogen) with no need to mediate repulsion. For only two atoms (h) one does not need the symmetrizing effect of the cavity when mediating the Coulomb repulsion with the Mott insulator (k). Different scalings for repulsion can also be explored in more simplified setups, such as using a single boson that hops on the lattice and has on-site interaction with the fermionic atoms (j).

form of a Gaussian, which does not require holographic techniques; or by using simpler schemes to obtain the fermionic potential, e.g., using a single boson instead of a Mott insulator, and without a cavity. The latter still provides an effective repulsion between two fermions. With these simplifications, there is a clear pathway from state-of-the-art setups towards more challenging experimental setups based on progress in technology. Most importantly, in all these intermediate proof-of-principle setups one could already observe molecular-like potentials, dissociation, and other basic phenomena in chemistry. Besides, such experiments can also prove valuable to benchmark various numerical techniques, and trigger the development of new theoretical methods. This would allow us to reach a deeper understanding of the problems that appear in chemistry and which are challenging to test with classical computers.

We also envision that the methods developed in Chapter 6 and 7 to engineer non-local interactions in ultra-cold atoms can be exported to explore other phenomena where such interactions play a role, like in long-range enhanced topological superconductors [378]. In this quest, we have also developed strategies to encode a non-local Hamiltonian into a discretized cold-atom simulator, as well as to mitigate finite-size effects, that can be readily exported to other platforms where long-range interactions become accessible, as it could be the case of recent experiments with semiconductor quantum dots [379].

Focusing on the chemistry perspective, a relevant opportunity unveils for the study of dynamical processes, such as chemical reactions or photo-assisted chemistry [380–382], which are typically numerically very hard, and where the slower timescales of lattice-trapped atoms and the excellent imaging techniques could provide real-time access to the wavefunction properties. Also, there is the possibility of tuning the effective fermion interaction by using, e.g., a different bound state to mediate attractive interactions. This would allow one to simulate chemistry beyond the BO approximation by including another atomic species that plays the role of the nuclei, opening the door to relevant challenges in chemistry, as it is the study of conical intersections when degenerate nuclear configuration are present [383, 384].

To sum up, and ending with the quote that opened this Thesis: *"The problems of chemistry and biology can be greatly helped ~~by~~ [now that] our ability to see what we are doing, and to do things on an atomic level, is ultimately developed."*

Appendix A

Additional notes on Chapter 3

A.1 Scattering approach for a single atom

In Eq. (3.6), we have provided the relation between the reflected and input fields for a coherently, weakly driven cavity and when the atom is placed in a fixed position [93]. Here, we will show that Eq. (3.6) relates to the scattering matrix for an atom whose motion constitutes a dynamical degree of freedom [131, 132]. In particular, we consider a situation where the joint cavity-atom-motional system is in its ground state $|0_c \downarrow\rangle |\psi_0\rangle$, and a single monochromatic photon of frequency ω_l (or corresponding detuning Δ_0) is sent in. The S-matrix formally provides the transformation from the total input state $|\Psi_{\text{in}}\rangle = |0_c \downarrow\rangle |\psi_0\rangle |1_{\text{in}}\rangle$, to the output state at infinite time, $|\Psi_{\text{out}}\rangle = S |\Psi_{\text{in}}\rangle$. For the output, we take into account that the input photon could have been emitted through a detectable reflection channel with rate κ_1 ($|1_r\rangle$), undetectable cavity channels (transmission or loss) with rate κ_2 ($|1_t\rangle$), or spontaneously decayed with rate γ after exciting the atom ($|1_a\rangle$). As the total energy of the system is conserved, the frequency of the output photon carries information about any possible change in the phononic state of the atom. To suppress any effect arising from this additional entanglement, we consider that the implemented detection scheme is not frequency-resolving. We also focus on the unresolved sideband regime, $\omega_m \ll \gamma, \kappa$, where the characteristic time-scale of the optomechanical interaction between the cavity and the internal state of the atom is much faster than the atomic dynamics inside the mechanical trap, which allows to describe the response of the cavity as effectively diagonal in the atomic position basis.

For an atom fixed in position x , the input photon then scatters as,

$$S(x) |1_{\text{in}}\rangle = S_r(x) |1_r\rangle + S_t(x) |1_t\rangle + S_a(x) |1_a\rangle, \quad (\text{A.1})$$

which obey the relation $|S_r(x)|^2 + |S_t(x)|^2 + |S_a(x)|^2 = 1$ to conserve the norm of the scattered state. To calculate these components, each of the matrix elements can be expressed in terms of the eigenvectors, $|\beta(x)\rangle$, and eigenvalues, $\lambda_\beta(x)$, of the effective (non-Hermitian) atom-cavity Hamiltonian $\hat{H}_{\text{eff}}(x) = -(\Delta + \Delta_0 + i\kappa/2)\hat{a}^\dagger\hat{a} - (\Delta_0 +$

$i\gamma/2)\hat{\sigma}^+\hat{\sigma} + g(x) (\hat{\sigma}\hat{a}^\dagger + \hat{\sigma}^\dagger\hat{a})$ as,

$$\begin{aligned} S_r(x) &= 1 + i\kappa_1 \sum_{\beta} \langle 1_c \downarrow | \beta(x) \rangle \frac{1}{\lambda_{\beta}(x)} \langle \beta^*(x) | 1_c \downarrow \rangle, \\ S_t(x) &= i\sqrt{\kappa_1\kappa_2} \sum_{\beta} \langle 1_c \downarrow | \beta(x) \rangle \frac{1}{\lambda_{\beta}(x)} \langle \beta^*(x) | 1_c \downarrow \rangle, \\ S_a(x) &= i\sqrt{\kappa_1\gamma} e^{ik_c x} \sum_{\beta} \langle 0_c \uparrow | \beta(x) \rangle \frac{1}{\lambda_{\beta}(x)} \langle \beta^*(x) | 1_c \downarrow \rangle, \end{aligned} \quad (\text{A.2})$$

which requires the orthogonality relation $\langle \beta^*(x) | \beta(x) \rangle = 1$ due to the non-Hermitian nature of the Hamiltonian. To calculate these scattering elements, one can note that this Hamiltonian is block-diagonal and, given the single-photon input, one can restrict to the relevant subspace spanned by states $|0_c, \uparrow\rangle$ $|1_c, \downarrow\rangle$. Projecting there, one gets,

$$\begin{aligned} S_r(x) &= 1 - \frac{i\kappa_1}{\Delta_0 + \Delta + i\kappa/2 - \frac{g(x)^2}{\Delta_0 + i\gamma/2}}, \\ S_t(x) &= \frac{-i\sqrt{\kappa_1\kappa_2}}{\Delta_0 + \Delta + i\kappa/2 - \frac{g(x)^2}{\Delta_0 + i\gamma/2}}, \\ S_a(x) &= \frac{-i\sqrt{\kappa_1\gamma}}{\Delta_0 + \Delta + i\kappa/2 - \frac{g(x)^2}{\Delta_0 + i\gamma/2}} \frac{g(x)e^{ik_c x}}{\Delta_0 + i\gamma/2}. \end{aligned} \quad (\text{A.3})$$

This leads to the scattering elements $S_{\alpha}(x)$ associated to the different possible routes the input photon could eventually decay through, $\alpha \in \{r, t, a\}$. A more rigorous derivation based on Nakajima-Zwanzig leading to an analogous result can be found in [123].

If one now considers the atom to be initially in a superposition of different locations inside the cavity, $|\psi_0\rangle = \int dx \psi_0(x) |x\rangle$, the probability of decaying in either of the emission channels is given by, $|S_{\alpha}|\psi_0\rangle|^2 = \int dx |S_{\alpha}(x)|^2 |\psi_0(x)|^2$ and, if a photon $|1_{\alpha}\rangle$ was detected in either of these channels, the measurement then projects the atomic wave function into the conditional state, $|\psi_{\alpha}\rangle = S_{\alpha}|\psi_0\rangle / |S_{\alpha}|\psi_0\rangle|$.

To get a better intuition on how the scattering matrices depend on atomic position, one can investigate these equations in the limit $C_{\text{in}} \gg 1$ for the optimal choice of parameters motivated in the main text (3.7,3.8), and $\kappa_1 = 2\kappa_2$. Then, expanding S_{α} to linear order in $\delta x = x - x_0$, one finds,

$$\begin{aligned} S_r(x) &\approx -i \frac{\eta\sqrt{C_{\text{in}}}}{\sqrt{2}} \frac{\delta x}{x_{\text{zp}}}, \\ S_t(x) &\approx -\frac{1}{\sqrt{2}} \left(1 + i \frac{\eta\sqrt{C_{\text{in}}}}{\sqrt{2}} \frac{\delta x}{x_{\text{zp}}} \right), \\ S_a(x) &\approx \frac{1}{\sqrt{2}} \left[1 + i \left(\frac{\eta\sqrt{C_{\text{in}}}}{\sqrt{2}} + \eta \right) \frac{\delta x}{x_{\text{zp}}} \right], \end{aligned} \quad (\text{A.4})$$

which are valid for $|\delta x| \ll \ell$. In the opposite limit, $|\delta x| \gg \ell$, the cavity becomes out of resonance and one recovers perfect reflectance: $|S_r(x)| \rightarrow 1$ and $|S_t(x)|, |S_a(x)| \rightarrow 0$.

Numerically, one can directly calculate the mechanical energy of the atomic state conditioned to detection, $|\psi_r\rangle$ (3.10), by transforming to a phonon basis $|\psi_r\rangle = \sum_n \beta_n |n\rangle$, and calculating the expected number of phonons, $H = \sum_n n |\beta_n|^2$, which already accounts for both the kinetic and potential terms of the trap Hamiltonian. This is the approach followed in Fig. 3.4(a), where up to $n_m = 50$ phonons are involved in the calculation and the initial spatial interval $(-10x_{zp}, 10x_{zp})$ is discretized in 1000 divisions.

For the calculation of second order correlations $g_{rr}^{(2)}(t)$ in Eq. (3.13), we operate in the Schrödinger picture, where the projected state is evolved in time as $|\psi_r(t)\rangle = \sum_n e^{-in\omega_m t} \beta_n |n\rangle$. Transforming back to a position basis one can use the scattering matrix to express the result as, $g_{rr}^{(2)}(t) = |S_r |\psi_r(t)\rangle|^2 / \mathcal{R}$.

A.2 Master equation simulation

To calculate the master equation in Eq. (3.4) for an open system, we operate in the Schrödinger picture the variation of the density matrix, $\partial_t \hat{\rho}$, associated to both the atom and cavity. The numerical strategy is as follows:

- We start with an initial density matrix $\hat{\rho}(t_0)$, corresponding to a pure state with no excitations in the system (cavity photon, atomic phonon or internal excitation).
- The differential equation (3.4) is numerically evolved in time using a fourth order Runge-Kutta interpolation method.
- We evolve in time until a steady state $\hat{\rho}_{ss}$ is observed. For this purpose, we monitor over time the expected values of \hat{a} and $\hat{\sigma}$, and iterate until oscillations are smaller than 1%. We additionally check by comparing this value to the steady state mean-field solution (not presented here).

One can use this approach for the benchmark in Fig. 3.4(b), where we calculate the average number of induced phonons caused by an incident photon once the system reaches the steady state. Using input-output relations analogous to Eq. (3.5) and normalizing by the number of incoming photons, we approximate the three contributions as,

$$\mathcal{J}_{r/t} = \kappa_{1/2} \text{Tr} \left(\hat{b}^\dagger \hat{b} \hat{a} \hat{\rho}_{ss} \hat{a}^\dagger \right) / \left\langle \hat{a}_{in}^\dagger \hat{a}_{in} \right\rangle, \quad (\text{A.5})$$

$$\mathcal{J}_0 = \gamma \text{Tr} \left(\hat{b}^\dagger \hat{b} \hat{\sigma} \hat{\rho}_{ss} \hat{\sigma}^\dagger \right) / \left\langle \hat{a}_{in}^\dagger \hat{a}_{in} \right\rangle. \quad (\text{A.6})$$

Adding them up (red dotted line), we observe good agreement with the scattering matrix prediction (continuous line).

We can also use this approach to analyze the second-order time correlations, $g_{rr}^{(2)}(t)$, introduced in Eq. (3.12), which can be calculated using the description of Eq. (3.13) for the open system. From the perspective of the density matrix, expected values can be calculated as $\langle \hat{O} \rangle(t_i) = \text{Tr}(\hat{O} \hat{\rho}(t_i))$. For the correlator of interest, we observe that $\langle \hat{a}_{out}^\dagger(0) \hat{a}_{out}^\dagger(t) \hat{a}_{out}(t) \hat{a}_{out}(0) \rangle = \text{Tr}(\hat{a}_{out}(t) \hat{a}_{out}(0) \hat{\rho} \hat{a}_{out}^\dagger(0) \hat{a}_{out}^\dagger(t))$. In the

Schrödinger picture, we encode this time dependence in the density matrix as follows:

- Once the steady-state is reached, we calculate the projected matrix associated to detection at time 0,

$$\hat{\rho}_r(0) = \hat{a}_{\text{out}} \hat{\rho}_{\text{SS}} \hat{a}_{\text{out}}^\dagger / \text{Tr} \left(\hat{a}_{\text{out}} \hat{\rho}_{\text{SS}} \hat{a}_{\text{out}}^\dagger \right), \quad (\text{A.7})$$

where the denominator in Eq. (3.12) is calculated as

$$\langle \hat{a}_{\text{out}}^\dagger(t) \hat{a}_{\text{out}}(t) \rangle = \langle \hat{a}_{\text{out}}^\dagger(0) \hat{a}_{\text{out}}(0) \rangle = \text{Tr} \left(\hat{a}_{\text{out}} \hat{\rho}_{\text{SS}} \hat{a}_{\text{out}}^\dagger \right).$$

- To calculate the numerator, the new density matrix $\hat{\rho}_r(0)$ is evolved to time t , using the same evolution procedure used before. At this point, the resulting matrix is projected again, so that

$$\langle \hat{a}_{\text{out}}^\dagger(0) \hat{a}_{\text{out}}^\dagger(t) \hat{a}_{\text{out}}(t) \hat{a}_{\text{out}}(0) \rangle = \text{Tr} \left(\hat{a}_{\text{out}} \hat{\rho}_r(t) \hat{a}_{\text{out}}^\dagger \right) \cdot \text{Tr} \left(\hat{a}_{\text{out}} \hat{\rho}_{\text{SS}} \hat{a}_{\text{out}}^\dagger \right).$$

This approach is used to calculate the second-order correlations pictured in Fig. 3.5(b,d) with dashed lines.

Appendix B

Additional notes on Chapter 6

In this Appendix, we will focus on the calculations associated to the two-dimensional simulator.

B.1 Scheme I: bound-state energy

To solve the bound-state energy of a boson localized by two fermionic atoms, one needs to find a common solution for Eqs. (6.30) and (6.35),

$$\frac{1}{\bar{N}_M} \sum_{\mathbf{k}} \frac{1}{E_{I,B} - \omega_{\mathbf{k}}} = \frac{1}{\bar{N}_M} \sum_{\mathbf{k}} \frac{1 \pm e^{i\mathbf{k} \cdot \mathbf{j}_{12}}}{E_{\pm}(\{\mathbf{j}\}) - \omega_{\mathbf{k}}}. \quad (\text{B.1})$$

This equation admits a solution given by a recurrence relation on \mathbf{j}_{12} [385]. Using the expansions derived in Section B.1.1 and B.1.2, one gets for $d/a \ll 1/\sqrt{\delta_B/t_b}$,

$$\delta_{\text{up}} = E_+ - 4t_b \approx \frac{2\sqrt{\delta_B t_b}}{|\mathbf{j}_{12}|} e^{-\gamma}, \quad (\text{B.2})$$

where $\delta_B = E_{B,I} - 4t_b \approx 2^5 e^{-4\pi t_b/U} t_b$, and $\gamma \approx 0.577\dots$ is the Euler-Mascheroni constant. This simple model then provides an effective repulsion between the two fermions that scales as $\delta_{\text{up}}(d)/t_b \propto V_{I,0}/|\mathbf{j}_{12}|$ with $V_{I,0} = 2^{7/2} e^{-\gamma - 2\pi t_b/U} t_b$.

From the expansion in Section B.1.2 one sees that the characteristic length of the bound states is $L_I/a \approx (\delta_B/t_b)^{-1/2}$. For the previous expansions in (B.2) to be valid, one needs to satisfy the regime $|\mathbf{j}_{12}| = d/a \ll L_I/a$. To prevent finite size effects, it is also necessary, that $L_I/a \ll N_M$. To illustrate this, in Fig. B.1 we observe that this expansion for δ_B/t_b is valid for $U/t_b > 1$, so that $L_I/a \ll N_M = 100$. In Fig. B.2 we also confirm that for this size, the scaling $1/d$ is maintained for $d/a \ll 10$, so that $d/a \ll L_I/a$.

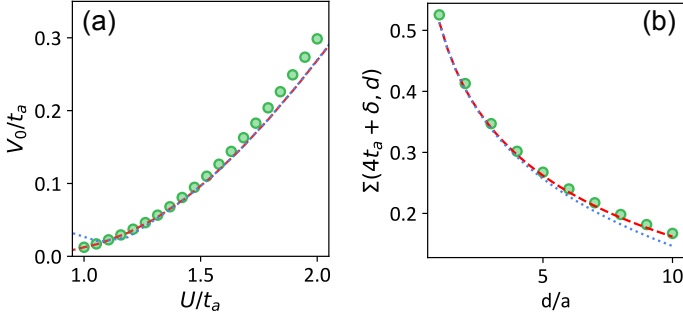


FIGURE B.1: Single-fermion bound state energy ($E_{B,I}$) as a function of the fermion-boson interaction U , as compared to the solution dictated by (6.30). Markers represent the ED calculation, while $\Sigma(z, 0)$ is evaluated using the analytical solution (B.3) (red dashed line) and the approximation (B.4) (blue dotted line). Inset shows the energy separation to the band edge, $\delta_B = E_{B,I} - 4t_b$. Here, $N_M = 100$ and finite-size effects appear for $U/t_b \lesssim 1$.

B.1.1 Calculation of the integral in Eq. (6.30)

Defining the energy and length units $t_b \equiv 1$, $a \equiv 1$ in the coming sections, we need to calculate,

$$\Sigma(z, 0) = \frac{1}{N_M} \sum_{\mathbf{k}} \frac{1}{z - \omega_{\mathbf{k}}}.$$

One can find an analytical solution [385],

$$\Sigma(z, 0) = 2K[4/z]/(\pi z), \quad (\text{B.3})$$

where $K[m] = \int_0^{\pi/2} d\theta (1 - m^2 \sin^2(\theta))^{-1/2}$ is the complete elliptic integral of the first kind for $|m| \leq 1$ [251]. For values $z = 4 + \delta$ close to the band-gap ($\delta > 0$ and $|\delta| \ll 1$), one can define,

$$\Sigma(z, 0) \approx (5 \log 2 - \log \delta)/(4\pi) + \mathcal{O}(\delta^2). \quad (\text{B.4})$$

B.1.2 Calculation of the integral in Eq. (6.35)

Now, we are interested in the calculation of,

$$\Sigma(z, \mathbf{j}) = \frac{1}{N_M} \sum_{\mathbf{k}} \frac{e^{i\mathbf{k}\mathbf{j}}}{z - \omega(\mathbf{k})}. \quad (\text{B.5})$$

In the limit $\mathbf{k}\mathbf{j} \gg 1$, we can expand the dispersion relation for frequencies close to the upper band-edge, $[(k_x, k_y) = (\pi, \pi)]$. Taking the translation $\tilde{k}_{x,y} \equiv -\pi + k_{x,y}$, we expand $\omega(\tilde{\mathbf{k}}) \approx 4 - \tilde{\mathbf{k}}^2$, and extend the integration domain to infinite. Note that the numerator $e^{i\mathbf{k}\mathbf{j}}$ prevents the otherwise divergent integral, and the frequency shift introduces a sign factor, $e^{i\pi|\mathbf{j}|}$, that does not enter in the mediated potentials for the strategies presented in this Letter. Without loss of generality, we align vector \mathbf{r} in the z -axis, and use spherical units,

$$\Sigma(z, \mathbf{j}) = e^{i\pi|\mathbf{j}|} K_0 \left[|\mathbf{j}| \sqrt{z - 4} \right] / (2\pi), \quad (\text{B.6})$$

where $K_n[x]$ is the modified Bessel function of the second kind [251]. For small arguments ($0 < x \ll 1$), one finds,

$$K_0[x] \approx -\log(x/2) - \gamma. \quad (\text{B.7})$$

B.2 Scheme II: Mediating atoms with two long-lived states

Let us now derive the effective potential mediated by scheme II (6.39), for $g/\Delta \ll 1$ and N_e fermions occupying fixed positions $\mathbf{j}_1 \dots \mathbf{j}_{N_e}$. Intuitively, mediating atoms localize around the fermionic positions, and double occupations are prevented by the hard-core boson interaction $W \gg U$. This then creates a bound-state in which each mediating atom localizes in a different fermionic position. As compared to the previous scheme, hopping from one fermion to the others now becomes a fourth-order process in the coupling g between the two atomic metastable states, as the movement of two mediating atoms is needed.

In particular, we are interested in the regime in which states a and b of the mediating atoms are weakly coupled $g/\Delta \ll 1$, and atoms in level a hop in a lattice much more shallow than the rest: $t_f \ll t_b \ll t_a$. This allows us to trace-out the effect of the mediating atom, writing an effective Hamiltonian for the fermions, $\sum_{ij} V(|\mathbf{i} - \mathbf{j}|) f_i^\dagger f_j^\dagger f_i f_j$ using perturbation theory. For this, let us separate the bosonic interactions, $\hat{H}_{\text{II,B}} = \hat{H}_{f\text{-aux}} + \hat{H}_{\text{II,aux}}$ (6.39), as $\hat{H}_{\text{II,B}} = \hat{H}_0 + \hat{H}_I$, where

$$\begin{aligned} \hat{H}_0 &= \Delta \sum_{\mathbf{j}} a_{\mathbf{j}}^\dagger a_{\mathbf{j}} - t_b \sum_{\langle i,j \rangle} b_i^\dagger b_j - t_a \sum_{\langle i,j \rangle} a_i^\dagger a_j + U \sum_{\mathbf{j}} b_j^\dagger b_j f_j^\dagger f_j + \frac{W}{2} \sum_{\mathbf{j}} b_j^\dagger b_j^\dagger b_j b_j, \\ \hat{H}_I &= g \sum_{\mathbf{i}} (b_{\mathbf{j}}^\dagger a_{\mathbf{j}} + \text{H.c.}). \end{aligned} \quad (\text{B.8})$$

In particular, we are interested in the energy correction of the zero-order ground-state $|\psi_{\text{II,B}}^{(0)}\rangle = \prod_{i=1}^{N_e} b_{\mathbf{j}_i}^\dagger |0\rangle$, that depends on the fermionic positions. For this, we need to expand the perturbed Hamiltonian. One can see that only even orders enter the calculation, and expanding to fourth order,

$$\begin{aligned} E_{\text{II,B}} |\psi_{\text{II,B}}\rangle &\approx \left(\hat{H}_0 + \hat{H}_I \frac{1}{E - \hat{H}_0} \hat{H}_I \right. \\ &\quad \left. + \hat{H}_I \frac{1}{E - \hat{H}_0} \hat{H}_I \frac{1}{E - \hat{H}_0} \hat{H}_I \frac{1}{E - \hat{H}_0} \hat{H}_I \right) |\psi_{\text{II,B}}\rangle, \end{aligned} \quad (\text{B.9})$$

one gets the equation,

$$\begin{aligned} E_{\text{II,B}} &= N_e U + N_e \frac{g^2}{N_M} \sum_{\mathbf{k}} \frac{1}{E_{\text{II,B}}/N_e - \Delta - \omega_{\mathbf{k}}} \\ &\quad + \frac{2g^4}{N_M^2} \sum_{m \neq n=1}^{N_e} \sum_{\mathbf{k}, \mathbf{q}} \frac{1 + e^{i(\mathbf{k}-\mathbf{q})(\mathbf{j}_m - \mathbf{j}_n)}}{(E_{\text{II,B}}/N_e - \Delta - \omega_{\mathbf{k}})^2 (E_{\text{II,B}}/N_e - \Delta - \omega_{\mathbf{q}})}. \end{aligned} \quad (\text{B.10})$$

This latter term originates from the pairwise repulsion introduced by the

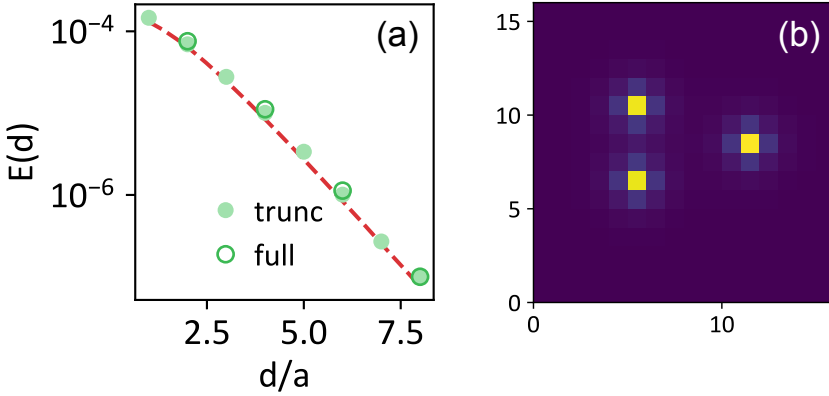


FIGURE B.2: (a) This initial value V_0 is calculated for different choices of bosonic-fermionic interaction U , and compared to the approximation (B.2). In this equation, the value of δ_B is calculated using the exact solution (B.3) (red dashed line), and using ED (blue dotted line). For the numerical calculation, $N_M = 100$. (b) Numerical evaluation of (B.5) for $N_M = 100$ (markers), as compared to the analytical solution in the continuum (B.6) (red dashed line) and approximation (B.7) (blue dotted line). Here, $\delta/t_a = 0.002$.

fourth-order correction of two mediating atoms swapping the fermionic position they localize around. This then leads to an effective pairwise potential, $\sum_{m \neq n=1}^{N_e} V_{\text{II}}(|\mathbf{j}_m - \mathbf{j}_n|) f_{j_1}^\dagger f_{j_2}^\dagger f_{j_1} f_{j_2}$ (6.25), where

$$V_{\text{II}}(\mathbf{j}_{12}) \approx \frac{2g^4}{N_M^2} \left(\sum_{\mathbf{k}} \frac{e^{i\mathbf{k}\mathbf{j}_{12}}}{(E_{\text{II,B}}/N_e - \Delta - \omega_{\mathbf{k}})^2} \right) \left(\sum_{\mathbf{q}} \frac{e^{-i\mathbf{q}\mathbf{j}_{12}}}{E_{\text{II,B}}/N_e - \Delta - \omega_{\mathbf{q}}} \right). \quad (\text{B.11})$$

These two independent sums can be calculated as in Section B.1.2. Note that the alternating sign derived in Section B.1.2 cancels after the double product $e^{i\mathbf{k}\mathbf{r}} e^{-i\mathbf{q}\mathbf{r}}$. Using that $\partial_x K_0[x] = -K_1[x]$, one obtains, $V_{\text{II}}(r) \approx \frac{2g^4}{(2\pi)^2} K_0[r\sqrt{\delta_{\text{II}}}] \frac{r}{2\sqrt{\delta_{\text{II}}}} K_1[r\sqrt{\delta_{\text{II}}}]$, which, to lowest order in the regime $r\sqrt{\delta_{\text{II}}} > 1$, scales as,

$$V_{\text{II}}(r) \approx \frac{g^4}{8\pi\delta_{\text{II}}} e^{-2r\sqrt{\delta_{\text{II}}}}. \quad (\text{B.12})$$

This then leads to a pairwise repulsion between the fermionic atoms that decays exponentially with their separation, following a decay length $L_{\text{II}} \equiv (2\sqrt{\delta_{\text{II}}})^{-1/2}$. In Fig. 6.7(a), we approximate δ_{II} to second order as

$$\delta_{\text{II}} \approx \delta + E_{\text{II,B}}^{(2)}(\delta)/N_e, \quad (\text{B.13})$$

where $E_{\text{II,B}}^{(2)}(\delta)$ approximates the second order correction (δ) in (B.10) as,

$$E_{\text{II,B}}^{(2)}(\delta) = N_e \frac{g^2}{N_M} \sum_{\mathbf{k}} \frac{1}{U - \Delta - \omega_{\mathbf{k}}}, \quad (\text{B.14})$$

which can be expanded as in (B.4).

B.3 Numerical methods

Here we provide further details about the numerical methods used in the figures of Chapter 6.

B.3.1 Exact diagonalization

Once the kinetic term is approximated as a nearest-neighbor hopping term (6.12), the Hamiltonian can be conveniently written in a position basis and the ground-state obtained using ED.

In Fig. 6.3 we use this approach to calculate the energies λ_n associated to the lowest part of the spectrum of Hamiltonian (6.11) for different choices of the ratio t_f/V_0 . These energies are shifted to correct the shift induced by the nearest-neighbor approximation, $\omega(\mathbf{k}) \approx 1 - k^2/2$. The result is divided by the Rydberg energy; this is, $E_n/\text{Ry} = [\lambda_n + N_e \cdot (2t_f)] / (V_0^2/t_f)$ where, in this case $N_e = 1$. The same strategy is applied to calculate the fermionic potential in Fig. 6.4(a), where only one mediating atom is involved.

This approach is also used in Fig. 6.4(a) to calculate the ground-state energy of an hydrogen cation for a given internuclear separation d/a_0 . In addition to the previous shift, nuclear repulsion $V_0/(d/a)$ needs to be included before expressing the result in Rydberg energies. Similarly to the atomic case, for a fixed interatomic distance, accuracy improves by increasing the effective Bohr radius $a_0/a = t_f/V_0$, up to the point in which finite-size effects become relevant. The number of lattice sites separating the nuclear positions d/a is then adjusted accordingly, identifying the optimal separation value as the one giving the lowest ground-state energy (see Fig. 6.4(b)).

The same strategy is followed to obtain the ground state energy of H_2 in Fig. 6.6(b). The main difference is that now $N_e = 2$, and further simplifications can be made taking into consideration the fermionic statistics. As each fermion can occupy \bar{N}_M sites which, together with the fermionics statistic $\{f_i, f_j^\dagger\} = \delta_{i,j}$ leads to a Hilbert space of space of size $\bar{N}_M(\bar{N}_M - 1)/2$. ED is also used in 6.6(b) to calculate the effective potential mediated by a single bosons, for fixed fermionic positions separated by d/a sites and centered in the lattice.

The exponential decaying potential explored in Fig. 6.7(b), requires a more careful analysis, as the natural rescalings to the Bohr radius and Rydberg energy does not apply now. In particular, three parameters can be independently tuned: the fermionic hopping t_f , the interacting potential V_0 and the decay length L_{II}/a . As compared to the previous case, one can remap $V_0 \rightarrow V_0^2/t_f$ and $L_{II} \rightarrow L_{II}t_f/V_0$, so that the final result is still dimensionless when normalizing the energies by the previous definition of Bohr radius V_0^2/t_f . As an illustration, in this Figure 6.7(b), $L_{II}/a = 5$ is chosen, and t_f/V_0 is fixed as the ratio providing maximum accuracy for the atomic case (one fermion an one nuclei) hopping in a lattice of side $\lfloor N_M/2 \rfloor$, so that the dissociation limit is properly captured. Modifying the separation d/a between nuclear positions then allows one to scan the different internuclear separations $d/a_0 = (d/a) \cdot (V_0/t_f)$ for this fixed value of t_f/V_0 .

B.3.2 Imaginary time evolution (ITE)

For the calculation of the effective potential mediated by the two metastable levels of atoms in 6.7(a), we use ITE. This is a useful strategy to numerically obtain the ground state of a gapped Hamiltonian with purely positive eigenvalues, and consists on iteratively evolving an initially random state as, $e^{-\hat{H}t}$. After each iteration the resulting state is normalized, and the contribution of the excited states is mostly reduced.

In more detail, one of the advantages of this method is that rather than writing the entire evolution operator $\mathcal{O}(\overline{N}_M^2)$, one can choose to work in a diagonal basis, so that only $\mathcal{O}(\overline{N}_M)$ terms are needed to describe the state at each point in time. From the computational perspective, this is specially useful when facing the multielectronic case. In principle, to calculate the interaction among N_b -bosons one would need a state with $(\overline{N}_M)^{N_b}$ entries. Using ED, one would need to write the Hamiltonian, of size $(\overline{N}_M)^{N_b} \times (\overline{N}_M)^{N_b}$. In contrast, evolving the state in ITE only needs to store the diagonal terms [with size $(\overline{N}_M)^{N_b}$], once the state is expressed in a basis that commutes with the terms of the Hamiltonian. For our particular case, this corresponds to the position representation for the on-site interactions, and momentum representation for the kinetic term. The Hamiltonian \hat{H}_{nuc} is already diagonal in position basis, and one can define a momentum basis,

$$f_{\mathbf{k}}^\dagger(b_{\mathbf{k}}^\dagger) = \frac{1}{(2\pi)^{D/2}} \sum_{\mathbf{j}} e^{-i\mathbf{k}\mathbf{j}} f_{\mathbf{j}}^\dagger(b_{\mathbf{j}}^\dagger). \quad (\text{B.15})$$

The kinetic terms reads as $H_{\text{kin}} = \sum_{\mathbf{k}} \omega_{\mathbf{k},f} f_{\mathbf{k}}^\dagger f_{\mathbf{k}}$, where $\omega_{\mathbf{k},f} = -2t_f [\cos(k_x) + \cos(k_y)]$ is the dispersion relation. This induces a periodic boundary condition in the lattice, which does not affect the calculation as long as finite-size effects are prevented. To confirm that is the case, for each choice of parameters we check that the same result is obtained for the single-boson case using ED, evidencing that boundary conditions are not affecting the result.

To calculate the ITE of Hamiltonian (6.39), a constant energy shift is added to H during the calculation to make all the spectrum positive, which is later subtracted at the end of the calculation. To evaluate the operation, $\psi(t) = e^{-Ht}\psi(0)$ we use a Suzuki-Trotter [386] expansion of the first kind, dividing the evolution in n steps as $e^{-Ht} \approx \prod_{k=1}^{n-1} e^{-H\Delta t} + \mathcal{O}(\Delta t)$, and $t_k = k \cdot \Delta t/t$. For each of these steps, we calculate

$$e^{-H\Delta t}\psi(t_k) \approx \text{IFFT} \left[e^{-\hat{H}_{\mathbf{k}}\Delta t} \text{FFT} \left(e^{-\hat{H}_{\mathbf{R}}\Delta t} e^{-\hat{H}_I\Delta t} \psi(t_{k-1}) \right) \right] + \mathcal{O}(\Delta t^2), \quad (\text{B.16})$$

where (I)FFT indicates the (inverse) fast Fourier transformation, and normalize the resulting state. Here, $\hat{H}_{\mathbf{R}}$ denote the terms that are diagonal in the position basis, and $\hat{H}_{\mathbf{K}}$ the ones in momentum basis. \hat{H}_I denotes the coupling term, whose exponential can be directly calculated noting that, $e^{-g(a_j^\dagger b_j + \text{H.c.})\Delta t} = \cosh(g\Delta t)(a_j^\dagger a_j + b_j^\dagger b_j) - \sinh(g\Delta t)(a_j^\dagger b_j + \text{H.c.})$. We iterate this procedure until the overlap between $\psi(t_{k-1})$ and $\psi(t_k)$ is smaller than 10^{-5} . We initialize the algorithm with a random state for the smallest value of t_f/V_0 , and use this converged solution as the initial state for the next configuration of t_f/V_0 .

In this second scheme, N_e atoms with two long-lived states are used to mediate the interaction among N_e fermions. For a given fermionic configuration, we desire

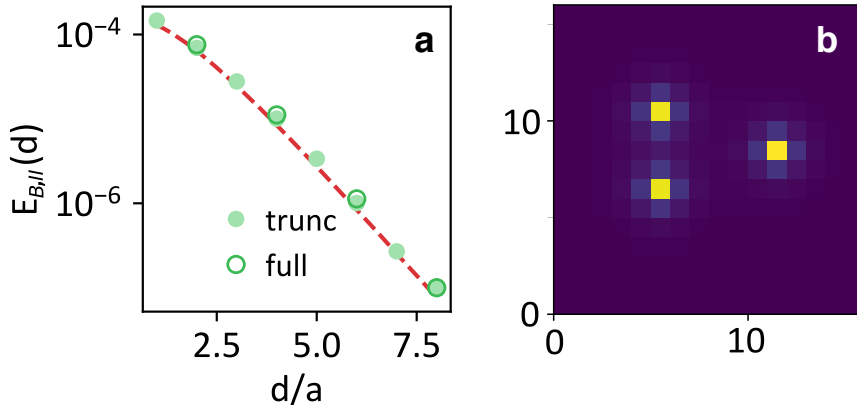


FIGURE B.3: (a) Bound-state energy dependence for 3 bosons affected by 3 fermionic atoms occupying fixed positions describing an isosceles triangle of basis 4 sites, and variable height, d/a . Contour markers refer to the full basis in which 3 bosonic atoms can simultaneously occupy level a , and full markers refer to the truncated basis (see Text). Dashed line is described by the solution in Eq. (B.11). (b) Occupation of state a for a height of 6 sites. Parameters: $N = 16$, $\delta/t_a = g/t_a = 0.3$.

to numerically calculate the bound state, and compare it to the analytical expansion previously introduced in Eq. (B.11). For this calculation, we use the ITE method (Section B.3.2), where now, each of the N_e mediating atoms can occupy any of the 2 levels at any of the \bar{N}_M lattice sites, which *a priori* accounts for states of size $(2\bar{N}_M)^{N_e}$. To reduce this space, we assume that $|g/(U - \Delta)| \ll 1$, so that we only consider the population of level b in those sites where they interact with the fermions; and $|W/U| \gg 1$, so that two mediating atoms in level b do not coexist in the same lattice site. For a configuration of 2 (3) fermions in sites $\mathbf{r}, \mathbf{s}(\mathbf{t})$, and given the indistinguishability of the mediating atoms, we can further reduce the Hilbert space to states written in the basis collected in Tables I and II.

Within this basis, in Fig. 6.6 we calculate how the energy of the bosonic ground-state energy $E(d)$ depends on their separation d between two fermionic atoms fixed in lattice sites $[N/2 - d/2, N/2]$ and $[N/2 + d/2, N/2]$, following the same strategy used in the previous case for $N_e = 2$. In the case $N_e = 3$, we observe that the biggest demand on computational memory corresponds to describing processes in which the three mediating atoms simultaneously populate the a -level. Such processes scale as $[g/(U - \delta)]^6$ in perturbation theory, and are subleading when compared to the second-order terms. Therefore, truncating $0 \leq N_a \leq 2$ would allow to push the calculation at a marginal error (see Table II).

To confirm this intuition, in Fig. B.3(a) we use ITE to calculate the bosonic bound state for 3 fermions describing a triangular isosceles configuration. For moderate sizes ($N = 16$), we compare the numerical result given by this truncated space to the one obtained for the total basis, including three mediating bosons in level a . As desired, we observe that (1) the truncation to the space with up to 2 excitations in state a does not modify the solution, and (2) the scaling is in agreement with the calculation for a pairwise repulsion given by (B.12).

N_b	N_a	State	Size
2	0	$b_r^\dagger b_s^\dagger 0\rangle$	1
1	1	$b_r^\dagger a_m^\dagger 0\rangle$ $b_s^\dagger a_m^\dagger 0\rangle$	$2\bar{N}_M$
0	2	$a_m^\dagger a_n^\dagger 0\rangle$	$\bar{N}_M(\bar{N}_M + 1)/2$

TABLE B.1: Basis used to describe states in which N_b of the two mediating atoms occupy level b in the fermionic sites r, s , and N_a atoms are in level a for any choice of sites m, n , in the lattice of size $N_M \times N_M$.

N_b	N_a	State	Size
3	0	$b_r^\dagger b_s^\dagger b_t^\dagger 0\rangle$	1
2	1	$b_r^\dagger b_s^\dagger a_m^\dagger 0\rangle$ $b_s^\dagger b_t^\dagger a_m^\dagger 0\rangle$ $b_t^\dagger b_r^\dagger a_m^\dagger 0\rangle$	$3\bar{N}_M$
1	2	$b_r^\dagger a_m^\dagger a_n^\dagger 0\rangle$ $b_s^\dagger a_m^\dagger a_n^\dagger 0\rangle$ $b_t^\dagger a_m^\dagger a_n^\dagger 0\rangle$	$3\bar{N}_M(\bar{N}_M + 1)/2$
0	3	$a_m^\dagger a_n^\dagger a_p^\dagger 0\rangle$	$(\bar{N}_M + 2)(\bar{N}_M + 1)\bar{N}_M/6$

TABLE B.2: Similarly to Table I, here we define the basis associated to N_b of the three mediating atoms occupying level b in the fermionic sites r, s, t , and N_a atoms being in level a for any choice of sites m, n, p , in the lattice of size $N_M \times N_M$. The truncated basis described in the Text corresponds to neglecting to states in the last row.

Appendix C

Additional notes on Chapter 7

C.1 Discretization error scaling in 3D

This discretization inherent to our lattice approach gives rise to certain errors that need to be considered and vanish in the infinite-size limit. Here we estimate the errors related to (i) the discretization of the integral appearing in the Coulomb term, and (ii) the discretization of the Laplacian appearing in the kinetic term.

C.1.1 Discretization of the integrals

The calculation of expected energies over the continuum limit are based on integrals on the entire real space. The discretization of the lattice, however, transforms these integrals into a finite sum of terms, introducing an error that vanishes in the limit of infinite sites. This effect is closely related to the definition of a Riemann integral evaluated at mid-point values, $\mathbf{m}_j = \mathbf{j} + (0.5, 0.5, 0.5)$, written in the units of the lattice spacing. Its error is given by,

$$\Delta_{\text{Int}} = \left| \int d\mathbf{s} f(\mathbf{s}) - a^3 \sum_j f(\mathbf{m}_j) \right| \approx \frac{a^2}{24} \int d\mathbf{s} [f_{xx}(\mathbf{s}) + f_{yy}(\mathbf{s}) + f_{zz}(\mathbf{s})], \quad (\text{C.1})$$

where $f_{\alpha\beta}(\mathbf{x}) = \partial_\alpha \partial_\beta f(\mathbf{x})$. A back-of-the-envelope calculation could be illustrative in this case. We focus on the integrals for the Coulomb potential, $f(\mathbf{r}) = |\psi_{n\ell}(\mathbf{r})|^2 \cdot V(\mathbf{r})$, for Hydrogen atomic orbitals, $\psi_{n\ell}(\mathbf{r}) \propto g_{n\ell}(r/a_0) \cdot \exp(-nr/a_0)$; being $g_{n\ell}$ an $(n-1)$ -degree polynomial. Rescaling coordinates the lattice units, $r \rightarrow ra_0$, one has

$$\Delta_{\text{Int}}^{(\text{C})} \equiv V_0 \frac{a^3 \int d\mathbf{r} \frac{\partial^2}{\partial x^2} [g_{n\ell}^2(r) \cdot \exp(-2nr)/r]}{a_0^3 \int d\mathbf{r} g_{n\ell}^2(r) \cdot \exp(-2nr)} \propto V_0 (a/a_0)^3.$$

Expressing this in Rydberg units, one gets the scaling,

$$\Delta_{\text{Int}}^{(\text{C})} / \text{Ry} \propto (V_0/t_f)^2. \quad (\text{C.2})$$

The precise constant accompanying this scaling is a geometrical factor, characteristic of each atomic orbital.

C.1.2 Approximation of the kinetic term

In the discrete Hamiltonian, the kinetic term is approximated as a first-neighbor hopping term. One can estimate the error in this approximation from the next order terms of the expansion of $\nabla^2 f$, that correspond to $\frac{a^4}{12} [\partial_x^4 f(\mathbf{r}) + \partial_y^4 f(\mathbf{r}) + \partial_z^4 f(\mathbf{r})]$.

Again, one can make an estimation on how this error of the kinetic term scales with the atomic units, and therefore with the size of the system. Using the Hydrogen wavefunctions used before, one gets,

$$\Delta_{\text{lin}}^{(L)} \equiv t_f \frac{a^4 \int d\mathbf{s} g_{nl}(r) \exp(-r/n) \cdot \frac{\partial^4}{\partial x^4} [g_{nl}(r) \exp(-nr)]}{a_0^4 \int d\mathbf{r} g_{nl}^2(r) \cdot \exp(-2nr)} \propto t_f (a/a_0)^4.$$

Expressing this result in atomic units, one obtains the leading correction for the final error in energies,

$$\Delta_{\text{lin}}^{(L)} / Ry \propto (V_0/t_f)^2. \quad (\text{C.3})$$

Interestingly, both effects lead to the heuristic scaling $\propto (V_0/t_f)^2$ for discretization error that we numerically observe in Fig. 7.2.

C.2 Details on the perturbative analysis in Section 7.4.

Here, we complete the details on the derivation of the bounds presented in the main text. In our derivation, one is interested in finding the mediating species in the state providing repulsion. Following the approach introduced in Eq. (7.8), our bound will arise from the coupling of this state to other orthogonal ones, and the energy gap between them, $\varepsilon_\alpha = \sum_{\text{all}\{\mathbf{r}\}} \sum_m \bar{\varepsilon}_\alpha \left(\varphi_{m,\{\mathbf{r}\}}^\perp \right)$, with

$$\bar{\varepsilon}_\alpha \left(\varphi_{m,\{\mathbf{r}\}}^\perp \right) = \left| \frac{f \langle \{j\} |_{\text{aux}} \langle \varphi_{m,\{\mathbf{r}\}}^\perp | \hat{H}_\alpha | \Psi \rangle}{\Delta_{m,\mathbf{r},j}} \right|^2. \quad (\text{C.4})$$

C.2.1 Useful analytical expressions

Here, we first derive the analytical expressions of certain integrals that appear several times in the calculations of the error bounds and mediated potential. In the three-dimensional continuum limit, these expressions are of the form,

$$\Sigma(z, \mathbf{r}) = \frac{1}{(2\pi)^3} \int_D d\mathbf{k} \frac{e^{i\mathbf{k}\cdot\mathbf{r}}}{z - \omega(\mathbf{k})}, \quad (\text{C.5})$$

for $D = [-\pi, \pi]^{\otimes 3}$, and $\omega(\mathbf{k}) = 2t_b [\cos(k_x) + \cos(k_y) + \cos(k_z)]$ (we assume $t_b \equiv 1$ from now on), that, for example, governs the shape of the single-fermion bound-state wavefunction. Other expressions that appear are of the type,

$$g(z, \mathbf{r}) = \frac{1}{(2\pi)^3} \int_D d\mathbf{k} \frac{e^{i\mathbf{k}\cdot\mathbf{r}}}{[z - \omega(\mathbf{k})]^2}, \quad (\text{C.6})$$

that governs the Franck-Condon coefficient in the same situation. Note that the latter is related to $\Sigma(z, \mathbf{r})$ by a derivative: $g(z, \mathbf{r}) = -\partial_z \Sigma(z, \mathbf{r})$. Remarkably, in the limit $\mathbf{k} \cdot \mathbf{r} \gg 1$, one can expand the dispersion relation around their band-edges, $\omega(\mathbf{k}) \approx 6 - \mathbf{k}^2$, and extend the integration domains to infinite to obtain an analytical expression:

$$\begin{aligned} \Sigma(z, \mathbf{r}) &= \frac{1}{(2\pi)^2} \int_0^\pi d\theta \int_0^\infty dk \frac{e^{ik \cdot r \cos \theta}}{(z-6) + k^2} k^2 \sin \theta \\ &= \frac{1}{(2\pi)^2} \int_{-1}^1 ds \int_0^\infty dk \frac{e^{ik \cdot rs}}{(z-6) + k^2} k^2 = \frac{-i}{r(2\pi)^2} \int_0^\infty dk \frac{e^{ik \cdot r} - e^{-ik \cdot r}}{(z-6) + k^2} k \quad (\text{C.7}) \\ &= \frac{-i}{r(2\pi)^2} \int_{-\infty}^\infty dk \frac{e^{ik \cdot r}}{(z-6) + k^2} = \frac{1}{4\pi r} e^{-r\sqrt{z-6}}. \end{aligned}$$

Note that for $\mathbf{r} = [0, 0, 0]$ the integral does not converge, because we have artificially introduced a divergence by expanding the domain of integration to infinite. A way of renormalizing consists in artificially introducing an exponential cut-off $e^{-k\Lambda}$ with $\Lambda \rightarrow 0$, such that,

$$\Sigma(z, 0) = \frac{1}{2\pi^2} \int_0^\infty dk \frac{k^2 e^{-k\Lambda}}{(z-6) + k^2} = \frac{1}{2\pi^2 \Lambda} - \frac{\sqrt{z-6}}{4\pi}. \quad (\text{C.8})$$

However, in lattice systems this cutoff appears naturally, and one can analytically obtain an expression for $\Sigma(z, 0)$ [387, 388],

$$\Sigma(z, 0) \approx 0.253 - \frac{\sqrt{z-6}}{4\pi}. \quad (\text{C.9})$$

Once we have the analytical expansions of $\Sigma(z, \mathbf{r})$ it is straightforward to obtain the higher order terms, e.g., $g(z, \mathbf{r})$ as follows,

$$g(z, r) = -\partial_z \Sigma(z, \mathbf{r}) = \frac{1}{8\pi\sqrt{z-6}} e^{-r\sqrt{z-6}}. \quad (\text{C.10})$$

C.2.2 Scheme I: Repulsion mediated by single atoms

In the single-fermion case of Scheme I, the maximum ratio between the hopping of the fermionic and mediating species was obtained in Eq. (7.14) from the coupling to the scattering states of the mediating atom when the fermion hops:

$$\sum_m \bar{\epsilon}_f \left(\varphi_{m, \mathbf{j}_0+1}^\perp \right) \leq t_f^2 \sum_{\mathbf{k}} \left| \frac{\hat{b}_{\mathbf{k}} |\varphi_{B, \mathbf{j}_0}\rangle}{E_{\text{LB}} - \omega_{\mathbf{k}}} \right|^2 \ll 1.$$

Note that in the three-dimensional lattice, the sum to nearest neighbors introduces a factor 6, that we have omitted along the text to focus on the scalings. Without loss of generality, we can consider \mathbf{j}_0 to be the origin of coordinates. Replacing the wavefunction (6.31) in momentum-space, one obtains $\left| \hat{b}_{\mathbf{k}} |\varphi_{B, \mathbf{j}_0}\rangle \right|^2 = 1 / \left[\mathcal{N} \bar{N}_M (E_{\text{LB}} - \omega_{\mathbf{k}})^2 \right]$. By considering the expression (C.10), and its second derivative, one obtains the inequality (7.14).

As we see, moving to momentum space simplifies the calculation of \mathcal{F}_1 in Eq. (7.15),

$$\langle \varphi_{B,j_0+1} | \varphi_{B,j_0} \rangle = \frac{1}{\mathcal{N}\overline{N}_M} \sum_{\mathbf{k}} \frac{e^{ik_z}}{(E_{I,B} - \omega_{\mathbf{k}})^2} = e^{-a/L_I}, \quad (\text{C.11})$$

where we have made use of Eq. (C.10).

Moving now to the two-fermion case, one can relate Eqs. (6.30) and (6.35) to obtain,

$$\frac{1}{\overline{N}_M} \sum_{\mathbf{k}} \frac{1}{E_{I,B} - \omega_{\mathbf{k}}} = \frac{1}{\overline{N}_M} \sum_{\mathbf{k}} \frac{1 + e^{i\mathbf{k} \cdot \mathbf{j}_{12}}}{E_+(\{\mathbf{j}\}) - \omega_{\mathbf{k}}}, \quad (\text{C.12})$$

and then replacing the expression (C.7) and (C.8) leads to:

$$-\sqrt{E_{I,B}/t_b - 6} = -\sqrt{E_+(|\mathbf{j}_{12}|)/t_b - 6} + \frac{e^{-|\mathbf{j}_{12}| \sqrt{E_+(d)/t_b - 6}}}{|\mathbf{j}_{12}|}. \quad (\text{C.13})$$

Here, we need to separate the discussion in two different regimes.

- In the case $|\mathbf{j}_{12}| \gg L_I/a$ the latter term in (C.13) is dominated by the exponential decay, and one can expand to lowest order the effective repulsive potential $V_{I,>}(\mathbf{j}_{12})$ in Eq. (7.17) by replacing $E_+(d) \approx E_{I,B}$ in the exponential.
- In the regime $|\mathbf{j}_{12}| \ll L_I/a$ that simplification is, however, not possible. A general expansion of Eq. (C.13) in this regime corresponds to,

$$V_{I,<}(\mathbf{j}_{12}) = \frac{\gamma^2}{|\mathbf{j}_{12}|^2} + \frac{2\gamma}{1+\gamma} \frac{a}{|\mathbf{j}_{12}|L_I} + \frac{\mathcal{O}\left[\left(\frac{|\mathbf{j}_{12}|a}{L_I}\right)^2\right]}{|\mathbf{j}_{12}|^2}, \quad (\text{C.14})$$

with $\gamma \approx 0.567$. This leads to Eq. (7.18).

In this exponential regime, we now need to bound the undesirable coupling to the antisymmetric state due to the fermionic hopping, $\bar{\epsilon}_f \left(\varphi_{-(j_1+1,j_2)} \right)$. From the bound-state wavefunction of Eq. (6.34), neglecting terms exponentially suppressed by the distance, we obtain:

$$\langle \varphi_{-(j_1+1,j_2)} | \varphi_{+(j_1,j_2)} \rangle \approx \frac{1}{2\mathcal{N}_B\overline{N}_M} \sum_{\mathbf{k}} \frac{1 - e^{ik_z}}{(E_{I,B} - \omega_{\mathbf{k}})^2} \approx \frac{1 - \mathcal{F}_1}{2}.$$

Within this regime, we can replace in the denominator $E_+(j_1, j_2) - E_-(j_1 + 1, j_2) \approx 2V_I(|j_{12}|)$, which leads to the result stated in Eq. (7.19).

C.2.3 Scheme II: Repulsion mediated by atoms subject to state-dependent potentials

As detailed in the main text, in this scheme to gain tunability we included a second level in the mediating species. To analyze its effect, we can separate the total

Hamiltonian into the unperturbed (\hat{H}_0) and perturbed (\hat{H}_1) terms,

$$\begin{aligned}\hat{H}_0 &= \Delta \sum_j \hat{b}_j^\dagger \hat{b}_j + U \sum_{j_i \in \{j\}} \hat{b}_{j_i}^\dagger \hat{b}_{j_i} - t_a \sum_{\langle i,j \rangle} \hat{a}_i^\dagger \hat{a}_j - t_b \sum_{\langle i,j \rangle} \hat{b}_i^\dagger \hat{b}_j, \\ \hat{H}_1 &= g \sum_j (\hat{b}_j^\dagger \hat{a}_j + \text{H.c.}).\end{aligned}\tag{C.15}$$

To lowest order, and assuming that t_b is negligible, the ground state of \hat{H}_0 corresponds to $|\varphi_{\text{II},+}^{(0)}\rangle = (\hat{b}_{j_1}^\dagger + \hat{b}_{j_2}^\dagger)/\sqrt{2}|0\rangle$, with energy $E_{\text{II},+}^{(0)} = U + \Delta$. The effective repulsion enters then as a second-order contribution in perturbation theory,

$$\begin{aligned}E_{\text{II},+}^{(2)} &= \frac{|\langle \text{vac} | \hat{a}_{\mathbf{k}} \hat{H}_1 | \varphi_{\text{II},+}^{(0)} \rangle|^2}{E_{\text{II},+}^{(0)} - \omega_{\text{II},\mathbf{k}}} = \frac{g^2}{2\bar{N}_M} \sum_{\mathbf{k}} \frac{|e^{i\mathbf{k}\cdot j_1} + e^{i\mathbf{k}\cdot j_2}|^2}{E_{\text{II},+}^{(0)} - \omega_{\text{II},\mathbf{k}}} \\ &= \frac{g^2}{\bar{N}_M} \sum_{\mathbf{k}} \frac{1}{E_{\text{II},+}^{(0)} - \omega_{\text{II},\mathbf{k}}} + \frac{g^2}{\bar{N}_M} \sum_{\mathbf{k}} \frac{e^{i\mathbf{k}(j_1-j_2)}}{E_{\text{II},+}^{(0)} - \omega_{\text{II},\mathbf{k}}},\end{aligned}\tag{C.16}$$

which is the expression written in Eq. (7.21).

To higher order, $|\varphi_{\text{II},+}\rangle$ will also have contribution in level a of the form, $|\varphi_{\text{II},+}\rangle = |\varphi_{\text{II},+}^{(0)}\rangle + \alpha_{\mathbf{k}} \hat{a}_{\mathbf{k}} |0\rangle$. To make this perturbative expansion valid, Eq. (7.24) bounds the first-order contributions as follows:

$$\begin{aligned}\varepsilon_{\text{aux}} &= \sum_{\mathbf{k}} |\alpha_{\mathbf{k}}^{(0)}|^2 = \sum_{\mathbf{k}} \left| \frac{\langle \text{vac} | \hat{a}_{\mathbf{k}} \hat{H}_1 | \varphi_{\text{II},+}^{(0)} \rangle}{E_{\text{II},+}^{(0)} - \omega_{\text{II},\mathbf{k}}} \right|^2 \approx \frac{g^2}{2\bar{N}_M} \sum_{\mathbf{k}} \left| \frac{e^{i\mathbf{k}\cdot j_1} + e^{i\mathbf{k}\cdot j_2}}{E_{\text{II},+}^{(0)} - \omega_{\text{II},\mathbf{k}}} \right|^2 \\ &\leq \frac{2g^2}{\bar{N}_M} \sum_{\mathbf{k}} \frac{1}{(E_{\text{II},+}^{(0)} - \omega_{\text{II},\mathbf{k}})^2} = \frac{V_{\text{II}} L_{\text{II}}}{t_a a}.\end{aligned}\tag{C.17}$$

While non-dominant, this population is relevant as it is responsible for the induced repulsion. To make the effective length independent on the particular fermionic configuration, in the derivation of Eq. (7.25), we have bounded the next-order contribution to this population. Exploring the next non-negligible order,

we obtain,

$$\begin{aligned}
\sum_{\mathbf{k}} \left| \alpha_{\mathbf{k}}^{(0)} + \alpha_{\mathbf{k}}^{(3)} \right|^2 &= \sum_{\mathbf{k}} \left| \frac{\langle \text{vac} | \hat{a}_{\mathbf{k}} \hat{H}_1 | \varphi_{\Pi,+}^{(0)} \rangle}{E_{\Pi,+}^{(0)} - \omega_{\Pi,\mathbf{k}}} + \sum_{\mathbf{q}} \frac{\left| \langle \text{vac} | \hat{a}_{\mathbf{q}} \hat{H}_1 | \varphi_{\Pi,+}^{(0)} \rangle \right|^2 \langle \text{vac} | \hat{a}_{\mathbf{k}} \hat{H}_1 | \varphi_{\Pi,+}^{(0)} \rangle}{\left(E_{\Pi,+}^{(0)} - \omega_{\Pi,\mathbf{k}} \right) \left(E_{\Pi,+}^{(0)} - \omega_{\Pi,\mathbf{q}} \right)} \right. \\
&\quad \left. \times \left(\frac{1}{E_{\Pi,+}^{(0)} - \omega_{\Pi,\mathbf{k}}} + \frac{1}{2 \left(E_{\Pi,+}^{(0)} - \omega_{\Pi,\mathbf{q}} \right)} \right) \right|^2 \\
&\approx \varepsilon_{aux} + \sum_{\mathbf{k}} \frac{\left| \langle \text{vac} | \hat{a}_{\mathbf{k}} \hat{H}_1 | \varphi_{\Pi,+}^{(0)} \rangle \right|^2}{\left(E_{\Pi,+}^{(0)} - \omega_{\Pi,\mathbf{k}} \right)^3} \sum_{\mathbf{q}} \frac{\left| \langle \text{vac} | \hat{a}_{\mathbf{q}} \hat{H}_1 | \varphi_{\Pi,+}^{(0)} \rangle \right|^2}{\left(E_{\Pi,+}^{(0)} - \omega_{\Pi,\mathbf{q}} \right)} + \dots \\
&\approx \frac{V_{\Pi} L_{\Pi}}{t_{a\mathbf{a}}} + \frac{V_{\Pi} L_{\Pi}}{t_{a\mathbf{a}}} \left(\frac{g L_{\Pi}}{4 t_{a\mathbf{a}}} \right)^2 + \dots,
\end{aligned} \tag{C.18}$$

where, in the right hand side, we have applied Eqs. (C.9) and (C.10) and omitted higher order terms in $\left(\frac{g L_{\Pi}}{4 t_{a\mathbf{a}}} \right)^2$. In Fig. 7.9 we observed that imposing now that the second term in Eq. (C.18) is smaller than the first one, e.g., using a ratio $\left(\frac{g L_{\Pi}}{4 t_{a\mathbf{a}}} \right)^2 = 0.01$ (dotted line), allows for a constant definition of L_{Π} for any fermionic configuration.

C.2.4 Scheme III: Repulsion mediated by atomic spin excitations and cavity assisted transitions

In this final scheme, we include a cavity interaction to ensure a pairwise effective repulsion when more than two fermions are included in the system. There are several errors one should account for:

- The cavity also couples the unperturbed state $|\phi_+^{(0)}\rangle = \frac{1}{\sqrt{N_e}} \sum_{\{j\}} \hat{B}_j^\dagger |\text{Mott}\rangle$, to the other symmetric state in positions not occupied by the fermions, $\frac{1}{\sqrt{N_M - N_e}} \sum_{\mathbf{r} \notin \{j\}} \hat{B}_{\mathbf{r}}^\dagger |\text{Mott}\rangle$. The coupling between them has intensity $J_c \sqrt{N_e (\overline{N}_M - N_e) / \overline{N}_M}$, and the energy difference is $U - (1 - 2N_e / \overline{N}_M) J_c$. Therefore, the error of Eq. (7.35) one needs to bound is,

$$\varepsilon_{\text{cav}} = \left| \frac{J_c \sqrt{N_e (\overline{N}_M - N_e) / \overline{N}_M}}{U - (1 - 2N_e / \overline{N}_M) J_c} \right|^2 \approx \left| \frac{J_c \sqrt{N_e / \overline{N}_M}}{U - J_c} \right|^2 \tag{C.19}$$

for $N_e \ll \overline{N}_M$.

- Even if the cavity does not couple this state with other antisymmetric ones, this can still occur as a consequence of coupling \hat{H}_A . For $J_c \ll U$, the relevant energy gap corresponds to U , which separates the excitation of state B in atoms placed at fermionic position, against unoccupied positions. Therefore, now we focus on the $N_e - 1$ orthogonal states, that are also orthogonal to $|\phi_+^{(0)}\rangle$, and can be written as $|\phi_{\perp,m}^{(0)}\rangle = \sum_{\mathbf{r} \in \{j\}} \lambda_{m,\mathbf{r}} \hat{B}_{\mathbf{r}}^\dagger |\text{Mott}\rangle$, with energy $U + \Delta$, and satisfying

$\sum_{\mathbf{r} \in \{\mathbf{j}\}} \lambda_{m,\mathbf{r}} = 0$ and $\sum_{\mathbf{r} \in \{\mathbf{j}\}} |\lambda_{m,\mathbf{r}}|^2 = 1$ for every $m = 1 \dots N_e - 1$. The error due to the coupling to these states reads as,

$$\begin{aligned} \varepsilon_{A,ii} &= \sum_m \bar{\varepsilon}_A \left(\left| \phi_{\perp,m}^{(0)} \right\rangle \right) = \sum_m \left| \sum_{\mathbf{k}} \frac{\langle \phi_{\perp,m}^{(0)} | \hat{H}_A \hat{A}_{\mathbf{k}}^\dagger | \text{Mott} \rangle \langle \text{Mott} | \hat{A}_{\mathbf{k}} \hat{H}_A | \phi_+^{(0)} \rangle}{\left(E_{\text{III},B}^{(1)} - \omega_{\text{III},\mathbf{k}} \right) \left(E_{\text{III},B}^{(1)} - U - \Delta \right)} \right|^2 \\ &= \left(\frac{g^2}{\rho_M J_c} \right)^2 \frac{1}{N_e} \sum_m \left| \frac{1}{\bar{N}_M} \sum_{\mathbf{k}} \frac{f_{\mathbf{k}}(m)}{E_{\text{III},B}^{(1)} - \omega_{\text{III},\mathbf{k}}} \right|^2. \end{aligned} \quad (\text{C.20})$$

where $f_{\mathbf{k}}(m) = \sum_{\mathbf{s}, \mathbf{r} \in \{\mathbf{s}\}; \mathbf{r} \neq \mathbf{s}} \lambda_{m,\mathbf{s}} e^{i\mathbf{k}(\mathbf{j}-\mathbf{r})}$ accounts for the relative distances weighted by the components of the states involved. To upper-bound this sum, it translates after integration into,

$$\sum_m \left| \frac{1}{\bar{N}_M} \sum_{\mathbf{k}} \frac{f_{\mathbf{k}}(m)}{E_s - \omega_{\mathbf{k}}} \right|^2 \approx \sum_m \left| \sum_{\mathbf{s} \in \{\mathbf{j}\}} \sum_{\mathbf{r} \in \{\mathbf{j}\}; \mathbf{r} \neq \mathbf{s}} \lambda_{m,\mathbf{s}} x_{\mathbf{s}\mathbf{r}} \right|^2,$$

where $x_{\mathbf{s}\mathbf{r}} = \frac{1}{4\pi J_A} \frac{a}{|\mathbf{s}-\mathbf{r}|} \in \frac{1}{4\pi J_A} (0, 1]$. To give a base-independent argument, one can simply reformulate the sum to express it in terms of the symmetric state which, in the basis $\left\{ \hat{B}_{j_1}^\dagger | \text{Mott} \rangle, \dots, \hat{B}_{j_{N_e}}^\dagger | \text{Mott} \rangle \right\}$, writes as $|\lambda_s\rangle = (1 \dots 1) / \sqrt{N_e}$. Then,

$$\begin{aligned} N_e \Delta^2 [y] &= \sum_m \left| \sum_{\mathbf{s} \in \{\mathbf{j}\}} \sum_{\mathbf{r} \in \{\mathbf{j}\}; \mathbf{r} \neq \mathbf{s}} \lambda_{m,\mathbf{s}} x_{\mathbf{s}\mathbf{r}} \right|^2 \\ &= \sum_m \left(|\langle 1 | X | \lambda_m \rangle|^2 = |X | 1 \rangle|^2 - |\langle 1 | X | \lambda_s \rangle|^2 \right) \\ &= \sum_{\mathbf{s} \in \{\mathbf{j}\}} \left(\sum_{\mathbf{r} \in \{\mathbf{j}\}; \mathbf{r} \neq \mathbf{s}} x_{\mathbf{s}\mathbf{r}} \right)^2 - \frac{1}{N_e} \left(\sum_{\mathbf{s} \in \{\mathbf{j}\}} \sum_{\mathbf{r} \in \{\mathbf{j}\}; \mathbf{r} \neq \mathbf{s}} x_{\mathbf{s}\mathbf{r}} \right)^2, \end{aligned} \quad (\text{C.21})$$

where $(X)_{\mathbf{s}\mathbf{r}} = x_{\mathbf{s}\mathbf{r}}$, and $\lambda_m = \left(\lambda_{m,j_1} \dots \lambda_{m,j_{N_e}} \right)$. The right hand side of the previous equation corresponds to N_e times the variance of an homogeneous distribution of variables $y_{\mathbf{s}} = \sum_{\mathbf{r} \in \{\mathbf{j}\}; \mathbf{r} \neq \mathbf{s}} x_{\mathbf{s}\mathbf{r}}$, with $\mathbf{s} \in \{\mathbf{j}\}$. It is therefore null when all fermions are equidistant, and the upper-bound is reached in the worst-case scenario of two fermions at distance 1 and the rest at infinite separation from each other. In this most-unfavourable situation, the latter expression reads as, $(2 - 4/N_e) (4\pi J_A)^{-2} \approx \left[2(2\pi J_A)^2 \right]^{-1}$. This contribution is therefore null for the two-fermion case. For many fermions it reduces the condition to $\varepsilon_{A,ii} = \left(\frac{V_{\text{III}}}{\rho_M J_c} \right)^2 G(\{\mathbf{j}\}) \ll 1$ with,

$$G(\{\mathbf{j}\}) = (2\pi J_A N_e)^2 \Delta^2 [y] \ll N_e/2, \quad (\text{C.22})$$

as used in Eq. (7.39). The population of antisymmetric states in positions not occupied by the fermions is already bounded with these conditions.

- One should also note that the fermionic hopping can also couple to symmetric to the antisymmetric states. This leads to an additional error that can be bounded by:

$$\begin{aligned}
\varepsilon_f &= \sum_m \bar{\varepsilon}_f \left(\left| \phi_{\perp,m}^{(0)} \right\rangle \right) \approx \sum_m \left| t_f \frac{\langle \phi_{\perp,m,\{j+1\}}^{(0)} | \phi_{+,\{j\}}^{(0)} \rangle}{\rho_M J_c} \right|^2 \\
&= \left(\frac{t_f}{\rho_M J_c} \right)^2 \left(1 - \left| \langle \phi_{+,\{j+1\}}^{(0)} | \phi_{+,\{j\}}^{(0)} \rangle \right|^2 \right) \\
&= \left(\frac{t_f}{\rho_M J_c} \right)^2 \left(1 - \frac{N_e - 1 + \mathcal{F}_{\text{III}}}{N_e} \right) \approx \left(\frac{t_f}{\rho_M J_c} \right)^2 \frac{a}{L_{\text{III}} N_e} \ll 1
\end{aligned} \tag{C.23}$$

which corresponds to inequality (7.40). Note that we have assumed that the nearest neighbor in $\{j+1\}$ is not occupied by a fermion, which is valid in the limit $\rho_M \ll 1$. In the last approximation, we have focused on the regime $L_{\text{III}}/a \gg 1$ where the Coulomb interaction dominates the Yukawa potential. This allows for a more relaxed condition than the one obtained when the effect of the Franck-Condon coefficient is neglected, as considered in [1].

C.3 Numerical methods for multi-electronic systems.

In this section, we first give more details on how we choose the simulator parameters to plot the figures of the manuscript, and explain the numerical methods employed for the two-electron wavefunction calculation.

C.3.1 A Hartree-Fock approximation

As compared to the single electron problem, ED involving two-fermions in a $N \times N \times N$ lattice is out of reach for our computational resources. To numerically capture both the geometry of the atom[molecule] and the interactions with other electrons in our analog simulator, we project the discretized fermionic Hamiltonian \hat{H}_e in Eqs. (6.8a-6.8c), on a set of atomic[molecular] orbitals $\{\phi_i\}_{i=1}^n$ composed of two types of orbitals:

- Single-electron orbitals, corresponding to the n first lowest energy eigenstates of a single electron attracted to the same nuclear configuration. That means only the terms in Eqs. (6.8a) and (6.8b) in \hat{H}_e .
- Electronic orbitals that interact with an average-charge caused by the rest of electrons. For the case of two-electrons that we benchmark in this work, these HF-like orbitals are iteratively calculated by adding to the nuclear and kinetic terms in Eqs. (6.8a) and (6.8b) the repulsion due to the lowest-energy state obtained in the previous iteration given by Eq. (6.8c).

Combining both sets of orbitals, the total basis is orthogonalized using Gram-Schmidt algorithm. The projected fermionic Hamiltonian then reads as,

$$\hat{H}_P = \sum_{i,j,r,s=1}^n h_{ijrs} |\phi_i \phi_j\rangle \langle \phi_r \phi_s|, \tag{C.24}$$

where $|\phi_i \phi_j\rangle$ denotes the product state $|\phi_i\rangle \otimes |\phi_j\rangle$ and $h_{ijrs} = \langle \phi_i \phi_j | \hat{H}_{\text{eff}} | \phi_r \phi_s \rangle$, similarly to the LCAO approach introduced in Section 6.2.1.

The success of this strategy now depends on how accurately the orbitals in this set can describe the interactions in the Hamiltonian. We then choose a basis composed by single-fermion states of H_2^+ calculated with ED, together with more orbitals obtained using a HF approximation [342]. This is, starting with the ground state obtained for a single fermion, we iterate the equation,

$$(\hat{H}_1 |\phi\rangle)^{\mathbf{i}} + \sum_{\mathbf{j}} (\phi^{\mathbf{j}})^2 V_{12}(|\mathbf{j} - \mathbf{i}|) \phi^{\mathbf{i}} = \lambda \phi^{\mathbf{i}}, \quad (\text{C.25})$$

until convergence is reached. In this way, orbitals interact with a mean charge induced by the rest of fermionic atoms in the lattice, while we neglect the exchange interaction.

Once we have built an approximated basis, we need to project the Hamiltonian \hat{H}_{qc} into the basis. The terms associated to the kinetic energy and nuclear interactions are easily projected, as they only depend on single fermionic orbitals, $\langle \phi_i \phi_j | \hat{H}_1 | \phi_r \phi_s \rangle = \delta_{js} \langle \phi_i | \hat{H}_1 | \phi_r \rangle + \delta_{ir} \langle \phi_j | \hat{H}_1 | \phi_s \rangle$. The lattice imposes a natural cutoff (7.33), corresponding to $V(0) \approx \pi V_0$, and the main difficulty comes from calculating terms associated to e-e interactions, $\hat{H}_{\text{e-e}}$. At a first glimpse, they involve a sum of N^6 coordinates,

$$\sum_{\mathbf{r}_1, \mathbf{r}_2} V(\mathbf{r}_1 - \mathbf{r}_2) \phi_i(\mathbf{r}_1) \phi_r(\mathbf{r}_1) \phi_j(\mathbf{r}_2) \phi_s(\mathbf{r}_2), \quad (\text{C.26})$$

where, $V(\mathbf{r}) = V_0/|\mathbf{r}|$. In the reciprocal space, however, this sum simplifies as

$$\langle \phi_i \phi_j | \hat{H}_{\text{e-e}} | \phi_r \phi_s \rangle = \sum_{\mathbf{k}} \tilde{V}(\mathbf{k}) \cdot \widetilde{(\phi_i \cdot \phi_r)}(\mathbf{k}) \cdot \widetilde{(\phi_j \cdot \phi_s)}(-\mathbf{k}), \quad (\text{C.27})$$

and only N^3 terms are involved, speeding-up the calculation. Here \tilde{f} denotes the Fourier transform of function f . In principle, this induces periodic boundary conditions in the system, which are undesirable as fermions would interact along the minimum distance measured on the periodic lattice, overestimating e-e interactions. To solve this issue, we double the size of the system before calculating the Fourier transform, and impose null probability of occupying these artificial positions. Fourier transforms are obtained using a Discrete Fast Fourier Algorithm.

This last calculation is the bottleneck from the computational time perspective and, at the expense of memory, we initially store the FFT for each of the $n(n+1)/2$ product of pairs of molecular orbitals, so that the transformation is not unnecessarily repeated. It is also useful to note that not every term h_{ijrs} needs to be calculated, due to the symmetries of the Hamiltonian. For example, $h_{1123} = h_{1132} = h_{2311} = h_{3211}$. In practice, this reduces the calculated terms from n^4 to $n^2(n^2+3)/4$ independent terms, where n is the number of molecular orbitals in the projected basis. For Figure 7.13(b), we observed that convergence in energies to the order of the discretization effects was reached for 15 HF orbitals and 15 low-energy H_2^+ states. This corresponds to $n = 30$, 203175 independent terms, and approximately 8h of total computational time in a 2.20 GHz CPU.

The mean charge interaction in the HF calculation can also be rewritten as,

$$\sum_{\mathbf{j}} \left(\phi^{\mathbf{j}} \right)^2 V_{12}(|\mathbf{i} - \mathbf{j}|) \cdot \phi^{\mathbf{i}} = \langle \phi | \mathcal{F}^{-1} \left(\tilde{V}(\mathbf{k}) \cdot \tilde{\phi}^2(-\mathbf{k}) \right) \rangle, \quad (\text{C.28})$$

where \mathcal{F}^{-1} denotes the inverse Fourier transform. We should emphasize that this projection on a single-particle basis is just a numerical strategy that enables us to numerically benchmark the model, but does not have any impact on the experimental implementation of the proposed analog simulator.

In the following, we illustrate the application of this approach to the species benchmarked in the main text: atomic Helium, and molecular H_2 and HeH^+ .

C.3.2 Numerical benchmarking of atomic Helium

In the case of Helium, one can explore the ortho-, and parahelium ground-states by restricting the projected Hamiltonian (6.25) to the corresponding symmetry sectors. As para(ortho)helium is characterized by a(n) (anti)symmetric spin configuration, their spatial configuration needs to be antisymmetric(symmetric) due to their fermionic character. While this will be naturally ensured by the fermionic nature of our atomic simulator, the computation cost of the numerical calculation gets simplified by imposing these symmetries. In particular, one can define the reduced Hamiltonian

$$\hat{H}_e|_{\text{para(ortho)}} = \sum_{i,r}^n \sum_{j \geq i, s \geq r}^n h_{ijrs}^{\text{para(ortho)}} ||\phi_i \phi_j\rangle\rangle^{\text{para(ortho)}} \langle\langle \phi_r \phi_s ||^{\text{para(ortho)}}, \quad (\text{C.29})$$

where $||\phi_i \phi_j\rangle\rangle^{\text{para(ortho)}} = [|\phi_i \phi_j\rangle + (-) |\phi_j \phi_i\rangle] / \sqrt{2}$, and $h_{ijrs}^{\text{para(ortho)}} = h_{ijrs} + (-)h_{jirs}$, where we have used the identity, $h_{ijrs} = h_{jisr}$.

We should emphasize that this projection on a single-particle basis is just a numerical strategy that enables us to numerically benchmark the model, but does not have any impact on the experimental implementation of the proposed analog simulator.

In Fig. C.1(a), we analyze the convergence of result by calculating plot the lowest energy of He atoms as a function of the type and number of orbitals included in the basis. As expected, orbitals obtained using the HF approach (coloured round markers) diminish more easily the ground-state energy than single electron orbitals (crossed markers). A combination of both basis (contoured round markers) show the greatest reduction. For the convergence of the results shown along the text, we have chosen 30 orbitals: 15 coming from the single electron calculation, and 15 obtained with the described HF method, which show energy variations smaller than the energy error provided.

C.3.3 Numerical benchmarking of H_2

To plot the molecular potential of Fig. 7.13(b), that is, to calculate the electronic energy, $E(d)$ as a function of the internuclear distance d , we center the nuclear potential in positions $\mathbf{r}_1 = (m - \lceil d/(2a) \rceil, m + 1/2, m)$ and $\mathbf{r}_2 = (m + \lfloor d/(2a) \rfloor, m + 1/2, m)$ and obtain the ground state energy using the

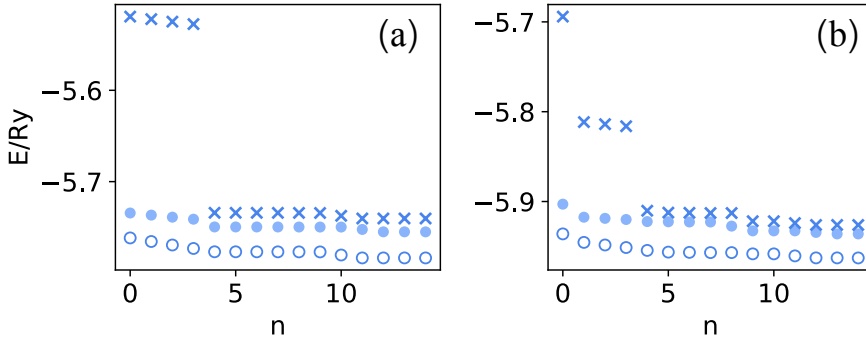


FIGURE C.1: (a) Numerical benchmarking for the ground-state energy of He for an increasing number of orbitals in the projective basis for the example of tunneling rate, $t_f/V_0 = 6$ and $N = 75$. In particular, we compare the lowest energy of the projected Hamiltonian for basis composed of the n lowest-energy single-electron orbitals of He⁺ (crossed markers), HF orbitals constructed as described in this section (coloured round markers), or a combination of the n -th first of them (contoured round markers). (b) We repeat this analysis for the lowest-energy of HeH⁺, for an internuclear distance $d/a_0 = 1.5$ simulated with a separation of $d/a = 15$ sites, and $N = 75$.

numerical methods explained in the next Section. Since two electrons are involved, the extracted energy is now shifted by $12t_f$, and finally written in atomic units. Notice also that, since we use spinless fermions, we have to restrict to the symmetric subspace of the electronic problem so that we can compare the results to those of the H_2 molecule, which is formed for two spins of opposite sign.

As it happens in the atomic case, accuracy increases as the Bohr radius grows up to a critical value at which finite-size effects are relevant. However, the optimal choice of the Bohr radius now depends on the number of lattice sites that separate the nuclei. To identify this critical Bohr radius at which the finiteness of the lattice $N = 75$ compromises the accuracy, we use the following procedure. First, for a given internuclear separation d/a_0 we solve the electronic structure for nuclear potentials separated a number of lattice sites d/a ranging between 1 and 30, increasing the Bohr radius accordingly, $t_f/V_0 = (d/a)/(2d/a_0)$. The same calculation is repeated for a bigger system size, $N = 100$. Both lattices provide compatible results as long as finite-size effects are not important. The point where both curves deviate corresponds to an approximate optimal t_f/V_0 , that provides maximum accuracy for the lattice size considered, e.g., $N = 75$ in our case. In practice, we choose the point at which finite-size energy deviations are one order of magnitude smaller than the discretization error (see Fig. C.2). Fitting these values for each internuclear separation d/a , we choose $t_f/V_0 = 4.2 - d/a \cdot 0.065$, i.e., as the nuclei are more separated, the border of the system linearly approaches, needing to reduce the Bohr radius accordingly.

C.3.4 Numerical benchmarking of molecular HHe⁺

In this case, the chosen Bohr-radius a_0/a modifies the effective internuclear separation d/a_0 . To explore the effect of discretization, for a given physical distance d/a_0 , we then modify the nuclear separation d/a taking integer values, and adjust the effective Bohr-radius a_0/a accordingly. In Fig. 7.14, this process is repeated for

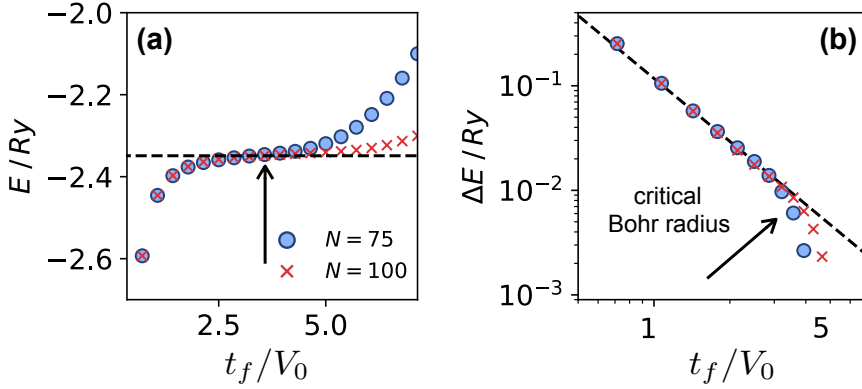


FIGURE C.2: (a) For each internuclear separation d/a_0 , we benchmark separations on the lattice d/a ranging from 1 to 30 sites, tuning the Bohr radius, a_0/a , accordingly. In the figure, $d = 1.4a_0$, close to the equilibrium distance. Similarly to what happened in the atomic case (see Fig. 7.2(a)), the calculated potential polynomially approaches the exact solution (dashed line) as the effective Bohr radius increases, up to the point in which finite size effects appear. To calculate this optimal t_f/V_0 , we repeat the calculation for a bigger system, and detect the point where both curves depart. (b) To identify this point, we fit the energy of the largest lattice to a universal scaling $m(t_f/V_0)^{-2} + n$, (dashed line). For $N = 75$ and a nuclear separation of $1.4a_0$, the critical point (indicated by the arrow) corresponds to $t_f/V_0 \approx 3.5$, providing an expected precision of 10^{-2} Ry in the energy of the minimum potential at this given distance.

lattice sizes $N = 75$ and $N = 100$, and the extrapolation method is then used to extract the best estimation of the ground-state energy in the continuum from our Hamiltonian in the lattice for each value of d/a_0 .

As it occurred in the case of He, a single-electron base obtained from a HF approach is used to solve the discretized molecular Hamiltonian in a projected basis. In Fig. C.1(b) we benchmark its convergence with the number of orbitals, observing energy variations smaller than the energy error for the choice of 15 orbitals using the single electron calculation, and 15 obtained with the described HF method.

Bibliography

- [1] J. Argüello-Luengo, A. González-Tudela, T. Shi, P. Zoller, and J. I. Cirac, “Analogue quantum chemistry simulation”, *Nature* **574**, 215 (2019) (Cited on p. 57, 148).
- [2] J. Argüello-Luengo, A. González-Tudela, T. Shi, P. Zoller, and J. I. Cirac, “Quantum simulation of two-dimensional quantum chemistry in optical lattices”, *Phys. Rev. Research* **2**, 042013 (2020) (Cited on p. 57).
- [3] J. Argüello-Luengo, T. Shi, and A. González-Tudela, “Engineering analog quantum chemistry Hamiltonians using cold atoms in optical lattices”, *Phys. Rev. A* **103**, 043318 (2021) (Cited on p. 57).
- [4] J. Argüello-Luengo, A. González-Tudela, and D. González-Cuadra, “Tuning Long-Range Fermion-Mediated Interactions in Cold-Atom Quantum Simulators”, *Phys. Rev. Lett.* **129**, 083401 (2022) (Cited on p. 11, 70).
- [5] J. Argüello-Luengo and D. E. Chang, “Optomechanical strong coupling between a single photon and a single atom”, *New J. Phys.* **24**, 023006 (2022).
- [6] J. Argüello-Luengo and A. González-Tudela, “Simuladores cuánticos analógicos: Una herramienta para entender la materia que nos rodea”, *Revista Española de Física* **35**, 5 (2021).
- [7] I. Bloch, J. Dalibard, and S. Nascimbène, “Quantum simulations with ultracold quantum gases”, *Nat. Phys.* **8**, 267 (2012) (Cited on p. 5).
- [8] J. I. Cirac and P. Zoller, “Goals and opportunities in quantum simulation”, *Nat. Phys.* **8**, 264 (2012) (Cited on p. 5).
- [9] I. M. Georgescu, S. Ashhab, and F. Nori, “Quantum simulation”, *Rev. Mod. Phys.* **86**, 153 (2014) (Cited on p. 5).
- [10] C. N. Cohen-Tannoudji, “Nobel Lecture: Manipulating atoms with photons”, *Rev. Mod. Phys.* **70**, 707 (1998) (Cited on p. 5).
- [11] H. J. Kimble, M. Dagenais, and L. Mandel, “Photon Antibunching in Resonance Fluorescence”, *Phys. Rev. Lett.* **39**, 691 (1977) (Cited on p. 5).
- [12] D. Meschede, H. Walther, and G. Müller, “One-Atom Maser”, *Phys. Rev. Lett.* **54**, 551 (1985) (Cited on p. 5).
- [13] R. J. Thompson, G. Rempe, and H. J. Kimble, “Observation of normal-mode splitting for an atom in an optical cavity”, *Phys. Rev. Lett.* **68**, 1132 (1992) (Cited on p. 5).
- [14] M. Brune, F. Schmidt-Kaler, A. Maali, J. Dreyer, E. Hagley, J. M. Raimond, and S. Haroche, “Quantum Rabi Oscillation: A Direct Test of Field Quantization in a Cavity”, *Phys. Rev. Lett.* **76**, 1800 (1996) (Cited on p. 5).
- [15] G. Rempe, H. Walther, and N. Klein, “Observation of quantum collapse and revival in a one-atom maser”, *Phys. Rev. Lett.* **58**, 353 (1987) (Cited on p. 5).

- [16] A. Ashkin, "Applications of Laser Radiation Pressure", *Science* **210**, 1081 (1980) (Cited on p. 5).
- [17] V. S. Letokhov and V. G. Minogin, "Laser radiation pressure on free atoms", *Phys. Rep.* **73**, 1 (1981) (Cited on p. 5).
- [18] S. Chu, L. Hollberg, J. E. Bjorkholm, A. Cable, and A. Ashkin, "Three-dimensional viscous confinement and cooling of atoms by resonance radiation pressure", *Phys. Rev. Lett.* **55**, 48 (1985) (Cited on p. 5).
- [19] S. Chu, J. E. Bjorkholm, A. Ashkin, and A. Cable, "Experimental Observation of Optically Trapped Atoms", *Phys. Rev. Lett.* **57**, 314 (1986) (Cited on p. 5).
- [20] C. S. Adams and E. Riis, "Laser cooling and trapping of neutral atoms", *Progress in Quantum Electron.* **21**, 1 (1997) (Cited on p. 5).
- [21] M. A. Kasevich, E. Riis, S. Chu, and R. G. Devoe, "RF spectroscopy in an atomic fountain", *Phys. Rev. Lett.* **63**, 612 (1989) (Cited on p. 5).
- [22] S. R. Jefferts, T. P. Heavner, T. E. Parker, and J. H. Shirley, "NIST cesium fountains: current status and future prospects", *Proceedings Time and Frequency Metrology* **6673**, 63 (2007) (Cited on p. 5).
- [23] K. B. Davis, M. .-. Mewes, M. R. Andrews, N. J. v. Druten, D. S. Durfee, D. M. Kurn, and W. Ketterle, "Bose-Einstein Condensation in a Gas of Sodium Atoms", *Phys. Rev. Lett.* **75**, 3969 (1995) (Cited on p. 5).
- [24] M. H. Anderson, J. R. Ensher, M. R. Matthews, C. E. Wieman, and E. A. Cornell, "Observation of Bose-Einstein condensation in a dilute atomic vapor", *Science* **269**, 198 (1995) (Cited on p. 5).
- [25] P. Avouris, "Manipulation of Matter at the Atomic and Molecular Levels", *Acc. Chem. Res.* **28**, 95 (1995) (Cited on p. 6).
- [26] H. Ott, "Single atom detection in ultracold quantum gases: a review of current progress", *Rep. Prog. Phys.* **79**, 054401 (2016) (Cited on p. 6).
- [27] W. Neuhauser, M. Hohenstatt, P. E. Toschek, and H. Dehmelt, "Localized visible Ba⁺ mono-ion oscillator", *Phys. Rev. A* **22**, 1137 (1980) (Cited on p. 6, 59).
- [28] D. J. Wineland and W. M. Itano, "Spectroscopy of a single Mg⁺ ion", *Phys. Lett. A* **82**, 75 (1981) (Cited on p. 6, 59).
- [29] W. D. Phillips, "Nobel Lecture: Laser cooling and trapping of neutral atoms", *Rev. Mod. Phys.* **70**, 721 (1998) (Cited on p. 6).
- [30] S. J. Van Enk and H. J. Kimble, "Strongly focused light beams interacting with single atoms in free space", *Phys. Rev. A* **63**, 023809 (2001) (Cited on p. 6, 19).
- [31] J. B. Beguin, J. Laurat, X. Luan, A. P. Burgers, Z. Qin, and H. J. Kimble, "Reduced volume and reflection for bright optical tweezers with radial Laguerre-Gauss beams", *Proc. Natl. Acad. Sci. U.S.A.* **117**, 26109 (2020) (Cited on p. 6, 19, 95, 96).
- [32] P. Maunz, T. Puppe, I. Schuster, N. Syassen, P. W. Pinkse, and G. Rempe, "Cavity cooling of a single atom", *Nature* **428**, 50 (2004) (Cited on p. 6).
- [33] K. Karrai, "Photonics: A cooling light breeze", *Nature* **444**, 41 (2006) (Cited on p. 6).
- [34] M. Aspelmeyer, T. J. Kippenberg, and F. Marquardt, "Cavity optomechanics", *Rev. Mod. Phys.* **86**, 1391 (2014) (Cited on p. 6, 27).
- [35] P. S. Jessen and I. H. Deutsch, "Optical Lattices", *Advances in Atomic, Molecular and Optical Physics* **37**, 95 (1996) (Cited on p. 6).
- [36] R. Grimm, M. Weidemüller, and Y. B. Ovchinnikov, "Optical Dipole Traps for Neutral Atoms", *Advances in Atomic, Molecular and Optical Physics* **42**, 95 (2000) (Cited on p. 6, 17).

- [37] D. Barredo, V. Lienhard, S. de Léséleuc, T. Lahaye, and A. Browaeys, “Synthetic three-dimensional atomic structures assembled atom by atom”, *Nature* **561**, 79 (2018) (Cited on p. 6, 19, 95).
- [38] T. Esslinger, “Fermi-Hubbard Physics with Atoms in an Optical Lattice”, *Annual Review of Condens. Matter Phys.* **1**, 129 (2010) (Cited on p. 6, 52, 79).
- [39] D. Jaksch, C. Bruder, J. I. Cirac, C. W. Gardiner, and P. Zoller, “Cold Bosonic Atoms in Optical Lattices”, *Phys. Rev. Lett.* **81**, 3108 (1998) (Cited on p. 6, 52, 55, 79).
- [40] M. Greiner, O. Mandel, T. Esslinger, T. W. Hänsch, and I. Bloch, “Quantum phase transition from a superfluid to a Mott insulator in a gas of ultracold atoms”, *Nature* **415**, 39 (2002) (Cited on p. 7, 54, 55).
- [41] R. Jördens, N. Strohmaier, K. Günter, H. Moritz, and T. Esslinger, “A Mott insulator of fermionic atoms in an optical lattice”, *Nature* **455**, 204 (2008) (Cited on p. 7).
- [42] H. Bernien, S. Schwartz, A. Keesling, H. Levine, A. Omran, H. Pichler, S. Choi, A. S. Zibrov, M. Endres, M. Greiner, V. Vuletić, and M. D. Lukin, “Probing many-body dynamics on a 51-atom quantum simulator”, *Nature* **551**, 579 (2017) (Cited on p. 7).
- [43] J.-y. Choi, S. Hild, J. Zeiher, P. Schauß, A. Rubio-Abadal, T. Yefsah, V. Khemani, D. A. Huse, I. Bloch, and C. Gross, “Exploring the many-body localization transition in two dimensions.”, *Science* **352**, 1547 (2016) (Cited on p. 7, 18, 54, 74, 80, 122, 123).
- [44] D. Wei, A. Rubio-Abadal, B. Ye, F. Machado, J. Kemp, K. Srakaew, S. Hollerith, J. Rui, S. Gopalakrishnan, N. Y. Yao, I. Bloch, and J. Zeiher, “Quantum gas microscopy of Kardar-Parisi-Zhang superdiffusion”, *Science* **376**, 716 (2022) (Cited on p. 7).
- [45] S. Trotzky, Y.-A. Chen, A. Flesch, I. P. McCulloch, U. Schollwöck, J. Eisert, and I. Bloch, “Probing the relaxation towards equilibrium in an isolated strongly correlated one-dimensional Bose gas”, *Nat. Phys.* **8**, 325 (2012) (Cited on p. 7, 74, 122, 123).
- [46] S. S. Kondov, W. R. McGehee, W. Xu, and B. Demarco, “Disorder-induced localization in a strongly correlated atomic Hubbard gas”, *Phys. Rev. Lett.* **114**, 083002 (2015) (Cited on p. 7).
- [47] A. Lukin, M. Rispoli, R. Schittko, M. E. Tai, A. M. Kaufman, S. Choi, V. Khemani, J. Léonard, and M. Greiner, “Probing entanglement in a many-body-localized system”, *Science* **364**, 256 (2019) (Cited on p. 7).
- [48] L. Tarruell, D. Greif, T. Uehlinger, G. Jotzu, and T. Esslinger, “Creating, moving and merging Dirac points with a Fermi gas in a tunable honeycomb lattice”, *Nature* **483**, 302 (2012) (Cited on p. 7, 56).
- [49] G. Jotzu, M. Messer, R. Desbuquois, M. Lebrat, T. Uehlinger, D. Greif, and T. Esslinger, “Experimental realization of the topological Haldane model with ultracold fermions”, *Nature* **515**, 237 (2014) (Cited on p. 7).
- [50] M. Aidelsburger, M. Lohse, C. Schweizer, M. Atala, J. T. Barreiro, S. Nascimbène, N. R. Cooper, I. Bloch, and N. Goldman, “Measuring the Chern number of Hofstadter bands with ultracold bosonic atoms”, *Nat. Phys.* **11**, 162 (2015) (Cited on p. 7).
- [51] E. Zohar, J. I. Cirac, and B. Reznik, “Quantum simulations of lattice gauge theories using ultracold atoms in optical lattices”, *Rep. Prog. Phys.* **79**, 014401 (2016) (Cited on p. 7, 54, 56).

- [52] D. González Cuadra, “A cold-atom approach to topological quantum matter across the energy scale”, PhD thesis (UPC, 2020) (Cited on p. 7).
- [53] C. Schweizer, F. Grusdt, M. Berngruber, L. Barbiero, E. Demler, N. Goldman, I. Bloch, and M. Aidelsburger, “Floquet approach to Z2 lattice gauge theories with ultracold atoms in optical lattices”, *Nat. Phys.* **15**, 1168 (2019) (Cited on p. 7, 15).
- [54] F. Görg, K. Sandholzer, J. Minguzzi, R. Desbuquois, M. Messer, and T. Esslinger, “Realization of density-dependent Peierls phases to engineer quantized gauge fields coupled to ultracold matter”, *Nat. Phys.* **15**, 1161 (2019) (Cited on p. 7).
- [55] A. Frölian, C. S. Chisholm, E. Neri, C. R. Cabrera, R. Ramos, A. Celi, and L. Tarruell, “Realizing a 1D topological gauge theory in an optically dressed BEC”, *Nature* **608**, 293 (2022) (Cited on p. 7).
- [56] P. Jurcevic, B. P. Lanyon, P. Hauke, C. Hempel, P. Zoller, R. Blatt, and C. F. Roos, “Quasiparticle engineering and entanglement propagation in a quantum many-body system”, *Nature* **511**, 202 (2014) (Cited on p. 7, 59).
- [57] K. Kim, M.-S. Chang, R. Islam, S. Korenblit, L.-M. Duan, and C. Monroe, “Entanglement and Tunable Spin-Spin Couplings between Trapped Ions Using Multiple Transverse Modes”, *Phys. Rev. Lett.* **103**, 120502 (2009) (Cited on p. 7, 59).
- [58] A. Reiserer, N. Kalb, G. Rempe, and S. Ritter, “A quantum gate between a flying optical photon and a single trapped atom”, *Nature* **508**, 237 (2014) (Cited on p. 15).
- [59] B. Julsgaard, J. Sherson, J. I. Cirac, J. Flurásek, and E. S. Polzik, “Experimental demonstration of quantum memory for light”, *Nature* **432**, 482 (2004) (Cited on p. 15).
- [60] J. Ma, X. Wang, C. P. Sun, and F. Nori, “Quantum spin squeezing”, *Phys. Rep.* **509**, 89 (2010) (Cited on p. 15).
- [61] D. Jaksch and P. Zoller, “Creation of effective magnetic fields in optical lattices: the Hofstadter butterfly for cold neutral atoms”, *New J. Phys.* **5**, 56 (2003) (Cited on p. 15).
- [62] N. Goldman, G. Jotzu, M. Messer, F. Görg, R. Desbuquois, and T. Esslinger, “Creating topological interfaces and detecting chiral edge modes in a two-dimensional optical lattice”, *Phys. Rev. A* **94**, 043611 (2016) (Cited on p. 15).
- [63] M. Bello, G. Platero, J. I. Cirac, and A. González-Tudela, “Unconventional Quantum Optics in topological waveguide QED”, *Sci. Adv.* **5**, eaaw0297 (2019) (Cited on p. 15, 56).
- [64] T. Ozawa, H. M. Price, A. Amo, N. Goldman, M. Hafezi, L. Lu, M. C. Rechtsman, D. Schuster, J. Simon, O. Zilberberg, and I. Carusotto, “Topological photonics”, *Rev. Mod. Phys.* **91**, 015006 (2019) (Cited on p. 15).
- [65] D. A. Steck, *Quantum and atom optics* (2007) (Cited on p. 16).
- [66] R. Grimm, M. Weidemüller, and Y. B. Ovchinnikov, “Optical Dipole Traps for Neutral Atoms”, *Advances in Atomic, Molecular and Optical Physics* **42**, 95 (2000) (Cited on p. 17).
- [67] C. Weitenberg, M. Endres, J. F. Sherson, M. Cheneau, P. Schauß, T. Fukuhara, I. Bloch, and S. Kuhr, “Single-spin addressing in an atomic Mott insulator”, *Nature* **471**, 319 (2011) (Cited on p. 18).
- [68] R. Gerchberg and O. Saxton, “A practical algorithm for the determination of phase from image and diffraction plane pictures”, *Optik* **35**, 237 (1972) (Cited on p. 19, 95).

- [69] A. Browaeys and T. Lahaye, “Many-body physics with individually controlled Rydberg atoms”, *Nat. Phys.* **16**, 132 (2020) (Cited on p. 19, 58).
- [70] D. Barredo, V. Lienhard, P. Scholl, S. d. Léséleuc, T. Boulier, A. Browaeys, and T. Lahaye, “Three-Dimensional Trapping of Individual Rydberg Atoms in Ponderomotive Bottle Beam Traps”, *Phys. Rev. Lett.* **124**, 023201 (2020) (Cited on p. 19).
- [71] J. D. Jackson, *Classical electrodynamics*, 1999 (Cited on p. 19).
- [72] D. E. Chang, J. S. Douglas, A. González-Tudela, C. L. Hung, and H. J. Kimble, “Colloquium: Quantum matter built from nanoscopic lattices of atoms and photons”, *Rev. Mod. Phys.* **90**, 031002 (2018) (Cited on p. 19, 22, 59).
- [73] K. Hammerer, A. S. Sørensen, and E. S. Polzik, “Quantum interface between light and atomic ensembles”, *Rev. Mod. Phys.* **82**, 1041 (2010) (Cited on p. 19).
- [74] S. Haroche and J. Raimond, *Exploring the quantum: atoms, cavities, and photons* (Oxford university press, 2006) (Cited on p. 19).
- [75] A. Reiserer and G. Rempe, “Cavity-based quantum networks with single atoms and optical photons”, *Rev. Mod. Phys.* **87**, 1379 (2015) (Cited on p. 19, 22, 29).
- [76] E. T. Jaynes and F. W. Cummings, “Comparison of Quantum and Semiclassical Radiation Theories with Application to the Beam Maser”, *Proceedings of the IEEE* **51**, 89 (1963) (Cited on p. 20).
- [77] H.-P. Breuer and F. Petruccione, *The Theory of Open Quantum Systems* (Oxford University Press, New York, 2002) (Cited on p. 21).
- [78] C. Cohen-Tannoudji, J. Dupont-Roc, and G. Grynberg, *Atom-photon interactions: basic processes and applications* (Wiley, 1998) (Cited on p. 21).
- [79] C. Gardiner and P. Zoller, *The Quantum World of Ultra-Cold Atoms and Light Book I: Foundations of Quantum Optics*, Cold Atoms (Imperial College Press, 2014) (Cited on p. 21, 24, 31, 33).
- [80] E. M. Purcell, “Spontaneous Emission Probabilities at Ratio Frequencies”, *Phys. Rev.* **69**, 674 (1946) (Cited on p. 21).
- [81] P. Goy, J. M. Raimond, M. Gross, and S. Haroche, “Observation of Cavity-Enhanced Single-Atom Spontaneous Emission”, *Phys. Rev. Lett.* **50**, 1903 (1983) (Cited on p. 21).
- [82] J. S. Douglas, T. Caneva, and D. E. Chang, “Photon Molecules in Atomic Gases Trapped Near Photonic Crystal Waveguides”, *Phys. Rev. X* **6**, 31017 (2016) (Cited on p. 22).
- [83] E. Vetsch, D. Reitz, G. Sagué, R. Schmidt, S. T. Dawkins, and A. Rauschenbeutel, “Optical interface created by laser-cooled atoms trapped in the evanescent field surrounding an optical nanofiber”, *Phys. Rev. Lett.* **104**, 203603 (2010) (Cited on p. 23).
- [84] E. Will, L. Masters, A. Rauschenbeutel, M. Scheucher, and J. Volz, “Coupling a Single Trapped Atom to a Whispering-Gallery-Mode Microresonator”, *Phys. Rev. Lett.* **126**, 233602 (2021) (Cited on p. 23, 29, 30).
- [85] P. Samutpraphoot, P. L. Ocola, H. Bernien, C. Senko, V. Vuletić, and M. D. Lukin, “Strong Coupling of Two Individually Controlled Atoms via a Nanophotonic Cavity”, *Phys. Rev. Lett.* **124**, 063602 (2020) (Cited on p. 23, 29, 30, 34, 38, 43, 61).
- [86] T. Đorđević, P. Samutpraphoot, P. L. Ocola, H. Bernien, B. Grinkemeyer, I. Dimitrova, V. Vuletić, and M. D. Lukin, “Entanglement transport and a nanophotonic interface for atoms in optical tweezers”, *Science* **373**, 1511 (2021) (Cited on p. 23).

- [87] C.-L. Hung, S. M. Meenehan, D. E. Chang, O. Painter, and H. J. Kimble, “Trapped atoms in one-dimensional photonic crystals”, *New J. Phys.* **15**, 83026 (2013) (Cited on p. 23).
- [88] A. González-Tudela, C. L. Hung, D. E. Chang, J. I. Cirac, and H. J. Kimble, “Subwavelength vacuum lattices and atom-atom interactions in two-dimensional photonic crystals”, *Nat. Photonics* **9**, 320 (2015) (Cited on p. 23, 60).
- [89] P. Ruchka, S. Hammer, M. Rockenhäuser, R. Albrecht, J. Drozella, S. Thiele, H. Giessen, and T. Langen, “Microscopic 3D printed optical tweezers for atomic quantum technology”, *Quantum Sci. Technol.* **7**, 045011 (2022) (Cited on p. 23).
- [90] D. Hunger, T. Steinmetz, Y. Colombe, C. Deutsch, T. W. Hänsch, and J. Reichel, “A fiber Fabry–Perot cavity with high finesse”, *New J. Phys.* **12**, 065038 (2010) (Cited on p. 23).
- [91] M. Brekenfeld, D. Niemietz, J. D. Christesen, and G. Rempe, “A quantum network node with crossed optical fibre cavities”, *Nat. Phys.* **16**, 647 (2020) (Cited on p. 23).
- [92] D. Niemietz, P. Farrera, S. Langenfeld, and G. Rempe, “Nondestructive detection of photonic qubits”, *Nature* **591**, 570 (2021) (Cited on p. 23, 29).
- [93] C. W. Gardiner and M. J. Collett, “Input and output in damped quantum systems: Quantum stochastic differential equations and the master equation”, *Phys. Rev. A* **31**, 3761 (1985) (Cited on p. 24, 31, 129).
- [94] M. Metcalfe, “Applications of cavity optomechanics”, *Appl. Phys. Lett.* **1**, 031105 (2014) (Cited on p. 27).
- [95] S. Schreppler, N. Spethmann, N. Brahms, T. Botter, M. Barrios, and D. M. Stamper-Kurn, “Quantum metrology. Optically measuring force near the standard quantum limit.”, *Science* **344**, 1486 (2014) (Cited on p. 27, 93).
- [96] M. Wu, N. L. Wu, T. Firdous, F. Fani Sani, J. E. Losby, M. R. Freeman, and P. E. Barclay, “Nanocavity optomechanical torque magnetometry and radiofrequency susceptometry”, *Nat. Nanotechnol.* **12**, 127 (2017) (Cited on p. 27).
- [97] E. Gil-Santos, J. J. Ruz, O. Malvar, I. Favero, A. Lemaître, P. M. Kosaka, S. García-López, M. Calleja, and J. Tamayo, “Optomechanical detection of vibration modes of a single bacterium”, *Nat. Nanotechnol.* **15**, 469 (2020) (Cited on p. 27).
- [98] R. Fischer, D. P. McNally, C. Reetz, G. G. Assumpção, T. Knief, Y. Lin, and C. A. Regal, “Spin detection with a micromechanical trampoline: Towards magnetic resonance microscopy harnessing cavity optomechanics”, *New J. Phys.* **21**, 43049 (2019) (Cited on p. 27).
- [99] J. Chan, T. P. M. Alegre, A. H. Safavi-Naeini, J. T. Hill, A. Krause, S. Gröblacher, M. Aspelmeyer, and O. Painter, “Laser cooling of a nanomechanical oscillator into its quantum ground state”, *Nature* **478**, 89 (2011) (Cited on p. 27).
- [100] J. D. Teufel, T. Donner, D. Li, J. W. Harlow, M. S. Allman, K. Cicak, A. J. Sirois, J. D. Whittaker, K. W. Lehnert, and R. W. Simmonds, “Sideband cooling of micromechanical motion to the quantum ground state”, *Nature* **475**, 359 (2011) (Cited on p. 27).
- [101] T. P. Purdy, P. L. Yu, R. W. Peterson, N. S. Kampel, and C. A. Regal, “Strong optomechanical squeezing of light”, *Phys. Rev. X* **3**, 031012 (2014) (Cited on p. 27).

- [102] A. H. Safavi-Naeini, S. Gröblacher, J. T. Hill, J. Chan, M. Aspelmeyer, and O. Painter, “Squeezed light from a silicon micromechanical resonator”, *Nature* **500**, 185 (2013) (Cited on p. 27).
- [103] N. Aggarwal, T. J. Cullen, J. Cripe, G. D. Cole, R. Lanza, A. Libson, D. Follman, P. Heu, T. Corbitt, and N. Mavalvala, “Room-temperature optomechanical squeezing”, *Nat. Phys.* **16**, 784 (2020) (Cited on p. 27).
- [104] H. Xu, L. Jiang, A. A. Clerk, and J. G. Harris, “Nonreciprocal control and cooling of phonon modes in an optomechanical system”, *Nature* **568**, 65 (2019) (Cited on p. 27).
- [105] P. Rabl, “Photon Blockade Effect in Optomechanical Systems”, *Phys. Rev. Lett.* **107**, 063601 (2011) (Cited on p. 28).
- [106] A. Nunnenkamp, K. Børkje, and S. M. Girvin, “Single-Photon Optomechanics”, *Phys. Rev. Lett.* **107**, 063602 (2011) (Cited on p. 28).
- [107] M. Brunelli, D. Malz, A. Schliesser, and A. Nunnenkamp, “Stroboscopic quantum optomechanics”, *Phys. Rev. Research* **2**, 023241 (2020) (Cited on p. 28).
- [108] T. S. Yin, X. Y. Lü, L. L. Zheng, M. Wang, S. Li, and Y. Wu, “Nonlinear effects in modulated quantum optomechanics”, *Phys. Rev. A* **95**, 053861 (2017) (Cited on p. 28).
- [109] M. A. Lemonde, N. Didier, and A. A. Clerk, “Enhanced nonlinear interactions in quantum optomechanics via mechanical amplification”, *Nat. Commun.* **7**, 1 (2016) (Cited on p. 28).
- [110] J. M. Pirkkalainen, S. U. Cho, F. Massel, J. Tuorila, T. T. Heikkilä, P. J. Hakonen, and M. A. Sillanpää, “Cavity optomechanics mediated by a quantum two-level system”, *Nat. Commun.* **6**, 1 (2015) (Cited on p. 28).
- [111] T. T. Heikkilä, F. Massel, J. Tuorila, R. Khan, and M. A. Sillanpää, “Enhancing optomechanical coupling via the Josephson effect”, *Phys. Rev. Lett.* **112**, 203603 (2014) (Cited on p. 28).
- [112] G. S. MacCabe, H. Ren, J. Luo, J. D. Cohen, H. Zhou, A. Sipahigil, M. Mirhosseini, and O. Painter, “Nano-acoustic resonator with ultralong phonon lifetime”, *Science* **370**, 840 (2020) (Cited on p. 28).
- [113] H. Ren, M. H. Matheny, G. S. MacCabe, J. Luo, H. Pfeifer, M. Mirhosseini, and O. Painter, “Two-dimensional optomechanical crystal cavity with high quantum cooperativity”, *Nat. Commun.* **11**, 1 (2020) (Cited on p. 28).
- [114] F. Brennecke, S. Ritter, T. Donner, and T. Esslinger, “Cavity optomechanics with a Bose-Einstein condensate.”, *Science* **322**, 235 (2008) (Cited on p. 29, 93).
- [115] D. M. Stamper-Kurn, in *Cavity optomechanics: nano- and micromechanical resonators interacting with light* (Springer, Berlin, Heidelberg, Jan. 2014), pp. 283–325 (Cited on p. 29).
- [116] T. P. Purdy, D. W. Brooks, T. Botter, N. Brahms, Z. Y. Ma, and D. M. Stamper-Kurn, “Tunable cavity optomechanics with ultracold atoms”, *Phys. Rev. Lett.* **105**, 133602 (2010) (Cited on p. 29).
- [117] I. Shomroni, S. Rosenblum, Y. Lovsky, O. Bechler, G. Guendelman, and B. Dayan, “All-optical routing of single photons by a one-atom switch controlled by a single photon”, *Science* **345**, 903 (2014) (Cited on p. 29).
- [118] B. Hacker, S. Welte, S. Daiss, A. Shaikat, S. Ritter, L. Li, and G. Rempe, “Deterministic creation of entangled atom–light Schrödinger-cat states”, *Nat. Photonics* **13**, 110 (2019) (Cited on p. 29).

- [119] C. Hamsen, K. N. Tolazzi, T. Wilk, and G. Rempe, “Strong coupling between photons of two light fields mediated by one atom”, *Nat. Phys.* **14**, 885 (2018) (Cited on p. 29).
- [120] K. M. Birnbaum, A. Boca, R. Miller, A. D. Boozer, T. E. Northup, and H. J. Kimble, “Photon blockade in an optical cavity with one trapped atom”, *Nature* **436**, 87 (2005) (Cited on p. 29).
- [121] S. Schütz, J. Schachenmayer, D. Hagenmüller, G. K. Brennen, T. Volz, V. Sandoghdar, T. W. Ebbesen, C. Genes, and G. Pupillo, “Ensemble-Induced Strong Light-Matter Coupling of a Single Quantum Emitter”, *Phys. Rev. Lett.* **124**, 113602 (2020) (Cited on p. 29).
- [122] L. Neumeier, T. E. Northup, and D. E. Chang, “Reaching the optomechanical strong-coupling regime with a single atom in a cavity”, *Phys. Rev. A* **97**, 063857 (2018) (Cited on p. 29).
- [123] L. Neumeier and D. E. Chang, “Exploring unresolved sideband, optomechanical strong coupling using a single atom coupled to a cavity”, *New J. Phys.* **20**, 083004 (2018) (Cited on p. 29, 33, 130).
- [124] T. G. Tiecke, J. D. Thompson, N. P. de Leon, L. R. Liu, V. Vuletić, and M. D. Lukin, “Nanophotonic quantum phase switch with a single atom”, *Nature* **508**, 241 (2014) (Cited on p. 29).
- [125] J. D. Thompson, T. G. Tiecke, N. P. De Leon, J. Feist, A. V. Akimov, M. Gullans, A. S. Zibrov, V. Vuletić, and M. D. Lukin, “Coupling a single trapped atom to a nanoscale optical cavity”, *Science* **340**, 1202 (2013) (Cited on p. 29).
- [126] O. Bechler, A. Borne, S. Rosenblum, G. Guendelman, O. E. Mor, M. Netser, T. Ohana, Z. Aqua, N. Drucker, R. Finkelstein, Y. Lovsky, R. Bruch, D. Gurovich, E. Shafir, and B. Dayan, “A passive photon–atom qubit swap operation”, *Nat. Phys.* **14**, 996 (2018) (Cited on p. 29, 30).
- [127] Y. Castin and J. Dalibard, “Quantization of Atomic Motion in Optical Molasses”, *EPL (Europhys. Lett.)* **14**, 761 (1991) (Cited on p. 30).
- [128] J. I. Cirac, R. Blatt, P. Zoller, and W. D. Phillips, “Laser cooling of trapped ions in a standing wave”, *Phys. Rev. A* **46**, 2668 (1992) (Cited on p. 30).
- [129] D. E. Chang, K. Sinha, J. M. Taylor, and H. J. Kimble, “Trapping atoms using nanoscale quantum vacuum forces”, *Nat. Commun.* **5**, 1 (2014) (Cited on p. 30).
- [130] P. Meystre and M. Sargent, *Elements of Quantum Optics* (Springer Science & Business Media, 2010), p. 435 (Cited on p. 31).
- [131] S. Xu and S. Fan, “Input-output formalism for few-photon transport: A systematic treatment beyond two photons”, *Phys. Rev. A* **91**, 043845 (2015) (Cited on p. 32, 33, 129).
- [132] T. Caneva, M. T. Manzoni, T. Shi, J. S. Douglas, J. I. Cirac, and D. E. Chang, “Quantum dynamics of propagating photons with strong interactions: a generalized input–output formalism”, *New J. Phys.* **17**, 113001 (2015) (Cited on p. 32, 33, 129).
- [133] K. W. Murch, K. L. Moore, S. Gupta, and D. M. Stamper-Kurn, “Observation of quantum-measurement backaction with an ultracold atomic gas”, *Nat. Phys.* **4**, 561 (2008) (Cited on p. 35, 93).
- [134] J. Restrepo, C. Ciuti, and I. Favero, “Single Polariton Optomechanics”, *Phys. Rev. Lett.* **112** (2013) (Cited on p. 37).
- [135] T. Holz, R. Betzholtz, and M. Bienert, “Suppression of Rabi oscillations in hybrid optomechanical systems”, *Phys. Rev. A* **92**, 043822 (2015) (Cited on p. 37).

- [136] M. T. Manzoni, L. Mathey, and D. E. Chang, “Designing exotic many-body states of atomic spin and motion in photonic crystals”, *Nat. Commun.* **8**, 14696 (2017) (Cited on p. 43).
- [137] M. Lewenstein, A. Sanpera, V. Ahufinger, B. Damski, A. Sen(De), and U. Sen, “Ultracold atomic gases in optical lattices: mimicking Condens. Matter Phys. and beyond”, *Adv. Phys.* **56**, 243 (2007) (Cited on p. 48).
- [138] L. Santos, M. A. Baranov, J. I. Cirac, H. U. Everts, H. Fehrmann, and M. Lewenstein, “Atomic quantum gases in kagomé lattices”, *Phys. Rev. Lett.* **93**, 030601 (2004) (Cited on p. 48, 56).
- [139] Z. Xu, H. Huangfu, Y. Zhang, and S. Chen, “Dynamical observation of mobility edges in one-dimensional incommensurate optical lattices”, *New J. Phys.* **22**, 013036 (2020) (Cited on p. 48, 56).
- [140] P. Wang, Y. Zheng, X. Chen, C. Huang, Y. V. Kartashov, L. Torner, V. V. Konotop, and F. Ye, “Localization and delocalization of light in photonic moire lattices”, *Nature* **577**, 42 (2020) (Cited on p. 48).
- [141] M. Greiner, “Ultracold quantum gases in three-dimensional optical lattice potentials”, PhD thesis (LMU, 2003) (Cited on p. 49).
- [142] G. H. Wannier, “The Structure of Electronic Excitation Levels in Insulating Crystals”, *Phys. Rev.* **52**, 191 (1937) (Cited on p. 50).
- [143] N. Marzari and D. Vanderbilt, “Maximally localized generalized Wannier functions for composite energy bands”, *Phys. Rev. B* **56**, 12847 (1997) (Cited on p. 50).
- [144] Y. Castin, in *Coherent atomic matter waves* (Springer Berlin Heidelberg, May 2001), pp. 1–136 (Cited on p. 51).
- [145] I. Bloch, J. Dalibard, and W. Zwerger, “Many-body physics with ultracold gases”, *Rev. Mod. Phys.* **80**, 885 (2008) (Cited on p. 52, 79, 93, 94).
- [146] W. Zwerger, “Mott–Hubbard transition of cold atoms in optical lattices”, *J. Opt. B: Quantum Semiclassical Opt.* **5**, S9 (2003) (Cited on p. 52–54).
- [147] J. Larson, S. Fernández-Vidal, G. Morigi, and M. Lewenstein, “Quantum stability of Mott-insulator states of ultracold atoms in optical resonators”, *New J. Phys.* **10**, 045002 (2008) (Cited on p. 53).
- [148] E. Tiesinga, A. J. Moerdijk, B. J. Verhaar, and H. T. C. Stoof, “Conditions for Bose-Einstein condensation in magnetically trapped atomic cesium”, *Phys. Rev. A* **46**, R1167 (1992) (Cited on p. 54).
- [149] H. T. C. Stoof, “Atomic Bose gas with a negative scattering length”, *Phys. Rev. A* **49**, 3824 (1994) (Cited on p. 54).
- [150] C. Chin, R. Grimm, P. Julienne, and E. Tiesinga, “Feshbach Resonances in Ultracold Gases”, *Rev. Mod. Phys.* **82**, 1225 (2010) (Cited on p. 54).
- [151] C. C. Chien, S. Peotta, and M. Di Ventra, “Quantum transport in ultracold atoms”, *Nat. Phys.* **11**, 998 (2015) (Cited on p. 54).
- [152] F. Schäfer, T. Fukuhara, S. Sugawa, Y. Takasu, and Y. Takahashi, “Tools for quantum simulation with ultracold atoms in optical lattices”, *Nat. Rev. Phys.* **2**, 411 (2020) (Cited on p. 54).
- [153] M. Aidelsburger, L. Barbiero, A. Bermudez, T. Chanda, A. Dauphin, D. González-Cuadra, P. R. Grzybowski, S. Hands, F. Jendrzejewski, J. Jünemann, G. Juzeliunas, V. Kasper, A. Piga, S.-J. Ran, M. Rizzi, G. Sierra, L. Tagliacozzo, E. Tirrito, T. V. Zache, J. Zakrzewski, E. Zohar, and M. Lewenstein, “Cold atoms meet lattice gauge theory”, *Philosophical Transactions of the Royal Society A: Mathematical, Physical and Eng. Sci.* **380**, 20210064 (2022) (Cited on p. 54, 56).

- [154] A. Rubio-Abadal, M. Ippoliti, S. Hollerith, D. Wei, J. Rui, S. L. Sondhi, V. Khemani, C. Gross, and I. Bloch, "Floquet Prethermalization in a Bose-Hubbard System", *Phys. Rev. X* **10**, 021044 (2020) (Cited on p. 54).
- [155] M. P. A. Fisher, P. B. Weichman, G. Grinstein, and D. S. Fisher, "Boson localization and the superfluid-insulator transition", *Phys. Rev. B* **40**, 546 (1989) (Cited on p. 55).
- [156] J. F. Sherson, C. Weitenberg, M. Endres, M. Cheneau, I. Bloch, and S. Kuhr, "Single-atom-resolved fluorescence imaging of an atomic Mott insulator", *Nature* **467**, 68 (2010) (Cited on p. 56).
- [157] P. Dyke, E. D. Kuhnle, S. Whitlock, H. Hu, M. Mark, S. Hoinka, M. Lingham, P. Hannaford, and C. J. Vale, "Crossover from 2D to 3D in a weakly interacting Fermi gas", *Phys. Rev. Lett.* **106**, 105304 (2010) (Cited on p. 56, 71).
- [158] K. Martiyanov, V. Makhalov, and A. Turlapov, "Observation of a two-dimensional Fermi gas of atoms", *Phys. Rev. Lett.* **105**, 030404 (2010) (Cited on p. 56, 71).
- [159] C. Becker, P. Soltan-Panahi, J. Kronjäger, S. Dörscher, K. Bongs, and K. Sengstock, "Ultracold quantum gases in triangular optical lattices", *New J. Phys.* **12**, 065025 (2010) (Cited on p. 56).
- [160] R. Yamamoto, H. Ozawa, D. C. Nak, I. Nakamura, and T. Fukuhara, "Single-site-resolved imaging of ultracold atoms in a triangular optical lattice", *New J. Phys.* **22**, 123028 (2020) (Cited on p. 56).
- [161] J. Struck, M. Weinberg, C. Ölschläger, P. Windpassinger, J. Simonet, K. Sengstock, R. Höppner, P. Hauke, A. Eckardt, M. Lewenstein, and L. Mathey, "Engineering Ising-XY spin-models in a triangular lattice using tunable artificial gauge fields", *Nat. Phys.* **9**, 738 (2013) (Cited on p. 56).
- [162] S. Safaei, C. Miniatura, and B. Grémaud, "Triangular and honeycomb lattices of cold atoms in optical cavities", *Phys. Rev. A* **92**, 043810 (2015) (Cited on p. 56).
- [163] G. Liu, S. L. Zhu, S. Jiang, F. Sun, and W. M. Liu, "Simulating and detecting the quantum spin Hall effect in the kagome optical lattice", *Phys. Rev. A* **82**, 053605 (2010) (Cited on p. 56).
- [164] G. B. Jo, J. Guzman, C. K. Thomas, P. Hosur, A. Vishwanath, and D. M. Stamper-Kurn, "Ultracold atoms in a tunable optical kagome lattice", *Phys. Rev. Lett.* **108**, 045305 (2012) (Cited on p. 56).
- [165] S. L. Zhu, B. Wang, and L. M. Duan, "Simulation and detection of dirac fermions with cold atoms in an optical lattice", *Phys. Rev. Lett.* **98**, 260402 (2007) (Cited on p. 56).
- [166] M. Polini, F. Guinea, M. Lewenstein, H. C. Manoharan, and V. Pellegrini, "Artificial honeycomb lattices for electrons, atoms and photons", *Nat. Nanotechnol.* **8**, 625 (2013) (Cited on p. 56).
- [167] B. Damski, J. Zakrzewski, L. Santos, P. Zoller, and M. Lewenstein, "Atomic Bose and Anderson Glasses in Optical Lattices", *Phys. Rev. Lett.* **91**, 080403 (2003) (Cited on p. 56).
- [168] J. Billy, V. Josse, Z. Zuo, A. Bernard, B. Hambrecht, P. Lugan, D. Clément, L. Sanchez-Palencia, P. Bouyer, and A. Aspect, "Direct observation of Anderson localization of matter waves in a controlled disorder", *Nature* **453**, 891 (2008) (Cited on p. 56).
- [169] J. B. Reeves, B. Gadway, T. Bergeman, I. Danshita, and D. Schneble, "Superfluid Bloch dynamics in an incommensurate optical lattice", *New J. Phys.* **16**, 065011 (2014) (Cited on p. 56).

- [170] M. Schreiber, S. S. Hodgman, P. Bordia, H. P. Lüschen, M. H. Fischer, R. Vosk, E. Altman, U. Schneider, and I. Bloch, "Observation of many-body localization of interacting fermions in a quasirandom optical lattice", *Science* **349**, 842 (2015) (Cited on p. 56).
- [171] J. J. García-Ripoll, M. A. Martin-Delgado, and J. I. Cirac, "Implementation of Spin Hamiltonians in Optical Lattices", *Phys. Rev. Lett.* **93**, 250405 (2004) (Cited on p. 56).
- [172] J. Simon, W. S. Bakr, R. Ma, M. E. Tai, P. M. Preiss, and M. Greiner, "Quantum simulation of antiferromagnetic spin chains in an optical lattice", *Nature* **472**, 307 (2011) (Cited on p. 56).
- [173] A. Friedenauer, H. Schmitz, J. T. Glueckert, D. Porras, and T. Schaetz, "Simulating a quantum magnet with trapped ions", *Nat. Phys.* **4**, 757 (2008) (Cited on p. 56).
- [174] J. J. García-Ripoll and J. I. Cirac, "Spin dynamics for bosons in an optical lattice", *New J. Phys.* **5**, 76 (2003) (Cited on p. 56).
- [175] T. Fukuhara, A. Kantian, M. Endres, M. Cheneau, P. Schauß, S. Hild, D. Bellem, U. Schollwöck, T. Giamarchi, C. Gross, et al., "Quantum dynamics of a mobile spin impurity", *Nat. Phys.* **9**, 235 (2013) (Cited on p. 56).
- [176] K. Góral, L. Santos, and M. Lewenstein, "Quantum Phases of Dipolar Bosons in Optical Lattices", *Phys. Rev. Lett.* **88**, 170406 (2002) (Cited on p. 56).
- [177] S. Bandyopadhyay, R. Bai, S. Pal, K. Suthar, R. Nath, and D. Angom, "Quantum phases of canted dipolar bosons in a two-dimensional square optical lattice", *Phys. Rev. A* **100**, 053623 (2019) (Cited on p. 56).
- [178] S. De and I. B. Spielman, "Fermion-mediated long-range interactions between bosons stored in an optical lattice", *Appl. Phys. B* **114**, 527 (2014) (Cited on p. 56, 63, 65).
- [179] B. Zhu, J. Cooper, J. Ye, and A. M. Rey, "Light scattering from dense cold atomic media", *Phys. Rev. A* **94**, 023612 (2016) (Cited on p. 56, 72).
- [180] S. Sinha and K. Sengupta, "Phases and collective modes of a hardcore Bose-Fermi mixture in an optical lattice", *Phys. Rev. B* **79**, 115124 (2009) (Cited on p. 56, 63).
- [181] A. Mering and M. Fleischhauer, "Fermion-mediated long-range interactions of bosons in the one-dimensional bose-fermi-hubbard model", *Phys. Rev. A* **81**, 11603 (2010) (Cited on p. 56, 63, 69).
- [182] H. P. Büchler and G. Blatter, "Supersolid versus phase separation in atomic bose-fermi mixtures", *Phys. Rev. Lett.* **91**, 130404 (2003) (Cited on p. 56).
- [183] E. Kim, X. Zhang, V. S. Ferreira, J. Banker, J. K. Iverson, A. Sipahigil, M. Bello, A. González-Tudela, M. Mirhosseini, and O. Painter, "Quantum Electrodynamics in a Topological Waveguide", *Phys. Rev. X* **11**, 011015 (2021) (Cited on p. 56).
- [184] R. Mottl, F. Brennecke, K. Baumann, R. Landig, T. Donner, and T. Esslinger, "Roton-type mode softening in a quantum gas with cavity-mediated long-range interactions", *Science* **336**, 1570 (2012) (Cited on p. 56).
- [185] C. Feng and Y. Chen, "Tunable Range Interactions and Multi-Roton Excitations for Bosons in a Bose-Fermi Mixture with Optical Lattices", *Commun. Theor. Phys.* **71**, 869 (2019) (Cited on p. 56, 63).
- [186] T. Karpiuk, M. Brewczyk, S. Ospelkaus-Schwarzer, K. Bongs, M. Gajda, and K. Rzazewski, "Soliton trains in Bose-Fermi mixtures", *Phys. Rev. Lett.* **93**, 100401 (2004) (Cited on p. 57).

- [187] J. Santhanam, V. M. Kenkre, and V. V. Konotop, "Solitons of Bose-Fermi mixtures in a strongly elongated trap", *Phys. Rev. A* **73**, 13612 (2006) (Cited on p. 57).
- [188] B. J. DeSalvo, K. Patel, G. Cai, and C. Chin, "Observation of fermion-mediated interactions between bosonic atoms", *Nature* **568**, 61 (2019) (Cited on p. 57, 63, 72).
- [189] P. Cheiney, C. R. Cabrera, J. Sanz, B. Naylor, L. Tanzi, and L. Tarruell, "Bright Soliton to Quantum Droplet Transition in a Mixture of Bose-Einstein Condensates", *Phys. Rev. Lett.* **120**, 135301 (2018) (Cited on p. 57).
- [190] I. Ferrier-Barbut, H. Kadau, M. Schmitt, M. Wenzel, and T. Pfau, "Observation of Quantum Droplets in a Strongly Dipolar Bose Gas", *Phys. Rev. Lett.* **116**, 215301 (2016) (Cited on p. 57).
- [191] L. Chomaz, S. Baier, D. Petter, M. J. Mark, F. Wächtler, L. Santos, and F. Ferlaino, "Quantum-Fluctuation-driven crossover from a dilute bose-einstein condensate to a macrodroplet in a dipolar quantum fluid", *Phys. Rev. X* **6**, 41039 (2016) (Cited on p. 57).
- [192] C. R. Cabrera, L. Tanzi, J. Sanz, B. Naylor, P. Thomas, P. Cheiney, and L. Tarrue, "Quantum liquid droplets in a mixture of bose-Einstein condensates", *Science* **359**, 301 (2018) (Cited on p. 57).
- [193] C. Cohen-Tannoudji, J. Dupont-Roc, and G. Grynberg, *Atom—Photon Interactions* (Wiley-VCH Verlag, 1998) (Cited on p. 57).
- [194] C. Menotti, M. Lewenstein, T. Lahaye, and T. Pfau, "Dipolar interaction in ultra-cold atomic gases", *AIP Conference Proceedings* **970**, 332 (2008) (Cited on p. 58).
- [195] J. L. Bohn, A. M. Rey, and J. Ye, "Cold molecules: Progress in quantum engineering of chemistry and quantum matter", *Science* **357**, 1002 (2017) (Cited on p. 58).
- [196] L. D. Carr, D. DeMille, R. V. Krems, and J. Ye, "Cold and ultracold molecules: science, technology and applications", *New J. Phys.* **11**, 055049 (2009) (Cited on p. 58).
- [197] A. Griesmaier, J. Stuhler, T. Koch, M. Fattori, T. Pfau, and S. Giovanazzi, "Comparing contact and dipolar interactions in a bose-einstein condensate", *Phys. Rev. Lett.* **97**, 250402 (2006) (Cited on p. 58).
- [198] A. d. Paz, A. Sharma, A. Chotia, E. Maréchal, J. H. Huckans, P. Pedri, L. Santos, O. Gorceix, L. Vernac, and B. Laburthe-Tolra, "Nonequilibrium Quantum Magnetism in a Dipolar Lattice Gas", *Phys. Rev. Lett.* **111**, 185305 (2013) (Cited on p. 58).
- [199] A. d. Paz, P. Pedri, A. Sharma, M. Efremov, B. Naylor, O. Gorceix, E. Maréchal, L. Vernac, and B. Laburthe-Tolra, "Probing spin dynamics from the Mott insulating to the superfluid regime in a dipolar lattice gas", *Phys. Rev. A* **93**, 021603 (2016) (Cited on p. 58).
- [200] S. Baier, M. J. Mark, D. Petter, K. Aikawa, L. Chomaz, Z. Cai, M. Baranov, P. Zoller, and F. Ferlaino, "Extended Bose-Hubbard models with ultracold magnetic atoms", *Science* **352**, 201 (2016) (Cited on p. 58, 61).
- [201] N. Šibalić and C. S. Adams, *Rydberg physics* (IOP Publishing, 2018) (Cited on p. 58, 61).
- [202] T. Peyronel, O. Firstenberg, Q.-Y. Liang, S. Hofferberth, A. V. Gorshkov, T. Pohl, M. D. Lukin, and V. Vuletić, "Quantum nonlinear optics with single photons enabled by strongly interacting atoms", *Nature* **488**, 57 (2012) (Cited on p. 58).

- [203] M. Saffman, T. G. Walker, and K. Mølmer, “Quantum information with Rydberg atoms”, *Rev. Mod. Phys.* **82**, 2313 (2010) (Cited on p. 58).
- [204] Y. O. Dudin and A. Kuzmich, “Strongly interacting Rydberg excitations of a cold atomic gas”, *Science* **336**, 887 (2012) (Cited on p. 58).
- [205] E. Distante, P. Farrera, A. Padrón-Brito, D. Paredes-Barato, G. Heinze, and H. de Riedmatten, “Storing single photons emitted by a quantum memory on a highly excited Rydberg state”, *Nat. Commun.* **8**, 1 (2017) (Cited on p. 58).
- [206] L. Li and A. Kuzmich, “Quantum memory with strong and controllable Rydberg-level interactions”, *Nat. Commun.* **7**, 1 (2016) (Cited on p. 58).
- [207] F. Ripka, H. Kübler, R. Löw, and T. Pfau, “A room-temperature single-photon source based on strongly interacting Rydberg atoms”, *Science* **362**, 446 (2018) (Cited on p. 58).
- [208] S. E. Anderson, K. C. Younge, and G. Raithel, “Trapping Rydberg Atoms in an Optical Lattice”, *Phys. Rev. Lett.* **107**, 263001 (2011) (Cited on p. 58).
- [209] P. Schauß, M. Cheneau, M. Endres, T. Fukuhara, S. Hild, A. Omran, T. Pohl, C. Gross, S. Kuhr, and I. Bloch, “Observation of spatially ordered structures in a two-dimensional Rydberg gas”, *Nature* **491**, 87 (2012) (Cited on p. 58).
- [210] J. B. Balewski, A. T. Krupp, A. Gaj, S. Hofferberth, R. Löw, and T. Pfau, “Rydberg dressing: understanding of collective many-body effects and implications for experiments”, *New J. Phys.* **16**, 063012 (2014) (Cited on p. 58).
- [211] D. Porras and J. I. Cirac, “Quantum Manipulation of Trapped Ions in Two Dimensional Coulomb Crystals”, *Phys. Rev. Lett.* **96**, 250501 (2006) (Cited on p. 59).
- [212] J. W. Britton, B. C. Sawyer, A. C. Keith, C.-C. J. Wang, J. K. Freericks, H. Uys, M. J. Biercuk, and J. J. Bollinger, “Engineered two-dimensional Ising interactions in a trapped-ion quantum simulator with hundreds of spins”, *Nature* **484**, 489 (2012) (Cited on p. 59).
- [213] C. Schneider, M. Enderlein, T. Huber, and T. Schaetz, “Optical trapping of an ion”, *Nat. Photonics* **4**, 772 (2010) (Cited on p. 59).
- [214] L. Karpa, *Trapping Single Ions and Coulomb Crystals with Light Fields* (Springer, Oct. 2019) (Cited on p. 59).
- [215] M. Enderlein, T. Huber, C. Schneider, and T. Schaetz, “Single ions trapped in a one-dimensional optical lattice”, *Phys. Rev. Lett.* **109**, 233004 (2012) (Cited on p. 59).
- [216] C. Cormick, T. Schaetz, and G. Morigi, “Trapping ions with lasers”, *New J. Phys.* **13**, 043019 (2011) (Cited on p. 59).
- [217] A. Lambrecht, J. Schmidt, P. Weckesser, M. Debatin, L. Karpa, and T. Schaetz, “Long lifetimes and effective isolation of ions in optical and electrostatic traps”, *Nat. Photonics* **11**, 704 (2017) (Cited on p. 59).
- [218] R. Schmied, T. Roscilde, V. Murg, D. Porras, and J. I. Cirac, “Quantum phases of trapped ions in an optical lattice”, *New J. Phys.* **10**, 045017 (2008) (Cited on p. 59).
- [219] I. García-Mata, O. V. Zhirov, and D. L. Shepelyansky, “Frenkel-Kontorova model with cold trapped ions”, *Eur. Phys. J. D* **2006** 41:2 **41**, 325 (2006) (Cited on p. 59).
- [220] J. I. Cirac and P. Zoller, “A scalable quantum computer with ions in an array of microtraps”, *Nature* **404**, 579 (2000) (Cited on p. 59).
- [221] B. P. Lanyon, C. Hempel, D. Nigg, M. Müller, R. Gerritsma, F. Zähringer, P. Schindler, J. T. Barreiro, M. Rambach, G. Kirchmair, M. Hennrich, P. Zoller,

- R. Blatt, and C. F. Roos, "Universal digital quantum simulation with trapped ions", *Science* **334**, 57 (2011) (Cited on p. 59).
- [222] M. Tomza, K. Jachymski, R. Gerritsma, A. Negretti, T. Calarco, Z. Idziaszek, and P. S. Julienne, "Cold hybrid ion-atom systems", *Rev. Mod. Phys.* **91**, 035001 (2019) (Cited on p. 59, 61).
- [223] M. Cetina, A. Bylinskii, L. Karpa, D. Gangloff, K. M. Beck, Y. Ge, M. Scholz, A. T. Grier, I. Chuang, and V. Vuletić, "One-dimensional array of ion chains coupled to an optical cavity", *New J. Phys.* **15**, 053001 (2013) (Cited on p. 59).
- [224] F. L. Kien, S. D. Gupta, V. I. Balykin, and K. Hakuta, "Spontaneous emission of a cesium atom near a nanofiber: Efficient coupling of light to guided modes", *Phys. Rev. A* **72**, 032509 (2005) (Cited on p. 60).
- [225] A. Goban, K. S. Choi, D. J. Alton, D. Ding, C. Lacroûte, M. Pototschnig, T. Thiele, N. P. Stern, and H. J. Kimble, "Demonstration of a State-Insensitive, Compensated Nanofiber Trap", *Phys. Rev. Lett.* **109**, 033603 (2012) (Cited on p. 60).
- [226] J. Hinney, A. S. Prasad, S. Mahmoodian, K. Hammerer, A. Rauschenbeutel, P. Schneeweiss, J. Volz, and M. Schemmer, "Unraveling Two-Photon Entanglement via the Squeezing Spectrum of Light Traveling through Nanofiber-Coupled Atoms", *Phys. Rev. Lett.* **127**, 123602 (2021) (Cited on p. 60, 61).
- [227] D. E. Chang, A. S. Sørensen, E. A. Demler, and M. D. Lukin, "A single-photon transistor using nano-scale surface plasmons", *Nat. Phys.* **3**, 807 (2007) (Cited on p. 60).
- [228] N. V. Corzo, J. Raskop, A. Chandra, A. S. Sheremet, B. Gouraud, and J. Laurat, "Waveguide-coupled single collective excitation of atomic arrays", *Nature* **566**, 359 (2019) (Cited on p. 60).
- [229] N. V. Corzo, B. Gouraud, A. Chandra, A. Goban, A. S. Sheremet, D. V. Kupriyanov, and J. Laurat, "Large Bragg Reflection from One-Dimensional Chains of Trapped Atoms Near a Nanoscale Waveguide", *Phys. Rev. Lett.* **117**, 133603 (2016) (Cited on p. 60).
- [230] C. Sayrin, C. Junge, R. Mitsch, B. Albrecht, D. O'Shea, P. Schneeweiss, J. Volz, and A. Rauschenbeutel, "Nanophotonic Optical Isolator Controlled by the Internal State of Cold Atoms", *Phys. Rev. X* **5**, 41036 (2015) (Cited on p. 60).
- [231] A. Goban, C.-L. Hung, S.-P. Yu, J. Hood, J. Muniz, J. Lee, M. Martin, A. McClung, K. Choi, D. Chang, O. Painter, and H. Kimble, "Atom-light interactions in photonic crystals", *Nat. Commun.* **5**, 1 (2014) (Cited on p. 60).
- [232] J. S. Douglas, H. Habibian, C.-L. Hung, A. V. Gorshkov, H. J. Kimble, and D. E. Chang, "Quantum many-body models with cold atoms coupled to photonic crystals", *Nat. Photonics* **9**, 326 (2015) (Cited on p. 60).
- [233] J. D. Hood, A. Goban, A. Asenjo-Garcia, M. Lu, S.-P. Yu, D. E. Chang, and H. J. Kimble, "Atom-atom interactions around the band edge of a photonic crystal waveguide", *Proc. Natl. Acad. Sci. U.S.A.* **113**, 10507 (2016) (Cited on p. 60).
- [234] K. Baumann, C. Guerlin, F. Brennecke, and T. Esslinger, "Dicke quantum phase transition with a superfluid gas in an optical cavity", *Nature* **464**, 1301 (2010) (Cited on p. 61).
- [235] A. Periwal, E. S. Cooper, P. Kunkel, J. F. Wienand, E. J. Davis, and M. Schleier-Smith, "Programmable interactions and emergent geometry in an array of atom clouds", *Nature* **600**, 630 (2021) (Cited on p. 61, 62).
- [236] S. T. Chui and V. N. Ryzhov, "Collapse transition in mixtures of bosons and fermions", *Phys. Rev. A* **69**, 43607 (2004) (Cited on p. 63).

- [237] K. Günter, T. Stöferle, H. Moritz, M. Köhl, and T. Esslinger, “Bose-Fermi Mixtures in a Three-Dimensional Optical Lattice”, *Phys. Rev. Lett.* **96**, 180402 (2006) (Cited on p. 63).
- [238] T. Best, S. Will, U. Schneider, L. Hackermüller, D. Van Oosten, I. Bloch, and D. S. Lühmann, “Role of interactions in Rb87-K40 Bose-Fermi mixtures in a 3D optical lattice”, *Phys. Rev. Lett.* **102**, 30408 (2009) (Cited on p. 63).
- [239] T. P. Polak and T. K. Kopeć, “Zero-temperature phase diagram of Bose-Fermi gaseous mixtures in optical lattices”, *Phys. Rev. A* **81**, 43612 (2010) (Cited on p. 63).
- [240] I. Ferrier-Barbut, M. Delehaye, S. Laurent, A. T. Grier, M. Pierce, B. S. Rem, F. Chevy, and C. Salomon, “A mixture of Bose and Fermi superfluids”, *Science* **345**, 1035 (2014) (Cited on p. 63).
- [241] D. Suchet, Z. Wu, F. Chevy, and G. M. Bruun, “Long-range mediated interactions in a mixed-dimensional system”, *Phys. Rev. A* **95**, 43643 (2017) (Cited on p. 63).
- [242] B. J. DeSalvo, K. Patel, J. Johansen, and C. Chin, “Observation of a Degenerate Fermi Gas Trapped by a Bose-Einstein Condensate”, *Phys. Rev. Lett.* **119**, 233401 (2017) (Cited on p. 63, 68, 69).
- [243] H. Edri, B. Raz, N. Matzliah, N. Davidson, and R. Ozeri, “Observation of Spin-Spin Fermion-Mediated Interactions between Ultracold Bosons”, *Phys. Rev. Lett.* **124**, 163401 (2020) (Cited on p. 63, 69, 72).
- [244] D. C. Zheng, C. R. Ye, L. Wen, and R. Liao, “Polarizing the medium: Fermion-mediated interactions between bosons”, *Phys. Rev. A* **103**, L021301 (2021) (Cited on p. 63).
- [245] D. H. Santamore and E. Timmermans, “Fermion-mediated interactions in a dilute Bose-Einstein condensate”, *Phys. Rev. A* **78**, 13619 (2008) (Cited on p. 63).
- [246] T. Kasuya, “A Theory of Metallic Ferro- and Antiferromagnetism on Zener’s Model”, *Prog. Theor. Phys.* **16**, 45 (1956) (Cited on p. 63).
- [247] M. A. Ruderman and C. Kittel, “Indirect exchange coupling of nuclear magnetic moments by conduction electrons”, *Phys. Rev.* **96**, 99 (1954) (Cited on p. 63, 66).
- [248] K. Yosida, “Magnetic properties of Cu-Mn alloys”, *Phys. Rev.* **106**, 893 (1957) (Cited on p. 63).
- [249] Q. D. Jiang, “On the sign of fermion-mediated interactions”, *Phys. Rev. B* **103**, L121107 (2021) (Cited on p. 65).
- [250] A. Galindo and P. Pascual, *Quantum mechanics I* (Springer Science & Business Media, 2012) (Cited on p. 65, 76).
- [251] M. Abramowitz and I. A. Stegun, *Handbook of Mathematical Functions with Formulas, Graphs and Mathematical Tables* (Dover, 1972) (Cited on p. 66, 134, 135).
- [252] T. M. Rusin and W. Zawadzki, “On calculation of RKKY range function in one dimension”, *J. Magn. Magn. Mater.* **441**, 387 (2017) (Cited on p. 66).
- [253] B. Fischer and M. W. Klein, “Magnetic and nonmagnetic impurities in two-dimensional metals”, *Phys. Rev. B* **11**, 2025 (1975) (Cited on p. 66).
- [254] L. Hruby, N. Dogra, M. Landini, T. Donner, and T. Esslinger, “Metastability and avalanche dynamics in strongly correlated gases with long-range interactions”, *Proc. Natl. Acad. Sci. U.S.A.* **115**, 3279 (2018) (Cited on p. 67, 68).

- [255] C. Silber, S. Günther, C. Marzok, B. Deh, P. W. Courteille, and C. Zimmermann, “Quantum-degenerate mixture of fermionic lithium and bosonic rubidium gases”, *Phys. Rev. Lett.* **95**, 170408 (2005) (Cited on p. 68, 69).
- [256] M. Schechter and A. Kamenev, “Phonon-mediated casimir interaction between mobile impurities in one-dimensional quantum liquids”, *Phys. Rev. Lett.* **112**, 155301 (2014) (Cited on p. 68).
- [257] J. Hauschild and F. Pollmann, “Efficient numerical simulations with Tensor Networks: Tensor Network Python (TeNPy)”, *SciPost Physics Lecture Notes* **5**, 5 (2018) (Cited on p. 69).
- [258] C. Lacroix, P. Mendels, and F. Mila, *Introduction to frustrated magnetism: materials, experiments, theory*, Vol. 164 (Springer Science & Business Media, 2011) (Cited on p. 69).
- [259] S. Julià-Farré, D. González-Cuadra, A. Patscheider, M. J. Mark, F. Ferlaino, M. Lewenstein, L. Barbiero, and A. Dauphin, “Revealing the topological nature of the bond order wave in a strongly correlated quantum system”, *Phys. Rev. Research* **4**, L032005 (2021) (Cited on p. 69).
- [260] T. Mishra, J. Carrasquilla, and M. Rigol, “Phase diagram of the half-filled one-dimensional t-V-V’ model”, *Phys. Rev. B* **84**, 115135 (2011) (Cited on p. 69).
- [261] Y. Hatsugai, “Quantized Berry Phases as a Local Order Parameter of a Quantum Liquid”, *J. Phys. Soc. Jpn.* **75**, 123601 (2006) (Cited on p. 69).
- [262] M. P. Zaletel, R. S. K. Mong, and F. Pollmann, “Flux insertion, entanglement, and quantized responses”, *J. Stat. Mech: Theory Exp.* **2014**, P10007 (2014) (Cited on p. 69).
- [263] D. González-Cuadra, P. R. Grzybowski, A. Dauphin, and M. Lewenstein, “Strongly Correlated Bosons on a Dynamical Lattice”, *Phys. Rev. Lett.* **121**, 90402 (2018) (Cited on p. 69).
- [264] D. González-Cuadra, A. Dauphin, P. R. Grzybowski, M. Wójcik Paweł and Lewenstein, and A. Bermudez, “Symmetry-breaking topological insulators in the Z2 Bose-Hubbard model”, *Phys. Rev. B* **99**, 45139 (2019) (Cited on p. 69).
- [265] D. González-Cuadra, A. Bermudez, P. R. Grzybowski, M. Lewenstein, and A. Dauphin, “Intertwined topological phases induced by emergent symmetry protection”, *Nat. Commun.* **10**, 2694 (2019) (Cited on p. 69).
- [266] D. González-Cuadra, A. Dauphin, P. R. Grzybowski, M. Lewenstein, and A. Bermudez, “Dynamical Solitons and Boson Fractionalization in Cold-Atom Topological Insulators”, *Phys. Rev. Lett.* **125**, 265301 (2020) (Cited on p. 69).
- [267] D. González-Cuadra, A. Dauphin, P. R. Grzybowski, M. Lewenstein, and A. Bermudez, “Zn solitons in intertwined topological phases”, *Phys. Rev. B* **102**, 245137 (2020) (Cited on p. 69).
- [268] T. Chanda, R. Kraus, G. Morigi, and J. Zakrzewski, “Self-organized topological insulator due to cavity-mediated correlated tunneling”, *Quantum* **5**, 501 (2021) (Cited on p. 69).
- [269] T. Chanda, D. González-Cuadra, M. Lewenstein, L. Tagliacozzo, and J. Zakrzewski, “Devil’s staircase of topological Peierls insulators and Peierls supersolids”, *SciPost Phys.* **12**, 76 (2022) (Cited on p. 69).
- [270] R. P. Feynman, “Simulating Physics with Computers”, *Int. J. Theor. Phys.* **217** (1982) (Cited on p. 73, 74).
- [271] P. Hohenberg and W. Kohn, “Inhomogeneous electron gas”, *Phys. Rev.* **136**, B864 (1964) (Cited on p. 73).

- [272] R. G. Parr and W. Yang, *Density-Functional Theory of Atoms and Molecules* (Oxford University Press, New York, 1989) (Cited on p. 73, 121).
- [273] A. C. Tsipis, "DFT flavor of coordination chemistry", *Coord. Chem. Rev.* **272**, 1 (2014) (Cited on p. 73).
- [274] M. Head-Gordon, "Quantum Chemistry and Molecular Processes", *The J. Phys. Chem.* **100**, 13213 (1996) (Cited on p. 73).
- [275] A. N. Alexandrova, A. I. Boldyrev, H. J. Zhai, and L. S. Wang, "All-boron aromatic clusters as potential new inorganic ligands and building blocks in chemistry", *Coord. Chem. Rev.* **250**, 2811 (2006) (Cited on p. 73).
- [276] L. Domingo, M. Ríos-Gutiérrez, and P. Pérez, "Applications of the Conceptual Density Functional Theory Indices to Organic Chemistry Reactivity", *Molecules* **21**, 748 (2016) (Cited on p. 73).
- [277] E. K. Gross and W. Kohn, "Time-dependent density-functional theory", *Adv. Quantum Chem.* **21**, 255 (1990) (Cited on p. 73).
- [278] R. Jones, "Density functional theory: Its origins, rise to prominence, and future", *Rev. Mod. Phys.* **87**, 897 (2015) (Cited on p. 73).
- [279] A. J. Cohen, P. Mori-Sánchez, and W. Yang, "Insights into current limitations of density functional theory", *Science* **321**, 792 (2008) (Cited on p. 73).
- [280] M. G. Medvedev, I. S. Bushmarinov, J. Sun, J. P. Perdew, and K. A. Lyssenko, "Density functional theory is straying from the path toward the exact functional", *Science* **355**, 49 (2017) (Cited on p. 73).
- [281] M. G. Medvedev, I. S. Bushmarinov, J. Sun, J. P. Perdew, and K. A. Lyssenko, "Response to Comment on "Density functional theory is straying from the path toward the exact functional"", *Science* **356**, 496 (2017) (Cited on p. 73).
- [282] S. Hammes-Schiffer, "A conundrum for density functional theory", *Science* **355**, 28 (2017) (Cited on p. 73).
- [283] K. R. Brorsen, Y. Yang, M. V. Pak, and S. Hammes-Schiffer, "Is the accuracy of density functional theory for atomization energies and densities in bonding regions correlated?", *The J. Phys. Chem. Lett.* **8**, 2076 (2017) (Cited on p. 73).
- [284] M. Korth, "Density functional theory: Not quite the right answer for the right reason yet", *Angew. Chem. Int. Ed.* **56**, 5396 (2017) (Cited on p. 73).
- [285] T. Gould, "What makes a density functional approximation good? Insights from the left Fukui function", *J. Chem. Theory Comput.* **13**, 2373 (2017) (Cited on p. 73).
- [286] P. D. Mezei, G. I. Csonka, and M. Kállay, "Electron density errors and density-driven exchange-correlation energy errors in approximate density functional calculations", *J. Chem. Theory Comput.* **13**, 4753 (2017) (Cited on p. 73).
- [287] Y. Wang, X. Wang, D. G. Truhlar, and X. He, "How well can the m06 suite of functionals describe the electron densities of Ne, Ne6+, and Ne8+?", *J. Chem. Theory Comput.* **13**, 6068 (2017) (Cited on p. 73).
- [288] K. P. Kepp, "Energy vs. density on paths toward more exact density functionals", *Phys. Chem. Chem. Phys.* **20**, 7538 (2018) (Cited on p. 73).
- [289] N. Q. Su, Z. Zhu, and X. Xu, "Doubly hybrid density functionals that correctly describe both density and energy for atoms", *Proc. Natl. Acad. Sci. U.S.A.* **115**, 2287 (2018) (Cited on p. 73).
- [290] A. Szabo and N. S. Ostlund, *Modern quantum chemistry: introduction to advanced electronic structure theory* (Courier Corporation, 2012) (Cited on p. 73, 76, 77, 121).

- [291] S. Lehtola, "A review on non-relativistic, fully numerical electronic structure calculations on atoms and diatomic molecules", *Int. J. Quantum Chem.* **119**, e25968 (2019) (Cited on p. 73, 77, 98).
- [292] S. Lloyd, "Universal quantum simulators", *Science* **273**, 1073 (1996) (Cited on p. 74).
- [293] A. Aspuru-Guzik, A. D. Dutoi, P. J. Love, and M. Head-Gordon, "Simulated Quantum Computation of Molecular Energies", *Science* **309**, 1704 (2005) (Cited on p. 74).
- [294] J. D. Whitfield, J. Biamonte, and A. Aspuru-Guzik, "Simulation of electronic structure Hamiltonians using quantum computers", *Mol. Phys.* **109**, 735 (2011) (Cited on p. 74).
- [295] D. Wecker, B. Bauer, B. K. Clark, M. B. Hastings, and M. Troyer, "Gate-count estimates for performing quantum chemistry on small quantum computers", *Phys. Rev. A* **90**, 022305 (2014) (Cited on p. 74).
- [296] D. W. Berry, C. Gidney, M. Motta, J. R. McClean, and R. Babbush, "Qubitization of arbitrary basis quantum chemistry leveraging sparsity and low rank factorization", *Quantum* **3**, 208 (2019) (Cited on p. 74).
- [297] R. Babbush, N. Wiebe, J. McClean, J. McClain, H. Neven, and G. K.-L. Chan, "Low-Depth Quantum Simulation of Materials", *Phys. Rev. X* **8**, 11044 (2018) (Cited on p. 74).
- [298] R. Babbush, D. W. Berry, J. R. McClean, and H. Neven, "Quantum simulation of chemistry with sublinear scaling in basis size", *npj Quantum Inf.* **5**, 1 (2019) (Cited on p. 74).
- [299] G. H. Low and I. L. Chuang, "Hamiltonian simulation by qubitization", *Quantum* **3**, 163 (2019) (Cited on p. 74).
- [300] J. Preskill, "Quantum Computing in the NISQ era and beyond", *Quantum* **2**, 79 (2018) (Cited on p. 74).
- [301] A. Peruzzo, J. McClean, P. Shadbolt, M.-H. Yung, X.-Q. Zhou, P. J. Love, A. Aspuru-Guzik, and J. L. O'Brien, "A variational eigenvalue solver on a photonic quantum processor", *Nat. Commun.* **5**, 4213 (2014) (Cited on p. 74).
- [302] P. J. J. O'Malley, R. Babbush, I. D. Kivlichan, J. Romero, J. R. McClean, R. Barends, J. Kelly, P. Roushan, A. Tranter, N. Ding, B. Campbell, Y. Chen, Z. Chen, B. Chiaro, A. Dunsworth, A. G. Fowler, E. Jeffrey, E. Lucero, A. Megrant, J. Y. Mutus, M. Neeley, C. Neill, C. Quintana, D. Sank, A. Vainsencher, J. Wenner, T. C. White, P. V. Coveney, P. J. Love, H. Neven, A. Aspuru-Guzik, and J. M. Martinis, "Scalable Quantum Simulation of Molecular Energies", *Phys. Rev. X* **6**, 031007 (2016) (Cited on p. 74).
- [303] A. Kandala, A. Mezzacapo, K. Temme, M. Takita, M. Brink, J. M. Chow, and J. M. Gambetta, "Hardware-efficient variational quantum eigensolver for Small Mol. and quantum magnets", *Nature* **549**, 242 (2017) (Cited on p. 74).
- [304] K. Bharti, A. Cervera-Lierta, T. H. Kyaw, T. Haug, S. Alperin-Lea, A. Anand, M. Degroote, H. Heimonen, J. S. Kottmann, T. Menke, W.-K. Mok, S. Sim, L.-C. Kwek, and A. Aspuru-Guzik, "Noisy intermediate-scale quantum (NISQ) algorithms", *Rev. Mod. Phys.* **94**, 015004 (2021) (Cited on p. 74).
- [305] S. Wang, E. Fontana, M. Cerezo, K. Sharma, A. Sone, L. Cincio, and P. J. Coles, "Noise-induced barren plateaus in variational quantum algorithms", *Nat. Commun.* **12**, 1 (2021) (Cited on p. 74).
- [306] P. Czarnik, A. Arrasmith, P. J. Coles, and L. Cincio, "Error mitigation with Clifford quantum-circuit data", *Quantum* **5**, 592 (2021) (Cited on p. 74).

- [307] Y. Cao, J. Romero, J. P. Olson, M. Degroote, P. D. Johnson, M. Kieferová, I. D. Kivlichan, T. Menke, B. Peropadre, N. P. D. Sawaya, S. Sim, L. Veis, and A. Aspuru-Guzik, "Quantum Chemistry in the Age of Quantum Computing", *Chem. Rev.* **119**, 10856 (2019) (Cited on p. 74, 77).
- [308] S. R. White, J. W. Wilkins, and M. P. Teter, "Finite-element method for electronic structure", *Phys. Rev. B* **39**, 5819 (1989) (Cited on p. 74, 77, 78).
- [309] S. R. White, "Hybrid grid/basis set discretizations of the Schrödinger equation", *J. Chem. Phys.* **147**, 244102 (2017) (Cited on p. 74, 78).
- [310] E. M. Stoudenmire and S. R. White, "Sliced Basis Density Matrix Renormalization Group for Electronic Structure", *Phys. Rev. Lett.* **119**, 46401 (2017) (Cited on p. 74, 78).
- [311] S. R. White and E. M. Stoudenmire, "Multisliced gausslet basis sets for electronic structure", *Phys. Rev. B* **99**, 81110 (2019) (Cited on p. 74, 78).
- [312] S. R. White and A. E. Feiguin, "Real-Time Evolution Using the Density Matrix Renormalization Group", *Phys. Rev. Lett.* **93**, 76401 (2004) (Cited on p. 74).
- [313] D.-S. Lühmann, C. Weitenberg, and K. Sengstock, "Emulating Molecular Orbitals and Electronic Dynamics with Ultracold Atoms", *Phys. Rev. X* **5**, 031016 (2015) (Cited on p. 75, 78).
- [314] S. Sala, J. Förster, and A. Saenz, "Ultracold-atom quantum simulator for attosecond science", *Phys. Rev. A* **95**, 11403 (2017) (Cited on p. 75, 78).
- [315] R. Senaratne, S. V. Rajagopal, T. Shimasaki, P. E. Dotti, K. M. Fujiwara, K. Singh, Z. A. Geiger, and D. M. Weld, "Quantum simulation of ultrafast dynamics using trapped ultracold atoms", *Nat. Commun.* **9**, 2065 (2018) (Cited on p. 75, 78).
- [316] G. D. Mahan, *Many-particle physics* (Springer Science & Business Media, 2013) (Cited on p. 76).
- [317] D. E. Woon and T. H. Dunning Jr, "Gaussian basis sets for use in correlated molecular calculations. IV. Calculation of static electrical response properties", *The J. Chem. Phys.* **100**, 2975 (1994) (Cited on p. 77).
- [318] F. Sim, D. R. Salahub, and S. Chin, "The accurate calculation of dipole moments and dipole polarizabilities using Gaussian-based density functional methods", *Int. J. Quantum Chem.* **43**, 463 (1992) (Cited on p. 77).
- [319] T. Helgaker, K. Jaszcuński Michałand Ruud, and A. Górska, "Basis-set dependence of nuclear spin-spin coupling constants", *Theor. Chem. Acc.* **99**, 175 (1998) (Cited on p. 77).
- [320] F. Jensen, "Basis set convergence of nuclear magnetic shielding constants calculated by density functional methods", *J. Chem. Theory Comput.* **4**, 719 (2008) (Cited on p. 77).
- [321] J. Lehtola, P. Manninen, M. Hakala, and K. Hämmäläinen, "Completeness-optimized basis sets: Application to ground-state electron momentum densities", *The J. Chem. Phys.* **137**, 104105 (2012) (Cited on p. 77).
- [322] S. Lehtola, P. Manninen, M. Hakala, and K. Hämmäläinen, "Contraction of completeness-optimized basis sets: Application to ground-state electron momentum densities", *The J. Chem. Phys.* **138**, 44109 (2013) (Cited on p. 77).
- [323] J. Soler, E. Kaxiras, and P. Maragakis, "Variational finite-difference representation of the kinetic energy operator", *Phys. Rev. B* **64**, 193101 (2001) (Cited on p. 78).
- [324] C. Hooley and J. Quintanilla, "Single-Atom Density of States of an Optical Lattice", *Phys. Rev. Lett.* **93**, 80404 (2004) (Cited on p. 80).

- [325] M. Rigol and A. Muramatsu, “Confinement control by optical lattices”, *Phys. Rev. A* **70**, 43627 (2004) (Cited on p. 80).
- [326] A. M. Rey, G. Pupillo, C. W. Clark, and C. J. Williams, “Ultracold atoms confined in an optical lattice plus parabolic potential: A closed-form approach”, *Phys. Rev. A* **72**, 33616 (2005) (Cited on p. 80).
- [327] J. K. Block and N. Nygaard, “Honeycomb optical lattices with harmonic confinement”, *Phys. Rev. A* **81**, 53421 (2010) (Cited on p. 80).
- [328] B. Zaslav and M. E. Zandler, “Two-Dimensional Analog to the Hydrogen Atom Exact analytical solutions of a two-dimensional hydrogen atom in a constant magnetic field”, *Am. J. Phys* **35**, 1118 (1967) (Cited on p. 81).
- [329] J.-L. Zhu and J.-J. Xiong, “Hydrogen molecular ions in two dimensions”, *Phys. Rev. B* **41**, 12274 (1990) (Cited on p. 81).
- [330] S. H. Patil, “Hydrogen molecular ion and molecule in two dimensions”, *The J. Chem. Phys.* **118**, 2197 (2003) (Cited on p. 83, 84).
- [331] G. Calajó, F. Ciccarello, D. Chang, and P. Rabl, “Atom-field dressed states in slow-light waveguide QED”, *Phys. Rev. A* **93**, 033833 (2016) (Cited on p. 88).
- [332] T. Shi, Y. H. Wu, A. González-Tudela, and J. I. Cirac, “Bound states in boson impurity models”, *Phys. Rev. X* **6**, 021027 (2016) (Cited on p. 88).
- [333] T. Shi, Y.-H. Wu, A. González-Tudela, and J. I. Cirac, “Effective many-body Hamiltonians of qubit-photon bound states”, *New J. Phys* **20**, 105005 (2018) (Cited on p. 88).
- [334] T. Müller, S. Fölling, A. Widera, and I. Bloch, “State Preparation and Dynamics of Ultracold Atoms in Higher Lattice Orbitals”, *Phys. Rev. Lett.* **99**, 200405 (2007) (Cited on p. 90).
- [335] C. Hofrichter, L. Riegger, F. Scazza, M. Höfer, D. R. Fernandes, I. Bloch, and S. Fölling, “Direct Probing of the Mott Crossover in the SU(N) Fermi-Hubbard Model”, *Phys. Rev. X* **6**, 21030 (2016) (Cited on p. 90).
- [336] S. Snigirev, A. J. Park, A. Heinz, S. Wissenberg, J. Dalibard, I. Bloch, and S. Blatt, “Towards Quantum State Engineering with Strontium Atoms in State-Dependent Optical Lattices”, in *Quantum information and measurement* (Optical Society of America, 2017), QT4A-2 (Cited on p. 90).
- [337] L. Riegger, N. Darkwah Oppong, M. Höfer, D. R. Fernandes, I. Bloch, and S. Fölling, “Localized Magnetic Moments with Tunable Spin Exchange in a Gas of Ultracold Fermions”, *Phys. Rev. Lett.* **120**, 143601 (2018) (Cited on p. 90).
- [338] L. Krinner, M. Stewart, A. Pazmiño, J. Kwon, and D. Schneble, “Spontaneous emission of matter waves from a tunable open quantum system”, *Nature* **559**, 589 (2018) (Cited on p. 90, 93).
- [339] A. Heinz, A. J. Park, N. Šantić, J. Trautmann, S. G. Porsev, M. S. Safronova, I. Bloch, and S. Blatt, “State-Dependent Optical Lattices for the Strontium Optical Qubit”, *Phys. Rev. Lett.* **124**, 203201 (2020) (Cited on p. 90, 91, 120).
- [340] H. Ritsch, P. Domokos, F. Brennecke, and T. Esslinger, “Cold atoms in cavity-generated dynamical optical potentials”, *Rev. Mod. Phys.* **85**, 553 (2013) (Cited on p. 93, 110).
- [341] F. Brennecke, T. Donner, S. Ritter, T. Bourdel, M. Köhl, and T. Esslinger, “Cavity QED with a Bose–Einstein condensate”, *Nature* **450**, 268 (2007) (Cited on p. 93).
- [342] P. Domokos and H. Ritsch, “Collective Cooling and Self-Organization of Atoms in a Cavity”, *Phys. Rev. Lett.* **89**, 253003 (2002) (Cited on p. 93, 149).

- [343] A. J. Daley, M. M. Boyd, J. Ye, and P. Zoller, “Quantum Computing with Alkaline-Earth-Metal Atoms”, *Phys. Rev. Lett.* **101**, 170504 (2008) (Cited on p. 94, 120).
- [344] G. Whyte and J. Courtial, “Experimental demonstration of holographic three-dimensional light shaping using a Gerchberg–Saxton algorithm”, *New J. Phys* **7**, 117 (2005) (Cited on p. 95, 96).
- [345] J. W. Goodman, *Introduction to Fourier optics* (Roberts and Company Publishers, 2005) (Cited on p. 95).
- [346] N. Bruno, L. C. Bianchet, V. Prakash, N. Li, N. Alves, and M. W. Mitchell, “Maltese cross coupling to individual cold atoms in free space”, *Opt. Express* **27**, 31042 (2019) (Cited on p. 95).
- [347] A. Glicenstein, G. Ferioli, L. Brossard, Y. R. Sortais, D. Barredo, F. Nogrette, I. Ferrier-Barbut, and A. Browaeys, “Preparation of one-dimensional chains and dense cold atomic clouds with a high numerical aperture four-lens system”, *Phys. Rev. A* **103**, 043301 (2021) (Cited on p. 95).
- [348] M. Pasienski and B. DeMarco, “A high-accuracy algorithm for designing arbitrary holographic atom traps”, *Opt. Express* **16**, 2176 (2008) (Cited on p. 95).
- [349] L. Wu, S. Cheng, and S. Tao, “Complex amplitudes reconstructed in multiple output planes with a phase-only hologram”, *J. Opt.* **17**, 125603 (2015) (Cited on p. 95).
- [350] C. Chang, J. Xia, L. Yang, W. Lei, Z. Yang, and J. Chen, “Speckle-suppressed phase-only holographic three-dimensional display based on double-constraint Gerchberg–Saxton algorithm”, *Appl. Opt.* **54**, 6994 (2015) (Cited on p. 95).
- [351] G. Shabtay, “Three-dimensional beam forming and Ewald’s surfaces”, *Opt. Commun.* **226**, 33 (2003) (Cited on p. 95).
- [352] R. Di Leonardo, F. Ianni, and G. Ruocco, “Computer generation of optimal holograms for optical trap arrays”, *Opt. Express* **15**, 1913 (2007) (Cited on p. 95).
- [353] J. P. Covey, A. Sipahigil, S. Szoke, N. Sinclair, M. Endres, and O. Painter, “Telecom-band Quantum Optics with ytterbium atoms and silicon nanophotonics”, *Phys. Rev. Appl* **11**, 34044 (2019) (Cited on p. 96).
- [354] S. Gupta, K. L. Moore, K. W. Murch, and D. M. Stamper-Kurn, “Cavity Nonlinear Optics at Low Photon Numbers from Collective Atomic Motion”, *Phys. Rev. Lett.* **99**, 213601 (2007) (Cited on p. 110).
- [355] R. Landig, L. Hruby, N. Dogra, M. Landini, R. Mottl, T. Donner, and T. Esslinger, “Quantum phases from competing short- and long-range interactions in an optical lattice”, *Nature* **532**, 476 (2016) (Cited on p. 110).
- [356] L.-M. Duan, E. Demler, and M. D. Lukin, “Controlling Spin Exchange Interactions of Ultracold Atoms in Optical Lattices”, *Phys. Rev. Lett.* **91**, 90402 (2003) (Cited on p. 110).
- [357] S. Trotzky, P. Cheinet, S. Fölling, M. Feld, U. Schnorrberger, A. M. Rey, A. Polkovnikov, E. A. Demler, M. D. Lukin, and I. Bloch, “Time-resolved observation and control of superexchange interactions with ultracold atoms in optical lattices”, *Science* **319**, 295 (2008) (Cited on p. 110).
- [358] I. de Vega, D. Porras, and J. I. Cirac, “Matter-Wave Emission in Optical Lattices: Single Particle and Collective Effects”, *Phys. Rev. Lett.* **101**, 260404 (2008) (Cited on p. 115).

- [359] C. L. Pekeris, "1 S1 and 2 S3 states of helium", *Phys. Rev.* **115**, 1216 (1959) (Cited on p. 117).
- [360] W. Kolost and L. Wolniewlcz, "Accurate Adiabatic Treatment of the Ground State of the Hydrogen Molecule", *The J. Chem. Phys.* **41**, 2429 (1964) (Cited on p. 118).
- [361] J. S. Sims and S. A. Hagstrom, "High precision variational calculations for the Born-Oppenheimer energies of the ground state of the hydrogen molecule", *The J. Chem. Phys.* **124**, 094101 (2006) (Cited on p. 118).
- [362] W. Kolos, B. Jeziorski, K. Szalewicz, and H. J. Monkhorst, "Molecular effects in tritium decay: Transitions to the discrete electronic states of the HeT+ molecule", *Phys. Rev. A* **31**, 551 (1985) (Cited on p. 119, 120).
- [363] M. M. Boyd, "High Precision Spectroscopy of Strontium in an Optical Lattice: Towards a New Standard for Frequency and Time", PhD thesis (University of Colorado at Boulder, 2002) (Cited on p. 120).
- [364] J. Ye, H. J. Kimble, and H. Katori, "Optical Atomic Coherence at the 1-Second Time Scale", *Science* **314**, 1430 (2008) (Cited on p. 121).
- [365] A. Crubellier, R. González-Férez, C. P. Koch, and E. Luc-Koenig, "Controlling the s -wave scattering length with nonresonant light: Predictions of an asymptotic model", *Phys. Rev. A* **95**, 023405 (2017) (Cited on p. 121).
- [366] T. Schuster, R. Scelle, A. Trautmann, S. Knoop, M. K. Oberthaler, M. M. Haverhals, M. R. Goosen, S. J. Kokkelmans, and E. Tiemann, "Feshbach spectroscopy and scattering properties of ultracold Li + Na mixtures", *Phys. Rev. A* **85**, 042721 (2012) (Cited on p. 121).
- [367] R. Scelle, T. Rentrop, A. Trautmann, T. Schuster, and M. K. Oberthaler, "Motional coherence of fermions immersed in a bose gas", *Phys. Rev. Lett.* **111**, 070401 (2013) (Cited on p. 121).
- [368] V. Kasper, F. Hebenstreit, F. Jendrzejewski, M. K. Oberthaler, and J. Berges, "Implementing quantum electrodynamics with ultracold atomic systems", *New J. Phys.* **19**, 23030 (2017) (Cited on p. 121).
- [369] F. Schäfer, H. Konishi, A. Bouscal, T. Yagami, and Y. Takahashi, "Spectroscopic determination of magnetic-field-dependent interactions in an ultracold Yb(3P2)-Li mixture", *Phys. Rev. A* **96**, 032711 (2017) (Cited on p. 121).
- [370] F. Schäfer, N. Mizukami, P. Yu, S. Koibuchi, A. Bouscal, and Y. Takahashi, "Experimental realization of ultracold Yb- Li 7 mixtures in mixed dimensions", *Phys. Rev. A* **98**, 051602 (2018) (Cited on p. 121).
- [371] D. Roy, C. M. Wilson, and O. Firstenberg, "Colloquium: Strongly interacting photons in one-dimensional continuum", *Rev. Mod. Phys.* **89**, 21001 (2017) (Cited on p. 121).
- [372] A. Omran, M. Boll, T. A. Hilker, K. Kleinlein, G. Salomon, I. Bloch, and C. Gross, "Microscopic Observation of Pauli Blocking in Degenerate Fermionic Lattice Gases", *Phys. Rev. Lett.* **115**, 263001 (2015) (Cited on p. 121).
- [373] V. P. Gupta, *Principles and applications of quantum chemistry* (Academic Press, 2015) (Cited on p. 122).
- [374] R. B. Hutson, A. Goban, G. E. Marti, L. Sonderhouse, C. Sanner, and J. Ye, "Engineering Quantum States of Matter for Atomic Clocks in Shallow Optical Lattices", *Phys. Rev. Lett.* **123**, 123401 (2019) (Cited on p. 122).
- [375] M. H. Schleier-Smith, I. D. Leroux, H. Zhang, M. A. Van Camp, and V. Vuletić, "Optomechanical cavity cooling of an atomic ensemble", *Phys. Rev. Lett.* **107**, 143005 (2011) (Cited on p. 122).

- [376] A. Heinz, A. Heinz, J. Trautmann, J. Trautmann, N. Šantić, N. Šantić, A. J. Park, A. J. Park, I. Bloch, I. Bloch, I. Bloch, S. Blatt, and S. Blatt, “Crossed optical cavities with large mode diameters”, *Opt. Lett.* **46**, 250 (2021) (Cited on p. 122).
- [377] A. J. Park, J. Trautmann, N. Šantić, V. Klüsener, A. Heinz, I. Bloch, and S. Blatt, “Cavity-Enhanced Optical Lattices for Scaling Neutral Atom Quantum Technologies to Higher Qubit Numbers”, *PRX Quantum* **3**, 030314 (2022) (Cited on p. 122).
- [378] O. Viyuela, L. Fu, and M. A. Martin-Delgado, “Chiral Topological Superconductors Enhanced by Long-Range Interactions”, *Phys. Rev. Lett.* **120**, 17001 (2018) (Cited on p. 127).
- [379] J. Knörzer, C. J. van Diepen, T.-K. Hsiao, G. Giedke, U. Mukhopadhyay, C. Reichl, W. Wegscheider, J. I. Cirac, and L. M. K. Vandersypen, “Long-range electron-electron interactions in quantum dot systems and applications in quantum chemistry”, [10.48550/arXiv.2202.06756](https://arxiv.org/abs/2202.06756) (2022) (Cited on p. 127).
- [380] J. Feist, J. Galego, and F. J. Garcia-Vidal, “Polaritonic Chemistry with Organic Molecules”, *ACS Photonics* **5**, 205 (2018) (Cited on p. 127).
- [381] J. Fregoni, F. J. Garcia-Vidal, and J. Feist, “Theoretical Challenges in Polaritonic Chemistry”, *ACS Photonics* **9**, 1096 (2022) (Cited on p. 127).
- [382] R. J. MacDonell, C. E. Dickerson, C. J. Birch, A. Kumar, C. L. Edmunds, M. J. Biercuk, C. Hempel, and I. Kassal, “Analog quantum simulation of chemical dynamics”, *Chem. Sci.* **12**, 9794 (2021) (Cited on p. 127).
- [383] F. M. Gabbetta, C. Zhang, M. Hennrich, I. Lesanovsky, and W. Li, “Exploring the Many-Body Dynamics near a Conical Intersection with Trapped Rydberg Ions”, *Phys. Rev. Lett.* **126**, 233404 (2021) (Cited on p. 127).
- [384] C. S. Wang, N. E. Frattini, B. J. Chapman, S. Puri, S. M. Girvin, M. H. Devoret, and R. J. Schoelkopf, “Observation of wave-packet branching through an engineered conical intersection”, [10.48550/arXiv.2202.02364](https://arxiv.org/abs/2202.02364) (2022) (Cited on p. 127).
- [385] S. Katsura and S. Inawashiro, “Lattice Green’s Functions for the Rectangular and the Square Lattices at Arbitrary Points”, *J. Math. Phys.* **12**, 1622 (1971) (Cited on p. 133, 134).
- [386] S. Schmid, G. Thalhammer, K. Winkler, F. Lang, and J. H. Denschlag, “Long distance transport of ultracold atoms using a 1D optical lattice”, *New J. Phys.* **8**, 159 (2006) (Cited on p. 138).
- [387] G. S. Joyce, “Exact evaluation of the simple cubic lattice Green function for a general lattice point”, *J. Phys. A: Math. Gen* **35**, 9811 (2002) (Cited on p. 143).
- [388] J. M. Borwein and I. J. Zucker, “Fast evaluation of the gamma function for small rational fractions using complete elliptic integrals of the first kind”, *IMA Journal of Numerical Analysis* **12**, 519 (1992) (Cited on p. 143).